Université Mohamed Boudiaf - M'sila

FACULTE DE TECHNOLOGIE
DEPARTEMENT DE GENIE ELECTRIQUE

Numéro de série…….
Numéro d'inscription :

Thèse

Présentée pour l'obtention du diplôme de

DOCTORAT LMD

Filière : Electrotechnique

Spécialité : Réseaux électrique

THEME

Commande non linéaire robuste d'un système éolien basé sur une génératrice asynchrone double étoile

Présentée Par

BENZAOUI Khaled

Soutenue le : / /
Devant le jury composé de :

Nom & Prénom	Grade	Etablissement	Qualité
BARKAT Said	**Professeur**	Univ. de M'sila, Algérie	Président
BOUGUERRA Abderrahmen	**Professeur**	Univ. de M'sila, Algérie	Encadreur
ZEGHLACHE Samir	**Professeur**	Univ. de M'sila, Algérie	Co-Encadreur
RAHALI Hilal	**MCA**	Univ. de M'sila, Algérie	Examinateur
BENKHORIS Mohamed Fouad	**Professeur**	Univ. de Nantes, France	Examinateur
TALHAOUI Hicham	**Professeur**	Univ. de BBA, Algérie	Examinateur
HEGAZY Rezk	**Professeur**	Univ.de PSBA,Arabie saoudite	Inviter

Année Universitaire : 2024/2025

Mohamed Boudiaf University - M'sila

FACULTY OF TECHNOLOGY

ELECTRICAL ENGINEERING DEPARTMENT

Serial Number:…….
Registration Number:

Thesis

Presented for the attainment of the

DOCTORATE LMD

Field: Electrical engineering

Specialization: Electrical Network

TITLE

Robust nonlinear control of a wind turbine system based on a dual-stator induction generator

Presented by:

BENZAOUI Khaled

Defended on: / /
Before the jury was composed of:

Name & Surname	Rank	Institution	Role
BARKAT Said	**Professor**	Univ. of M'sila, Algeria	President
BOUGUERRA Abderrahmen	**Professor**	Univ. of M'sila, Algeria	Supervisor
ZEGHLACHE Samir	**Professor**	Univ. of M'sila, Algeria	Co-Supervisor
RAHALI Hilal	**MCA**	Univ. of M'sila, Algeria	Examiner
BENKHORIS Mohamed Fouad	**Professor**	Univ. of Nantes, France	Examiner
TALHAOUI Hicham	**Professor**	Univ. of BBA, Algeria	Examiner
HEGAZY Rezk	**Professor**	Univ. of PSBA, Saudi Arabia	Invit

Academic Year: 2024/2025

Dedications

- ***إلى والدتي؛ سندي وتاج رأسي, حفظك الله لنا وأدام الله عليك بالصحة والعافية.***

- ***إلى والدي, اللهم إنه كان عبدا صالحا فغفرله ورحمه, أكرم نزله ووسع مدخله, نقه من الذنوب والخطايا كما ينقى الثوب الأبيض من الدنس, اللهم إن كان محسنا فزد في إحسانه وإن كان مسيئًا فتجاوز عنه, اللهم أرزقه الجنة بغير حساب.***

- ***إلى أخي وأخواتي؛ أسأل الله أن يرزقكم من حيث لاتحتسبون.***

- ***إلى مشرفي، بوقرة عبد الرحمن؛ ومساعد المشرف، زغلاش سمير؛ لدعمهما المتواصل, جزاكم الله كل خير.***

- ***إلى أستاذي، بركات سعيد؛ جزاك الله عنا كل خير, ورزقك الله الصحة والعافية, ونسأل الله أن يحفظك لأهلك.***

- ***إلى جميع أصدقائي الأعزاء شكرا جزيلا.***

- ***إلى أساتذة مخبر الهندسة الكهربائية كل باسمه كان لي شرف العمل معكم جزاكم الله كل خير.***

- ***إلى الأساتذة الكرام ''أحمد بن ذيب, سعد مخيلف, أحمد السنباري, حجازي رزق, جزاكم الله كل خير على ماقدمتموه لي من يد العون وكان لي شرف العمل معكم, شكرا جزيلا.***

Résumé

Commande non linéaire robuste d'un système éolien basé sur une génératrice asynchrone double étoile.

Cette thèse de doctorat porte sur la commande non linéaire robuste d'un système éolien basé sur une génératrice asynchrone double étoile (GASDE). L'objectif de la recherche est d'optimiser les performances de l'éolienne en développant des stratégies de commande avancées pour améliorer l'extraction de puissance et la stabilité du système. L'étude commence par une vue d'ensemble des systèmes éoliens, mettant en avant l'importance d'une conversion énergétique efficace. La modélisation mécanique de l'éolienne est présentée, incluant les équations aérodynamiques, la loi de Betz, ainsi que la stratégie de suivi du point de puissance maximale (MPPT). La modélisation électrique de la DSIG est également détaillée, en utilisant des techniques de commande vectorielle telles que la commande orientée champ (FOC) avec des régulateurs Proportionnel-Intégral (PI). Afin d'améliorer l'efficacité de la commande, la thèse explore la commande Backstepping (BS), optimisée grâce à l'algorithme d'optimisation basé sur la soustraction-moyenne (SABO). Les résultats montrent que le régulateur BS optimisé améliore la stabilité, réduit les erreurs de suivi et diminue la distorsion harmonique totale (THD). De plus, l'étude s'intéresse à la commande par mode glissant (SMC) sous ses formes premier, second et haut ordre, afin de réduire l'effet de chattering et d'améliorer la robustesse du système. L'algorithme logique intelligent en temps réel (ILA) est proposé pour l'optimisation du contrôleur HOSMC, démontrant une performance supérieure en régime transitoire et permanent. Enfin, la thèse valide les contrôleurs développés grâce à des tests Hardware-in-the-Loop (HIL) sur la plateforme RT-BOX1, prouvant leur efficacité en application temps réel. Cette recherche contribue à l'avancement des systèmes éoliens, en proposant des stratégies de commande adaptatives et optimisées, garantissant une meilleure efficacité, fiabilité et intégration au réseau.

Mots clés: Système éolien, Génératrice Asynchrone Double Etoile (GASDE), Commande non linéaire, Commande Orientée Champ (FOC), Régulateur Proportionnel-Intégral (PI), Commande Backstepping (BS), Algorithme d'Optimisation Basé sur la Soustraction-Moyenne (SABO), Commande par Mode Glissant (SMC), Commande par Mode Glissant d'Ordre Supérieur (HOSMC), Algorithme Logique Intelligent en Temps Réel (ILA), Suivi du Point de Puissance Maximale (MPPT), Distorsion Harmonique Totale (THD), Hardware-in-the-Loop (HIL), RT-BOX1.

Summary

Robust nonlinear control of a wind turbine system based on a dual-stator induction generator

This doctoral thesis focuses on the robust nonlinear control of a wind energy system (WES) based on a dual-stator induction generator (DSIG). The research aims to optimize wind turbine (WT) performance by developing advanced control strategies to enhance power extraction and system stability. The study begins with an overview of WES, emphasizing the importance of efficient energy conversion. The mechanical modeling of the WT is presented, including aerodynamic equations, Betz's law, and the maximum power point tracking (MPPT) strategy. The electrical modeling of the DSIG is also detailed, using vector control techniques such as field-oriented control (FOC) with proportional-integral (PI) controllers. To improve control efficiency, the thesis explores backstepping (BS) control, optimized using the subtraction-average-based optimizer (SABO). The results show that the optimized BS controller enhances stability, reduces tracking errors, and lowers total harmonic distortion (THD). Additionally, the study investigates sliding mode control (SMC) in its first, second, and high-order forms to minimize chattering effects and improve system robustness. The intelligent-in-time logic algorithm (ILA) is proposed for tuning the HOSMC controller, demonstrating superior transient and steady-state performance. Finally, the thesis validates the developed controllers using hardware-in-the-loop (HIL) testing on the RT-BOX1 platform, proving their effectiveness in real-time applications. The research advances wind energy systems by proposing adaptive and optimized control strategies, ensuring improved efficiency, reliability, and grid integration.

Keywords: Wind Energy System (WES), Dual-Stator Induction Generator (DSIG), Nonlinear Control, Field-Oriented Control (FOC), Proportional-Integral (PI) Controller, Backstepping (BS) control, Subtraction-Average-Based Optimizer (SABO), Sliding Mode Control (SMC), High-Order Sliding Mode Control (HOSMC), Intelligent-in-Time Logic Algorithm (ILA), Maximum Power Point Tracking (MPPT), Wind Turbine (WT), Total Harmonic Distortion (THD), Hardware-in-the-Loop (HIL), RT-BOX1.

ملخص

(GASDE) مساهمة في تحكم نظام طاقة رياح يعتمد على مولد تحريضي نو نجمتين

تتناول هذه الأطروحة التحكم غير الخطي القوي في نظام طاقة الرياح (WES) القائم على مولد حثي ذو نجمتين .(DSIG) وتهدف هذه الدراسة إلى تحسين أداء التوربين الريحي (WT) من خلال تطوير استراتيجيات تحكم متقدمة لتعزيز استخراج الطاقة واستقرار النظام .تبدأ الدراسة بعرض نظرة عامة على أنظمة طاقة الرياح، مع التركيز على أهمية تحويل الطاقة بكفاءة. كما يتم تقديم النمذجة الميكانيكية للتوربين الريحي، والتي تشمل المعادلات الديناميكية الهوائية، وقانون بيتز، واستراتيجية تتبع نقطة الطاقة القصوى .(MPPT) بالإضافة إلى ذلك، يتم تفصيل النمذجة الكهربائية للمولد DSIG، باستخدام تقنيات التحكم المتجهي مثل التحكم الموجه للمجال (FOC) مع المتحكم التناسبي-التكاملي .(PI) لتحسين كفاءة التحكم، تستكشف الأطروحة التحكم بطريقة(BS) Backstepping ، الذي تم تحسينه باستخدام خوارزمية التحسين القائمة على الطرح-المتوسط.(SABO) وتظهر النتائج أن المتحكم BS المحسن يعزز الاستقرار، ويقلل من أخطاء التتبع، ويخفض التشوه التوافقي الكلي .(THD) علاوة على ذلك، تتناول الدراسة التحكم بالانزلاق (SMC) بأشكاله الأول والثاني والعالي الرتبة بهدف تقليل تأثير التذبذب (chattering)وتحسين مقاومة النظام للاضطرابات .كما تم اقتراح خوارزمية المنطق الذكي في الوقت الحقيقي (ILA) لضبط متحكمHOSMC ، مما أظهر أداءً متفوقًا في الاستجابة الديناميكية وفي الحالة المستقرة .أخيرًا، تم التحقق من كفاءة المتحكمات المطورة من خلال اختبارات Hardware-in-the-Loop (HIL) على منصة RT-BOX1، مما أثبت فعاليتها في التطبيقات الزمنية الفعلية .تساهم هذه الدراسة في تطوير أنظمة طاقة الرياح من خلال تقديم استراتيجيات تحكم متكيفة ومحسنة، تضمن كفاءة أعلى، موثوقية محسنة، وتكامل أفضل مع الشبكة الكهربائية.

الكلمات المفتاحية: نظام طاقة الرياح (WES)، المولد الحثي ذو النجمتين(DSIG) ،التحكم غير الخطي، التحكم الموجه للمجال (FOC)، المتحكم التناسبي-التكاملي(PI) ، التحكم بطريقة(BS) Backstepping ، خوارزمية التحسين القائمة على الطرح-المتوسط(SABO) ، التحكم بالانزلاق(SMC) ، التحكم بالانزلاق عالي الرتبة(HOSMC) ، خوارزمية المنطق الذكي في الوقت الحقيقي(ILA) ، تتبع نقطة الطاقة القصوى(MPPT) ، التشوه التوافقي الكلي(THD) ، الاختبار-Hardware-in-the Loop (HIL)، منصة.RT-BOX1

List of Figures

List of Tables

List of abbreviations

RE	Renewable Energies
WE	Wind Energy
AC	Alternative Current
WT	Wind Turbine
DSIG	Dual Stator Induction Generator
AC-DC	Alternative Current-Direct Current
PI	Proportional-Integral
WTS	Wind Turbine System
MPPT	Maximum Power Point Tracking
FOC	Field-Oriented Control
BS	Backstepping
WT-DSIG	Wind Turbine based on Dual Stator Induction Generator
SABO	Subtraction-Average-Based Optimizer
ITAE	Integral Time Absolute Errors
IAE	Integral Absolute Error
ISE	Integral Squared Error
THD	Total Harmonic Distortion
SMC	Sliding Mode Control
ILA	Intelligent-in-Time Logic Algorithm
HOSMC	High-Order Sliding Mode Control
FOSMC	First-Order Sliding Mode Control
SOSMC	Second-Order Sliding Mode Control
HIL	Hardware-In-the-Loop
RT-BOX1	Real-Time BOX1
m.m.f	Magnetomotive Force
PWM	Pulse Width Modulation
SVM	Spatial Vector Modulation

List of Symbols

Symbole	Meaning	Unit
V_t	Stationary random process	m/s
V_{moy}	Average wind speed	m/s
V_{wind}	Instantaneous wind speed	m/s
a_k	Amplitude of the harmonic of order k	m/s
ω_k	Pulsation of the harmonic of order k	rad/s
n	rank of the last harmonic	-
γ	rotor attenuation factor	-
R	blade length	m
δ	value of the time constant	-
ρ	density of air	kg/m^3
S	cross-sectional area	m^2
dm	Mass of air	kg
P_{wind}	The mechanical power of wind	W
E	wind kinetic energy	J
P_{turb}	aerodynamic power of the wind turbine	W
C_p	power coefficient	-
λ	tip speed ratio	-
β	The pitch angle of the turbine	[°]
a	interference factor	-
C_{pmax}	maximum value of the power coefficient	-
λ_{opt}	The optimal value of the tip speed ratio	-
Ω_{mec}	rotor mechanical speed	rad/s
G	gearbox gain	-
Ω_{turb}	angular velocity of the turbine	rad/s
T_g	generator torque	N.m
T_{turb}	aerodynamic torque of the turbine	N.m
J	Global inertia moment of the wind turbine system	$kg.m^2$
T_{em}	electromagnetic torque	N.m
k_f	viscous coefficient	N.m.s/rd
α	electrical angle between the phase inputs of the two stars	[°]
θ_0	Initial position of the rotor relative to star 1	[°]
θ_1	Position between the magnetic axes of phases a_r and a_{S1}	[°]
θ_2	Position between the magnetic axes of phases a_r and a_{S2}	[°]
v_{as1}, v_{bs1}, v_{cs1}	phase-to-neutral voltages of star 1	V
i_{as1}, i_{bs1}, i_{cs1}	phase currents of star 1	A
φ_{as1}, φ_{bs1}, φ_{cs1}	self-fluxes circulating in star 1	Wb
R_{as1}, R_{bs1}, R_{cs1}	resistances of the stator phases in star 1	Ω
v_{as2}, v_{bs2}, v_{cs2}	phase-to-neutral voltages of star 2	V
i_{as2}, i_{bs2}, i_{cs2}	phase currents of star 2	A
φ_{as2}, φ_{bs2}, φ_{cs2}	self-fluxes circulating in star 2	Wb
R_{as2}, R_{bs2}, R_{cs2}	resistances of the stator phases in star 2	Ω
v_{ar}, v_{br}, v_{cr}	voltages in the rotor circuit (assumed to be three-phase)	V

i_{ar}, i_{br}, i_{cr}	currents in the rotor circuit	A
φ_{ar}, φ_{br}, φ_{cr}	self-fluxes circulating in the rotor circuit	Wb
R_{ar}, R_{br}, R_{cr}	resistances of the rotor phases	Ω
L_s	self-inductance of each phase of star 1	H
L_{ps}	main inductance of each phase of star 1	H
l_s	leakage inductance of a phase of star 1	H
M_s	mutual inductance between two phases of star 1	H
ℓ_s	self-cyclic inductance of the star	H
ℓ_r	cyclo-inductance of the rotor	H
l_r	leakage inductance of the rotor	H
ℓ_{pr}	main cyclo-inductance of the rotor	H
θ_{s1}	angle between the magnetic axis of phase a_{s1} and axis d	[O]
θ_{s2}	angle between the magnetic axis of phase a_{s2} and axis d	[O]
θ_r	angle between the magnetic axis of phase a_r and axis d	[O]
ω_{coor}	speed of the rotating field	Rad/s
L_{ds1}, L_{qs1}, L_{ds2}, L_{qs2}	Direct and quadrature inductances of the fictitious phases of stators 1 and 2	H
L_m	Cyclic mutual inductance between the stators and the rotor	H
L_{md}, L_{mq}	Direct and quadrature magnetizing inductances	H
ω_s	synchronous speed	Rad/s
ω_r	rotor electrical angular speed	Rad/s
ω_{sl}	slip-speed	Rad/s
P	number of pole pairs	-
P_{em}	electromagnetic powe	W
P_s	absorbed power	W
v_{as1}, v_{bs1}, v_{cs1}	Simple voltages of the phases of star 1	V
v^*_{as1}, v^*_{bs1}, v^*_{cs1}	Simple reference voltages to generate the PWM	V
f_p	modulation frequency	Hz
v_{pm}	modulation wave	-
T_1, T_2 and T_0	Duration of application of the voltage vectors	s
T_s	Sampling time	s
f	Fundamental frequency	Hz
C_f	Filter capacitor	F
V_{LL}	grid line-to-line RMS voltage	V
P_n	rated active power	W
$\omega_{s,g}$	grid angular frequency	Rad/s
$f_{s,g}$	grid frequency	Hz
L_c, L_g	Filter inductors	H
ω_r	resonant frequency	Rad/s
R_D	damping resistor	Ω
φ	Flux imposed by the excitation current I_f	Wb
I_a	Armature current	A

K', K	Constants	-
R_r	resistances of the rotor	Ω
L_r	inductance of the rotor	H
ω_s^*	synchronous speed reference	Rad/s
ω_{sl}^*	slip-speed reference	Rad/s
k_{si}	damping factor	-
P_n	Nominal power	W
$V_{rms} = E$	root mean square (RMS) line voltage	V
X	smoothing inductor's impedance	mH
C_{dc}	DC bus capacitor	F
P_{max}	maximum real power of the load	W
V_{max}	Maximum voltage of the grid	V
$V_{g1,2,3}$	single-phase voltages of the grid	V
L_f	law filter inductence	H
R_f	law filter resistence	Ω

List of Publications Related to the Thesis

- **Publications in International Journals**

  - ✓ **K. Benzaoui** and al., "SABO optimization algorithm-based backstepping controller for DSIG within a wind turbine system," Electr Eng, Nov. 2024, doi: 10.1007/s00202-024-02839-1.
  - ✓ **K. Benzaoui** and al., "IbI logics optimization algorithm-based high-order sliding mode control for DSIG within a wind turbine system," Results in Engineering, vol. 25, p. 103916, Mar. 2025, doi: 10.1016/j.rineng.2025.103916.

- **Publications in International Conferences**

  - ✓ **K. Benzaoui**, A. Bouguerra, S. Zeghlache, M. Boukhari, and A. Zeghlache, "Field Oriented Control Technique of a Wind System Based on a Dual Stator Induction Generator," in 2022 International Conference of Advanced Technology in Electronic and Electrical Engineering (ICATEEE), Nov. 2022, pp. 1–6. doi: 10.1109/ICATEEE57445.2022.10093703.
  - ✓ **K. Benzaoui**, " Optimization of Wind Turbine Systems Using Dual Stator Induction Generators for Improved Power Output," 4th International Conference on Engineering, Natural and Social Sciences, ICENSOS 2024, 22-23 October, Konya, Turkey 2024, pp. 161.

Conferences Website: https://www.icensos.com

  - ✓ **K. Benzaoui**, " Design and Control of Wind Turbine Systems Using Dual Stator Induction Generators for Enhanced Power Output," 3rd International Conference on Contemporary Academic Research, ICCAR 2024, 10-11 November, Konya, Turkey 2024, pp. 40.

Conferences Website: https://as-proceeding.com/index.php/iccar/home

- **Publications in National Conferences**

  - ✓ **K. Benzaoui**, A. Bouguerra, S. Zeghlache, A. Elsanabary, S. Mekhilef, and A. Bendib " HIL platform for Wind Turbine system based on DSIG controlled by backstepping," The 8th Conference on Inductive Techniques University - Industry, *INDUCTICS-CONF* 2024, 17-19 November, M'sila, Algeria 2024, Paper: P3-3, pp. 356-359.

Conferences Website: http://www.inductics-asso.dz/ci2024

Table of Contents

General Introduction

General Introduction

Renewable energies (RE) accounted for nearly a quarter of the world's annual electricity production in 2016 across all sectors. Hydropower remains by far the most widespread source of renewable electricity generation. Wind energy (WE) dates back to around 3,000 BC with the first sailboats. The etymological root of the term "wind energy" comes from Aeolus, the mythological figure known in Greece as the master of the winds. Later, the first windmills were invented by the Persians around 200 BC. The effective use of this energy in Europe only began in the 12th century. Two centuries later, Dutch windmills appeared, used WE for sawing wood or producing oil. However, it was in England that the first advanced blade designs were developed. By the 19th century, England had around 10,000 windmills [1]. WE is an indirect form of solar energy: solar radiation absorbed in the atmosphere causes differences in temperature and pressure. As air masses move, they accumulate kinetic energy, which can be converted into:

- Mechanical energy to propel boats, pump water, or turn windmills.
- Electrical energy to generate direct or alternating current (AC).

In 1891, Danish scientist Paul La Cour built the first wind turbine (WT) capable of generating electricity. Following the creation of the first wind-powered generator, Danish engineers improved the technology during World War I and World War II to cope with electricity shortages. Despite some technological successes during this period, large-scale WE development saw little interest after World War II. However, the 1973 oil crisis revived research into WT development and design, leading to significant advancements since the 1990s. A WT is referred to as an "aerogenerator" when it produces electricity. WE emits no greenhouse gases, and its raw material, the wind, is available worldwide and completely free. Europe, Asia, and North America are the leading regions in adopting wind power as a sustainable electricity source, supported by policies aimed at reducing CO_2 emissions. Today, the WE sector is integrated into energy systems as a complementary source of electrical power. It is experiencing rapid growth both technically (increasing converted power) and economically (reducing installation and maintenance costs). According to [2]:

- The mechanical energy captured by a WT depends on three factors: the shape and length of the blades, wind speed, and temperature, which affect air density;
- The global wind power capacity reached 1,136 GW by the end of 2024, accounting for approximately 11.5%–12.6% of total electricity production;
- Three countries with the largest wind farms today are China, the United States, and Germany;
- A WT starts operating at a wind speed of around 3 m/s and stops, for safety reasons, when the speed reaches 25 m/s;
- A modern WT generates power ranging from a few kW to over 6 MW [3], [4].

In addition, the top five WT manufacturers in 2023–2024 were:

- **Goldwind (China)** – 16.3 GW market share;

- **Envision (China)** – 14.1 GW;
- **Vestas (Denmark)** – 11.5 GW;
- **Windey (China)** – 10.1 GW;
- **Mingyang (China)** – 9.9 GW [3], [4].

System Overview

The studied system consists of a three-bladed, horizontal-axis WT connected to the grid through a dual-stator induction generator (DSIG). The two sets of stator windings are linked to bidirectional AC-DC power converters, which supply a voltage inverter via a DC bus. Finally, the inverter feeds power into the grid through a voltage adaptation transformer.

Control Challenges

This conversion requires control algorithms to efficiently manage energy exchange with the grid and ensure the system's proper operation. A high-performance control system ensures good regulation and tracking response while also being resistant to variations in operating conditions and system parameters.

Over the past decades, several advanced control methods have been developed for WE generation systems. However, ensuring optimal control performance remains challenging due to the complexity of control algorithms and the nonlinear characteristics of the systems involved.

Research Focus

The work presented in this thesis focuses on developing control strategies for a WE conversion system equipped with a DSIG. The simulation results obtained with these controllers will be compared to evaluate their performance in transient and steady-state operating conditions.

Thesis Structure

Chapter I: Modeling and control of the wind turbine system

This study explores the integration of modeling and control strategies to optimize wind energy (WE) systems, emphasizing wind turbines (WTs) as critical tools for converting kinetic wind energy into electrical power. The introduction highlights the growing significance of renewable energy, particularly wind power [5]. It introduces the dual stator induction generator (DSIG), a multi-phase machine valued for reliability and enhanced power output in WE applications. The fundamentals of WE conversion systems are detailed, covering WT components (blades, gearbox, generator), mechanical modeling assumptions (uniform wind distribution, negligible friction), and stochastic wind modeling using Fourier series to simulate realistic conditions. Aerodynamic principles, including Betz's law (theoretical efficiency limit) and power coefficient (C_p) dependencies on tip-speed ratio (λ) and blade pitch angle (β), are analyzed alongside operational zones and optimization techniques like maximum power point tracking (MPPT) to maximize energy extraction [6]. The DSIG's design featuring dual three-phase stator windings and a squirrel-cage rotor is modeled mathematically, with voltage equations transformed into the *dq* reference frame via Park transformations to simplify control. Field-oriented control (FOC) strategies employing PI regulators for rotor speed, flux, and current loops are implemented to enhance efficiency [7]. Simulations in Matlab/Simulink validate the models and control strategies, demonstrating improved dynamic response, power extraction, and adaptability under

varying wind conditions. The study concludes that integrating theoretical modeling, aerodynamic insights, and advanced control methods significantly enhances WT performance, offering a robust framework for sustainable energy optimization.

Chapter II: Optimal Backstepping Control Technique for DSIG-based Wind Turbine System

This chapter focuses on developing an optimized backstepping (BS) controller for a wind turbine based on a dual stator induction generator (WT-DSIG) using the subtraction-average-based optimizer (SABO), a metaheuristic algorithm [8]. The challenge of tuning BS controllers for stable operation and precise tracking is addressed through SABO, which optimizes the natural frequencies of flux, speed, and current controller gains, surpassing traditional trial-and-error methods. The BS control method, a recursive nonlinear technique using Lyapunov functions, ensures robustness by stabilizing the system step-by-step through virtual controls, divided into speed/flux and current loops for tracking and stability [9]. The SABO algorithm initializes search agents, iteratively updates positions using arithmetic means and error-sign-based adjustments, and minimizes the integral time absolute error (ITAE) to refine controller parameters. Simulation results demonstrate the optimized BS controller's superiority, showing lower integral absolute error (IAE), integral squared error (ISE), faster transient responses, reduced steady-state ripples, and cleaner power output with lower total harmonic distortion (THD) (39.68% vs. 47.77%) compared to traditional methods. The study concludes that SABO-optimized BS control enhances tracking, stability, and efficiency in WT-DSIG systems, with potential applications in other renewable energy systems. Future research could explore hybrid optimization techniques or other metaheuristic algorithms to further advance control performance, underscoring the role of advanced optimization in improving renewable energy reliability and efficiency [10].

Chapter III: Optimal first, second, and high-order sliding mode control for DSIG-based wind turbine system

This chapter explores the application of sliding mode control (SMC) strategies, particularly high-order sliding mode control (HOSMC), optimized via the intelligent-in-time logic algorithm (ILA), to enhance the performance and stability of a wind turbine with a dual stator induction generator (WT-DSIG) [11], [12]. Addressing tracking precision and robustness challenges, the study introduces ILA a metaheuristic algorithm to simultaneously tune parameters for flux, speed, and current HOSMC controllers integrated with field-oriented control (FOC). The framework progresses from first-order SMC (FOSMC), a robust but chatter-prone method, to second-order SMC (SOSMC), which mitigates chattering via the super-twisting algorithm, and finally to third-order SMC (TOSMC), incorporating integral and fractional power terms to further reduce oscillations and improve transient performance [13]. The ILA optimizes these controllers through a three-stage process (exploration, integration, exploitation), minimizing integral time absolute error (ITAE) for system variables. Simulations on a 1.5 MW WT-DSIG in MATLAB/Simulink demonstrate the superiority of ILA-tuned HOSMC, showcasing faster transient responses, lower steady-state errors (IAE, ISE), reduced total harmonic distortion (THD), and minimal chattering compared to traditional methods. The optimized HOSMC also excels under variable wind speeds, achieving rapid, overshoot-free adjustments. The study concludes that ILA-driven HOSMC significantly enhances control precision and reliability in renewable energy systems, with potential applications extending to other wind turbine configurations and hybrid optimization approaches [14].

Chapter IV: Hardware-in-the-loop (HIL) testing using RT-BOX1

This chapter discusses the RT-BOX1, a high-performance real-time simulation, and hardware-in-the-loop (HIL) testing platform developed by Plexim. It is a crucial tool for researchers and engineers working on control systems, power electronics, and embedded system development. The RT-BOX1 bridges the gap between theoretical simulations and practical implementations by allowing real-time execution of complex models with low latency and precise timing. Equipped with a high-speed FPGA and a multicore processor, it supports a range of analog and digital I/O interfaces, enabling seamless integration with external devices like sensors, actuators, and controllers [15].

The chapter highlights key features of the RT-BOX1, including real-time simulation capabilities, high I/O versatility, and seamless integration with PLECS software. The implementation process on the RT-BOX1 involves model development using PLECS, model deployment onto the RT-BOX1, hardware integration with external components, real-time execution, and HIL testing. This process allows engineers to test control algorithms and validate system performance under different conditions without the risks and costs associated with full-scale physical testing [16].

HIL testing results focus on the performance of various controllers, including PI, BS, and HOSMC, for a wind turbine system using a DSIG. The optimized controllers demonstrate superior performance over conventional ones, ensuring better tracking of reference signals, faster transient response, and lower steady-state errors. Specifically, optimized PI and BS controllers significantly reduce THD, while optimized HOSMC outperforms all controllers regarding transient response, control accuracy, and steady-state performance. The chapter concludes that using optimization techniques for controller tuning enhances control performance, improves system stability, and provides a scalable solution for diverse applications [17], [18].

Chapter I. Modeling and control of the wind turbine system

Chapter I. Modeling and control of the wind turbine system

I.1 Introduction

As the demand for renewable energy sources (RESs) continues to grow, wind energy has emerged as a key solution for sustainable power generation. WTs play a crucial role in converting wind's kinetic energy into electrical power, but optimizing their performance requires advanced modeling, control, and simulation techniques. This chapter provides a comprehensive study of WTS modeling, focusing on both the mechanical and electrical aspects, with a particular emphasis on DSIG control. Using Matlab/Simulink, the study develops and validates aerodynamic models, electrical models, and control strategies to improve wind energy conversion efficiency.

The first section introduces the fundamentals of wind energy conversion, detailing the key components of a WT, including the blade system, gearbox, and generator. The aerodynamic modeling of the turbine is explored through power coefficient analysis, Betz's law, and the tip speed ratio, all of which influence the efficiency of power extraction. Additionally, wind speed modeling techniques are discussed to account for the stochastic nature of wind, ensuring realistic system simulations. The chapter concludes with the concept of MPPT, which enables the turbine to operate at its optimal efficiency under varying wind conditions.

The chapter then shifts focus to the electrical modeling of the DSIG, a multi-phase machine that offers higher power output and improved reliability for wind energy applications. The natural reference frame (*a, b, c*) model is developed, followed by a transformation into the (*d, q*) rotating reference frame using the Park transformation. This approach simplifies the machine's control and analysis, providing a foundation for vector control strategies.

To ensure efficient wind energy conversion, a field-oriented control (FOC) strategy with a PI controller is implemented for the DSIG. This vector control technique allows independent regulation of torque and flux, enabling precise speed and power control. The PI controller is employed to regulate three key control loops:

- Rotor speed control, ensuring stable generator operation under fluctuating wind conditions.
- Flux control, maintaining optimal excitation levels for improved efficiency.
- Stator current control, managing power flow and minimizing losses.

Finally, a simulation study using Matlab/Simulink is conducted to validate the proposed models and control strategies. The simulation results assess WT performance, DSIG dynamic response, power extraction efficiency, and the effectiveness of the PI-based vector control strategy. Through these analyses, the study demonstrates how advanced control techniques can significantly enhance WT operation, making them more efficient and adaptable to varying wind conditions.

By integrating mechanical modeling, electrical modeling, and control optimization, this document provides a comprehensive framework for improving wind energy conversion systems. The findings serve as a valuable resource for researchers and engineers working on renewable energy systems, wind turbine optimization, and power electronics control.

I.2 Modeling of the wind turbine system

I.2.1 Conversion of wind energy

A WT (or wind generator) is a device that transforms part of the kinetic energy of the wind into mechanical energy available on the transmission shaft through a speed multiplier G, without which the generator cannot operate, as its rotation speed cannot be too low. The mechanical energy received on the rotor shaft of the electric generator is thus transformed into electrical energy [19],[20]. In our case, the wind system is mainly composed of the following components:

- A horizontal-axis turbine with three adjustable blades with inertia, elasticity, and friction coefficients concerning the air and the turbine support.
- A speed gearbox with gain G.
- A generator with a moment of inertia and viscous coefficient.

In this section, we describe the basic interaction principles between the wind turbine blades and the wind to derive the simplified expressions for the converted power.

I.2.2 Simplifying hypotheses for the mechanical modeling of the turbine

The models most frequently encountered in electromechanical studies are relatively simple and obey simplifying hypotheses [6]-[21]:

- The wind speed is assumed to be uniformly distributed across all the blades, which allows the entire set of blades to be considered as a single mechanical system.
- The viscous coefficient of the blades relative to the air is very low and can be ignored.
- The friction losses of the turbine rotor are considered negligible compared to the friction losses on the generator side.

I.2.3 Wind modeling

Wind serves as the main energy source captured by wind turbines WTs [22]. In numerous studies, wind is treated as a random variable characterized by statistical parameters [23]. A common method for modeling wind involves simulating its time-dependent behavior by applying a transfer function to white noise. The choice of this transfer function depends on the site-specific conditions and wind characteristics [24].

The wind model is represented using a Fourier series, depicting wind as a combination of multiple harmonic components. This decomposition splits wind speed into two parts:

- The turbulent component, $V_t(t)$, given by (I.2), is a stationary random process. It remains constant regardless of changes in the mean wind speed, playing a key role in wind modeling.
- The slow-varying component, V_{moy}, as defined in (I.1), represents the average wind speed, which fluctuates gradually over long periods at a specific location.

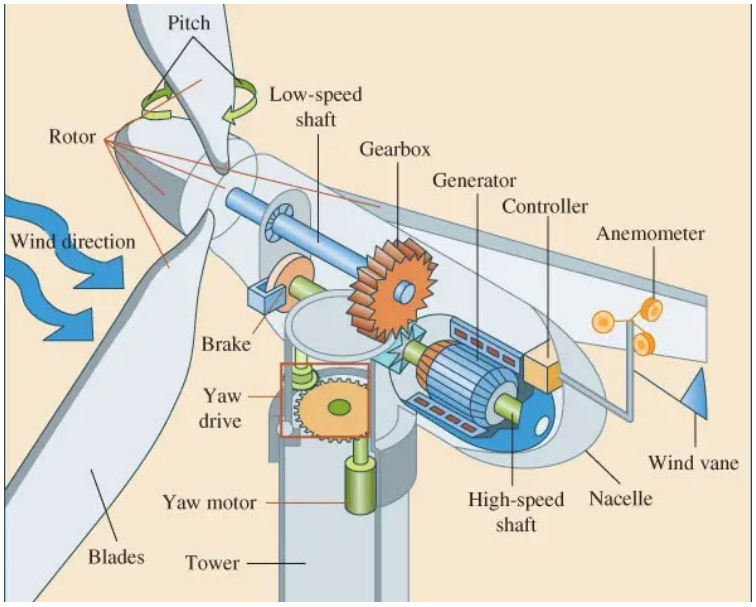

Figure I.1- General configuration of a wind turbine system [1].

$$V_{wind}(t) = V_{moy} + V_t(t) \tag{I.1}$$

$$V_t(t) = \sum_{k=1}^{n} a_k \sin(\omega_k t) \tag{I.2}$$

Here, V_{wind} represents the instantaneous wind speed, a_k is the amplitude of the k^{th} harmonic, ω_k denotes the angular frequency of the k^{th} harmonic, and n indicates the highest-order harmonic included in the wind profile calculation.

It should be noted that wind turbines inherently filter out high-frequency fluctuations. To account for this, the turbulent component is processed through a low-pass filter (LPF) to better emulate real-world behavior. The transfer function of this filter is given by:

$$G_f(s) = \frac{1}{1+\delta s} \tag{I.3}$$

with:

$$\delta = \gamma \frac{R}{V_{moy}} \tag{I.4}$$

The time constant δ [24]-[10] is influenced by two key parameters: γ (the rotor attenuation factor) and R (the blade length).

I.2.3.1 Mechanical power of the wind

The kinetic energy of a column with a density of air ρ, moving at a velocity V_{wind}, of length dx, and cross-sectional area S, as **Figure I.2** shows, can be derived as follows:

$$dE = \frac{1}{2}.dm.V_{wind}^2 \tag{I.5}$$

where $dm = \rho.S.dx$ is the mass of this air column.

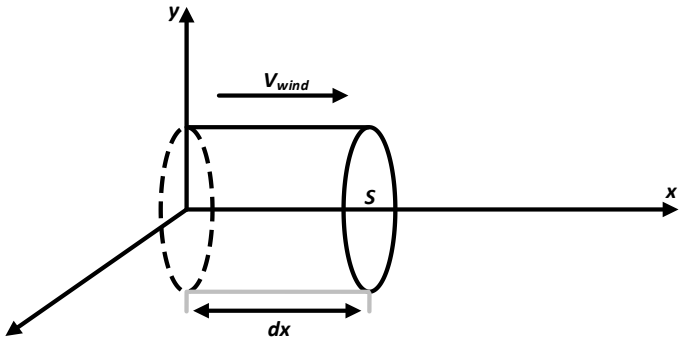

Figure I.2- Representation of an air column

Now we know that: $V_{wind} = \frac{dx}{dt}$, therefore (I.5) yields:

$$dE = \frac{1}{2}.\rho.S.V_{wind}^{3}.dt \tag{I.6}$$

We thus deduce the expression for the available power, P_{wind}:

$$P_{wind} = \frac{dE}{dt} = \frac{1}{2}.\rho.S.V_{wind}^{3} = \frac{1}{2}.\rho.\pi.R^{2}.V_{wind}^{3} = P_{\text{incidental}} \tag{I.7}$$

Wind energy is the kinetic energy of recoverable air passing through a certain surface $S = \pi.R^2$. Power is proportional to the cube of the wind speed:

I.2.4 Aerodynamic parameters of the wind turbine

A WT is a device that transforms the wind's kinetic energy into mechanical energy.

I.2.4.1 Mechanical power of the wind turbine

Considering expression (I.7), the aerodynamic power extracted from the wind power can be written as follows. [25]-[26]:

$$P_{turb} = C_p.P_{wind} = \frac{1}{2}.\rho.\pi.R^{2}.C_p.V_{wind}^{3} \tag{I.8}$$

with :

- P_{turb}: Aerodynamic power of the wind turbine [W].
- C_p: Power coefficient representing the efficiency of converting wind energy.

I.2.4.2 Power coefficient of the turbine

According to the aerodynamic efficiency of the turbine, only a part of the mechanical power of the wind is converted into mechanical power. The dimensionless power coefficient, characteristic of the turbine, expresses this conversion efficiency. It depends on its aerodynamic profile and the number of its blades. It is a nonlinear function of both the pitch angle of the turbine blades β and the tip speed ratio λ [2]:

$$\lambda = \frac{Tip\ speed\ of\ the\ blades}{Wind\ speed} \tag{I.9}$$

This coefficient is denoted as $C_p(\lambda, \beta)$. As we will see below, its theoretical maximum value is approximately 0.59. In practice, it ranges between 0.4 and 0.45.

Numerical approximations have been developed in the literature to calculate $C_p(\lambda, \beta)$. For the type of turbine studied here, its expression is given by [1]:

$$C_p = 0.5109\left(116\delta - 0.4\beta - 5\right)e^{(-21\delta)} + 0.0068\lambda \tag{I.10}$$

with:

$$\delta = \frac{1}{\lambda + 0.08\beta} - \frac{0.035}{1+\beta^3} \tag{I.11}$$

Appendix C describes this power coefficient in detail.

I.2.4.3 Albert Betz's Law

According to Betz's theory, we can express $C_p(\lambda, \beta)$ as a function of an interference factor a [27], [28]:

$$C_p\left(\lambda, \beta\right) = 4a.\left(1-a\right)^2 \tag{I.12}$$

The maximum value of the power coefficient is called the Betz limit. Betz derived it using the following approach:

$\frac{dC_p}{da} = 0$ therefore $\frac{d[4a(1-a)^2]}{da} = 0$ and $4 - 16a + 12a^2 = 0$ from where $a = 1$ (rejected solution) and $a = \frac{1}{3}$

Then, we obtain $C_{pmax} \approx 0.5926 = 59.26\%$.

This limit indicates that the turbine cannot extract more than 59.26% of the wind's power.

I.2.4.4 Specific speed

To facilitate the practical use of the power coefficient C_p, the specific speed λ is typically introduced using the following expression:

$$\lambda = \frac{R.\Omega_{turb}}{V_{wind}} \tag{I.13}$$

Figure I. 3 illustrates the graphical representation of the power coefficient C_p, obtained using expression (I.10).

It can be observed that the power coefficient reaches a maximum ($C_{p\max} = 0.47$) for a blade pitch angle $\beta = 0$. This corresponds to an optimal value of the specific speed $\lambda_{opt} = 8.1$.

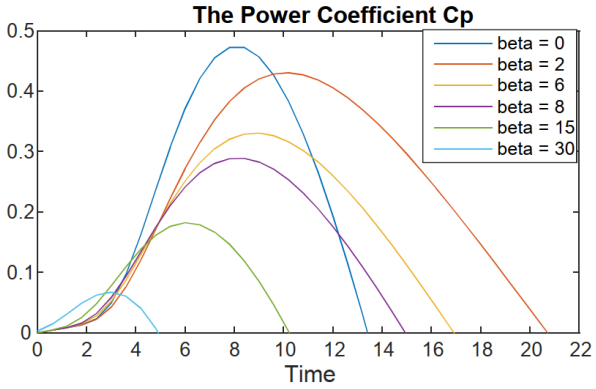

Figure I.3- Graphical representation of the power coefficient and determination of the optimal specific speed

I.2.4.5 Mechanical torque of the turbine

From expression (I.8) of the power produced by the turbine and knowing its angular velocity Ω_{turb}, the mechanical torque of the turbine T_{turb} is expressed as follows:

$$T_{turb} = \frac{P_{turb}}{\Omega_{turb}} = \frac{1}{2}.\rho.\pi.R^2.C_p\left(\lambda,\beta\right).V_{wind}^3.\frac{1}{\Omega_{turb}} \tag{I.14}$$

I.2.4.6 Gearbox model

The gearbox converts the mechanical speed of the turbine into the generator speed and the aerodynamic torque of the turbine into the generator's driving torque according to the following expressions:

$$T_g = \frac{T_{turb}}{G} \tag{I.15}$$

$$\Omega_{mec} = G.\Omega_{turb} \tag{I.16}$$

with:

- Ω_{mec}: Rotor mechanical speed [rad/s],
- G: Gearbox gain,
- Ω_{turb}: Angular velocity of the turbine [rad/s],
- T_g: Generator torque [N.m],
- T_{turb}: Aerodynamic torque of the turbine [N.m].

I.2.4.7 Dynamic equation of the drive shaft

The fundamental dynamic equation makes it possible to determine the evolution of the mechanical speed from the mechanical torque applied to the WT rotor shaft T_g and the electromagnetic torque T_{em}:

$$\Omega_{mec} = \frac{1}{Js + k_f}(T_g - T_{em}) \tag{I.17}$$

with: $\Omega_{mec} = \frac{d\theta_{mec}}{dt}$

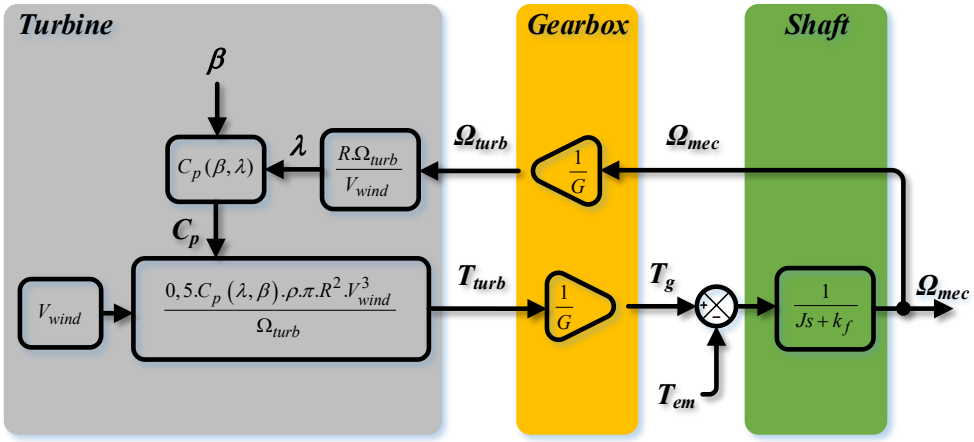

Figure I.4- Block diagram of the WT model.

- J: Global inertia moment of the WTS [kg.m^2],
- T_{em}: Electromagnetic torque [N.m],
- k_f: Viscous coefficient [N.m.s/rd].

From the previous expressions, the block diagram corresponding to the turbine modeling can be derived as depicted in **Figure I.4**.

I.3 Variable speed operating zones of a wind turbine

The maximum power that a WT can produce (captured) is its nominal power. The wind speed at which the wind turbine reaches its nominal power is called the nominal wind speed. Above this speed, power production remains constant regardless of the wind speed until reaching a maximum operating wind speed, at which the wind turbine is designed to stop to protect its mechanical components from the harmful effects of high wind speeds. The lowest wind speed at which a wind turbine will operate is called the starting speed. Between these two speeds, power production varies with the wind speed, as shown in **Figure I.5** [29].

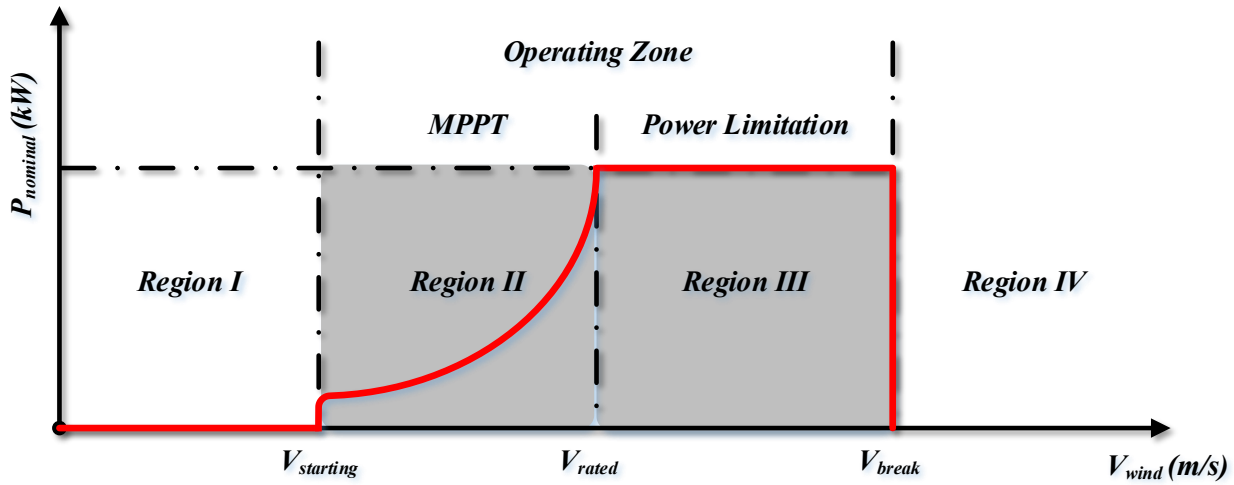

Figure I.5- Operating zones of a WT

- **Region I:** $V_{wind} < V_{starting}$ where $P = 0$: standby phase (the turbine is not operating);
- **Region II:** $V_{starting} < V_{wind} < V_{rated}$: the power delivered to the shaft depends on the wind speed (normal production until reaching nominal power);
- **Region III:** $V_{rated} < V_{wind} < V_{break}$: the rotational speed is kept constant (power regulated at its nominal value);
- **Region IV:** $V_{wind} > V_{break}$ (approximately 90 km/h): the safety system halts energy transfer (WT stops operating).

I.4 Optimization of energy conversion for a variable-speed wind turbine

The use and development of wind energy have become a significant part of global energy development, as wind is a sustainable and environmentally friendly energy source. However, due to the erratic nature of this energy, turbine design and control modes must be optimized to extract the maximum possible power from wind energy. Several algorithms have been developed to achieve optimal operating points for maximum power transfer. In general, they determine turbine operation based on its internal characteristics. MPPT is a set of wind energy conversion techniques [30]. Various studies have been conducted to develop faster MPPT techniques for any wind energy conversion system.

I.4.1 Principle of Maximum Power Point Tracking (MPPT)

The principle of the MPPT strategy consists, for a given blade pitch angle, of adjusting the turbine's rotational speed, depending on the wind speed V_{wind}, to a reference value Ω_{turb} to maintain an optimal relative speed and thus achieve a maximum power coefficient C_{pmax}. Considering expression (I.13), we can rewrite expression (I.16) as follows [31]:

$$\Omega_{mec}^{*} = \frac{V_{wind}.\lambda_{opt}}{R} G \tag{I.18}$$

The action on the electromagnetic torque (and thus on the power converted by the generator) enables the determination of Ω^{*}_{mec} and thus maximize the extracted power while maintaining C_{pmax}. **Figure I.6** depicts the block diagram of an MPPT intended for WT power maximixation.

I.5 Modeling of the dual-stator induction generator (DSIG)

Multi-phase machines are increasingly being used for the following two key reasons [32], [33]:

- To segment power and create a high-power machine-converter system using smaller power components, which reduces costs;
- To improve reliability.

I.5.1 Brief description of the DSIG

The DSIG consists of a stator with two identical three-phase windings offset by an electrical angle (e.g., $\alpha = 30^{o}$) and a squirrel-cage rotor.

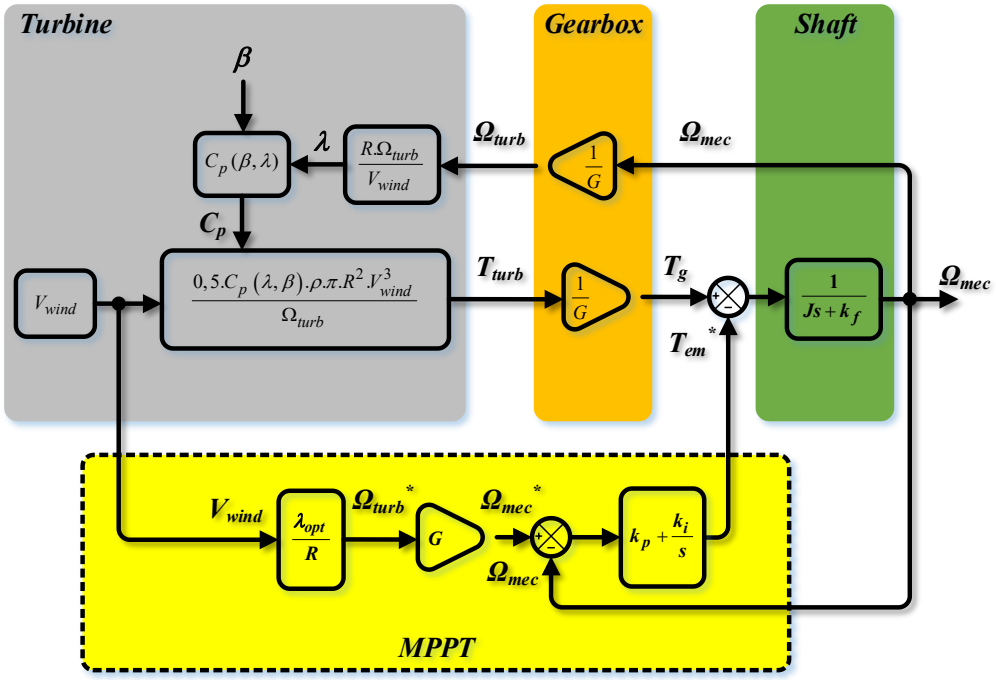

Figure I.6- Maximization of extracted power with speed control [1].

Figure I.7 shows the positions of the magnetic axes of the windings forming the machine's phases. Quantities related to the first star will be denoted with index 1, and those associated with the second star will be denoted with index 2.

The angle θ_1 represents the position of the rotor (phase a_r) relative to stator 1 (phase a_{S1}), and θ_2 represents the position of the rotor relative to stator 2 (phase a_{S2}).

$$\theta_1 = \Omega_{mec} t + \theta_0 \tag{I.19}$$

$$\theta_2 = \theta_1 - \alpha \tag{I.20}$$

- Ω_{mec}: Rotor mechanical speed [rad/s];
- θ_0: Initial position of the rotor relative to star 1.

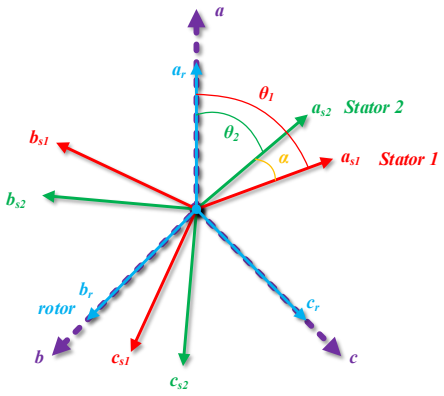

Figure I.7- Representation of the windings of the DSIG.

I.5.2 Simplifying hypotheses for the study of the DSIG

The DSIG, with its winding distribution and geometry, is highly complex for analysis considering its exact configuration. It is therefore necessary to adopt certain simplifying hypotheses [34]:

- The machine is assumed to be "linear," neglecting magnetic saturation and hysteresis effects, as well as phenomena causing variations in resistance and inductance (e.g., temperature and frequency dependence);
- Core losses are disregarded in the machine equations, with the magnetic permeability assumed to be infinite;
- The air-gap magnetomotive force produced by each winding is assumed to have a sinusoidal spatial distribution, thereby neglecting spatial harmonics;
- The effect of slotting is neglected, implying a constant air-gap width;
- It is assumed that the two-stator three-phase windings are balanced and identical.

I.5.3 Model in the natural (*a, b, c*) reference frame of the DSIG

Individually, the three-phase windings of both stars and the rotor circuit (squirrel-cage or three-phase winding) can be governed by Faraday's law of the form (I.21), which represents a combination of Ohm's and Lenz's laws. The same law can also govern the entire machine by superimposing the effects due to the simultaneous presence of the three circuits.

I.5.3.1 Generator mode voltage equations

Considering the simplification hypotheses stated above, the voltage equations of the DSIG operating in generator mode are as follows:

a. Voltage equations for star 1:

$$\left[v_{s1}\right] = -\left[R_{s1}\right]\left[i_{s1}\right] - \frac{d\left[\varphi_{s1}\right]}{dt} \tag{I.21}$$

$$\text{with : } \left[v_{s1}\right] = \begin{bmatrix} v_{as1} \\ v_{bs1} \\ v_{cs1} \end{bmatrix}, \left[i_{s1}\right] = \begin{bmatrix} i_{as1} \\ i_{bs1} \\ i_{cs1} \end{bmatrix}, \left[\varphi_{s1}\right] = \begin{bmatrix} \varphi_{as1} \\ \varphi_{bs1} \\ \varphi_{cs1} \end{bmatrix}, \left[R_{s1}\right] = \begin{bmatrix} R_{as1} & 0 & 0 \\ 0 & R_{bs1} & 0 \\ 0 & 0 & R_{cs1} \end{bmatrix}$$

v_{as1}, v_{bs1}, v_{cs1}: Phase-to-neutral voltages of star 1;
i_{as1}, i_{bs1}, i_{cs1}: Phase currents of star 1;
φ_{as1}, φ_{bs1}, φ_{cs1}: Self-fluxes circulating in star 1;
R_{as1}, R_{bs1}, R_{cs1}: Resistances of the stator phases in star 1.

For a balanced star 1 circuit, we have: $R_{as1} = R_{bs1} = R_{cs1} = R_{s1}$

b. Voltage equations for star 2:

$$[v_{s2}] = -[R_{s2}][i_{s2}] - \frac{d[\varphi_{s2}]}{dt} \tag{I.22}$$

$$\text{with : } [v_{s2}] = \begin{bmatrix} v_{as2} \\ v_{bs2} \\ v_{cs2} \end{bmatrix}, [i_{s2}] = \begin{bmatrix} i_{as2} \\ i_{bs2} \\ i_{cs2} \end{bmatrix}, [\varphi_{s2}] = \begin{bmatrix} \varphi_{as2} \\ \varphi_{bs2} \\ \varphi_{cs2} \end{bmatrix}, [R_{s2}] = \begin{bmatrix} R_{as2} & 0 & 0 \\ 0 & R_{bs2} & 0 \\ 0 & 0 & R_{cs2} \end{bmatrix}$$

v_{as2}, v_{bs2}, v_{cs2}: Phase-to-neutral voltages of star 2;
i_{as2}, i_{bs2}, i_{cs2}: Phase currents of star 2;
φ_{as2}, φ_{bs2}, φ_{cs2}: Self-fluxes circulating in star 2;
R_{as2}, R_{bs2}, R_{cs2}: Resistances of the stator phases in star 2.

Similarly, for a balanced star 2 circuit, we have: $R_{as2} = R_{bs2} = R_{cs2} = R_{s2}$

c. Voltage equations for the rotor:

$$[v_r] = -[R_r][i_r] - \frac{d[\varphi_r]}{dt} \tag{I.23}$$

$$\text{with : } [v_r] = \begin{bmatrix} v_{ar} \\ v_{br} \\ v_{cr} \end{bmatrix}, [i_r] = \begin{bmatrix} i_{ar} \\ i_{br} \\ i_{cr} \end{bmatrix}, [\varphi_r] = \begin{bmatrix} \varphi_{ar} \\ \varphi_{br} \\ \varphi_{cr} \end{bmatrix}, [R_r] = \begin{bmatrix} R_{ar} & 0 & 0 \\ 0 & R_{br} & 0 \\ 0 & 0 & R_{cr} \end{bmatrix}$$

v_{ar}, v_{br}, v_{cr}: Voltages in the rotor circuit (assumed to be three-phase);
i_{ar}, i_{br}, i_{cr}: Currents in the rotor circuit;
φ_{ar}, φ_{br}, φ_{cr}: Self-fluxes circulating in the rotor circuit;
R_{ar}, R_{br}, R_{cr}: Resistances of the rotor phases.

For a balanced rotor circuit, we have: $R_{ar} = R_{br} = R_{cr} = R_r$

For a squirrel-cage rotor circuit: $v_{ar} = v_{br} = v_{cr} = 0$

d. Voltage equations for the DSIG:

In matrix notation, we can write:

$$[v] = -[R].[i] - \frac{d[\varphi]}{dt} \tag{I.24}$$

with :

$$[v] = \left[[v_{s1}]\ [v_{s2}]\ [v_r]\right]^{tr} = [v_{as1}\ v_{bs1}\ v_{cs1}\ v_{as2}\ v_{bs2}\ v_{cs2}\ 0\ 0\ 0]^{tr}$$

$$[i] = \left[[i_{s1}]\ [i_{s2}]\ [i_r]\right]^{tr} = [i_{as1}\ i_{bs1}\ i_{cs1}\ i_{as2}\ i_{bs2}\ i_{cs2}\ i_{ar}\ i_{br}\ i_{cr}]^{tr}$$

$$[\varphi] = \left[[\varphi_{s1}]\ [\varphi_{s2}]\ [\varphi_r]\right]^{tr} = [\varphi_{as1}\ \varphi_{bs1}\ \varphi_{cs1}\ \varphi_{as2}\ \varphi_{bs2}\ \varphi_{cs2}\ \varphi_{ar}\ \varphi_{br}\ \varphi_{cr}]^{tr}$$

$$[R]=\begin{bmatrix}[R_{s1}] & [0] & [0]\\ [0] & [R_{s2}] & [0]\\ [0] & [0] & [R_r]\end{bmatrix}=\begin{bmatrix}R_{as1} & 0 & 0 & 0 & 0 & 0 & 0 & 0 & 0\\ 0 & R_{bs1} & 0 & 0 & 0 & 0 & 0 & 0 & 0\\ 0 & 0 & R_{cs1} & 0 & 0 & 0 & 0 & 0 & 0\\ 0 & 0 & 0 & R_{as2} & 0 & 0 & 0 & 0 & 0\\ 0 & 0 & 0 & 0 & R_{bs2} & 0 & 0 & 0 & 0\\ 0 & 0 & 0 & 0 & 0 & R_{cs2} & 0 & 0 & 0\\ 0 & 0 & 0 & 0 & 0 & 0 & R_{ar} & 0 & 0\\ 0 & 0 & 0 & 0 & 0 & 0 & 0 & R_{br} & 0\\ 0 & 0 & 0 & 0 & 0 & 0 & 0 & 0 & R_{cr}\end{bmatrix}$$

I.5.3.2 Expressions for flux

The total flux embraced by a phase of star 1 is obtained by the vector sum of the effect of the current in the considered coil and the impact of the currents circulating in the other coils.

This addition can be expressed in matrix form.

- For **star 1**:

$$[\varphi_{s1}]=[L_{s1}].[i_{s1}]+[M_{s1s2}].[i_{s2}]+[M_{s1r}(\theta_1)].[i_r] \tag{I.25}$$

- For **star 2**:

$$[\varphi_{s2}]=[L_{s2}].[i_{s2}]+[M_{s2s1}].[i_{s1}]+[M_{s2r}(\theta_2)].[i_r] \tag{I.26}$$

- For the **rotor**:

$$[\varphi_r]=[M_{rs1}(\theta_1)].[i_{s1}]+[M_{rs2}(\theta_2)].[i_{s2}]+[L_r].[i_r] \tag{I.27}$$

By rewriting all of this in a compact form, we obtain the inductance matrix for the DSIG as:

$$[\varphi]=\begin{bmatrix}[\varphi_{s1}]\\ [\varphi_{s2}]\\ [\varphi_r]\end{bmatrix}=\begin{bmatrix}[L_{s1}] & [M_{s1s2}] & [M_{s1r}(\theta_1)]\\ [M_{s2s1}] & [L_{s2}] & [M_{s2r}(\theta_2)]\\ [M_{rs1}(\theta_1)] & [M_{rs2}(\theta_2)] & [L_r]\end{bmatrix}.\begin{bmatrix}[i_{s1}]\\ [i_{s2}]\\ [i_r]\end{bmatrix} \tag{I.28}$$

I.5.3.3 Inductances in Star 1

For example, the inductances from equation (I.25) are defined as follows.

$$[L_{s1}]=\begin{bmatrix}L_s & M_s & M_s\\ M_s & L_s & M_s\\ M_s & M_s & L_s\end{bmatrix} \tag{I.29}$$

with:

- L_s: Self-inductance of each phase of star 1;

$$L_s = L_{ps} + l_s \tag{I.30}$$

- L_{ps}: Main inductance of each phase of star 1;
- l_s: Leakage inductance of a phase of star 1;
- M_s: Mutual inductance between two phases of star 1.

The sum of the three currents in the three-phase winding (star 1) is necessarily zero ($i_{as1} + i_{bs1} + i_{cs1} = 0$), the expression $[L_{s1}].[i_{s1}]$ can be written as:

$$[L_{s1}].[i_{s1}] = \begin{bmatrix} L_s & M_s & M_s \\ M_s & L_s & M_s \\ M_s & M_s & L_s \end{bmatrix}.\begin{bmatrix} i_{as1} \\ i_{bs1} \\ i_{cs1} \end{bmatrix} = \begin{bmatrix} L_{ps}+l_s & -\frac{1}{2}L_{ps} & -\frac{1}{2}L_{ps} \\ -\frac{1}{2}L_{ps} & L_{ps}+l_s & -\frac{1}{2}L_{ps} \\ -\frac{1}{2}L_{ps} & -\frac{1}{2}L_{ps} & L_{ps}+l_s \end{bmatrix}.\begin{bmatrix} i_{as1} \\ i_{bs1} \\ -(i_{as1}+i_{bs1}) \end{bmatrix} \tag{I.31}$$

It is also shown that the diagonalization of the inductance matrix allows for writing [34]:

$$[L_{s1}].[i_{s1}] = \begin{bmatrix} L_s & M_s & M_s \\ M_s & L_s & M_s \\ M_s & M_s & L_s \end{bmatrix}.\begin{bmatrix} i_{as1} \\ i_{bs1} \\ i_{cs1} \end{bmatrix} = \begin{bmatrix} l_s+\frac{3}{2}L_{ps} & 0 & 0 \\ 0 & l_s+\frac{3}{2}L_{ps} & 0 \\ 0 & 0 & l_s+\frac{3}{2}L_{ps} \end{bmatrix}.\begin{bmatrix} i_{as1} \\ i_{bs1} \\ i_{cs1} \end{bmatrix} \tag{I.32}$$

The quantity $\frac{3}{2}.L_{ps}$ is the main cyclic inductance of star 1, denoted as ℓ_{ps} . Thus, we write:

$$\ell_s = l_s + \ell_{ps} \tag{I.33}$$

- ℓ_s : Self-cyclic inductance of the star.

Finally, we obtain:

$$[L_{s1}].[i_{s1}] = \begin{bmatrix} \ell_s & 0 & 0 \\ 0 & \ell_s & 0 \\ 0 & 0 & \ell_s \end{bmatrix}.\begin{bmatrix} i_{as1} \\ i_{bs1} \\ i_{cs1} \end{bmatrix} = \ell_s \begin{bmatrix} 1 & 0 & 0 \\ 0 & 1 & 0 \\ 0 & 0 & 1 \end{bmatrix}.\begin{bmatrix} i_{as1} \\ i_{bs1} \\ i_{cs1} \end{bmatrix} \tag{I.34}$$

I.5.3.4 Flux in the DSIG machine

The flux expressions for the entire machine are:

- ***For star 1:*** From expression (III.7), we have:

$$[\varphi_{s1}] = [L_{s1}].[i_{s1}] + [M_{s1s2}].[i_{s2}] + [M_{s1r}(\theta_1)].[i_r] \tag{I.35}$$

Thus:

$$[\varphi_{s1}] = \begin{bmatrix} \varphi_{as1} \\ \varphi_{bs1} \\ \varphi_{cs1} \end{bmatrix} = \ell_s . \begin{bmatrix} 1 & 0 & 0 \\ 0 & 1 & 0 \\ 0 & 0 & 1 \end{bmatrix} . \begin{bmatrix} i_{as1} \\ i_{bs1} \\ i_{cs1} \end{bmatrix} + [M_{s1s2}(\alpha)] . \begin{bmatrix} i_{as1} \\ i_{bs1} \\ i_{cs1} \end{bmatrix} + [M_{s1r}(\theta_1)] . \begin{bmatrix} i_{ar} \\ i_{br} \\ i_{cr} \end{bmatrix} \quad \text{(I.36)}$$

- ***For star 2:*** If the two stars are of the same design, the cyclic inductance is identical, and the relationship linking the flux of star 2 to the current in star 1 is expressed by the transposed matrix $[M_{s1s2}]^t$. According to expression (I.26), we have:

$$[\varphi_{s2}] = [L_{s2}] . [i_{s2}] + [M_{s2s1}] . [i_{s1}] + [M_{s2r}(\theta_2)] . [i_r] \quad \text{(I.37)}$$

Therefore:

$$[\varphi_{s2}] = \begin{bmatrix} \varphi_{as2} \\ \varphi_{bs2} \\ \varphi_{cs2} \end{bmatrix} = \ell_s . \begin{bmatrix} 1 & 0 & 0 \\ 0 & 1 & 0 \\ 0 & 0 & 1 \end{bmatrix} . \begin{bmatrix} i_{as2} \\ i_{bs2} \\ i_{cs2} \end{bmatrix} + [M_{s1s2}(\alpha)]^t . \begin{bmatrix} i_{as1} \\ i_{bs1} \\ i_{cs1} \end{bmatrix} + [M_{s2r}(\theta_2)] . \begin{bmatrix} i_{ar} \\ i_{br} \\ i_{cr} \end{bmatrix} \quad \text{(I.38)}$$

- ***For the rotor circuit:*** The three-phase rotor winding has a cyclic inductance defined in the same way as for a stator. The matrices linking rotor fluxes to stator currents are the transposed versions of the corresponding matrices [34]. According to expression (I.27), we have:

$$[\varphi_r] = [M_{rs1}(\theta_1)] . [i_{s1}] + [M_{rs2}(\theta_2)] . [i_{s2}] + [L_r] . [i_r] \quad \text{(I.39)}$$

Thus:

$$[\varphi_R] = \begin{bmatrix} \varphi_{ar} \\ \varphi_{br} \\ \varphi_{cr} \end{bmatrix} = \ell_r . \begin{bmatrix} 1 & 0 & 0 \\ 0 & 1 & 0 \\ 0 & 0 & 1 \end{bmatrix} . \begin{bmatrix} i_{ar} \\ i_{br} \\ i_{cr} \end{bmatrix} + [M_{s1r}(\theta_1)]^t . \begin{bmatrix} i_{as1} \\ i_{bs1} \\ i_{cs1} \end{bmatrix} + [M_{s2r}(\theta_2)]^t . \begin{bmatrix} i_{as2} \\ i_{bs2} \\ i_{cs2} \end{bmatrix} \quad \text{(I.40)}$$

with:

$$\ell_r = l_r + \ell_{pr} \quad \text{(I.41)}$$

$$\ell_{pr} = \frac{3}{2} . L_{pr} \quad \text{(I.42)}$$

- ℓ_r : cyclo-inductance of the rotor;
- l_r : leakage inductance of the rotor;
- ℓ_{pr} : main cyclo-inductance of the rotor.

I.5.3.5 Mechanical equation

The fundamental equation of motion of the machine is given by expression (I.17).

I.5.3.6 Expression of the electromagnetic torque

The general relationship expressing the instantaneous electromagnetic torque of an electric machine is based on the principle of energy conservation. Electromagnetic torque is the partial derivative of the electromagnetic energy stored by the geometric angle of rotor rotation.

$$T_{em} = \frac{1}{2}.[i]^{tr}.\left\{\frac{d[L]}{d\theta_q}\right\}.[i] \tag{I.43}$$

with: T_{em} is the electromagnetic torque.

The vector $[i]$ is defined in relation (I.24) as:

$$[i] = \left[[i_{s1}]\ [i_{s2}]\ [i_r]\right]^{tr} = \left[i_{as1}\ i_{bs1}\ i_{cs1}\ i_{as2}\ i_{bs2}\ i_{cs2}\ i_{ar}\ i_{br}\ i_{cr}\right]^{tr} \tag{I.44}$$

The angle θ_q represents the position of the rotor relative to the stator. In our case, $\theta_q = \theta_1$ or θ_2 depending on the stator. However, since $\theta_1 = \theta_2 + \alpha$, we have $\frac{d[L]}{d\theta_1} = \frac{d[L]}{d\theta_2}$ because α is a constant angle.

All the self and mutual inductances of the machine are included in the matrix $[L]$ of expression (III.6). For identical stars, we have:

$$[L] = \begin{bmatrix} [L_{s1}] & [M_{s1s2}] & [M_{s1r}(\theta_1)] \\ [M_{s2s1}] & [L_{s2}] & [M_{s2r}(\theta_2)] \\ [M_{rs1}(\theta_1)] & [M_{rs2}(\theta_2)] & [L_r] \end{bmatrix} = \begin{bmatrix} [L_s] & [M_{ss}] & [M_{sr}(\theta_1)] \\ [M_{s2s1}] & [L_s] & [M_{s2r}(\theta_2)] \\ [M_{rs1}(\theta_1)] & [M_{rs2}(\theta_2)] & [L_s] \end{bmatrix}$$

$$\frac{d[L]}{d\theta_q} = \begin{bmatrix} 0 & 0 & \frac{d[M_{sr}(\theta_1)]}{d\theta_1} \\ 0 & 0 & \frac{d[M_{sr}(\theta_2)]}{d\theta_2} \\ \frac{d[M_{sr}(\theta_1)]^{tr}}{d\theta_1} & \frac{d[M_{sr}(\theta_2)]^{tr}}{d\theta_2} & 0 \end{bmatrix} \tag{I.45}$$

Expression (I.43) thus becomes:

$$T_{em} = \frac{1}{2}.[i]^{tr}.\left\{\frac{d[L]}{d\theta_q}\right\}.[i] = \frac{1}{2}.\left[[i_{s1}]^{tr}\ [i_{s2}]^{tr}\ [i_r]^{tr}\right].\begin{bmatrix} \frac{d[M_{sr}(\theta_1)]}{d\theta_1}.[i_r] \\ \frac{d[M_{sr}(\theta_2)]}{d\theta_2}.[i_r] \\ \frac{d[M_{sr}(\theta_1)]^{tr}}{d\theta_1}.[i_{s1}] + \frac{d[M_{sr}(\theta_2)]^{tr}}{d\theta_2}.[i_{s2}] \end{bmatrix} \tag{I.46}$$

By expanding, we get:

$$T_{em} = \frac{1}{2}\cdot\left\{[i_{s1}]^{tr}\cdot\frac{d[M_{sr}(\theta_1)]}{d\theta_1}\cdot[i_r]+[i_{s2}]^{tr}\cdot\frac{d[M_{sr}(\theta_2)]}{d\theta_2}\cdot[i_r]+[i_r]^{tr}\cdot\frac{d[M_{sr}(\theta_1)]}{d\theta_1}\cdot[i_{s1}]+[i_r]^{tr}\cdot\frac{d[M_{sr}(\theta_2)]}{d\theta_2}\cdot[i_{s2}]\right\} \tag{I.47}$$

In this expression, the first term is equal to the third, and the second is equal to the fourth. We finally obtain:

$$T_{em} = \left\{[i_{s1}]^{tr}\cdot\frac{d[M_{sr}(\theta_1)]}{d\theta_1}\cdot[i_r]+[i_{s2}]^{tr}\cdot\frac{d[M_{sr}(\theta_2)]}{d\theta_2}\cdot[i_r]\right\} \tag{I.48}$$

I.5.3.7 Biphase model of the DSIG

a. Park transformation

The Park transformation is often referred to as a two-axis transformation. Physically, applying this transformation to the DSIG corresponds to transforming the three windings into two equivalent windings, maintaining the same considerations or aspects regarding m.m.f (magnetomotive force), flux, torque, or at least a proportional image of them [35].

Figure I.8 illustrates the schematic representation of an equivalent biphasic DSIG derived from the Park transformation, where the axis system rotates at the speed ω_{coor}. From this figure, we deduce the relationships between the angles:

$$\theta_{s1} = \theta_1 - \theta_r \tag{I.49}$$

$$\theta_{s2} = \theta_{s1} - \alpha = \theta_1 - \theta_r - \alpha \tag{I.50}$$

- θ_{s1}: angle between the magnetic axis of phase a_{s1} and axis d;
- θ_{s2}: angle between the magnetic axis of phase a_{s2} and axis d;
- θ_r: angle between the magnetic axis of phase a_r and axis d.

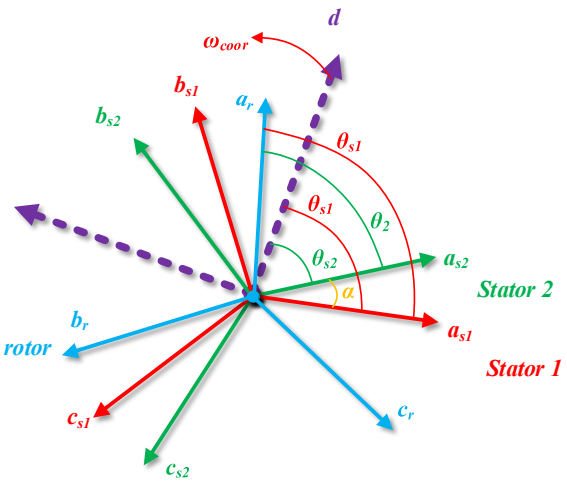

Figure I.8- Representation of the DSIG model according to the (d, q) axes

We define a unique transformation matrix for currents, voltages, and fluxes. It preserves power invariance and is orthogonal. Additionally, we assume that all homopolar quantities are zero (balanced system). The transformation that translates from the three-phase system (*a, b, c*) to the two-phase system (*d, q*) is given by the normalized Park transformation matrix [6]. For the **star 1**, it is defined as follows:

$$\left[P(\theta_{s1})\right]=\sqrt{\frac{2}{3}}\begin{bmatrix}\cos(\theta_{s1}) & \cos\left(\theta_{s1}-\frac{2\pi}{3}\right) & \cos\left(\theta_{s1}+\frac{2\pi}{3}\right)\\ -\sin(\theta_{s1}) & -\sin\left(\theta_{s1}-\frac{2\pi}{3}\right) & -\sin\left(\theta_{s1}+\frac{2\pi}{3}\right)\\ \frac{1}{\sqrt{2}} & \frac{1}{\sqrt{2}} & \frac{1}{\sqrt{2}}\end{bmatrix} \tag{I.51}$$

The three-phase voltage system of star 1 is transformed as follows:

$$\begin{bmatrix}v_{ds1}\\ v_{qs1}\\ v_{0s1}\end{bmatrix}=\left[P(\theta_{s1})\right].\begin{bmatrix}v_{as1}\\ v_{bs1}\\ v_{cs1}\end{bmatrix} \tag{I.52}$$

The Park matrix for star 2 is defined as follows:

$$\left[P(\theta_{s2})\right]=\sqrt{\frac{2}{3}}\begin{bmatrix}\cos(\theta_{s2}) & \cos\left(\theta_{s2}-\frac{2\pi}{3}\right) & \cos\left(\theta_{s2}+\frac{2\pi}{3}\right)\\ -\sin(\theta_{s2}) & -\sin\left(\theta_{s2}-\frac{2\pi}{3}\right) & -\sin\left(\theta_{s2}+\frac{2\pi}{3}\right)\\ \frac{1}{\sqrt{2}} & \frac{1}{\sqrt{2}} & \frac{1}{\sqrt{2}}\end{bmatrix}=\sqrt{\frac{2}{3}}\begin{bmatrix}\cos(\theta_{s1}-\alpha) & \cos\left(\theta_{s1}-\alpha-\frac{2\pi}{3}\right) & \cos\left(\theta_{s1}-\alpha+\frac{2\pi}{3}\right)\\ -\sin(\theta_{s1}-\alpha) & -\sin\left(\theta_{s1}-\alpha-\frac{2\pi}{3}\right) & -\sin\left(\theta_{s1}-\alpha+\frac{2\pi}{3}\right)\\ \frac{1}{\sqrt{2}} & \frac{1}{\sqrt{2}} & \frac{1}{\sqrt{2}}\end{bmatrix} \tag{I.53}$$

The three-phase voltage system of star 2 transforms as follows:

$$\begin{bmatrix}v_{ds2}\\ v_{qs2}\\ v_{0s2}\end{bmatrix}=\left[P(\theta_{s1}-\alpha)\right].\begin{bmatrix}v_{as2}\\ v_{bs2}\\ v_{cs2}\end{bmatrix} \tag{I.54}$$

The Park matrix for the rotor is defined as follows:

$$\left[P(\theta_r)\right]=\sqrt{\frac{2}{3}}\begin{bmatrix}\cos(\theta_r) & \cos\left(\theta_r-\frac{2\pi}{3}\right) & \cos\left(\theta_r+\frac{2\pi}{3}\right)\\ -\sin(\theta_r) & -\sin\left(\theta_r-\frac{2\pi}{3}\right) & -\sin\left(\theta_r+\frac{2\pi}{3}\right)\\ \frac{1}{\sqrt{2}} & \frac{1}{\sqrt{2}} & \frac{1}{\sqrt{2}}\end{bmatrix} \tag{I.55}$$

b. Choice of the Reference frame

Three types of reference frames exist in practice. The choice is made based on the problem to be studied [36].

- **Reference frame fixed to the stator (*α, β*):** In this frame, the axes (*d, q*) are stationary relative to the stator ($\theta_{s1} = 0$). It is used during transient regimes with significant variations in rotational speed.
- **Reference frame fixed to the rotor (*x, y*):** In this frame, the electrical speed of the (*d, q*) axes is equal to the mechanical rotational speed of the rotor ($\theta_r = 0$). This frame is stationary relative to the rotor and is used to study transient regimes in asynchronous and synchronous machines.
- **Reference frame fixed to the rotating field (*d, q*):** In this frame, the electrical speed of the (*d, q*) axes matches the speed of the rotating field ($\omega_{coor} = \omega_s = \frac{d\theta_s}{dt}$). This frame is generally used for speed, torque control, etc., as the quantities in this frame are continuous in form. This frame does not introduce simplifications in the transformation of electrical equations. It is the reference frame chosen for our study.

I.6 Modeling of the DSIG in a (*d, q*) reference frame linked to the rotating field

I.6.1 Voltage equations

The representation of the DSIG model in a two-phase (*d, q*) reference frame linked to the rotating field is achieved using normalized Park transformations to preserve power. By applying these transformations to the stator voltages and fluxes, we derive the electrical model (I.64) and magnetic model (I.65) [37], [38], [39].

In the Park model, the voltage equation can also be written in matrix form, analogous to (I.24):

$$\left[v_{dqo}\right] = -\left[R\right].\left[i_{dqo}\right] - \frac{d\left[\varphi_{dqo}\right]}{dt} \tag{I.56}$$

with: $\left[v_{dqo}\right] = \left[\left[v_{s1}\right]\left[v_{s2}\right]\left[v_r\right]\right]^{tr} = \left[v_{ds1}\ v_{qs1}\ v_{os1}\ v_{ds2}\ v_{qs2}\ v_{os2}\ v_{dr}\ v_{qr}\ v_{or}\right]^{tr}$

Since the rotor circuit is short-circuited (squirrel cage), we have:

$$\left[v_r\right] = \left[0\ 0\ 0\right]^{tr} \tag{I.58}$$

In the case of a balanced system, the homopolar component does not contribute to the production of the electromagnetic torque, and thus we obtain:

$$\left[v_{dqo}\right] = \left[\left[v_{s1}\right]\left[v_{s2}\right]\left[0\right]\right]^{tr} = \left[v_{ds1}\ v_{qs1}\ 0\ v_{ds2}\ v_{qs2}\ 0\ 0\ 0\ 0\right]^{tr} \tag{I.59}$$

In the case of a supply without neutral wires, the homopolar component is zero:

$$\begin{cases}\left[i_{dqo}\right]=\left[\left[i_{s1}\right]\left[i_{s2}\right]\left[i_{r}\right]\right]^{tr}=\left[i_{ds1}\ i_{qs1}\ 0\ i_{ds2}\ i_{qs2}\ 0\ i_{dr}\ i_{qr}\ 0\right]^{tr}\\ \left[\varphi_{dqo}\right]=\left[\left[\varphi_{s1}\right]\ \left[\varphi_{s2}\right]\ \left[\varphi_{r}\right]\right]^{tr}=\left[\varphi_{ds1}\ \varphi_{qs1}\ \varphi_{os1}\ \varphi_{ds2}\ \varphi_{qs2}\ \varphi_{os2}\ \varphi_{dr}\ \varphi_{qr}\ \varphi_{or}\right]^{tr}\end{cases} \tag{I.60}$$

The matrix equation (I.56) is decomposed as follows.

$$\begin{bmatrix}v_{ds1}\\ v_{qs1}\\ 0\end{bmatrix}=-\begin{bmatrix}R_{s1}&0&0\\ 0&R_{s1}&0\\ 0&0&R_{s1}\end{bmatrix}.\begin{bmatrix}i_{ds1}\\ i_{qs1}\\ 0\end{bmatrix}+\frac{d}{dt}\begin{bmatrix}\varphi_{ds1}\\ \varphi_{qs1}\\ \varphi_{os1}\end{bmatrix}+\frac{d\theta_{s}}{dt}.\begin{bmatrix}0&-1&0\\ 1&0&0\\ 0&0&0\end{bmatrix}.\begin{bmatrix}\varphi_{ds1}\\ \varphi_{qs1}\\ \varphi_{os1}\end{bmatrix} \tag{I.61}$$

$$\begin{bmatrix}v_{ds2}\\ v_{qs2}\\ 0\end{bmatrix}=-\begin{bmatrix}R_{s2}&0&0\\ 0&R_{s2}&0\\ 0&0&R_{s2}\end{bmatrix}.\begin{bmatrix}i_{ds2}\\ i_{qs2}\\ 0\end{bmatrix}+\frac{d}{dt}\begin{bmatrix}\varphi_{ds2}\\ \varphi_{qs2}\\ \varphi_{os2}\end{bmatrix}+\frac{d\theta_{s}}{dt}.\begin{bmatrix}0&-1&0\\ 1&0&0\\ 0&0&0\end{bmatrix}.\begin{bmatrix}\varphi_{ds2}\\ \varphi_{qs2}\\ \varphi_{os2}\end{bmatrix} \tag{I.62}$$

$$\begin{bmatrix}0\\ 0\\ 0\end{bmatrix}=-\begin{bmatrix}R_{r}&0&0\\ 0&R_{r}&0\\ 0&0&R_{r}\end{bmatrix}.\begin{bmatrix}i_{dr}\\ i_{qr}\\ 0\end{bmatrix}+\frac{d}{dt}\begin{bmatrix}\varphi_{dr}\\ \varphi_{qr}\\ \varphi_{or}\end{bmatrix}+\frac{d\left(\theta_{s}-\theta_{r}\right)}{dt}.\begin{bmatrix}0&-1&0\\ 1&0&0\\ 0&0&0\end{bmatrix}.\begin{bmatrix}\varphi_{dr}\\ \varphi_{qr}\\ \varphi_{or}\end{bmatrix} \tag{I.63}$$

- $\frac{d(\theta_{s1})}{dt}$: Rotation speed of the (*d, q*) reference frame relative to star 1;
- $\frac{d(\theta_{r})}{dt}$: Rotation speed of the (*d, q*) reference frame relative to the rotor.

$$\begin{cases}v_{ds1}=-R_{s1}i_{ds1}+\dfrac{d\varphi_{ds1}}{dt}-\omega_{s}\varphi_{qs1}\\ v_{qs1}=-R_{s1}i_{qs1}+\dfrac{d\varphi_{qs1}}{dt}+\omega_{s}\varphi_{ds1}\\ v_{ds2}=-R_{s2}i_{ds2}+\dfrac{d\varphi_{ds2}}{dt}-\omega_{s}\varphi_{qs2}\\ v_{qs2}=-R_{s2}i_{qs2}+\dfrac{d\varphi_{qs2}}{dt}+\omega_{s}\varphi_{ds2}\\ v_{dr}=0=R_{r}i_{dr}+\dfrac{d\varphi_{dr}}{dt}-\left(\omega_{s}-\omega_{r}\right)\varphi_{qr}\\ v_{qr}=0=R_{r}i_{qr}+\dfrac{d\varphi_{qr}}{dt}--+\left(\omega_{s}-\omega_{r}\right)\varphi_{dr}\end{cases} \tag{I.64}$$

I.6.2 Flux expressions

The following relationships give the linkage fluxes of the two fictitious stator windings and the rotor in the (*d, q*) reference frame [3]-[4], [23]-[24].

$$\begin{cases} \varphi_{ds1} = -L_{ds1} i_{ds1} - L_m \left(i_{ds1} + i_{ds2} \right) + L_{dq} i_{qs2} + L_{md} \left(-i_{ds1} - i_{ds2} + i_{dr} \right) \\ \varphi_{qs1} = -L_{qs1} i_{qs1} - L_m \left(i_{qs1} + i_{qs2} \right) + L_{dq} i_{ds2} + L_{mq} \left(-i_{qs1} - i_{qs2} + i_{qr} \right) \\ \varphi_{ds2} = -L_{ds2} i_{ds2} - L_m \left(i_{ds1} + i_{ds2} \right) + L_{dq} i_{qs1} + L_{md} \left(-i_{ds1} - i_{ds2} + i_{dr} \right) \\ \varphi_{qs2} = -L_{qs2} i_{qs2} - L_m \left(i_{qs1} + i_{qs2} \right) + L_{dq} i_{ds1} + L_{mq} \left(-i_{qs1} - i_{qs2} + i_{qr} \right) \\ \varphi_{dr} = L_{dr} i_{dr} + L_{md} \left(-i_{ds1} - i_{ds2} + i_{dr} \right) \\ \varphi_{qr} = L_{qr} i_{qr} + L_{mq} \left(-i_{qs1} - i_{qs2} + i_{qr} \right) \end{cases} \tag{I.65}$$

with: $L_{ds1} = L_m + L_{md}$, $L_{qs1} = L_m + L_{mq}$, $L_{ds2} = L_m + L_{md}$, $L_{qs1} = L_m + L_{mq}$

- L_{ds1}, L_{qs1}, L_{ds2}, L_{qs2}: Direct and quadrature inductances of the fictitious phases of stators 1 and 2;
- L_m: Cyclic mutual inductance between the stators and the rotor;
- L_{md}, L_{mq}: Direct and quadrature magnetizing inductances.

Under linear magnetic conditions (no saturation of the machine), we can write [37]:

$$L_{md} = L_{mq} = L_m ,\ L_{dq} = 0,\ L_{ds1} = L_{qs1},\ L_{ds2} = L_{qs2} ,\ L_{dr} = L_{qr} \tag{I.66}$$

We obtain the magnetization fluxes along the *d* and *q* axes by setting:

$$\varphi_{md} = L_{md} . \left(-i_{ds1} - i_{ds2} + i_{dr} \right) \tag{I.67}$$

$$\varphi_{mq} = L_{mq} . \left(-i_{qs1} - i_{qs2} + i_{qr} \right) \tag{I.68}$$

The magnitude of the total magnetizing flux is given by:

$$\left\| \varphi_m \right\| = \sqrt{\left(\varphi_{md} \right)^2 + \left(\varphi_{mq} \right)^2} \tag{I.69}$$

The magnitude of the magnetizing current can be calculated by:

$$\left\| i_m \right\| = \sqrt{\left(-i_{ds1} - i_{ds2} + i_{dr} \right)^2 + \left(-i_{qs1} - i_{qs2} + i_{qr} \right)^2} \tag{I.70}$$

The system (I.32) is therefore written as:

$$\begin{cases} \varphi_{ds1} = -L_{ds1} i_{ds1} - L_m \left(i_{ds1} + i_{ds2} \right) + \varphi_{md} \\ \varphi_{qs1} = -L_{qs1} i_{qs1} - L_m \left(i_{qs1} + i_{qs2} \right) + \varphi_{mq} \\ \varphi_{ds2} = -L_{ds2} i_{ds2} - L_m \left(i_{ds1} + i_{ds2} \right) + \varphi_{md} \\ \varphi_{qs2} = -L_{qs2} i_{qs2} - L_m \left(i_{qs1} + i_{qs2} \right) + \varphi_{mq} \\ \varphi_{dr} = L_{dr} i_{dr} + \varphi_{md} \\ \varphi_{qr} = L_{qr} i_{qr} + \varphi_{mq} \end{cases} \tag{I.71}$$

The electromagnetic torque can be calculated using the following expression [40]:

$$T_{em} = \frac{3P}{4}.\left(\frac{L_m}{L_r + L_m}\right).\left[\left(i_{qs1} + i_{qs2}\right).\varphi_{dr} - \left(i_{ds1} + i_{ds2}\right).\varphi_{qr}\right] \tag{I.72}$$

In **Figure I.9**, the schematic digram of the DISG model in the *d, q* reference frame is presented.

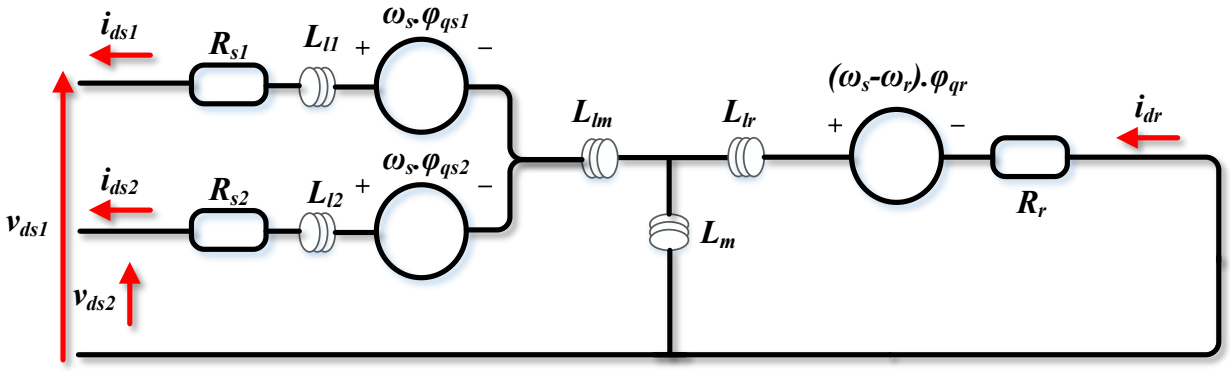

a) Along the d-axis

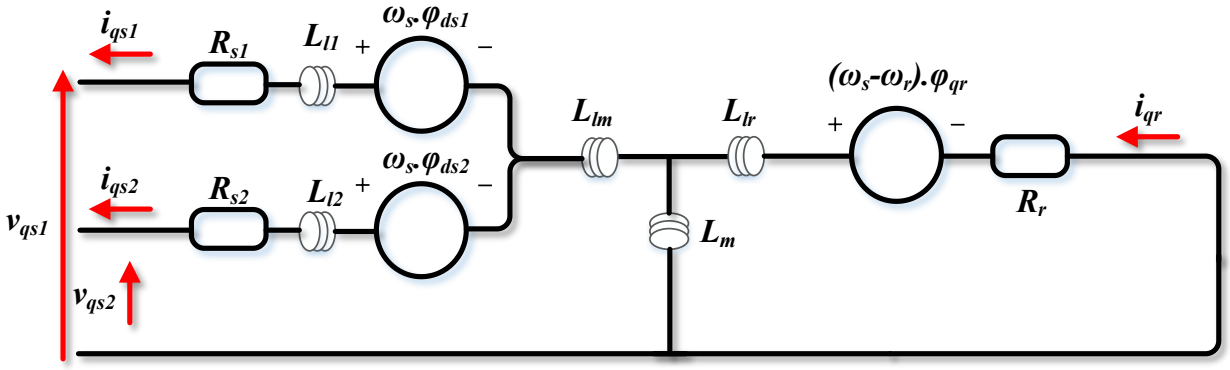

b) Along the q-axis

Figure I.9- Representation of the DSIG in the (*d, q*) reference frame aligned with the rotating field

I.6.3 Representation in state-space form of the machine model

By substituting the system of equations (I.31) into (I.43) and presenting everything in a compact form, we obtain [6], [10], [40]:

$$\left[\dot{I}\right] = \left[L\right]^{-1}\left\{\left[B\right]\left[V\right] - \omega_{sl}\left[C\right]\left[I\right] - \left\{\omega_s\left[D_1\right] + \left[D_2\right]\right\}\left[I\right]\right\} \tag{I.73}$$

Here, ω_s represents the synchronous speed, ω_r denotes the rotor's electrical angular speed, and ω_{sl} indicates the slip speed, which is defined as:

$$\omega_{sl} = \omega_s - \omega_r \tag{I.74}$$

with: $\omega_r = P.\Omega_{mec}$ and P defines the number of pole pairs.

Furthermore, the matrices and vectors introduced in equation (I.73) are formally defined as:

$\left[I\right] = \left[i_{ds1} \quad i_{qs1} \quad i_{ds2} \quad i_{qs2} \quad i_{dr} \quad i_{qr}\right]^T$: State vector;

$[V] = \begin{bmatrix} v_{ds1} & v_{qs1} & v_{ds2} & v_{qs2} & v_{dr} & v_{qr} \end{bmatrix}^T$: Control vector;

$[B] = diag\begin{bmatrix} 1 & 1 & 1 & 1 & 0 & 0 \end{bmatrix}$

$[D_2] = diag\begin{bmatrix} R_{s1} & R_{s1} & R_{s2} & R_{s2} & R_r & R_r \end{bmatrix}$

$$[C] = \begin{bmatrix} 0 & 0 & 0 & 0 & 0 & 0 \\ 0 & 0 & 0 & 0 & 0 & 0 \\ 0 & 0 & 0 & 0 & 0 & 0 \\ 0 & 0 & 0 & 0 & 0 & 0 \\ 0 & -L_m & 0 & -L_m & 0 & -(L_r + L_m) \\ L_m & 0 & L_m & 0 & L_r + L_m & 0 \end{bmatrix}$$

$$[L] = \begin{bmatrix} L_{s1} + L_m & 0 & L_m & 0 & L_m & 0 \\ 0 & L_{s1} + L_m & 0 & L_m & 0 & L_m \\ L_m & 0 & L_{s2} + L_m & 0 & L_m & 0 \\ 0 & L_m & 0 & L_{s2} + L_m & 0 & L_m \\ L_m & 0 & L_m & 0 & L_r + L_m & 0 \\ 0 & L_m & 0 & L_m & 0 & L_r + L_m \end{bmatrix}$$

$$[D_1] = \begin{bmatrix} 0 & -(L_{s1} + L_m) & 0 & -L_m & 0 & -L_m \\ (L_{s1} + L_m) & 0 & L_m & 0 & L_m & 0 \\ 0 & -L_m & 0 & -(L_{s2} + L_m) & 0 & -L_m \\ L_m & 0 & (L_{s2} + L_m) & 0 & L_m & 0 \\ 0 & 0 & 0 & 0 & 0 & 0 \\ 0 & 0 & 0 & 0 & 0 & 0 \end{bmatrix}$$

I.6.4 Absorbed power and electromagnetic torque

Neglecting the homopolar components, the absorbed power by the DSIG in the (*d, q*) axis system is expressed as:

$$P_s = v_{ds1}.i_{ds1} + v_{qs1}.i_{qs1} + v_{ds2}.i_{ds2} + v_{qs2}.i_{qs2} \tag{I.75}$$

By substituting the voltages (v_{ds1}, v_{qs1}, v_{ds2}, v_{qs2}) into the expression (I.75), we obtain:

$$\begin{aligned} P_s = &\left[R_{s1}i_{ds1}^2 + R_{s1}i_{qs1}^2 + R_{s2}i_{ds2}^2 + R_{s2}i_{qs2}^2 \right] + \left(\frac{d\varphi_{ds1}}{dt} i_{ds1} + \frac{d\varphi_{qs1}}{dt} i_{qs1} + \frac{d\varphi_{ds2}}{dt} i_{ds2} + \frac{d\varphi_{qs2}}{dt} i_{qs2} \right) \\ &+ \omega_s \left(\varphi_{ds1}i_{ds1} - \varphi_{qs1}i_{qs1} + \varphi_{ds2}i_{ds2} - \varphi_{qs2}i_{qs2} \right) \end{aligned} \tag{I.76}$$

This expression consists of three terms: the first corresponds to Joule losses, the second represents the variation in electromagnetic energy (stored energy), and the last is electromagnetic power (P_{em}).

Moreover, the expression for the electromagnetic torque is:

$$T_{em} = \frac{P_{em}}{\Omega_s} = P\frac{P_{em}}{\omega_s} = P\left[\varphi_{ds1}i_{ds1} - \varphi_{qs1}i_{qs1} + \varphi_{ds2}i_{ds2} - \varphi_{qs2}i_{qs2}\right] \quad \text{(I.77)}$$

By substituting the flux components (φ_{ds1}, φ_{qs1}, φ_{ds2}, φ_{qs2}) given by (I.43) into (I.50), we obtain:

$$T_{em} = P.L_m.\left[\left(i_{qs1} + i_{qs2}\right).i_{dr} + \left(i_{ds1} + i_{ds2}\right).i_{qr}\right] \quad \text{(I.78)}$$

From the rotor flux equations (φ_{dr} and φ_{qr}) expressed by (I.43), we derive:

$$i_{dr} = \frac{1}{L_m + L_r}.\left[\varphi_{dr} - L_m.\left(i_{ds1} + i_{ds2}\right)\right] \quad \text{(I.79)}$$

$$i_{qr} = \frac{1}{L_m + L_r}.\left[\varphi_{qr} - L_m.\left(i_{qs1} + i_{qs2}\right)\right] \quad \text{(I.80)}$$

Replacing (I.79) and (I.80) into equation (III.68), the electromagnetic torque can be expressed in terms of stator currents and rotor fluxes in the Park (d, q) reference frame [41]:

$$T_{em} = P.\frac{L_m}{L_m + L_r}.\left[\varphi_{dr}.\left(i_{qs1} + i_{qs2}\right) - \varphi_{qr}.\left(i_{ds1} + i_{ds2}\right)\right] \quad \text{(I.81)}$$

I.7 Voltage inverters with PWM control

I.7.1 Modeling of the inverter

An autonomous inverter (with adjacent control or PWM control) is a static converter that ensures energy transformation from a DC source into AC energy, which can be at either fixed or variable frequency. It can also act on the amplitude of the delivered voltage. A three-phase inverter consists of three legs, each composed of two pairs of switches assumed to be ideal, with disjoint and complementary control. Each switch is represented by a transistor-diode pair, modelled by two states defined by the following logical connection function [36], [40]:

$$f_i = \begin{cases} 1 & \text{The switch i is open (the transistor } \bar{K}_i \text{ is blocked, and the diode } K_i \text{ conducts)} \\ 0 & \text{The switch i is closed (the transistor } \bar{K}_i \text{ is conducts, and the diode } K_i \text{ blocked)} \end{cases}$$

with: $f_i + \bar{f}_i = 1$ and $i = 1 \ldots 3$

Figure I.10 illustrates the schematic diagram of the three-phase inverter.

The composed voltages are:

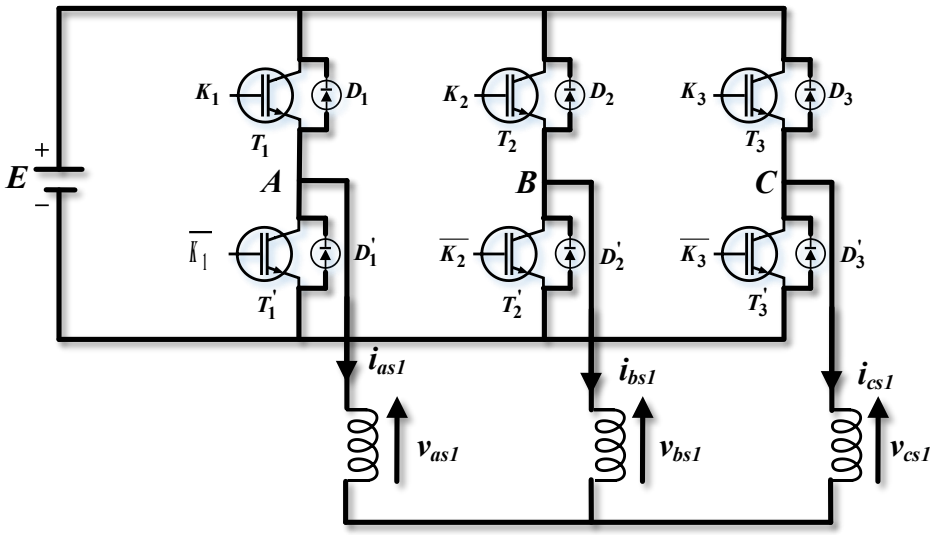

Figure I.10- Diagram of a three-phase inverter

$$\begin{aligned} V_{AB} &= v_{as} - v_{bc} = E.(f_1 + f_2) \\ V_{BC} &= v_{bs} - v_{cs} = E.(f_2 + f_3) \\ V_{CA} &= v_{cs} - v_{as} = E.(f_3 + f_1) \end{aligned} \tag{I.82}$$

The line to naturle voltages v_{as1}, v_{bs1}, v_{cs1} form a balanced three-phase system, such that:

$$v_{as1} + v_{bs1} + v_{cs1} = 0 \tag{I.83}$$

The resolution of equations (I.82) and (I.83) gives us:

$$\begin{bmatrix} v_{as} \\ v_{bs} \\ v_{cs} \end{bmatrix} = \frac{E}{3} \begin{bmatrix} 2 & -1 & -1 \\ -1 & 2 & -1 \\ -1 & -1 & 2 \end{bmatrix} \begin{bmatrix} f_1 \\ f_2 \\ f_3 \end{bmatrix} \tag{I.84}$$

I.7.2 Sinus-triangle modulation control strategy

The sinus-triangle PWM is achieved by comparing a low-frequency modulating wave (reference voltage) with a high-frequency triangular carrier wave. The intersection points between the carrier and the modulating wave determine the switching moments. The carrier frequency determines the switch commutation frequency [42].

The sinusoidal reference voltages are expressed as:

$$\begin{aligned} v_{as1}^{*} &= v_m.\sin(2\pi ft) \\ v_{bs1}^{*} &= v_m.\sin\left(2\pi ft - \frac{2\pi}{3}\right) \\ v_{cs1}^{*} &= v_m.\sin\left(2\pi ft + \frac{2\pi}{3}\right) \end{aligned} \tag{I.85}$$

The carrier is given by:

$$v_p(t) = \begin{cases} V_{pm}\left[4\left(\dfrac{t}{T_p}\right) - 1\right] & \text{whene } 0 \le t \le \dfrac{T_p}{2} \\ V_{pm}\left[-4\left(\dfrac{t}{T_p}\right) + 3\right] & \text{whene } \dfrac{T_p}{2} < t \le T_p \end{cases} \tag{I.86}$$

The following two parameters characterize this technique:

- The modulation index ***m*** equals the ratio of the modulation frequency (f_p) to the reference frequency (f);
- The voltage control coefficient ***r*** equals the ratio of the reference voltage amplitude (f_p) to the peak value of the modulation wave (v_{pm});

Figure I.11 displays the voltages vectors for different switch states.

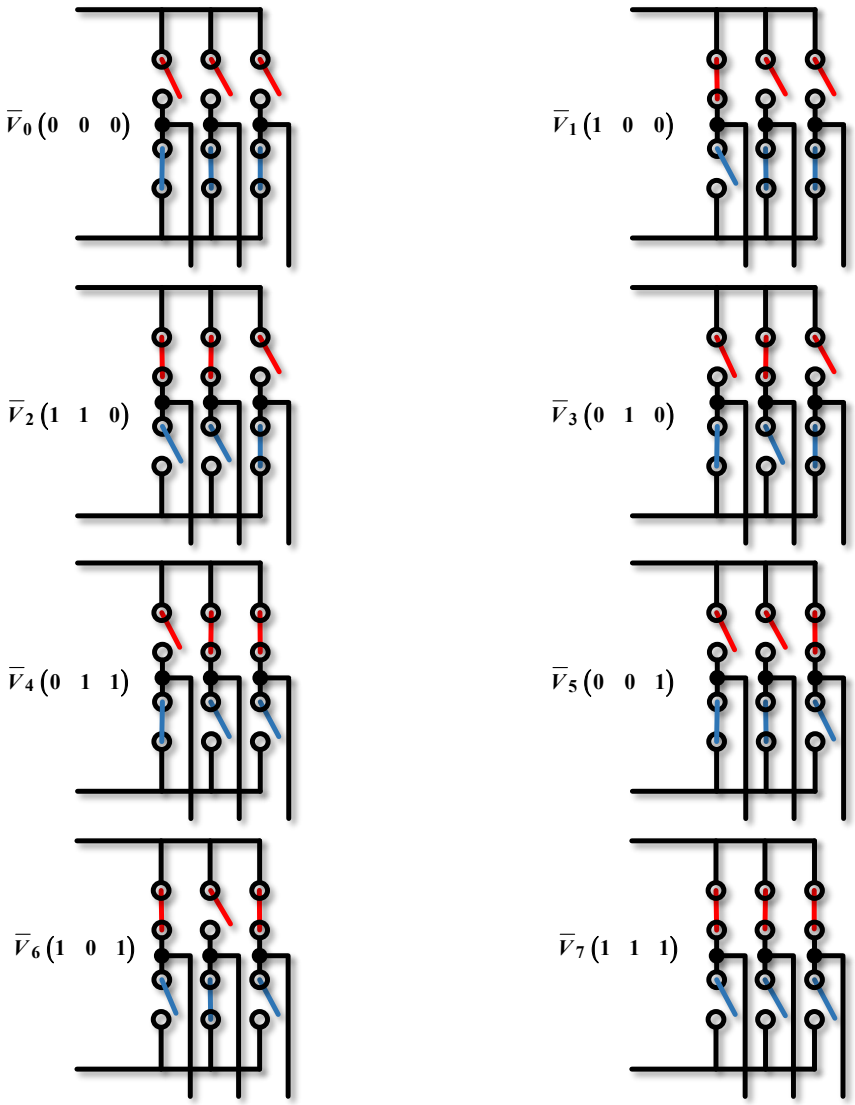

Figure I.11- Vectors of voltages for different switch states

I.7.3 Vector modulation control strategy

I.7.3.1 Principe

SVM is different from conventional Pulse Width Modulation (PWM). It is based on the spatial vector representation of the inverter output. There are no separate modulators for each phase. The reference voltages are given by the voltage vector in space (i.e., the components of the voltage vector in the complex plane). The principle of SVM is predicting the inverter voltage vector by projecting the reference vector $\bar{V}_{ref}$ on the adjacent vectors corresponding to two non-zero switching states. For a two-level inverter, the switching vector diagram forms a hexagon divided into six 60° sectors, as shown in **Figure I.12**. The objective of the spatial vector modulation (SVM) technique is to approximate the reference voltage vector $\bar{V}_{ref}$ using the eight switching models. A simple method of approximation is to generate the inverter output's average over a short period, T which is identical to $\bar{V}_{ref}$ in the same period [43].

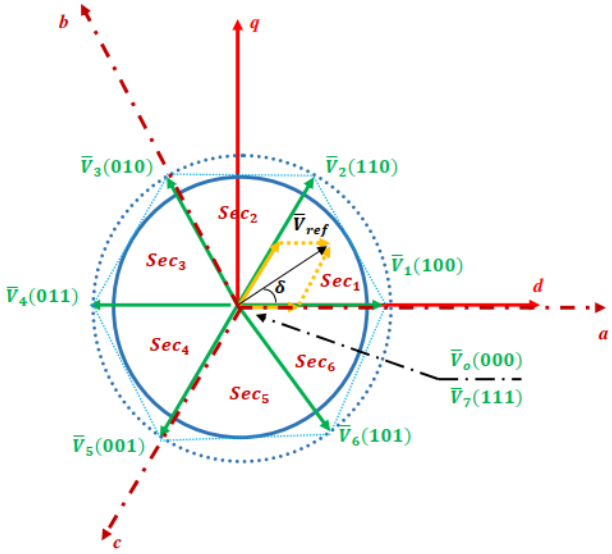

Figure I.12- Diagram of the space vector voltage

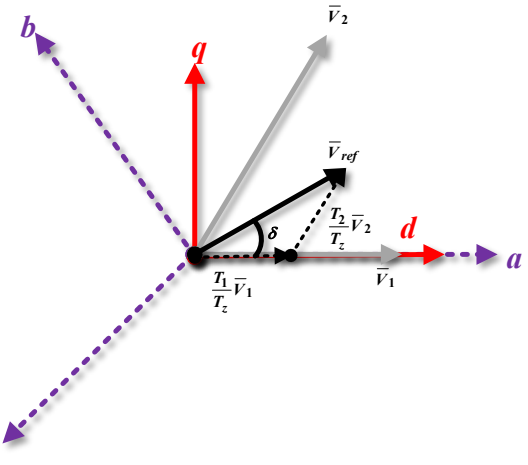

Figure I.13- Reference vector based on the adjacent voltage vectors in sector 1

The duration of each vector (e.g., $\bar{V}_1$ applied for a time T_1) can be obtained through vector calculations, and the rest of the period T_s will be spent applying the zero vector $\bar{V}_0$ for a time T_0.

$$T_s = T_1 + T_2 + T_0 \tag{I.87}$$

with: T_1, T_2 and T_0 denote the duration of application of the voltage vectors and T_s is the sampling time.

When the reference voltage is in sector 1 (**see Figure I.13**), it can be synthesized using the vectors $\bar{V}_1$, $\bar{V}_2$, and $\bar{V}_0$ (null vector).

$$\int_0^{T_s} \bar{V}_{ref}.dt = \int_0^{T_1} \bar{V}_1.dt = \int_{T_1}^{T_1+T_2} \bar{V}_2.dt + \int_{T_1+T_2}^{T_s} \bar{V}_0.dt \tag{I.88}$$

Hence:

$$T_s.\bar{V}_{ref} = \left(T_1.\bar{V}_1 + T_2.\bar{V}_2\right) + \bar{V}_0.\left(T_s - T_1 - T_2\right) = \left(T_1.\bar{V}_1 + T_2.\bar{V}_2\right) + T_0.\bar{V}_0 \tag{I.89}$$

The space vector PWM can be determined according to steps presented in the following sections.

I.7.3.2 Determination of V_d, V_q, V_{ref} and the angle δ

The expression of the voltage in d, q frame can be obtained as follows:

$$\begin{cases} V_d = V_{an} - V_{bn}.\cos\left(60^\circ\right) - V_{cn}.\cos\left(60^\circ\right) = V_{an} - \frac{1}{2}.V_{bn} - \frac{1}{2}.V_{cn} \\ V_q = 0 + V_{bn}.\cos\left(30^\circ\right) - V_{cn}.\cos\left(30^\circ\right) = 0 + \frac{\sqrt{3}}{2}.V_{bn} - \frac{\sqrt{3}}{2}.V_{cn} \end{cases} \tag{I.90}$$

In matrix from:

$$\begin{bmatrix} V_d \\ V_q \end{bmatrix} = \begin{bmatrix} 1 & -\frac{1}{2} & -\frac{1}{2} \\ 0 & \frac{\sqrt{3}}{2} & -\frac{\sqrt{3}}{2} \end{bmatrix} \begin{bmatrix} V_{an} \\ V_{bn} \\ V_{cn} \end{bmatrix} \tag{I.91}$$

where the voltage amplitude and phase angle can be written as follows:

$$\left|\bar{V}_{ref}\right| = \sqrt{V_d^2 + V_q^2} \tag{I.92}$$

$$\delta = arctg\left(\frac{V_d}{V_q}\right) = \omega t = 2\pi f t \tag{I.93}$$

with f is the fundamental frequency.

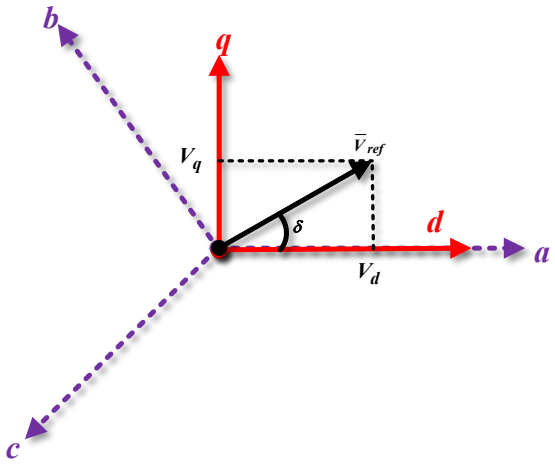

Figure I.14- Determination of V_{ref} and δ

I.7.3.3 Determination of durations T_1, T_2, T_0

The durations of voltage application to the switches are calculated as follows.

a. Calculation in Sector 1: Using (I.78) and projecting $\bar{V}_1$ and $\bar{V}_2$ onto the axis system, we get:

$$T_s.\bar{V}_{ref} = T_1.\bar{V}_1 + T_2.\bar{V}_2 + T_0.\bar{V}_0 \tag{I.94}$$

$$T_s.\left|\bar{V}_{ref}\right|.\left(\cos(\delta)+i.\sin(\delta)\right) = T_1.\frac{2}{3}.V_{dc}.(1+i.0) + T_2.\frac{2}{3}.V_{dc}.\left(\cos\left(\frac{\pi}{3}\right)+i.\sin\left(\frac{\pi}{3}\right)\right) \tag{I.95}$$

By identifying the real and imaginary parts, we successively obtain:

$$T_1 = T_s.a.\frac{\sin\left(\frac{\pi}{3}-\delta\right)}{\sin\left(\frac{\pi}{3}\right)} \tag{I.96}$$

$$T_2 = T_s.a.\frac{\sin(\delta)}{\sin\left(\frac{\pi}{3}\right)} \tag{I.97}$$

with: $T_0 = T_s - (T_1 + T_2)$

Then:

$$T_s = \frac{1}{f_s},\ a = \frac{\left|V_{ref}\right|}{\frac{2}{3}.V_{dc}} \tag{I.98}$$

And: $0 \le \delta \le 60^\circ$

b. Calculation in Sector n

$$T_s = \frac{1}{f_s},\ a = \frac{|V_{ref}|}{\frac{2}{3}.V_{dc}} \tag{I.99}$$

$$T_s = \frac{1}{f_s},\ a = \frac{|V_{ref}|}{\frac{2}{3}.V_{dc}} \tag{I.100}$$

with T_s is given by equations (I.88) and (I.98), n = 1 to 6 (Sector 1 to Sector 6), and $0 \le \delta \le 60^{\circ}$.

I.7.3.4 Determination of the switching time t_i for each switch K_i

The switching time t_i corresponding to the inverter switches K_i is given in **Table I.1** [43].

Table I.1– Switching time t_i of the inverter switches K_i [43].

Sector	Upper switches (K_1, K_3, K_5)	Lower switches (K_4, K_6, K_2)
Sec_1	$t_1 = T_1 + T_2 + \frac{T_0}{2}$ $t_3 = T_2 + \frac{T_0}{2}$ $t_5 = \frac{T_0}{2}$	$t_4 = \frac{T_0}{2}$ $t_6 = T_1 + \frac{T_0}{2}$ $t_2 = T_1 + T_2 + \frac{T_0}{2}$
Sec_2	$t_1 = T_1 + \frac{T_0}{2}$ $t_3 = T_1 + T_2 + \frac{T_0}{2}$ $t_5 = \frac{T_0}{2}$	$t_4 = T_2 + \frac{T_0}{2}$ $t_6 = \frac{T_0}{2}$ $t_2 = T_1 + T_2 + \frac{T_0}{2}$
Sec_3	$t_1 = \frac{T_0}{2}$ $t_3 = T_1 + T_2 + \frac{T_0}{2}$ $t_5 = T_2 + \frac{T_0}{2}$	$t_4 = T_1 + T_2 + \frac{T_0}{2}$ $t_6 = \frac{T_0}{2}$ $t_2 = T_1 + \frac{T_0}{2}$
Sec_4	$t_1 = \frac{T_0}{2}$ $t_3 = T_1 + \frac{T_0}{2}$ $t_5 = T_1 + T_2 + \frac{T_0}{2}$	$t_4 = T_1 + T_2 + \frac{T_0}{2}$ $t_6 = T_2 + \frac{T_0}{2}$ $t_2 = \frac{T_0}{2}$
Sec_5	$t_1 = T_2 + \frac{T_0}{2}$ $t_3 = \frac{T_0}{2}$ $t_5 = T_1 + T_2 + \frac{T_0}{2}$	$t_4 = T_1 + \frac{T_0}{2}$ $t_6 = T_1 + T_2 + \frac{T_0}{2}$ $t_2 = \frac{T_0}{2}$
Sec_6	$t_1 = T_1 + T_2 + \frac{T_0}{2}$ $t_3 = \frac{T_0}{2}$ $t_1 = T_1 + \frac{T_0}{2}$	$t_4 = \frac{T_0}{2}$ $t_6 = T_1 + T_2 + \frac{T_0}{2}$ $t_2 = T_2 + \frac{T_0}{2}$

I.8 LCL-filter design

To mitigate the switching harmonics caused by pulsating voltages at the three-level inverter output, filtering components must be installed between the inverter and the grid connection. A typical LCL filter configuration - utilizing inductive and capacitive elements - enables controlled active and reactive power exchange with the grid. The present design methodology for the LCL filter implementation adheres to the specifications outlined in references [44], [45].

I.8.1 Filter capacitor C_f design

The capacitor C_f design must account for reactive power fluctuations introduced by the LCL filter. The fundamental design parameters are established as follows:

$$Z_b = \frac{V_{LL}^2}{P_n},\ C_b = \frac{1}{\omega_{s,g} Z_b},\ L_b = \frac{Z_b}{\omega_{s,g}} \tag{I.101}$$

where V_{LL}^2 is grid line-to-line RMS voltage, P_n is the rated active power, and $\omega_{s,g} = 2\pi f_{s,g}$ is the grid angular frequency. Filter capacitance is related to the base value C_b as a percentage of it. Setting the maximum power variation seen by the grid as 5% (empirical value 1% - 5%), we can obtain:

$$C_f = 0.05 C_b \tag{I.102}$$

I.8.2 Filter inductors L_c and L_g design

At low frequencies the LCL filter behaves like an inductor with a total inductance of:

$$L_{dc} = L_c + L_g \tag{I.103}$$

It should be noted that the current flowing through the filter capacitors C_f is significantly smaller than that through the filter inductors. An optimal relationship exists between the converter-side inductance L_c and grid-side inductance L_g that simultaneously minimizes fundamental frequency voltage drop and maximizes harmonic attenuation. When expressed as fractional components of the total inductance L_{dc} using a weighting factor $\alpha \in [0, 1]$, this relationship becomes:

$$L_c = \alpha L_{dc} \tag{I.104}$$

$$L_g = (1-\alpha) L_{dc} \tag{I.105}$$

The LCL filter's resonant frequency is determined by the parallel combination of its components: converter-side inductance L_c, filter capacitance C_f, and grid-side inductance L_g. This resonant frequency can be calculated as:

$$\omega_r = \sqrt{\frac{L_c + L_g}{L_c C_f L_g}} \tag{I.106}$$

The equivalent inductance L_{eq} that determines the resonant frequency is obtained from the parallel combination of the converter-side inductance L_c and grid-side inductance L_g:

$$L_{eq} = \frac{L_c L_g}{L_c + L_g} = \alpha(1-\alpha) L_{dc} \tag{I.107}$$

The minimum equivalent inductance L_{eq} occurs when both converter-side and grid-side inductances are balanced at half the total inductance $L_c = L_g = 0{,}5L_{dc}$. Using the standard empirical design practice where L_{dc} equals 10% of the base inductance L_b, the individual inductances can be readily calculated as:

$$L_c = L_g = 0.05 L_b \tag{I.108}$$

I.9 Active damping via capacitor current feedback

The resonant peak in LCL filters can be mitigated through passive damping by adding a resistor to the input filter [46]. While this method is simple to implement, it reduces system efficiency through power dissipation. An alternative solution, active damping, employs control-based virtual resistance to achieve equivalent resonance suppression without energy losses. **Figure I.15** [1] illustrates the standard LCL filter configuration, while **Figure I.16** [44] shows the modified version with a series damping resistor. The same figure reveals how a virtual resistance component (emulating " R_D ") can replicate the damping effect in the control system, eliminating the need for physical resistors. Implementing active damping requires capacitor current measurement, necessitating either three analog inputs (or two for balanced three-phase systems).

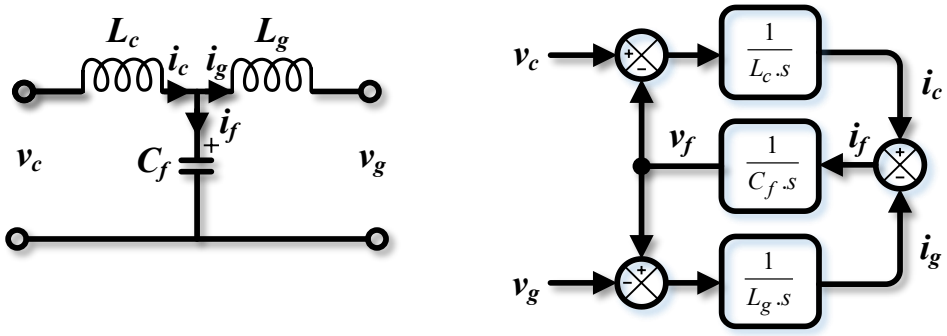

Figure I.15- The equivalent circuit and block diagram representation of an idealized single-phase LCL filter configuration

The filter in **Figure I.15** can be described with the state equations in the *s*-domain:

$$v_c(s) = sL_c i_c(s) + v_f(s) \tag{I.109}$$

$$v_g(s) = v_f(s) - sL_g i_g(s) \tag{I.110}$$

$$v_f(s) = \frac{i_f(s)}{sC_f} \tag{I.111}$$

$$i_c(s) = i_f(s) + i_g(s) \tag{I.112}$$

Consequently, the voltage and current transfer functions for the idealized LCL filter can be expressed as:

$$H_{v_f}(s) = \frac{v_f(s)}{v_c(s)} = \frac{1}{L_c C_f} \frac{1}{s^2 + \omega_r^2} \tag{I.113}$$

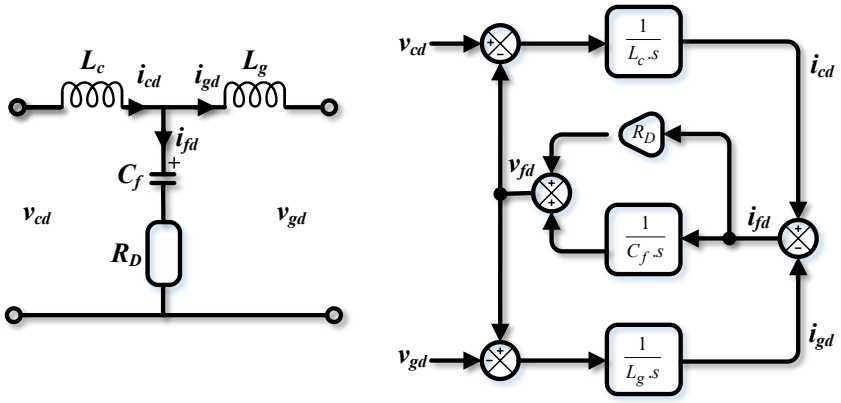

Figure I.16- Damped LCL filter single-phase model with series capacitor resistor

$$H_{i_f}(s) = \frac{i_f(s)}{v_c(s)} = \frac{i_f(s)}{v_f(s)} \frac{v_f(s)}{v_c(s)} = \frac{1}{L_c} \frac{s}{s^2 + \omega_r^2} \tag{I.114}$$

Where ω_r represents the resonant frequency previously defined.

The transfer function for the damped LCL-filter configuration shown in **Figure I.16** becomes:

$$v_c^d(s) = s.L_c.i_c^d(s) + v_f^d(s) \tag{I.115}$$

$$v_g^d(s) = v_f^d(s) - s.L_g i_g^d(s) \tag{I.116}$$

$$v_f^d(s) = i_f^d(s)\left(R_D + \frac{1}{sC_f}\right) \tag{I.117}$$

$$i_c^d(s) = i_f^d(s) + i_g^d(s) \tag{I.118}$$

The damping resistance R_D is typically chosen to equal one-third of the capacitive reactance of C_f at the resonant frequency, as established in reference [44]:

$$R_D = \frac{1}{3\omega_r C_f} \tag{I.119}$$

Through this approach, we can derive the equivalent voltage and current transfer functions that are of fundamental importance to the system analysis:

$$H_{v_f}^d(s) = \frac{v_f^d(s)}{v_c^d(s)} = \frac{1}{L_c C_f} \frac{1 + sR_D C_f}{s^2 + \omega_r^2\left(1 + sR_D C_f\right)} \tag{I.120}$$

$$H_{i_f}^d(s) = \frac{i_f^d(s)}{v_c^d(s)} = \frac{i_f^d(s)}{v_f^d(s)} \frac{v_f^d(s)}{v_c^d(s)} = \frac{1}{L_c} \frac{s}{s^2 + \omega_r^2\left(1 + sR_D C_f\right)} \tag{I.121}$$

For the undamped LCL filter configuration, we establish the following definitions:

$$H_{v_f}(s)=\frac{v_f(s)}{v_c(s)}=\frac{L_g}{s^2L_cC_fL_g+L_c+L_g}=H_1(s) \tag{I.122}$$

$$\frac{i_f(s)}{v_f(s)}=sC_f=H_2(s) \tag{I.123}$$

For the damped LCL filter configuration, we establish the following parameter definitions:

$$H^d_{v_f}(s)=\frac{v^d_f(s)}{v^d_c(s)}=\frac{L_g\left(1+sR_DC_f\right)}{s^2L_cC_fL_g+\left(L_c+L_g\right)\left(1+sR_DC_f\right)}=H_3(s) \tag{I.124}$$

The active damping method aims to replicate the transfer function $H_3(s)$ using a virtual resistor (emulating R_D) instead of a physical component. As illustrated in **Figure I.17**, the control loop incorporates an active damping gain (K_{AD}) to achieve this effect. The objective is for the closed-loop transfer function in **Figure I.17** to match $H_3(s)$, ensuring equivalent damping performance without energy losses.

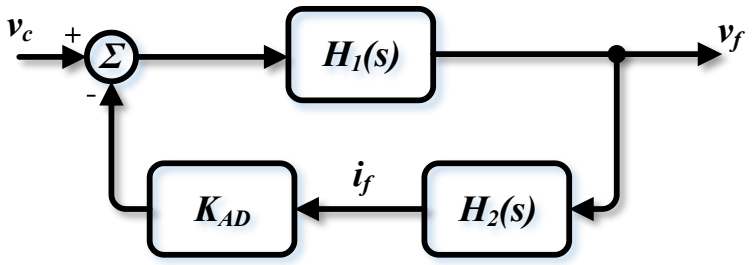

Figure I.17- The active damping control scheme utilizes capacitor voltage/current feedback signals.

From **Figure I.17**, the closed-loop model can be derived as follows:

$$H_{CL}(s)=\frac{H_1(s)}{1+H_1(s)H_2(s)K_{AD}}=\frac{\dfrac{L_g}{s^2L_cC_fL_g+L_c+L_g}}{1+\dfrac{L_g}{s^2L_cC_fL_g+L_c+L_g}sC_fK_{AD}}=\frac{L_g}{s^2L_cC_fL_g+L_c+L_g+sL_gC_fK_{AD}} \tag{I.125}$$

with K_{AD} is selected as:

$$K_{AD}=\frac{L_c+L_g}{L_g}R_D \tag{I.126}$$

Therefore, we obtain:

$$H_{CL}(s)=\frac{L_g}{s^2L_cC_fL_g+L_c+L_g+sL_gC_f\dfrac{L_c+L_g}{L_g}R_D}=\frac{L_g}{s^2L_cC_fL_g+\left(L_c+L_g\right)\left(1+sR_DC_f\right)} \tag{I.127}$$

The transfer function $H_{CL}(s)$ sufficiently approximates $H_3(s)$, allowing the term R_DC_f in $H_3(s)$'s numerator to be neglected (as $R_DC_f \ll 1$). Notably, this implementation must be applied to both axis regulators (i_d and i_q). The virtual damping gain K_{AD}, which emulates the passive resistor R_D, is integrated within the controller subsystem as the *"Virtual damping resistor"* block.

I.10 Indirect vector control by rotor flux orientation of the DSIG

In the field of electrical drives operating interchangeably as motors or generators, various control strategies exist. Due to their complex models, controlling induction machines under variable-speed operation is more challenging than controlling direct current (DC) machines.

Historically, scalar control (*V/f* = constant) was one of the first techniques used to control the speed of induction motors. Its principle is based on maintaining a constant ratio between the stator voltage and frequency to ensure maximum available torque. This technique can operate in open-loop control but provides poor speed regulation that depends on the external load applied. Additionally, it has slow and less precise dynamic responses. Since control is applied during steady-state operation, the stator flux amplitude is not controlled during transients, and the machine's torque cannot respond quickly.

FOC also known as vector control, was proposed in the early 1970s by *Hasse* and *Blaschke* [47]. The figure below **(Figure I.18)** summarizes the classification of various control strategies for variable-frequency drives that are widely used today.

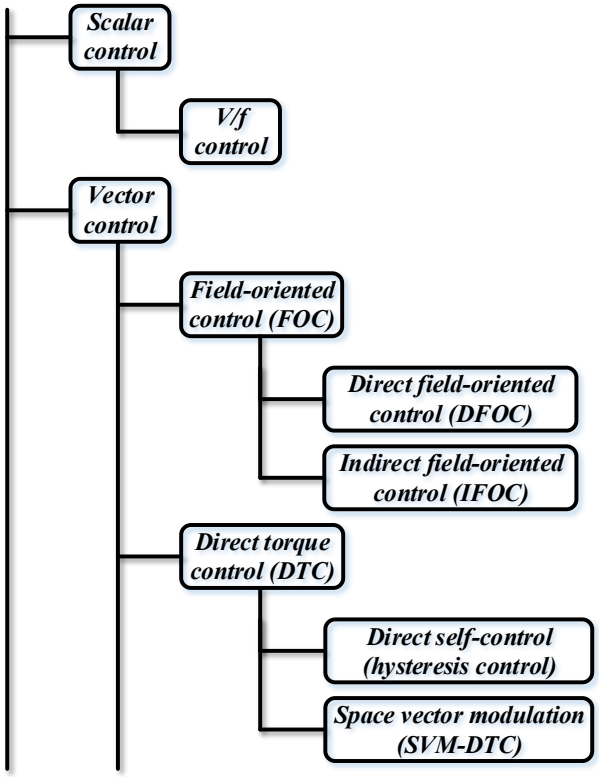

Figure I.18- Classifications of Control Strategies for Variable-Frequency Drives.

I.11 Description of the system under study

As illustrated in **Figure I.19**, the studied variable-speed wind system employs a DSIG connected to the power grid. On the DSIG side, the stator is coupled to the DC bus through two

static converters, while a gearbox transmits mechanical power from the turbine. The DSIG features two fixed three-phase stators with a 30° electrical displacement and a squirrel cage rotor, offering benefits such as power splitting, lower harmonic currents in the rotor, and enhanced reliability. On the grid side, a three-phase inverter with an LCL filter interfaces with the DC bus, enabling power delivery to the main grid. The system's control, as depicted in **Figure I.19**, is divided into two main stages: grid-side control and DSIG-side control.

- The DSIG-side control architecture employs three fundamental control loops: rotor speed regulation, rotor flux adjustment, and stator current management. The speed controller maintains the measured rotor speed at its optimal reference value derived from wind speed measurements. Simultaneously, the flux controller ensures proper alignment between the actual rotor flux and its predetermined reference value. These controllers work in tandem to generate the necessary current references - the speed controller provides the quadrature-axis stator current references based on torque requirements, while the flux controller establishes the direct-axis stator current references. The stator current controllers then compare these reference values with actual currents obtained through *dq*-to-*αβ* transformation, producing appropriate voltage references for the converters. These voltage signals are subsequently processed using SVM to generate precise switching commands for the power electronic converters, completing the control implementation.
- The grid side control stage is intended to control the power injection while ensuring synchronization to the main grid. This control stage involves: a voltage DC bus controller, a grid-side current controller, and an LCL filter voltage. The DC bus controller regulates the measured DC voltage to its set reference and offers the active power reference, which is used to compute the grid-side current reference. These current references are entered into the current controller for adjusting the actual grid-side currents. The current control block is responsible for providing the inverter side voltages as outputs. These outputs are passed to an SVM block to generate the inverter switches' commands. Note that a PLL is introduced to estimate the phase angle required for *dq-abc* and *abc-dq* transformation.

I.12 Control of the DSIG using a vector control strategy with a PI controller

I.12.1 Principle

The control of the DSIG can be implemented using a vector control strategy with a PI controller. Various control techniques have been proposed in the literature.

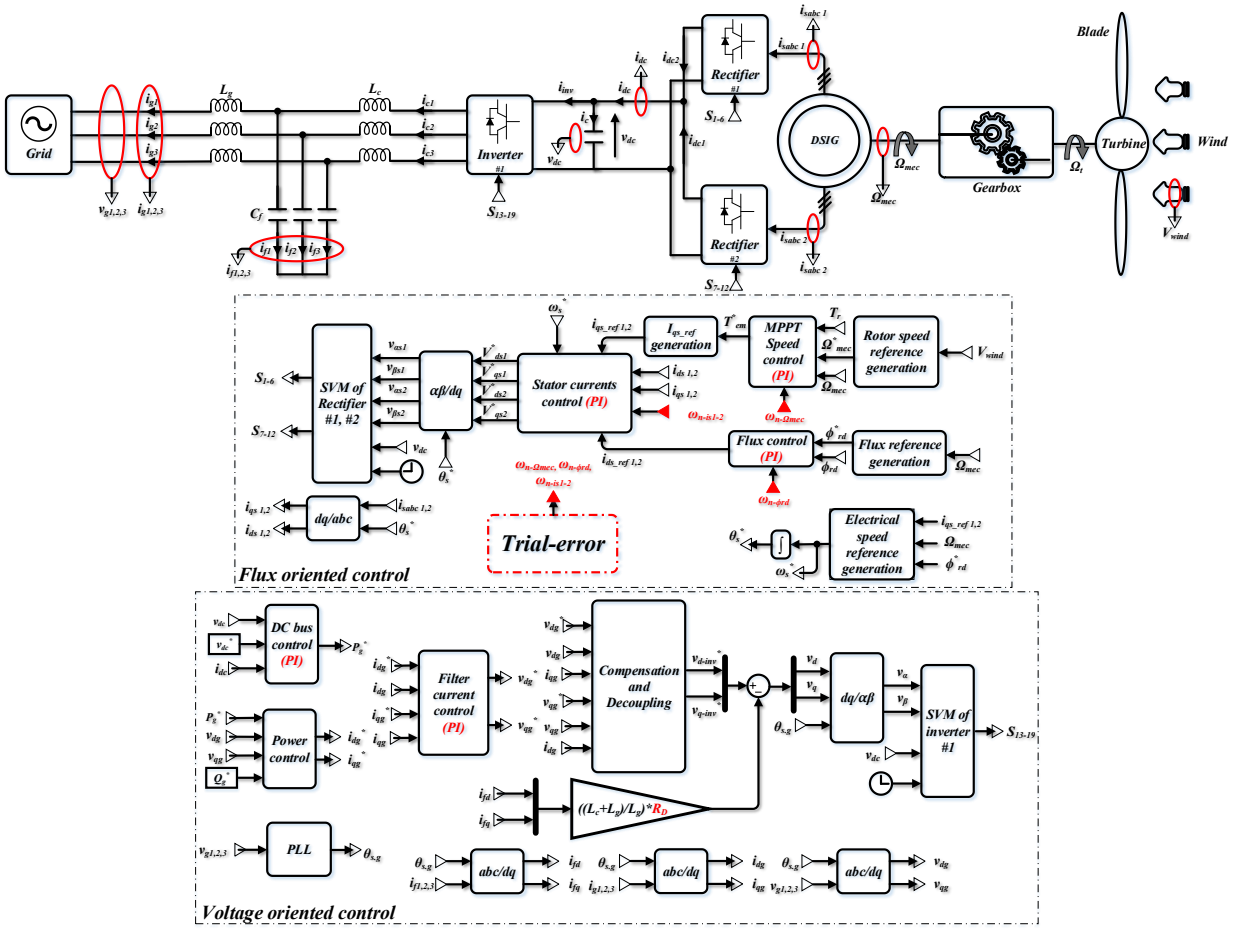

Figure I.19- WT-DSIG system with its designed PI controller scheme.

Among them, those based on flux orientation, which ensure decoupled control of the command variables, remain the most widely used in a broad range of industrial applications due to their high dynamic performance.

Flux-oriented control operates by synchronizing the stator, rotor, or air gap flux with an axis of the synchronous rotating reference frame, as depicted in **Figure I.20(a)**. This control strategy aims to make the DSIG perform similarly to a separately excited DC motor, illustrated in **Figure I.20(b)**. In such DC machines, torque regulation is achieved through the armature current I_a, while flux control is maintained via the field current I_f. The following equation can express the electromagnetic torque in a DC machine:

$$T_{em} = K.\varphi.I_a = K^{'}.I_a.I_f \tag{I.128}$$

with:

- φ: Flux imposed by the excitation current I_f
- I_a: Armature current
- K', K: Constants

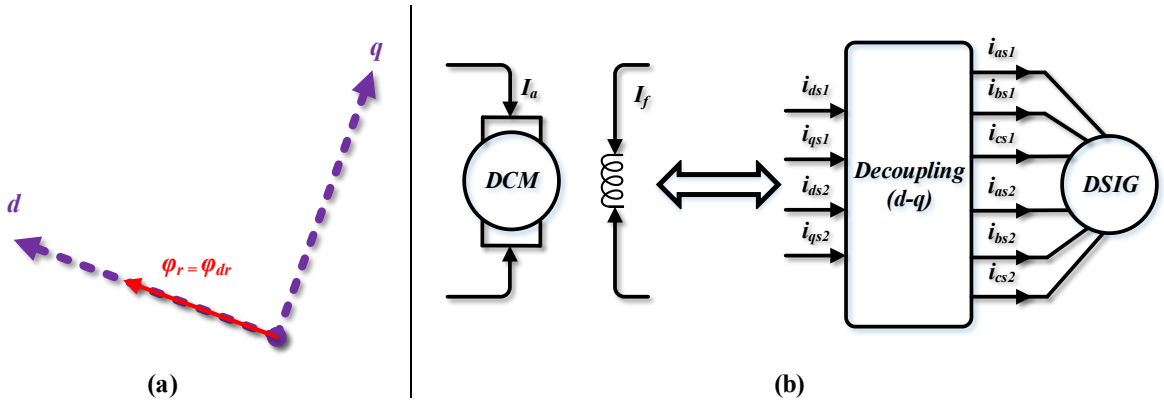

Figure I.20- Principle of Field-Oriented Vector Control: (a) Rotor flux orientation (b) Decoupled control for DC machines and (DSIG).

I.12.2 Flux orientation process

Many variants of this type of control have been presented in the literature, which can be classified based on the orientation of the *d, q* reference frame:

- Rotor flux orientation with the conditions $\varphi_{dr} = \varphi_r$, $\varphi_{qr} = 0$
- Stator flux orientation with the conditions $\varphi_{ds} = \varphi_s$, $\varphi_{qs} = 0$
- Airgap flux orientation with the conditions $\varphi_{dm} = \varphi_m$, $\varphi_{qm} = 0$.

In this work, we adopted the rotor flux orientation approach for vector control of the DSIG. This method enables independent regulation of the electromagnetic torque and rotor flux by decoupling their governing variables. By aligning the rotor flux entirely with the *d*-axis of the rotating reference frame (i.e., setting $\varphi_{dr} = \varphi_r$, $\varphi_{qr} = 0$), the electromagnetic torque expression (I.74) of the DSIG simplifies to:

$$T_{em} = P.\frac{L_m}{L_m + L_r}.\left[\varphi_{dr}.\left(i_{qs1} + i_{qs2}\right)\right] = K.\varphi_r.I_{qs} \tag{I.129}$$

With: $i_{qs} = i_{qs1} + i_{qs2}$

I.12.3 Methods of vector control

All the research work conducted on the subject uses two main methods. The first, called the direct method, was initiated by *F. Blaschke*, and the second, known as the indirect method, was introduced by *K. Hasse*.

I.12.3.1 Direct method

This method requires a good understanding of both the flux magnitude and its phase. This must be verified regardless of the operating conditions [48]. To achieve this, two processes are considered:

- The airgap flux measurement method employs dedicated sensors within the machine. However, this approach presents significant limitations due to the inherent mechanical fragility of flux sensors. These components demonstrate poor reliability when subjected to harsh operating environments, particularly under conditions involving excessive vibration or elevated temperatures.
- Flux can be computationally estimated, though this approach demonstrates parameter-dependent characteristics that affect its accuracy.

I.12.3.2 Indirect method

The principle of this method consists of not using the amplitude of the rotor flux but only its position. The term "indirect method" means that the flux estimator can be eliminated. However, this method requires the presence of a rotor position sensor. Furthermore, it is sensitive to variations in the machine parameters [6].

I.12.4 Proposed control strategy for WT-DSIG

This study implements a rotor FOC strategy for the WT-DSIG system, enabling decoupled control of flux and electromagnetic torque. The approach achieves independent speed regulation through coordinated management of direct (*d*-axis) and quadrature (*q*-axis) stator current components.

Following the implementation of field-oriented control on the DSIG model presented in equation (I.66), we derive the following system of state equations

$$\begin{cases} \dot{i}_{ds1} = \dfrac{1}{L_{s1}}\left\{v_{ds1} - R_{s1}i_{ds1} + \omega_s^*(L_{s1}i_{qs1} + \tau_r\varphi_{rd}^*\omega_{sl}^*)\right\} \\ \dot{i}_{qs1} = \dfrac{1}{L_{s1}}\left\{v_{qs1} - R_{s1}i_{qs1} - \omega_s^*(L_{s1}i_{ds1} + \varphi_{rd}^*)\right\} \\ \dot{i}_{ds2} = \dfrac{1}{L_{s2}}\left\{v_{ds2} - R_{s2}i_{ds2} + \omega_s^*(L_{s2}i_{qs2} + \tau_r\varphi_{rd}^*\omega_{sl}^*)\right\} \\ \dot{i}_{qs2} = \dfrac{1}{L_{s2}}\left\{v_{qs2} - R_{s2}i_{qs2} - \omega_s^*(L_{s2}i_{ds2} + \varphi_{rd}^*)\right\} \\ \dot{\varphi}_{rd}^* = \mu\left(i_{ds1} + i_{ds2}\right) - \xi\varphi_{rd} \\ \dot{\Omega}_{mec} = \dfrac{1}{J}\left(P\mu\varphi_{rd}^*\left(i_{qs1} + i_{qs2}\right) - T_g - k_f\Omega_{mec}\right) \end{cases} \tag{I.130}$$

where τ, μ, and ξ are given by: $\tau = \dfrac{L_r}{R_r}$, $\mu = \dfrac{L_m}{L_m + L_r}$, $\xi = \dfrac{R_r}{L_m + L_r}$

Figure I.19 illustrates the proposed FOC architecture, which incorporates three PI-based control loops for: rotor speed regulation, flux control, and stator current management, as detailed in the following analysis.

I.12.4.1 PI Vector Control

a. Control of the rectifier on the DSIG side: In this initial configuration, the three control loops governing rotor speed, flux, and stator currents employ PI regulators, whose architectural implementations are respectively illustrated in **Figures I.21, I.22, and I.23**. Consequently, the output equations for the rotor speed and flux controllers can be expressed as:

$$T_{em}^{*}(t) = k_{p-\Omega}\left(\Omega_{mec}^{*}(t) - \Omega_{mec}(t)\right) + k_{i-\Omega}\int\left(\Omega_{mec}^{*}(t) - \Omega_{mec}(t)\right)\,dt \tag{I.131}$$

$$i_{ds1,2}^{*}(t) = k_{p-\varphi}\left(\varphi_{rd}^{*}(t) - \varphi_{rd}(t)\right) + k_{i-\varphi}\int\left(\varphi_{rd}^{*}(t) - \varphi_{rd}(t)\right)\,dt \tag{I.132}$$

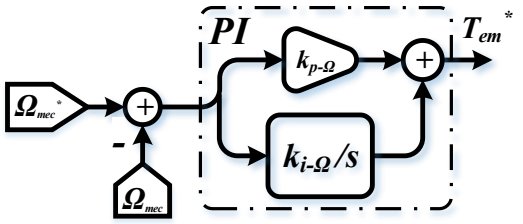

Figure I.21- PI controller-based speed (Ω_{mec}) control loop.

The proportional $k_{p\text{-}\Omega}$, $k_{p\text{-}\phi}$ and integral $k_{i\text{-}\Omega}$, $k_{i\text{-}\phi}$ gains correspond to the rotor speed and flux controllers, respectively. The reference values for mechanical rotor speed Ω_{mec}^{*} and φ_{rd}^{*} are computed using the following expressions:

$$\Omega_{mec}^{*} = \frac{V_{wind}\,\lambda_{opt}\,G}{R} \tag{I.133}$$

The flux is generally maintained constant at its nominal value φ_{rd}^{n} for rotor speeds less than or equal to the nominal speed of the machine Ω_{r}^{n}. For higher speeds, the flux decreases as the speed increases to limit the voltage at the machine's terminals.

The rotor flux is typically held constant at its nominal value. φ_{rd}^{n} When operating at or below the machine's rated speed Ω_{r}^{n}. In the field-weakening region ($\Omega_{r} > \Omega_{r}^{n}$), the flux magnitude is progressively reduced in inverse proportion to speed to maintain terminal voltage within acceptable limits.

To achieve this, the reference flux φ_{rd}^{*} is defined as follows:

$$\varphi_{rd}^{*} = \begin{cases} \varphi_{rd}^{n} & \text{if} \quad \Omega_{mec} \le \Omega_{mec}^{n} \\ \dfrac{\Omega_{r}^{n}}{\Omega_{r}}\varphi_{rd}^{n} & \text{if} \quad \Omega_{mec} > \Omega_{mec}^{n} \end{cases} \tag{I.134}$$

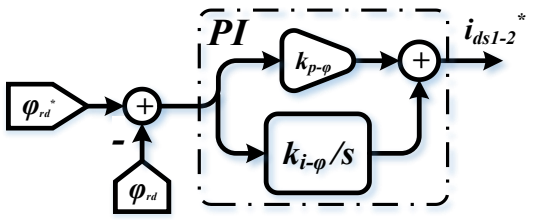

Figure I.22- PI controller-based flux (φ_{rd}) control loop.

where φ_{rd}^{n}denotes the nominal rotor flux, while Ω_{mec} and Ω_{mec}^{n} represent the actual mechanical rotor speed and its rated nominal value, respectively.

Under the assumption of identical current references for both stators ($i_{ds1}^{*} = i_{ds2}^{*}$ and $i_{qs1}^{*} = i_{qs2}^{*}$), the current controllers produce the following stator voltage references for both winding sets: $v_{ds1,2}^{*}$and $v_{qs1,2}^{*}$.

$$\begin{cases} v_{ds1}^{*} = k_{p-is}\left(i_{ds1}^{*} - i_{ds1}\right) + k_{i-is}\int\left(i_{ds1}^{*} - i_{ds1}\right)\,dt - C_{t1} \\ v_{qs1}^{*} = k_{p-is}\left(i_{qs1}^{*} - i_{qs1}\right) + k_{i-is}\int\left(i_{qs1}^{*} - i_{qs1}\right)\,dt + C_{t2} \\ v_{ds2}^{*} = k_{p-is}\left(i_{ds2}^{*} - i_{ds2}\right) + k_{i-is}\int\left(i_{ds2}^{*} - i_{ds2}\right)\,dt - C_{t3} \\ v_{qs2}^{*} = k_{p-is}\left(i_{qs2}^{*} - i_{qs2}\right) + k_{i-is}\int\left(i_{qs2}^{*} - i_{qs2}\right)\,dt + C_{t4} \end{cases} \tag{I.135}$$

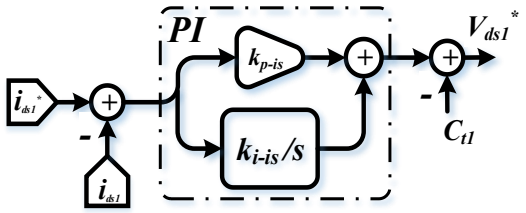

Figure I.23- PI controller-based current (i_{ds1}) control loop.

where $k_{p\text{-}is}$ and $k_{i\text{-}is}$ represent the proportional and integral gains of the current control loops, while i_{qs1}^{*} and i_{qs2}^{*} denote the quadrature-axis current references. The coefficients C_{t1} through C_{t4} are defined as follows:

$$(i_{qs1}^{*} + i_{qs2}^{*}) = T_{em}^{*}\,\frac{L_m + L_r}{PL_m\varphi_{rd}^{*}} \tag{I.136}$$

$$\begin{cases} C_{t1} = \omega_s^{*}(L_{s1}i_{qs1} + \tau_r\varphi_{rd}^{*}\omega_{sl}^{*}) \\ C_{t2} = \omega_s^{*}(L_{s1}i_{ds1} + \varphi_{rd}^{*}) \\ C_{t3} = \omega_s^{*}(L_{s2}i_{qs2} + \tau_r\varphi_{rd}^{*}\omega_{sl}^{*}) \\ C_{t4} = \omega_s^{*}(L_{s2}i_{ds2} + \varphi_{rd}^{*}) \end{cases} \tag{I.137}$$

where ω_s^{*} represents the stator reference frequency and ω_{sl}^{*} denotes the slip-speed reference, with their respective expressions given by:

$$\omega_{sl}^{*} = \frac{R_r L_m}{L_m + L_r}\,\frac{i_{qs1}^{*} + i_{qs2}^{*}}{\varphi_{rd}^{*}} \tag{I.138}$$

$$\omega_s^{*} = \omega_{sl}^{*} + \omega_r \tag{I.139}$$

Notably, the controller gains are functionally related to the natural frequencies $\omega_{n\text{-}\Omega mec}$, $\omega_{n\text{-}\varphi rd}$, and $\omega_{n\text{-}is1,2}$ through specific mathematical relationships. These relationships are derived by

equating the characteristic equations of the closed-loop transfer function (I.141) with ideal second-order system representations.

$$\begin{cases} k_{p-\Omega} = 2k_{si}\omega_{n-\Omega mec}J - k_f \\ k_{i-\Omega} = J\omega_{n-\Omega mec}^2 \end{cases}$$

$$\begin{cases} k_{p-\varphi} = \dfrac{\left(2\left(L_m + L_r\right)k_{si}\omega_{n-\varphi rd} - R_r\right)}{\left(R_r L_m\right)} \\ k_{i-\varphi} = \dfrac{\left(\left(L_m + L_r\right)\omega_{n-\varphi rd}^2\right)}{\left(R_r L_m\right)} \end{cases} \quad \text{(I.140)}$$

$$\begin{cases} k_{p-is} = 2k_{si}\omega_{n-is1,2}L_{s1,2} - R_{s1,2} \\ k_{i-is} = L_{s1,2}\omega_{n-is1,2}^2 \end{cases}$$

$$T(s) = \frac{\omega_n^2}{s^2 + 2k_{si}\omega_n s + \omega_n^2} \quad \text{(I.141)}$$

where k_{si} is the damping factor set to $\frac{1}{\sqrt{2}}$.

b. Rotor Flux estimation for DSIG: Each stator contributes to the rotor flux, so total stator flux is:

$$\varphi_{ds\_total} = \varphi_{ds1} + \varphi_{ds2} \quad \text{(I.142)}$$

Then the total rotor flux is:

$$\varphi_{rd} = \frac{L_m}{L_r}\left(\varphi_{ds1} + \varphi_{ds2}\right) \quad \text{(I.143)}$$

Where each stator flux is:

$$\varphi_{ds1} = \int \left(v_{ds1} - R_{ds1}.i_{ds1}\right) dt \quad \text{(I.144)}$$

$$\varphi_{ds2} = \int \left(v_{ds2} - R_{ds2}.i_{ds2}\right) dt \quad \text{(I.145)}$$

Then combine:

$$\varphi_{rd} = \frac{L_m}{L_r}\int \left(\left(v_{ds1} - R_{s1}.i_{ds1}\right) + \left(v_{ds2} - R_{s2}.i_{ds2}\right)\right) dt \quad \text{(I.146)}$$

c. Control of the inverter on the grid side: This inverter regulates the DC bus to a sufficiently high value to ensure the proper operation of the power electronics. After adaptation using a transformer, the inverter must also supply the electrical grid with a voltage ideally equal to that of the grid.

- ***Calculation of the DC bus voltage***

To determine the value of the DC bus required to transmit a given power, the following expressions are used [29], [47], [49]:

$$\alpha_1 = \sqrt{\frac{P_{\max} X^2}{9E^4} + 1} \tag{I.147}$$

$$v_{dc} = 2\sqrt{2}\alpha_1 E \tag{I.148}$$

The nominal power $P_n = 1.5\ MW$ is considered for a root mean square (RMS) line voltage of $V_{rms}=E=400\ V$. The smoothing inductor's impedance, with an inductance of $1\ mH$, has a value of $X=0.314\ \Omega$.

After all calculations, we find: $\alpha_1=1.00005$; $v_{dc}=1131V$.

- ***Calculation of the DC bus capacitor***

This approach is based on the role of the DC bus capacitor, which is responsible for absorbing or supplying the power required by the load during transient conditions. In [50], [51], the calculation of the capacitor value is based on the maximum power demand of the load over a period of the source voltage. From the maximum real power of the load P_{max}, the required capacitance value, which must supply the equivalent energy in the most unfavorable transient case, is given by:

$$C_{dc} = \frac{2.P_{\max}.20.10^{-3}}{v_{dc}^2(1-k^2)} \tag{I.149}$$

with: $k = v_{dcmin}/v_{dc}$

The voltage v_{dcmin} must be carefully chosen to ensure the controllability of the current at all operating points.

- ***Regulation of the DC bus voltage***

The DC bus consists of a capacitor designed to smooth the voltage. The evolution of this voltage is obtained from the integration of the capacitive current [29]:

$$\frac{dv_{dc}}{dt} = \frac{1}{C_{dc}}\left(i_{dc} - i_{inv}\right) \tag{I.150}$$

Hence:

$$i_c = i_{dc} - i_{inv} \tag{I.151}$$

with:

$$\begin{aligned} i_{inv} &= f_{11}i_{c1} + f_{12}i_{c2} + f_{13}i_{c3} \\ i_{dc} &= i_{dc1} + i_{dc2} \\ i_{dc1} &= f_{11}i_{as1} + f_{12}i_{bs1} + f_{13}i_{cs1} \\ i_{dc2} &= f_{21}i_{as2} + f_{22}i_{bs2} + f_{23}i_{cs2} \end{aligned} \tag{I.152}$$

- ***Phase-Locked Loop (PLL)***

The block diagram of the *3ph* PLL of MATLAB is given in **Figure I.24**. This PLL is closed-loop control system, which tracks the frequency and phase of a sinusoidal three-phase signal by using an internal frequency oscillator. The control system adjusts the internal oscillator frequency to keep the phase difference to 0.

Appendix E describes this PLL in detail.

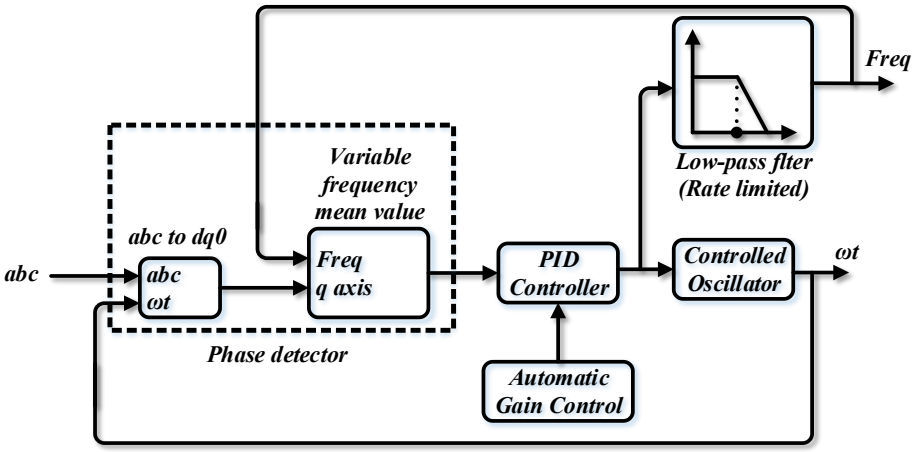

Figure I.24- The PLL's block diagram.

The three-phase input signal is converted to a *dq0* rotating frame (*Park transform*) using the angular speed ($\theta_{s.g} = \omega t$) of an internal oscillator. The quadrature axis of the signal, proportional to the phase difference between the *abc* signal and the internal oscillator rotating frame, is filtered with a Mean (Variable Frequency) block. A PID controller, with an optional automatic gain control (AGC), keeps the phase difference to 0 by acting on a controlled oscillator. The PID output, corresponding to the angular velocity, is filtered and converted to the frequency, in hertz, which is used by the mean value [52].

- ***Current Regulation***

The single-phase voltages of the grid are expressed as:

$$\begin{cases} v_{g1} = V_{\max}.\sin\left(\omega_{s.g}t\right) \\ v_{g2} = V_{\max}.\sin\left(\omega_{s.g}t - \dfrac{2\pi}{3}\right) \\ v_{g3} = V_{\max}.\sin\left(\omega_{s.g}t + \dfrac{2\pi}{3}\right) \end{cases} \quad \text{(I.153)}$$

with $\omega_{s.g} = 2\pi f_{s,g}$ and $V_{max} = \sqrt{2}.V_{rms}$

The voltages on the stator side and the grid side are transformed in the same way:

$$\begin{bmatrix} v_{ds1} \\ v_{qs1} \\ v_{0s1} \end{bmatrix} = \left[P\left(\theta_{s1}\right) \right] . \begin{bmatrix} v_{as1} \\ v_{bs1} \\ v_{cs1} \end{bmatrix} \tag{I.154}$$

$$\begin{bmatrix} v_{dg} \\ v_{qg} \\ v_{0g} \end{bmatrix} = \left[P\left(\theta_{s.g}\right) \right] . \begin{bmatrix} v_{g1} \\ v_{g2} \\ v_{g3} \end{bmatrix} \tag{I.155}$$

The currents on the grid side are expressed as:

$$\begin{cases} i_{dg} = \dfrac{1}{R_f + L_f s} \left(v_{d\_inv} - v_{dg} - L_f \omega_{s.g} i_{qg} \right) \\ i_{qg} = \dfrac{1}{R_f + L_f s} \left(v_{q\_inv} - v_{qg} + L_f \omega_{s.g} i_{dg} \right) \end{cases} \tag{I.156}$$

with:

$$L_f = L_c + L_g \tag{I.157}$$

$$R_f = R_c + R_g \tag{I.158}$$

where L_f and R_f is the law filter inductence and resistence. The reference single-phase voltages for the grid, expressed in the Park reference frame, are given by the following relations:

$$\begin{cases} v^*_{d\_inv} = v^*_{dg} + v_{dg} - L_f \omega_{s.g} i_{qg} \\ v^*_{q\_inv} = v^*_{qg} + v_{qg} + L_f \omega_{s.g} i_{dg} \end{cases} \tag{I.159}$$

with:

$$\begin{cases} v^*_{dg} = k_{p-ig} \left(i^*_{dg} - i_{dg} \right) + k_{i-ig} \int \left(i^*_{dg} - i_{dg} \right) \, dt \\ v^*_{qg} = k_{p-ig} \left(i^*_{qg} - i_{qg} \right) + k_{i-ig} \int \left(i^*_{qg} - i_{qg} \right) \, dt \end{cases} \tag{I.160}$$

The controllers' gains are:

$$\begin{cases} k_{p-ig} = 2 k_{si} \omega_{n-ig} L_f - R_f \\ k_{i-ig} = L_f \omega^2_{n-ig} \end{cases} \tag{I.161}$$

- ***Calculation of the reference currents***

The active and reactive reference powers are expressed as:

$$\begin{cases} P^*_g = v_{dg} . i^*_{dg} + v_{qg} . i^*_{qg} \\ Q^*_g = v_{qg} . i^*_{dg} - v_{dg} . i^*_{qg} \end{cases} \tag{I.162}$$

The reference reactive power is set to zero. Therefore, the power factor on the electrical grid side is unity.

$$Q_g^* = 0 \tag{I.163}$$

The following relation gives the reference active power on the electrical grid side:

$$P_g^* = v_{dc}.i_{dc} - v_{dc}.i_c^* \tag{I.164}$$

with:

$$i_c^* = k_{p-dc}\left(v_{dc}^* - v_{dc}\right) + k_{i-dc}\int\left(v_{dc}^* - v_{dc}\right)\,dt \tag{I.165}$$

The controllers' gains are:

$$\begin{cases} k_{p-dc} = 2k_{si}\omega_{n-dc}C_{dc} \\ k_{i-dc} = C_{dc}\omega_{n-dc}^2 \end{cases} \tag{I.166}$$

According to expressions (I.155), the reference currents of the electrical grid, expressed in the Park reference frame, are calculated as:

$$\begin{cases} i_{dg}^* = \dfrac{2}{3}\dfrac{P_g^* v_{dg} + Q_g^* v_{qg}}{v_{dg}^2 + v_{qg}^2} \\ i_{qg}^* = \dfrac{2}{3}\dfrac{P_g^* v_{qg} - Q_g^* v_{dg}}{v_{dg}^2 + v_{qg}^2} \end{cases} \tag{I.167}$$

Table I.2–PI controller gains of all system

Tuning method	Controller	Gains				
		Rotor speed control	Rotor flux control	Stators currents control	DC bus control	Filter control
Trial and Error	PI	$\omega_{n\_\Omega mec} = 1100$	$\omega_{n\_\varphi} = 10$	$\omega_{n\_is\_1,2} = 10000$	$\omega_{n\_dc} = 50$	$\omega_{n\_ig} = 8000$

I.13 Simulation results and discussion

The simulations are conducted using MATLAB software and the associated libraries: SimPowerSystems and Simulink.

- **Figure I.25-(b)** represents the speed profile. It can be observed that the rotational speed perfectly follows its reference, which varies according to the imposed wind profile **Figure I.25-(a)**. The reference torque, derived from the MPPT algorithm, and the electromagnetic torque of the generator are illustrated in **Figure I.25-(c)**.
- **Figure I.25-(e)** shows the stator currents of the two stators, where it can be seen that the second star is phase-shifted by an electrical angle of **(α = 30°)** relative to the first stator.

- The evolution of the rotor flux is illustrated in **Figure I.25-(d)**. The behavior of the rotor flux components demonstrates good flux orientation, ensuring a well-decoupled vector control of the DSIG.
- **Figure I.25-(f)** presents the profiles of the total active and reactive stator powers of the DSIG. The active power is negative, meaning that the DSIG generates this power while exhibiting fluctuations. On the other hand, the reactive power is positive, indicating that the machine absorbs this energy necessary for its magnetization.
- The DC bus voltages v_{dc} and v_{dc}^{*} in **Figure I.27-(a)** are clipped at a value of $1130V$ for a nominal power of $1.5MW$.
- **Figure I.27-(e)** shows the evolution of the stator voltage and current of the first phase corresponding to the first star. These reveal that the voltage and current are almost 180° out of phase, meaning they have opposite signs. This indicates that the generated power is negative, signifying the transfer of active power from the machine to the grid.
- To maintain a unitary power factor on the grid side, the reference reactive power Q_g^{*} is set to zero. **Figure I.27-(c)** represents the active and reactive powers supplied to the electrical grid, showing that the active power follows its reference, while the reactive power remains zero as per its imposed setpoint (a negative power represents generated power).
- **Figure I.27-(d)** demonstrates that the grid-side currents are well-sinusoidal.
- **Figure I.27-(b)** illustrates the voltage and current of one phase connected to the grid, with the electrical grid frequency being 50Hz. It is shown that the voltage is imposed by the grid, while the amplitude of the injected current is controlled by the system. It is also indicated that the grid voltage and current waveforms are in phase opposition, confirming that power flow is always from the wind generator to the electrical grid.
- **Figure I.27-(f)** presents the Total Harmonic Distortion (THD) of the current I_{ag}. The THD is defined as the ratio of the total RMS value of harmonics (their quadratic sum) to the RMS value of the fundamental component. Analyzing a time sequence, we observe that the harmonics present in the grid current I_{ag} are minimized.

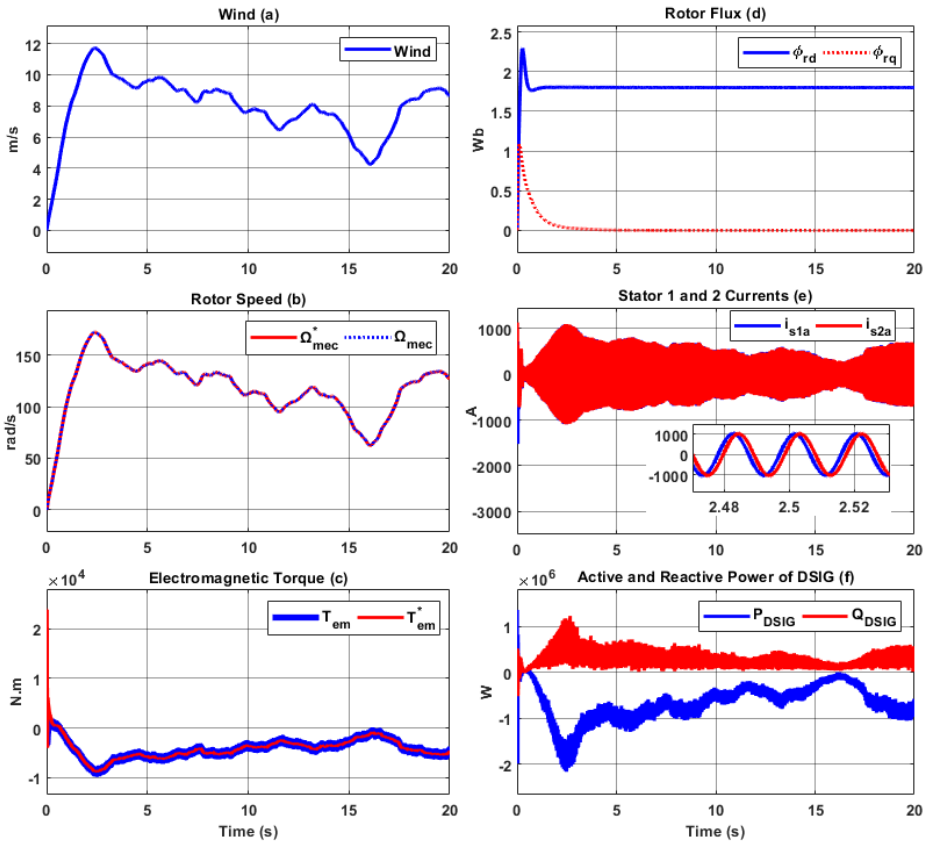

Figure I.25- Results simulation generator side.

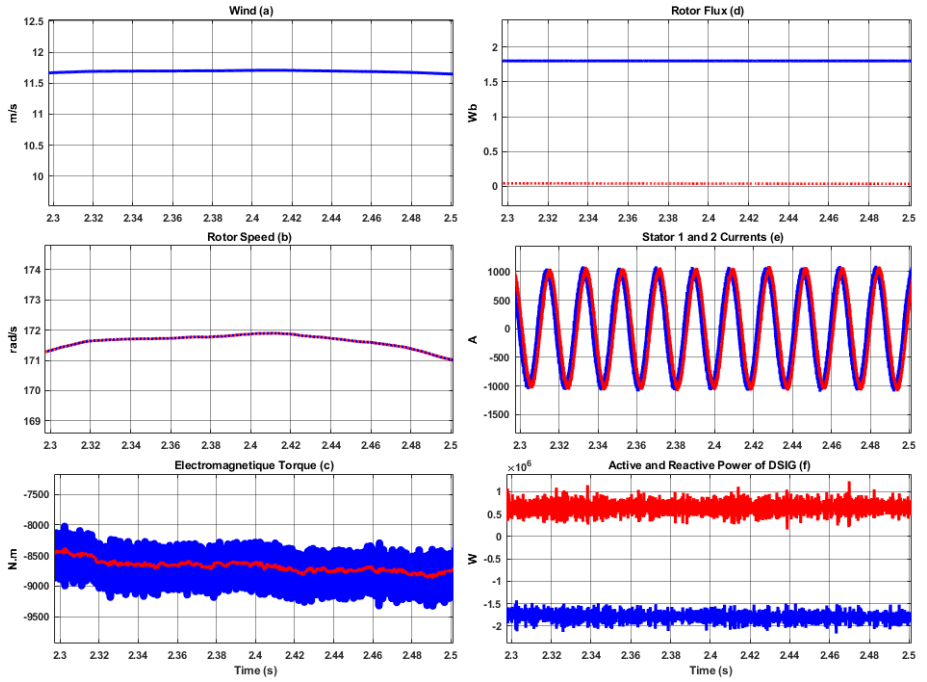

Figure I.26- Zoom in Results simulation generator side.

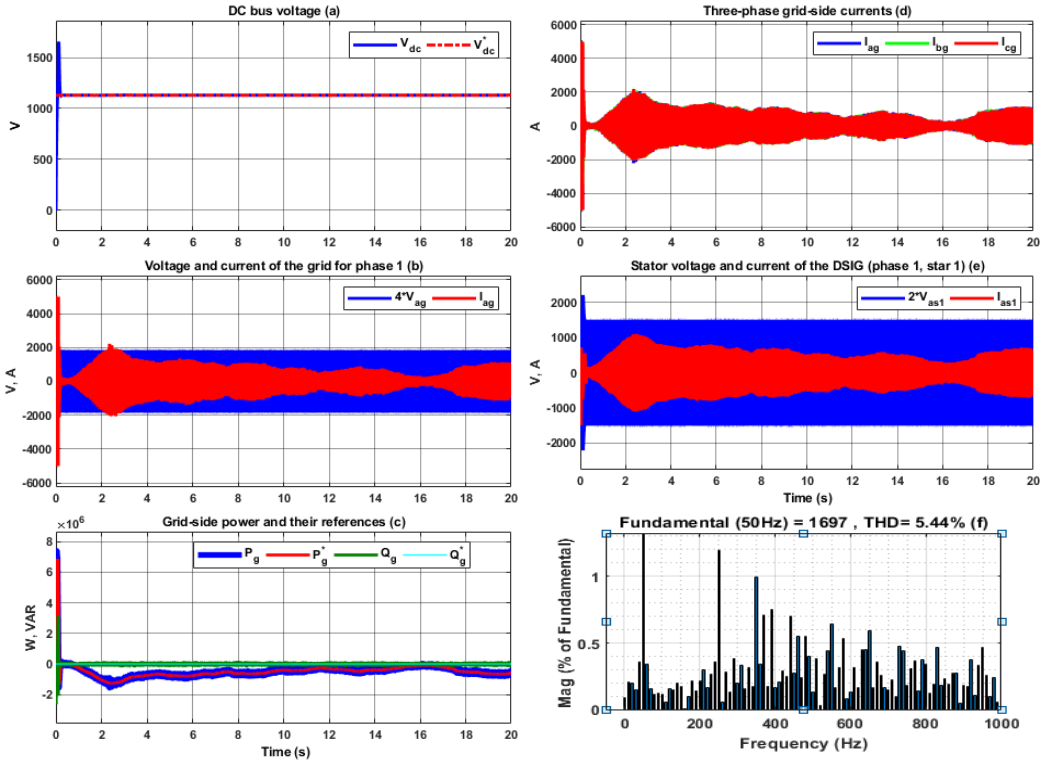

Figure I.27- Results simulation grid side.

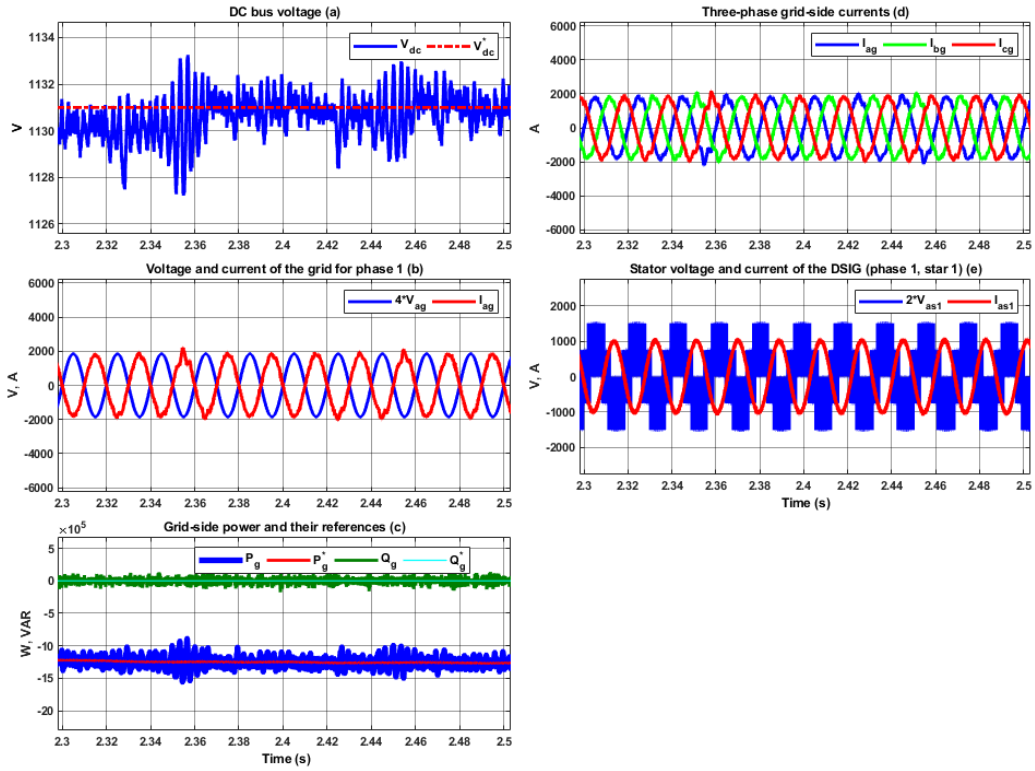

Figure I.28- Zoom in Results simulation grid side.

I.14 Conclusion

This study has provided a comprehensive analysis of the modeling, control, and optimization of a variable-speed wind turbine system, with a particular focus on the DSIG. By integrating aerodynamic modeling, electrical modeling, and advanced control strategies, the research demonstrates how wind energy conversion can be maximized for efficiency and reliability.

The modeling of the wind turbine system began with a detailed examination of wind energy conversion principles, highlighting key aerodynamic parameters such as the power coefficient, tip speed ratio, and Betz's law. Additionally, wind speed modeling techniques were explored to account for the unpredictable nature of wind, ensuring accurate system simulations. The study then moved into the mechanical and electrical aspects of the wind turbine, developing a state-space representation of the DSIG to facilitate control and optimization.

To achieve efficient energy conversion, a FOC strategy was implemented, using a PI controller to regulate rotor speed, flux, and stator currents. This vector control approach successfully decouples torque and flux, enabling precise generator control and improved power output. The simulation study in Matlab/Simulink validated the theoretical models, confirming the effectiveness of the PI-based control strategy in optimizing the wind turbine's performance under varying wind conditions. The results of this study emphasize the importance of advanced control techniques in renewable energy systems, demonstrating that PI-controlled vector control can significantly enhance wind turbine efficiency. In the previous chapter, we focus on nonlinear control, by using a BS controller, proposes an innovative tuning method using the subtraction-average-based optimizer (SABO) to ensure optimal backstepping controller parameters tuning.

Chapter II. Optimal Backstepping Control Technique for DSIG-based Wind Turbine System

Chapter II. Optimal Backstepping Control Technique for DSIG-based Wind Turbine System

II.1 Introduction

The tuning of BS controllers for WT-DSIG is critical to ensure stability and tracking performance, yet existing literature lacks a comprehensive parameter optimization approach. To address this gap, this chapter proposes an innovative tuning strategy using the SABO, a metaheuristic stochastic algorithm, to optimally determine BS control parameters. The method is integrated into an FOC scheme for WT-DSIG systems, aiming to simplify and enhance control performance by optimizing the natural frequencies of flux, speed, and current controllers. MATLAB simulations validate the strategy's superiority over conventional techniques, demonstrating improved dynamic response and steady-state accuracy.

II.2 Backstepping vector control

II.2.1 Brief history of the backstepping control method

The backstepping control technique is a systematic and recursive method for synthesizing nonlinear control laws using Lyapunov functions. It ensures step-by-step stabilization at each synthesis stage. A virtual control is formed at each process step to ensure the system converges to its equilibrium state. This technique enables the synthesis of control laws while potentially accounting for disturbances or uncertainties in the system parameters.

The fundamental idea of backstepping control is to render the closed-loop systems equivalent to stable first-order subsystems in a cascade, in the Lyapunov sense. This imparts robustness and ensures global asymptotic stability. The backstepping control synthesize aims to regulate the output variables (flux and speed). To carry out a trajectory on these outputs, we have selected the stator currents as intermediate variables, which must track their rated values provided by the "virtual control." Finally, we will calculate the voltage controls (stator voltages) necessary to ensure the convergence of the "virtual controls" to the desired values while maintaining the stability of the associated *Lyapunov* function at each step.

The backstepping technique was developed by *Kanellakopoulos* and al. (1991) [53], drawing inspiration from the works of *Feurer Morse* (1978), *Tsinias* (1989), and *Kokotović Sussmann* (1989) [54]. The term "backstepping" is particularly justified by the recursive process intrinsic to the synthesis. This process enables a constructive synthesis of control laws for triangular nonlinear systems using *Lyapunov* theory [55]. The core idea is to choose a positive definite *Lyapunov* function such that its derivative is always negative.

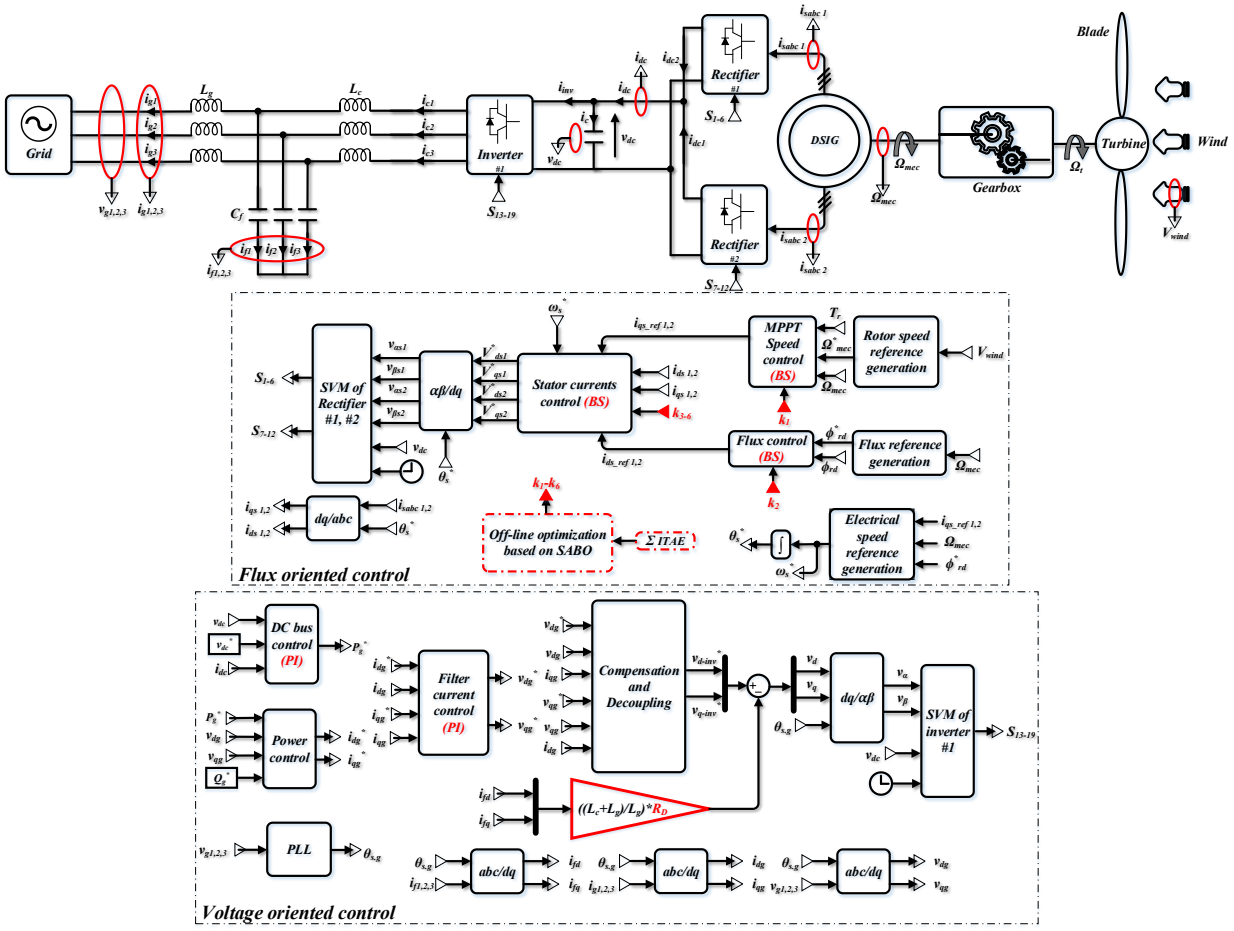

Figure II.1- Proposed BS control scheme for WT-DSIG system.

II.2.2 Design of backstepping control

The synthesis of controllers using the backstepping technique described in this section is divided into two main parts. First, the speed and flux loops are synthesized to control these two output variables to their desired values, Ω^* and φ_{rd}^*, respectively. Next, the second step focuses on the synthesis of the current loops.

II.2.2.1 Step 1: Speed and flux loops

In this section, we will limit ourselves to applying the backstepping method to the double-star asynchronous generator and will establish the expressions for the control parameters based on the model developed in the previous chapter. Recall that this model was derived using the principle of rotor flux orientation. To design a backstepping control law that ensures speed and flux tracking for the machine, the speed and flux tracking errors are defined as:

$$\begin{cases} e_1 = \Omega_{mec}^* - \Omega_{mec} \\ e_2 = \varphi_{rd}^* - \varphi_{rd} \end{cases} \tag{II.1}$$

The derivatives are given as follows:

$$\begin{cases} \dot{e}_1 = \dot{\Omega}^*_{mec} - \dot{\Omega}_{mec} \\ \dot{e}_2 = \dot{\varphi}^*_{rd} - \dot{\varphi}_{rd} \end{cases} \tag{II.2}$$

From the system of equations (I.116) and (II.2), we conclude:

$$\begin{cases} \dot{e}_1 = \dot{\Omega}^*_{mec} - \frac{1}{J}\left(P\mu\varphi^*_{rd}\left(i_{qs1} + i_{qs2}\right) - T_g - k_f\Omega_{mec}\right) \\ \dot{e}_2 = \dot{\varphi}^*_{rd} - \mu\left(i_{ds1} + i_{ds2}\right) - \xi\varphi_{rd} \end{cases} \tag{II.3}$$

The first function of Lyapunov, v_1, and its first derivative are defined as:

$$v_1 = \frac{1}{2}(e_1^2 + e_2^2) \tag{II.4}$$

$$\dot{v}_1 = e_1\dot{e}_1 + e_2\dot{e}_2 \tag{II.5}$$

According to equation (II.3), we can derive the first derivative v_1 as:

$$\dot{v}_1 = e_1\left[\dot{\Omega}^*_{mec} - \frac{1}{J}\left[P\mu\varphi^*_{rd}(i_{qs1} + i_{qs2}) - T_g - k_f\Omega_{mec}\right]\right] + e_2\left[\dot{\varphi}^*_{rd} - \mu\left(i_{ds1} + i_{ds2}\right) - \xi\varphi_{rd}\right] \tag{II.6}$$

Based on *Lyapunov* theory, to achieve stability, $\dot{v}_1$ must be negative ($\dot{v}_1 < 0$), thus we can consider:

$$\begin{cases} \dot{e}_1 = -k_1 e_1 \\ \dot{e}_2 = -k_2 e_2 \end{cases} \tag{II.7}$$

where k_1 and k_2 stand for positive gains.

Based on equation (II.7), equation (II.3) can be rewritten as follows:

$$\begin{cases} \dot{\Omega}^*_{mec} - \frac{1}{J}\left[P\mu\varphi^*_{rd}(i_{qs1} + i_{qs2}) - T_g - k_f\Omega_{mec}\right] = -k_1 e_1 \\ \dot{\varphi}^*_{rd} - \left(\mu\left(i_{ds1} + i_{ds2}\right) - \xi\varphi_{rd}\right) = -k_2 e_2 \end{cases} \tag{II.8}$$

We consider i_{ds} and i_{qs} as virtual commands of our first subsystem by requesting:

$$\begin{cases} i_{qs1} + i_{qs2} = i^*_{qs1} + i^*_{qs2} = i^*_{qs} \\ i_{ds1} + i_{ds2} = i^*_{ds1} + i^*_{ds2} = i^*_{ds} \end{cases} \tag{II.9}$$

Accordingly, the virtual order components are obtained as follows:

$$\begin{cases} i_{qs1}^{*} + i_{qs2}^{*} = \dfrac{1}{P\mu\varphi_{rd}^{*}}\left[J\left(k_1 e_1 + \dot{\Omega}_{mec}^{*} \right) + T_r + k_f \Omega_{mec} \right] \\ i_{ds1}^{*} + i_{ds2}^{*} = \dfrac{1}{\mu}\left[k_2 e_2 + \dot{\varphi}_{rd}^{*} + \xi\varphi_{rd} \right] \end{cases} \tag{II.10}$$

II.2.2.2 Step 2: Current loop

By definiting the expressions of the following errors and their derivatives:

$$\begin{cases} e_3 = i_{qs1}^{*} - i_{qs1} \\ e_4 = i_{ds1}^{*} - i_{ds1} \\ e_5 = i_{qs2}^{*} - i_{qs2} \\ e_6 = i_{ds2}^{*} - i_{ds2} \end{cases} \tag{II.11}$$

$$\begin{cases} \dot{e}_3 = \dot{i}_{qs1}^{*} - \dot{i}_{qs1} \\ \dot{e}_4 = \dot{i}_{ds1}^{*} - \dot{i}_{ds1} \\ \dot{e}_5 = \dot{i}_{qs2}^{*} - \dot{i}_{qs2} \\ \dot{e}_6 = \dot{i}_{ds2}^{*} - \dot{i}_{ds2} \end{cases} \tag{II.12}$$

Considering equation (I.116), equation (II.12) yields:

$$\begin{cases} \dot{e}_3 = \dot{i}_{qs1}^{*} - \dfrac{1}{L_{s1}}\left\{ v_{qs1} - R_{s1} i_{qs1} - \omega_s^{*}\left(L_{s1} i_{ds1} + \varphi_{rd}^{*} \right) \right\} \\ \dot{e}_4 = \dot{i}_{ds1}^{*} - \dfrac{1}{L_{s1}}\left\{ v_{ds1} - R_{s1} i_{ds1} + \omega_s^{*}\left(L_{s1} i_{qs1} + \tau_r \varphi_{rd}^{*} \omega_{sl}^{*} \right) \right\} \\ \dot{e}_5 = \dot{i}_{qs2}^{*} - \dfrac{1}{L_{s2}}\left\{ v_{qs2} - R_{s2} i_{qs2} - \omega_s^{*}\left(L_{s2} i_{ds2} + \varphi_{rd}^{*} \right) \right\} \\ \dot{e}_6 = \dot{i}_{ds2}^{*} - \dfrac{1}{L_{s2}}\left\{ v_{ds2} - R_{s2} i_{ds2} + \omega_s^{*}\left(L_{s2} i_{qs2} + \tau_r \varphi_{rd}^{*} \omega_{sl}^{*} \right) \right\} \end{cases} \tag{II.13}$$

The final function of Lyapunov and its corresponding derivative can obtaind as:

$$v_2 = \frac{1}{2}\left(e_1^2 + e_2^2 + e_3^2 + e_4^2 + e_5^2 + e_6^2 \right) \tag{II.14}$$

$$\dot{v}_2 = e_1 \dot{e}_1 + e_2 \dot{e}_2 + e_3 \dot{e}_3 + e_4 \dot{e}_4 + e_5 \dot{e}_5 + e_6 \dot{e}_6 \tag{II.15}$$

Applying the theory of Lyapunov's stability, i.e., $\dot{v}_2$ must be negative ($\dot{v}_2 < 0$), we consider:

$$\begin{cases} \dot{e}_3 = -k_3 e_3 \\ \dot{e}_4 = -k_4 e_4 \\ \dot{e}_5 = -k_5 e_5 \\ \dot{e}_6 = -k_6 e_6 \end{cases} \tag{II.16}$$

where k_3, k_4, k_5, and k_6 are gains with positive values.

Considering equations (II.13) and (II.16), the actual control can be formulated as follows:

$$\begin{cases} v_{qs1}^* = L_{s1}\left[k_3 e_3 - \rho_1 + \dot{i}_{qs1}^*\right] \\ v_{ds1}^* = L_{s1}\left[k_4 e_4 - \rho_2 + \dot{i}_{ds1}^*\right] \\ v_{qs2}^* = L_{s2}\left[k_5 e_5 - \rho_3 + \dot{i}_{qs2}^*\right] \\ v_{ds2}^* = L_{s2}\left[k_6 e_6 - \rho_4 + \dot{i}_{ds2}^*\right] \end{cases} \tag{II.17}$$

with:

$$\begin{cases} \rho_1 = \dfrac{1}{L_{s1}}\left\{-R_{s1} i_{qs1} - \omega_s^* (L_{s1} i_{ds1} + \varphi_{rd}^*)\right\} \\ \rho_2 = \dfrac{1}{L_{s1}}\left\{-R_{s1} i_{ds1} + \omega_s^* (L_{s1} i_{qs1} + \tau_r \varphi_{rd}^* \omega_{sl}^*)\right\} \\ \rho_3 = \dfrac{1}{L_{s2}}\left\{-R_{s2} i_{qs2} - \omega_s^* (L_{s2} i_{ds2} + \varphi_{rd}^*)\right\} \\ \rho_4 = \dfrac{1}{L_{s2}}\left\{-R_{s2} i_{ds2} + \omega_s^* (L_{s2} i_{qs2} + \tau_r \varphi_{rd}^* \omega_{sl}^*)\right\} \end{cases} \tag{II.18}$$

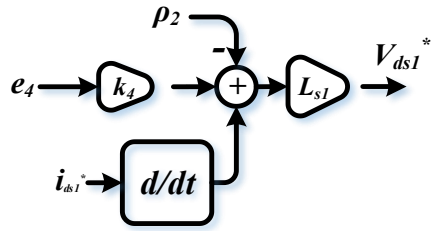

Figure II.2- BS controller-based current (i_{ds1}) control loop

Note that the proper operation of the WT-DSIG system is ensured only when chosing optimally the BS gains (i.e., k_1, k_2, k_3, k_4, k_5, and k_6). Thus, the SABO optimization algorithm is applied to reach optimal tunnig of the BS controller parameters.

II.3 SABO optimization algorithm

This section discusses the principle of operation and modeling of the adopted SABO.

II.3.1 Initialization

In optimization problems, the search space defines the domain containing the optimal solution. The dimension of this space corresponds to the number of variables in the problem, forming a subset of the search space. Each search agent (or population member) selects values for the decision variables depending on its position within the search space. Mathematically, every search agent is represented as a decision variable vector. The entire set of these agents constitutes the algorithm's population, which is numerically represented by a matrix (II.19). The initial positions of the search agents are randomly assigned within the search space, as described by Equation (II.20) [42].

$$X = \begin{bmatrix} X_1 \\ . \\ . \\ . \\ X_i \\ . \\ . \\ . \\ X_N \end{bmatrix}_{N\times m} = \begin{bmatrix} x_{1,1} & . & . & . & x_{1,d} & . & . & . & x_{1,m} \\ . & . & & & . & & & . & . \\ . & & . & & . & & . & & . \\ . & & & . & . & . & & & . \\ x_{i,1} & . & . & . & x_{i,d} & . & . & . & x_{i,m} \\ . & & & . & . & . & & & . \\ . & & . & & . & & . & & . \\ . & . & & & . & & & . & . \\ x_{N,1} & . & . & . & x_{N,d} & . & . & . & x_{N,m} \end{bmatrix}_{N\times m} \tag{II.19}$$

$$x_{i,d} = lb_d + r_{i,d}.\left(ub_d - lb_d\right), i = 1,...,N, d = 1,...,m, \tag{II.20}$$

where m and N represent the problem variables and search members numbers, respectively, $r_{i,d}$ is a random integer number between [0, 1], while ub_d and lb_d denote the upper and lower bounds of the d^{th} variable. A key element of the SABO algorithm is its population matrix, X, which includes the positions of all search agents, with corresponding to the i^{th} agent (population member).

Each search agent corresponds to a potential solution, providing specific values for the decision variables. The objective function is then evaluated for every search agent, and these computed values are stored in a vector $\vec{F}$, as defined in Equation (II.21). The evaluation depends on the values assigned to the decision variables by each population member. Consequently, the size of $\vec{F}$ matches the population size NN, meaning the vector contains exactly N elements—one for each search agent.

F_i defines the evaluated value of the objective function for the i^{th} search member; while $\vec{F}$ is a vector involves the values of the objective function.

The evaluated values of the objective function act as key indicators for measuring the performance of each search agent. The best value corresponds to the most optimal solution found, while the worst value represents the least effective search agent. The algorithm continuously identifies and retains the best-performing agent until the final iteration is reached.

$$\vec{F} = \begin{bmatrix} F_1 \\ . \\ . \\ . \\ F_i \\ . \\ . \\ . \\ F_N \end{bmatrix}_{N\times 1} = \begin{bmatrix} F(X_1) \\ . \\ . \\ . \\ F(X_i) \\ . \\ . \\ . \\ F(X_N) \end{bmatrix}_{N\times m} \tag{II.21}$$

II.3.2 Modeling of SABO

The SABO algorithm is founded on three key mathematical concepts: (i) averaging, (ii) changes in search agent positions, and (iii) the sign of the error between two objective function values. Unlike traditional approaches that depend only on the best or worst agent to update positions, SABO calculates the arithmetic mean of all search agents from the current iteration t to form the population for the next iteration ($t + 1$). However, SABO introduces a distinct method for computing this mean by employing a specialized operation called *v-subtraction*, defined as:

$$SA -_v SB = sign\left(F(SA) - F(SB)\right)\left(SA - \vec{v} * SB\right) \tag{II.22}$$

Here, $\vec{v}$ is an m-dimensional vector with elements randomly selected from {1,2}, and sign(·) is the signum function. The objective function values for agents SA and SB are $F(SA)$ and $F(SB)$, respectively. The operator '$*$' denotes the Hadamard product, which multiplies corresponding elements of the input vectors. Due to the random nature of $\vec{v}$, the *v-subtraction* produces points within a subset of the search space, with a total of 2^{m+1} possible outcomes.

In SABO, the displacement of each search agent X_i is determined by the arithmetic mean of the *v-subtractions* between X_i and every other agent X_j(j=1,2,…,N). This leads to the new position update rule:

$$X_i^{new} = X_i + \vec{r}_i * \frac{1}{N}\sum_{j=1}^{N}\left(X_i -_v X_j\right), i = 1,2,...,N, \tag{II.23}$$

Here, $\vec{r}_i$ is an m-dimensional vector with components drawn from a normal distribution in [0,1]. The proposed position X_i^{new} is accepted only if it improves the objective function value, as per:

$$X_i = \begin{cases} X_i^{new}, & F_i^{new} < F_i; \\ X_i, & else, \end{cases} \tag{II.24}$$

where F_i and F_i^{new} represent the search agents X_i and X_i^{new} respective objective function values.

Rewriting the position update as $X_i^{new} = X_i + \vec{r}_i * \vec{M}_i$, we can interpret it as a motion equation, where the direction of movement is governed by the mean vector $\vec{M}_i = \frac{1}{N}\sum_{j=1}^{N}\left(X_i - X_j\right) = \frac{1}{N}\sum_{j=1}^{N}\vec{\chi}_{ij}$, with $\vec{\chi}_{ij}$ representing the *v-subtraction* $X_i -_v X_j$.

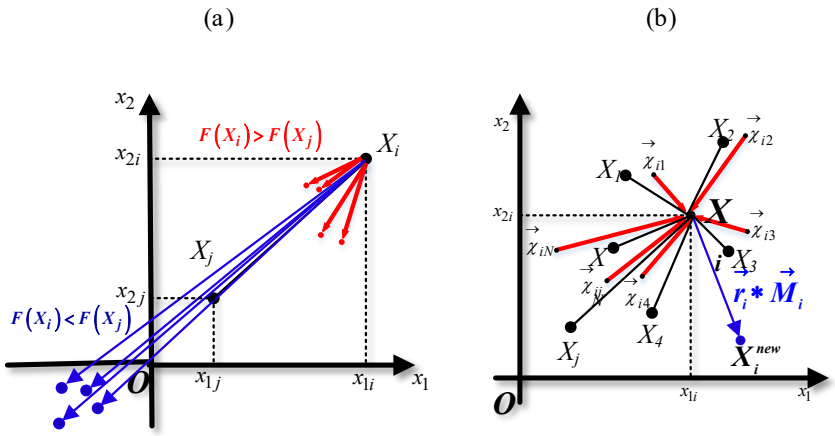

Figures II.3 Diagram illustrating the exploration phase for $m = 2$, showing (a) 'v-subtractions' and (b) 'arithmetic mean of the v-subtractions'

This mechanism efficiently balances *exploration* (via *v-subtraction*) and *exploitation* (via the mean vector) to identify optimal regions in the search space, as illustrated in **Figures II.3 (a) and (b)**.

II.3.3 Iteration Process and Flowchart

Once all search agents have been updated, the algorithm completes its first iteration. It then proceeds to the next iteration using the newly computed positions of the search agents and their corresponding objective function values. In each cycle, the best candidate solution found so far is retained as the optimal search agent. The update process for the search agents—as defined in steps (II.19) to (II.24)—continues until the final iteration is reached. The best solution obtained across all iterations is selected as the final output. **Figure II.4** illustrates the flowchart outlining the implementation steps of the SABO algorithm.

II.3.4 Optimization algorithms for comparison study

To analyze the performance quality of the SABO in optimization tasks referred to [8], the results that were obtained from the proposed approach have been compared with twelve well-known metaheuristic algorithms: Genetic Algorithm (GA), Particle Swarm Optimization (PSO), Gravitational Search Algorithm (GSA), Teaching-Learning-Based Optimization (TLBO), Gray Wolf Optimizer (GWO), Multi-Verse Optimizer (MVO), Whale Optimization Algorithm (WOA), Marine Predators Algorithm (MPA), Tree-Seed Algorithm (TSA), Reptile Search Algorithm (RSA), Water Strider Optimization (WSO), and African Vultures Optimization Algorithm (AVOA).

Based on the obtained results, the proposed SABO, with a high exploitation ability, provided the global optimal. Additionally, the SABO is the best optimizer compared to this metaheuristic algorithm.

II.3.5 Implementation of SABO for BS Parameter Optimization

The SABO algorithm is employed to optimize the parameters of the BS controller. The objective function for minimization is formulated as the sum of Integral Time Absolute Errors (ITAE)

between the actual values and reference values for:

- Rotational speed
- Magnetic flux
- Stator currents

This objective function is mathematically expressed in equation (II.25). Key optimization parameters including population size, iteration count, and variable boundaries are specified in **Table II.1.**

$$\begin{aligned}\min(Obj) = &\int_0^t t.\left(\Omega_{mec}^* - \Omega_{mec}\right)\,dt + \int_0^t t.\left(\phi_{rd}^* - \phi_{rd}\right)\,dt + \frac{1}{w_1}\int_0^t t.\left(i_{ds1}^* - i_{ds1}\right)\,dt \\ &+ \frac{1}{w_2}\int_0^t t.\left(i_{qs1}^* - i_{qs1}\right)\,dt + \frac{1}{w_3}\int_0^t t.\left(i_{ds2}^* - i_{ds2}\right)\,dt + \frac{1}{w_4}\int_0^t t.\left(i_{qs2}^* - i_{qs2}\right)\,dt\end{aligned} \tag{II.25}$$

Where w_1-w_4 are the weights allowing the adjustment of the current errors to be close to each other, and the speed and flux errors. The weight values are determined through manual tuning (Trial and Error) by choosing w_1-w_4 based on error values during simulation. The values of this weight are found as: $w_1 = 90$, $w_2 = 50$, $w_3 = 70$, $w_4 = 60$.

The specific BS controller parameters targeted for optimization are:

- Gain coefficients k_1 through k_6, corresponding to:
  - Speed control
  - Flux regulation
  - Stator current control

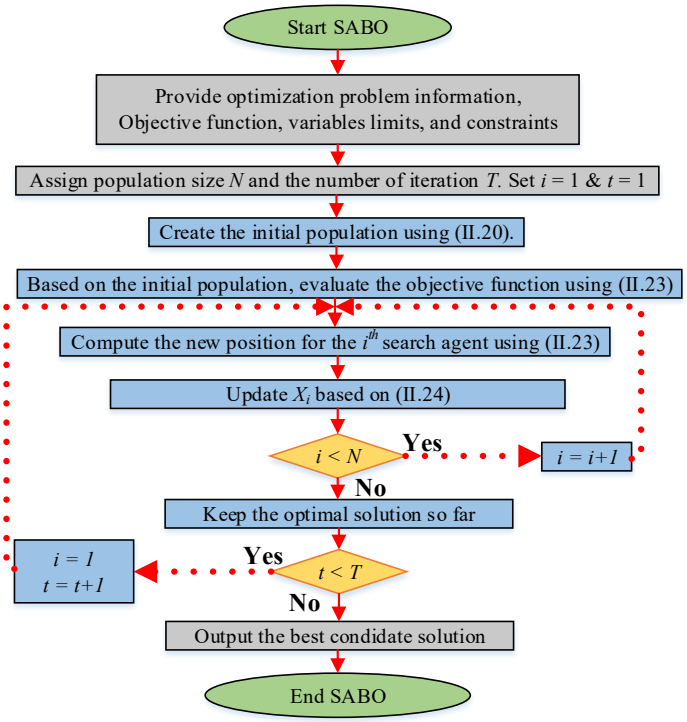

Figure II.4 Flowchart of the SABO algorithm

Table II.1– SABO Parameters

Parameters	Controller	Values
Variables number	BS	3; [k_1 k_2 $k_{3\text{-}6}$]
Population size		15
Maximum iteration		5
Lower bound		[1000 1000 20000]
Upper bound		[10000 8000 60000]

Table II.2–BS controller gains and performance of the tuned controllers

Tuning method	Controller	Gains			ITAEs		
		Rotor speed control	Rotor flux control	Stators currents control	$\Delta e_{\Omega mec}$	$\Delta e_{\phi rd}$	Δe_{ids1}
Trial and Error	BS	$k_1 = 30$	$k_2 = 5$	$k_{3\text{-}6} = 70000$	0.3064	0.2885	9.9842
SABO	BS	$k_1 = 2.2754e^3$	$k_2 = 1.1735e^3$	$k_{3\text{-}6} = 5.0747e^4$	0.0211	0.0355	0.0798

Table II.3 Time-integral performance criteria and THD for BS controllers

Tuning method		BS						THD_{BS}%
		Ω_{mec}	ϕ_{rd}	i_{ds1}	i_{qs1}	i_{ds2}	i_{qs2}	i_{as1}
Trial-error	ISE	15	0.3	$2e^3$	$1e^4$	$2e^3$	$1e^4$	47.77%
	IAE	5	0.4	300	250	300	250	
SABO	ISE	0.6	0.17	$1e^3$	$5e^3$	$1e^3$	$5e^3$	39.68%
	IAE	0.3	0.15	200	100	200	100	

The SABO algorithm was implemented in MATLAB simulations to determine the optimal BS controller parameters through offline computation. This approach systematically accounts for the interdependencies between different controller components. The complete set of system parameters employed in these simulations is provided in **Appendix D**. For comparative analysis, **Table II.2** presents the optimized BS gain values obtained through SABO alongside those derived using conventional trial-and-error tuning methods.

II.4 Simulation results and Discussion

The results, which illustrate the performance of the specified controllers under the given wind speed conditions, are presented in **Figs II.(5-10)**. These **figures** display the rotor speed, electromagnetic torque, direct rotor flux, direct and quadrature stator #1 current, and a-phase currents of both stators (#1 and #2), along with their reference values for each controller. They also include the wind profile and detailed views of both transient and steady-state responses. Moreover, **Table II.3** provides the THD for each controller, as well as the integral performance metrics, IAE and ISE.

From these results and **Table II.3**, the main conclusions are:

- Each of the designed controllers ensures constant rotor flux while maintaining precise tracking of the wind profile by the speed, electromagnetic torque, and stator currents of the DSIG.
- As evidenced by **Table II.3** and **Figs II.(7–10)**, the enhanced BS controller surpasses the standard BS regulator in both dynamic and steady-state performance, achieving the smallest IAE and ISE values. Notably, the optimized design ensures close alignment

between the actual speed, electromagnetic torque, flux, and stator #1 current *dq* components and their reference averages **Figs II.10(b)-(f)**, with significantly reduced steady-state oscillations. In contrast, **Figs II.9(b)-(d)** reveal pronounced fluctuations and steady-state deviations in these same variables when using conventional control methods.

- **Figures II.7** and **II.8** reveal that the optimized BS controller achieves faster transient performance with a settling time (t_s) of approximately 0.17s, compared to about 0.4s for the conventional BS controller.
- Similarly, the optimized BS controller exhibits superior performance compared to conventional BS control, featuring faster dynamic response, reduced steady-state oscillations, and lower IAE/ISE error values. As **Figs II.9-II.10** illustrate, the system achieves exceptional reference tracking with a settling time of approximately 0.1s for rotor speed, electromagnetic torque, flux, and stator #1 current *dq* components.
- Comparative analysis reveals the optimized BS controller's dual advantages: (i) enhanced transient performance with faster reaction times and (ii) superior steady-state operation with minimized ripples and errors, outperforming the standard BS controller in both operational regimes.
- The optimized regulators demonstrate significant harmonic distortion reduction, achieving 39.68% THD compared to 47.77% for conventional BS regulators. This improvement yields cleaner sinusoidal waveforms in the stator phase currents.

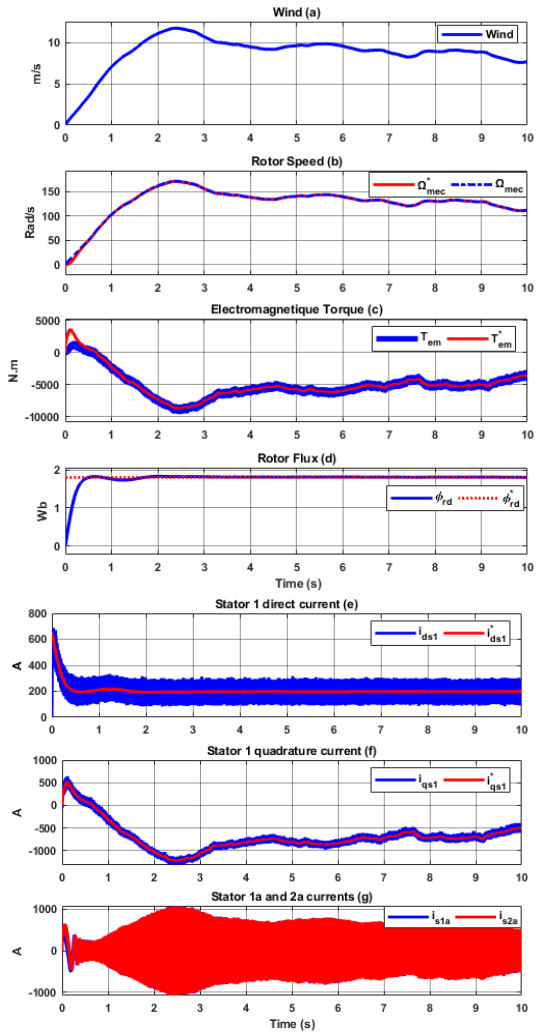

Figure II.5- Matlab results for variable wind with the conventional BS regulator

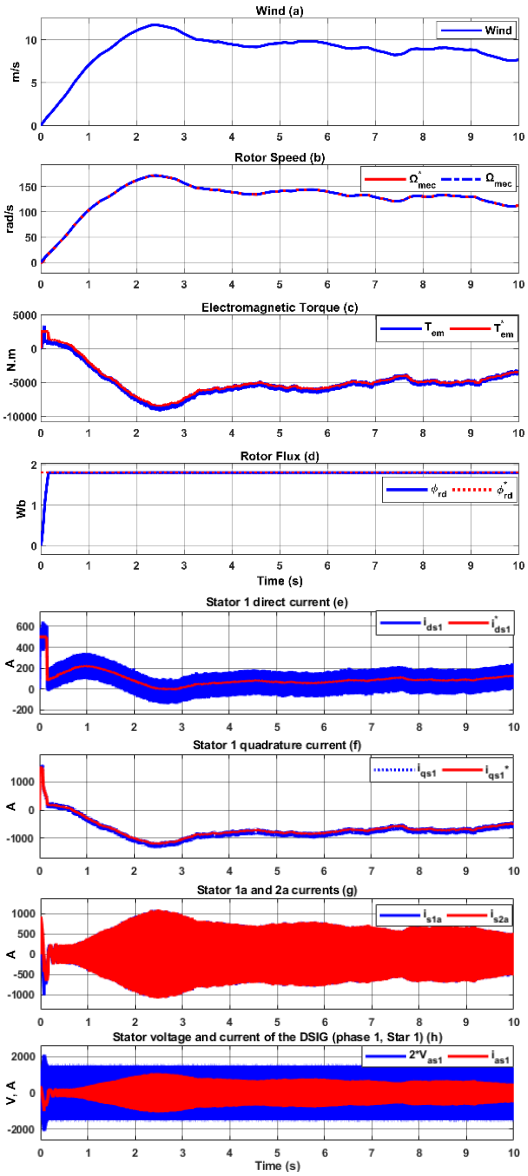

Figure II.6- Matlab results for variable wind with the optimized BS regulator

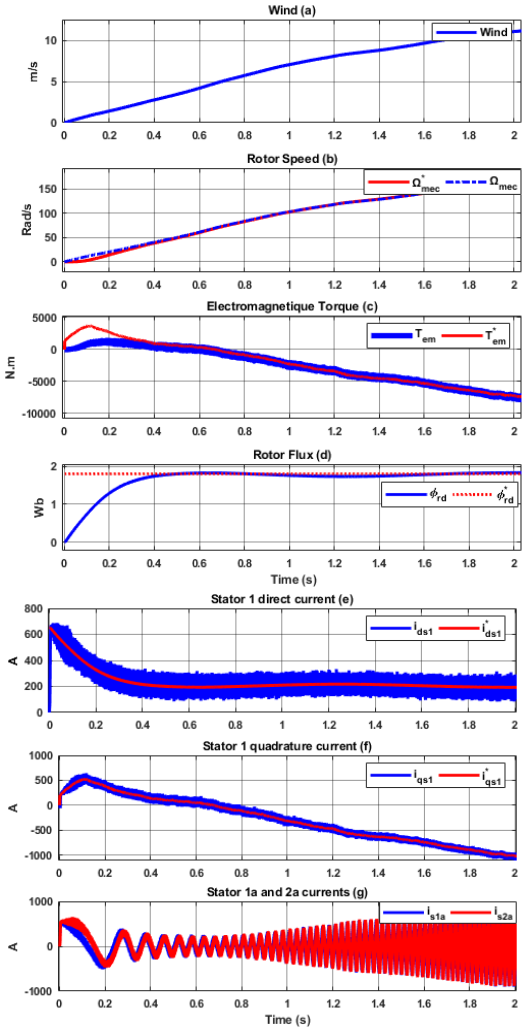

Figure II.7- Zoom in transient response matlab results with the conventional BS regulator

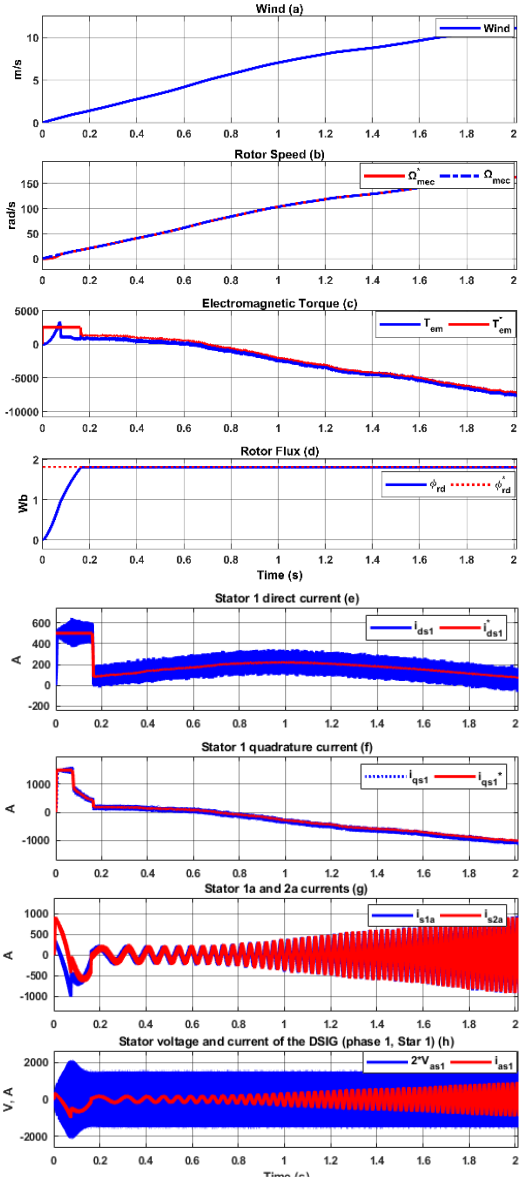

Figure II.8- Zoom in transient response matlab results with the optimized BS regulator

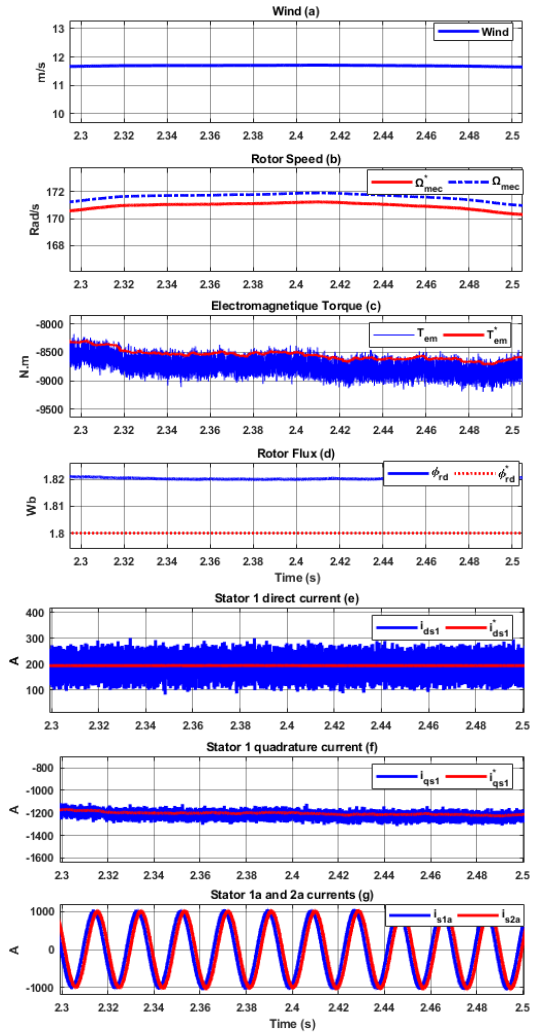

Figure II.9- Steady-state performance conventional BS: Matlab results Zoom in

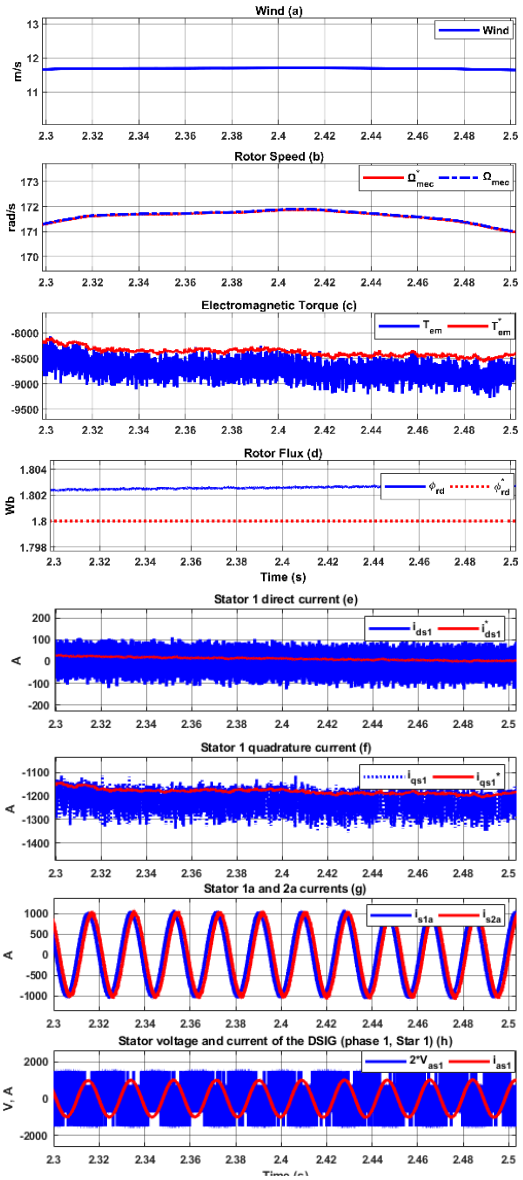

Figure II.10- Steady-state performance optimized BS: Matlab results Zoom in

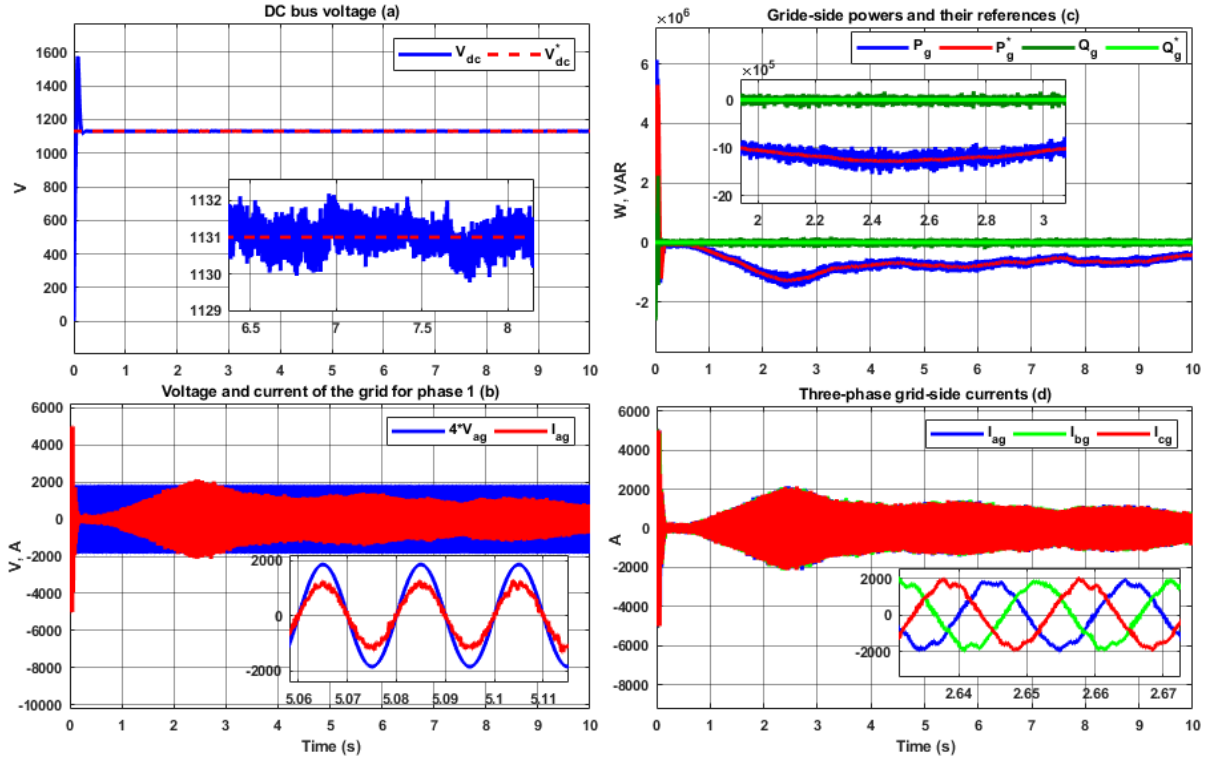

Figure II.11- Grid-side BS results

II.5 Conclusion

This chapter presented an optimized BS controller for a WT-DSIG. The tuning of BS controllers is crucial for ensuring system stability and performance, but existing research lacks a comprehensive tuning method. To address this, the chapter introduced a novel tuning approach using the SABO.

The BS control strategy was explained in detail, highlighting its ability to systematically stabilize nonlinear systems through Lyapunov-based recursive design. The proposed control scheme focused on regulating rotor speed, flux, and stator currents using optimally tuned BS controllers.

Simulation results demonstrated the superiority of the SABO-tuned BS controller over conventional trial-and-error methods. The optimized controller exhibited faster transient response, reduced steady-state errors, and lower THD. Specifically, the SABO-based controller achieved significantly improved time-integral performance criteria, with reduced IAE and ISE.

Overall, the results confirmed that the proposed SABO-optimized BS controller enhances both dynamic and steady-state performance, improving the efficiency and reliability of WT-DSIG systems.

Chapter III. Optimal first, second, and high-order sliding mode control for DSIG-based wind turbine system

Chapter III. Optimal first, second, and high-order sliding mode control for DSIG-based wind turbine system

III.1 Introduction

Implementing advanced control strategies with optimized parameters presents significant challenges in achieving precise tracking and stable operation for WT-DSIG systems. This chapter introduces a novel tuning approach utilizing an Intelligent-in-Time Logic Algorithm (ILA) to optimally determine HOSMC controller parameters. The developed FOC scheme incorporating these optimized HOSMC controllers demonstrates enhanced performance in WT-DSIG applications. The proposed methodology provides an efficient solution for parameter optimization, significantly improving system stability and control effectiveness. Leveraging the IbI metaheuristic stochastic algorithm, this approach simultaneously optimizes gains for flux, speed, and current control loops, outperforming conventional techniques.

III.2 First-order sliding mode control (FOSMC)

III.2.1 Brief history of sliding mode control

A first-order sliding mode vector control (FOSMC) is presented in this section. This control method is nonlinear. Its success in controlling electric motors is due to its robustness, ease of implementation, and ability to reject disturbances. The sliding mode is a specific operating mode of variable structure systems. The theory of these systems was initially studied and developed in the former Soviet Union, first by Professor *Emelyanov* [56], and later by other collaborators such as *Utkin*, based on the results of studies by the mathematician *Filippov* on differential equations with discontinuous right-hand sides.

However, the use of this control method was long limited by oscillations caused by the phenomenon of chattering, which requires significant oscillations in the control element and the need to use the regulated quantity (sometimes inaccessible) along with a number of its derivatives, depending on the order of the system [57], [58]. This control strategy has been applied to asynchronous machines with speed sensors (*Sabanovic*, 1981), (*Soto*, 1992), (*Utkin*, 1993), and (*Utkin*, 1999). The basic idea of sliding mode control is to force the system state, via a discontinuous control, to evolve in finite time on a sliding surface.

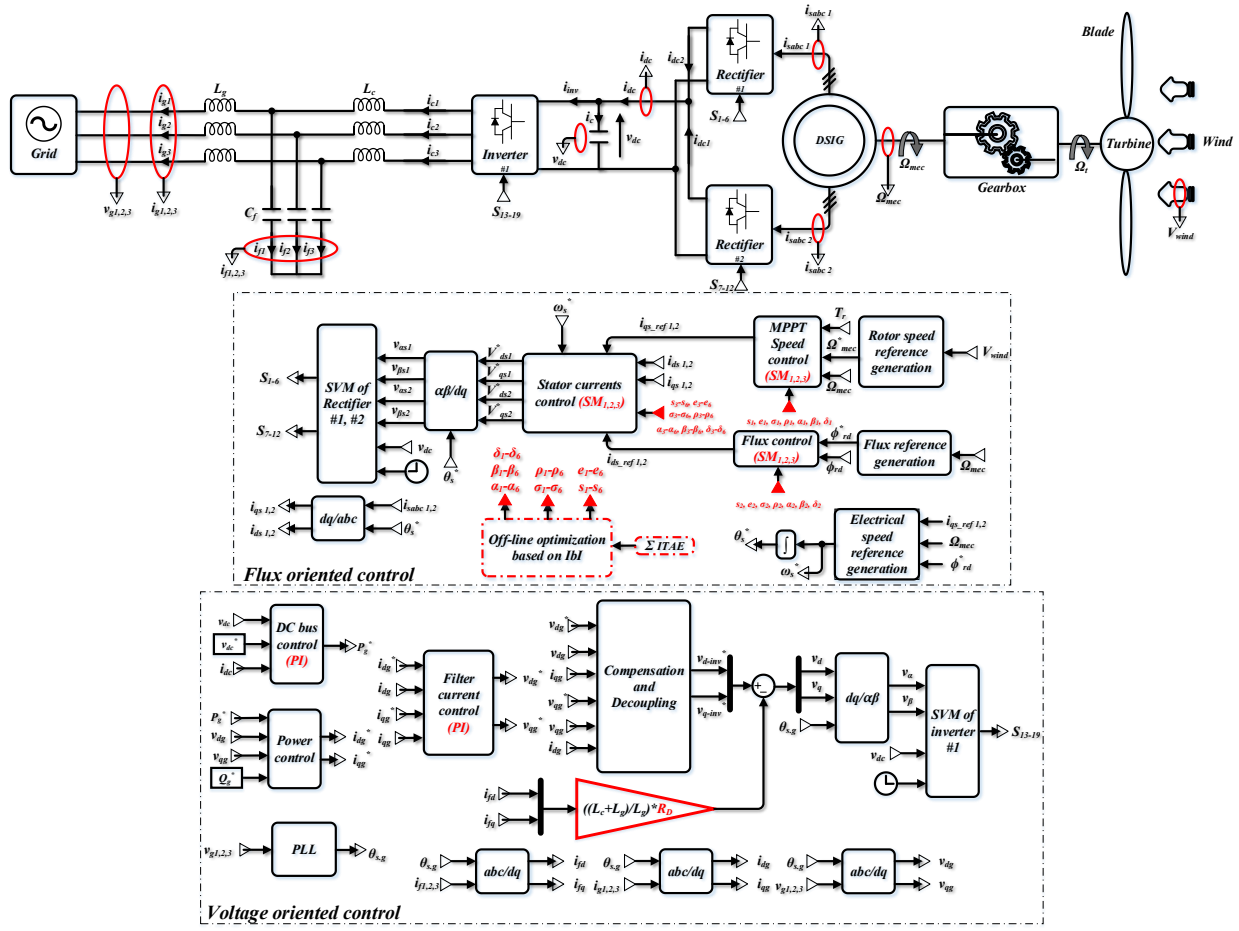

Figure III.1- WT-DSIG system with its designed SM controller scheme

The initial work on variable structure systems was proposed in the former Soviet Union by Anosov [59], [60], *Tzypkin* [61], and *Emelyanov* [56], followed by other collaborators like Utkin, building on the results of studies by the mathematician *Filippov* on differential equations with discontinuous right-hand sides. Subsequently, this work was further developed elsewhere, notably in the United States by *Slotine* and in Japan by Tong, *Harashima*, and *Hashimoto* [62]. These studies experienced a resurgence in the late 1970s when Utkin introduced sliding mode theory as a nonlinear control technique.

We will present the sliding mode vector control based on the concept of equivalent and discontinuous control. The equivalent component of the control enforces ideal sliding motion, meaning a system without uncertainties. It is achieved by ensuring the invariance conditions of the sliding surface (S).

In this work, we present the general concept of sliding mode control and apply this control technique to a Dual-Stator Induction Generator (DSIG) integrated into a wind energy system. The synthesis of control laws is based on the model obtained after decoupling using the vector control method.

III.2.2 Principle of sliding mode control

The term "variable structure system" arises due to the particular structure of the system or regulator used, where this structure changes discontinuously between two or more configurations.

In variable structure systems with sliding mode, the state trajectory is brought toward a surface (hyperplane) and, with the help of the switching law, is forced to remain in the vicinity of this surface. This surface is referred to as the sliding surface, and the motion along it is called sliding motion.

The control of such systems in sliding mode generally consists of three distinct modes **(Figure III.2)**:

- **The non-sliding mode (reaching mode), also known as the access mode or convergence mode (CM):** During this phase, the regulated variable moves from any initial point in the phase plane and tends toward the switching surface $S(x,y) = 0$. This mode is characterized by the control law and the convergence criterion.
- **The sliding mode:** During this phase, the state variable reaches the sliding surface and tends toward the origin of the phase plane. The dynamics in this mode are characterized by the choice of the sliding surface $S(x,y)$.
- **The steady-state mode (SSM):** The phase trajectory, starting from any initial condition, reaches the switching surface in finite time (non-sliding mode) and then asymptotically tends toward the equilibrium point with dynamics defined by the sliding mode [63].

The three operating modes are illustrated in the following figure:

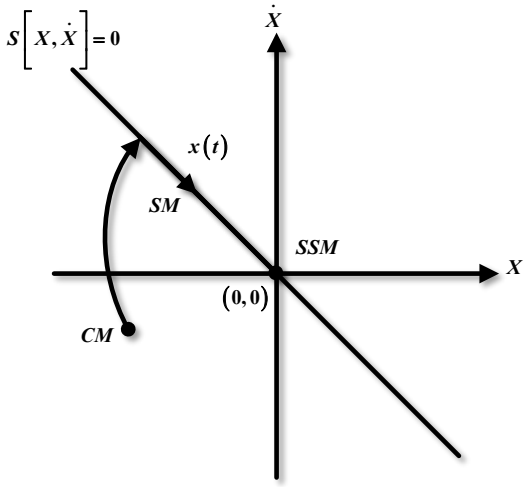

Figure III.2 Operating modes in the phase plane

III.2.3 Design of the sliding mode control algorithm

The sliding mode control design systematically addresses issues of stability and good performance. Often, it is preferable to specify the system's dynamics during the convergence mode. In this case, the structure of a controller consists of two parts: a continuous part, representing the system dynamics during the sliding mode, and a discontinuous part, representing the system dynamics during the convergence mode. The second part is crucial in nonlinear control, as it aims to eliminate the effects of model imprecision and disturbances.

The design of this control method can be divided into three complementary steps defined as:

- Selection of the sliding surfaces;
- Definition of the conditions for the existence and convergence of the sliding regime;
- Determination of the control law.

II.2.3.1 FOSMC design methodology

The FOSMC design process begins with the state-space representation of the system:

$$\left[\dot{X}\right] = [M][X] + [N][U] \tag{III.1}$$

Where $[X] \in \Re^n$ denotes the state vector, $[U] \in \Re^m$ represents the control input vector, and $[M]$, $[N]$ are system parameter matrices.

The control design procedure begins with the selection of switching surfaces *S(x),* where the number of surfaces typically equals the dimension of the control vector [U] [64]. A general switching surface function ensuring convergence of the state variable x to its reference x^* is proposed:

$$S(x) = \left(\frac{d}{dt} + \gamma\right)^{r-1} e(x) \tag{III.2}$$

where γ is a strictly positive constant; r is the smallest positive integer such that $\partial \dot{S}/\partial t \neq 0$: ensure controllability; $e(x) = x^* - x$ is the error variable.

The next step involves deriving the control law that satisfies sliding mode existence and reachability conditions [58], [65]:

$$S(x)\dot{S}(x) < 0 \tag{III.3}$$

System stability is guaranteed when sliding mode occurs on the sliding surface. The control solution consists of:

$$U_c = U_{eq} + U_n \tag{III.4}$$

where U_{eq} denotes the equivalent control, providing feedback linearization through:

$$\dot{S}(x) = 0 \Leftrightarrow \frac{\partial S}{\partial X}\{[M][X] + [N]U_{eq}\} + \frac{\partial S}{\partial X}[N]U_n = 0 \tag{III.5}$$

During sliding mode ($U_n = 0$), U_{eq} becomes:

$$U_{eq} = -\left\{\frac{\partial S}{\partial X}[N]\right\}^{-1}\left\{\frac{\partial S}{\partial X}[M][X]\right\} \tag{III.6}$$

with:

$$\frac{\partial S}{\partial X}[N] \neq 0 \tag{III.7}$$

During convergence mode ($U_n \neq 0$), substituting (III.6) into (III.5) yields:

$$\dot{S}(x) = \frac{\partial S}{\partial X}[N]U_n \tag{III.8}$$

Inserting (III.8) into (III.3) gives:

$$S(x)\frac{\partial S}{\partial X}[N]U_n < 0 \tag{III.9}$$

The state trajectory converges to $S(x) = 0$ when using the typical relay control form:

$$U_n = s_x sign\left(S(x)\right) \tag{III.10}$$

where k_x is constant and *Sign(S(x))* is defined as:

$$sign\left(S\left(x\right)\right)=\begin{cases}-1 & \text{if } S\left(x\right)<0\\ 1 & \text{if } S\left(x\right)>0\end{cases} \tag{III.11}$$

To mitigate chattering effects, U $U_{n\ \mathrm{n}}$ is modified as:

$$U_n = s_x \frac{S\left(x\right)}{\left|S\left(x\right)\right|+\xi_x} \tag{III.12}$$

where ξ_x is a small positive scalar.

a. Application of FOSMC for a DSIG: The proposed control architecture, illustrated in **Figure III.1**, employs a six-surface cascade configuration. The outer control loops manage flux φ_{rd} and rotational speed Ω_{mec}, whereas the inner loops govern the stator current components i_{ds1}, i_{qs1}, i_{ds2}, and i_{qs2}.

The six first-order sliding surfaces are defined as:

$$\begin{cases}S\left(\Omega_{mec}\right)=\Omega_{mec}^{*}-\Omega_{mec}\\ S\left(\varphi_{rd}\right)=\varphi_{rd}^{*}-\varphi_{rd}\\ S\left(i_{ds1}\right)=i_{ds1}^{*}-i_{ds1}\\ S\left(i_{qs1}\right)=i_{qs1}^{*}-i_{qs1}\\ S\left(i_{ds2}\right)=i_{ds2}^{*}-i_{ds2}\\ S\left(i_{qs2}\right)=i_{qs2}^{*}-i_{qs2}\end{cases} \tag{III.13}$$

Based on (II.3), (III.4), and (III.12), the control laws are derived as follows:

- For the speed regulator:

$$S\left(\Omega_{mec}\right)\dot{S}\left(\Omega_{mec}\right)<0\Rightarrow i_{qs}^{*}=i_{qs\_eq}+i_{qs\_n} \tag{III.14}$$

with

$$i^{*}_{qs}=i^{*}_{qs1}+i^{*}_{qs2} \tag{III.15}$$

$$i_{qs\_eq}=\frac{J}{P^2}\frac{L_r+L_m}{L_m\varphi_{rd}^{*}}\left[\dot{\Omega}_{mec}^{*}+\frac{k_f}{J}\Omega_{mec}+\frac{P}{J}T_g\right] \tag{III.16}$$

$$i_{qs\_n}=s_1\frac{S\left(\Omega_{mec}\right)}{\left|S\left(\Omega_{mec}\right)\right|+e_1} \tag{III.17}$$

- For the flux regulator:

$$S\left(\varphi_{rd}\right)\dot{S}\left(\varphi_{rd}\right)<0\Rightarrow i_{ds}^{*}=i_{ds\_eq}+i_{ds\_n} \tag{III.18}$$

with

$$i^{*}_{ds}=i^{*}_{ds1}+i^{*}_{ds2} \tag{III.19}$$

$$i_{ds\_eq} = \frac{L_r + L_m}{R_r L_m}\left[\dot{\phi}_{rd}^{*} + \frac{R_r}{L_r + L_m}\phi_{rd}\right] \tag{III.20}$$

$$i_{ds\_n} = s_2 \frac{S(\phi_{rd})}{|S(\phi_{rd})| + e_2} \tag{III.21}$$

Assuming identical reference currents for both stators, i.e., $i_{ds1}^{*} = i_{ds2}^{*}$ and $i_{qs1}^{*} = i_{qs2}^{*}$.

- For the stator current regulators:

$$S(i_{ds1})\dot{S}(i_{ds1}) < 0 \Rightarrow v_{ds1}^{*} = v_{ds1\_eq} + v_{ds1\_n} \tag{III.22}$$

$$S(i_{qs1})\dot{S}(i_{qs1}) < 0 \Rightarrow v_{qs1}^{*} = v_{qs1\_eq} + v_{qs1\_n} \tag{III.23}$$

$$S(i_{ds2})\dot{S}(i_{ds2}) < 0 \Rightarrow v_{ds2}^{*} = v_{ds2\_eq} + v_{ds2\_n} \tag{III.24}$$

$$S(i_{qs2})\dot{S}(i_{qs2}) < 0 \Rightarrow v_{qs2}^{*} = v_{qs2\_eq} + v_{qs2\_n} \tag{III.25}$$

with

$$v_{ds1\_eq} = R_{s1} i_{ds1} + L_{s1}\dot{i}_{ds1}^{*} - \omega_s^{*}(L_{s1} i_{qs1} + \tau_r \varphi_{rd}^{*} \omega_{sl}^{*}) \tag{III.26}$$

$$v_{qs1\_eq} = R_{s1} i_{qs1} + L_{s1}\dot{i}_{qs1}^{*} + \omega_s^{*}(L_{s1} i_{ds1} + \varphi_{rd}^{*}) \tag{III.27}$$

$$v_{ds2\_eq} = R_{s2} i_{ds2} + L_{s2}\dot{i}_{ds2}^{*} - \omega_s^{*}(L_{s2} i_{qs2} + \tau_r \varphi_{rd}^{*} \omega_{sl}^{*}) \tag{III.28}$$

$$v_{qs2\_eq} = R_{s2} i_{qs2} + L_{s2}\dot{i}_{qs2}^{*} + \omega_s^{*}(L_{s2} i_{ds2} + \varphi_{rd}^{*}) \tag{III.29}$$

And:

$$v_{ds1\_n} = s_3 \frac{S(i_{ds1})}{|S(i_{ds1})| + e_3} \tag{III.30}$$

$$v_{qs1\_n} = s_4 \frac{S(i_{qs1})}{|S(i_{qs1})| + e_4} \tag{III.31}$$

$$v_{ds2\_n} = s_5 \frac{S(i_{ds2})}{|S(i_{ds2})| + e_5} \tag{III.32}$$

$$v_{qs2\_n} = s_6 \frac{S(i_{qs2})}{|S(i_{qs2})| + e_6} \tag{III.33}$$

The positive gains s_1- s_6 must be properly selected to satisfy system stability conditions.

III.3 Second-order sliding mode control (SOSMC)

III.3.1 SOSMC-based control loop design

The control of this part of the system aims to ensure that the maximum power the wind turbine can generate flows to the DC bus by controlling the rectifier when operating in zone II. Among the control techniques for wind generators, the sliding mode approach has demonstrated satisfactory effectiveness, given the nature of the wind energy source, which is characterized by its turbulence.

Although first-order sliding mode control is simple to implement, its major drawback is the phenomenon of chattering. We propose a second-order sliding mode control (super twisting) for more robust control, which will be presented later.

Emelyanov [66] and Levantovsky [67] introduced higher-order sliding modes, an advanced evolution of first-order sliding modes. While preserving the core robustness of traditional sliding modes, this approach reduces the key drawback of the chattering effect near the sliding surface. The transition from first-order to higher-order sliding modes involves applying discontinuous control to the higher derivatives of the sliding surface rather than the surface itself. [68], [69].

This controller drives both the sliding variable S and its derivative $\dot{S}$ to zero in finite time ($S = \dot{S} = 0$), establishing a second-order sliding regime. The distinguishing feature of this strategy is that the discontinuous component acts on the control derivative $\dot{u}$. As a result, the actual control input $u = \int \dot{u}$ becomes continuous, mitigating chattering [69], [70].

Among second-order sliding mode algorithms, the super-twisting method is widely used, though it is restricted to systems with a relative degree of one [71]. As illustrated in **Figure III.3**, the algorithm converges through twisting motions around the origin in the phase plane. The Super-Twisting control law consists of two parts: the first, u_1, is defined by its time derivative, while the second, u_2, is a continuous function of the sliding variable. The control law for a real sliding mode is expressed as [72]:

$$\begin{cases} u = u_1 + u_2 \\ u_1 = \rho_x \int sign(S) \\ u_2 = \sigma_x |S|^{0.5} sign(S) \end{cases} \quad \text{(III.34)}$$

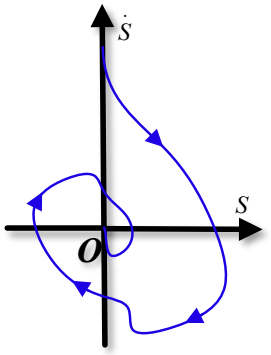

Figure III.3 Convergence in finite time of the Super-Twisting algorithm

III.3.1.1 Application of SOSMC for a DSIG

Using the system equations (III.13) and (III.34), the control laws for the regulator are derived as follows:

- For the speed regulator:

$$\begin{cases} i_{qs}^{*} = i_{qs\_1} + i_{qs\_2} \\ i_{qs\_1} = \rho_1 \int sign\left(S\left(\Omega_{mec}\right)\right) \\ i_{qs\_2} = \sigma_1 \left|S\left(\Omega_{mec}\right)\right|^{0.5} sign\left(S\left(\Omega_{mec}\right)\right) \end{cases} \tag{III.35}$$

with

$$i^{*}_{qs} = i^{*}_{qs1} + i^{*}_{qs2} \tag{III.36}$$

$$i^{*}_{qs1} = i^{*}_{qs2} \tag{III.37}$$

- For the flux regulator:

$$\begin{cases} i_{ds}^{*} = i_{ds\_1} + i_{ds\_2} \\ i_{ds\_1} = \rho_2 \int sign\left(S\left(\phi_{rd}\right)\right) \\ i_{ds\_2} = \sigma_2 \left|S\left(\phi_{rd}\right)\right|^{0.5} sign\left(S\left(\phi_{rd}\right)\right) \end{cases} \tag{III.38}$$

with

$$i^{*}_{ds} = i^{*}_{ds1} + i^{*}_{ds2} \tag{III.39}$$

$$i^{*}_{ds1} = i^{*}_{ds2} \tag{III.40}$$

- For the stator currents regulators:

$$\begin{cases} v_{ds1}^{*} = v_{ds\_1} + v_{ds\_2} \\ v_{ds\_1} = \rho_3 \int sign\left(S\left(i_{ds1}\right)\right) \\ v_{ds\_2} = \sigma_3 \left|S\left(i_{ds1}\right)\right|^{0.5} sign\left(S\left(i_{ds1}\right)\right) \end{cases} \tag{III.41}$$

$$\begin{cases} v_{qs1}^{*} = v_{qs\_1} + v_{qs\_2} \\ v_{qs\_1} = \rho_4 \int sign\left(S\left(i_{qs1}\right)\right) \\ v_{qs\_2} = \sigma_4 \left|S\left(i_{qs1}\right)\right|^{0.5} sign\left(S\left(i_{qs1}\right)\right) \end{cases} \tag{III.42}$$

$$\begin{cases} v_{ds2}^{*} = v_{ds\_1} + v_{ds\_2} \\ v_{ds\_1} = \rho_5 \int sign\left(S\left(i_{ds2}\right)\right) \\ v_{ds\_2} = \sigma_5 \left|S\left(i_{ds2}\right)\right|^{0.5} sign\left(S\left(i_{ds2}\right)\right) \end{cases} \tag{III.43}$$

$$\begin{cases} v_{qs2}^{*} = v_{qs\_1} + v_{qs\_2} \\ v_{qs\_1} = \rho_6 \int sign\left(S\left(i_{qs2}\right)\right) \\ v_{qs\_2} = \sigma_6 \left|S\left(i_{qs2}\right)\right|^{0.5} sign\left(S\left(i_{qs2}\right)\right) \end{cases} \quad \text{(III.44)}$$

III.4 High-order sliding mode control (HOSMC)

III.4.1 HOSMC-based control loop design

In AC machines, torque and flux ripples can be managed and minimized using different control strategies. Among these, the super-twisting algorithm (STA) stands out as an effective higher-order sliding mode control (HOSMC) technique that requires only knowledge of the sliding surface [73]. Another advanced method, the third-order sliding mode controller (TOSMC), is particularly suitable for uncertain systems and overcomes many limitations of conventional sliding mode control (SMC).

TOSMC is a robust and reliable alternative for both linear and nonlinear systems. While traditional SMC operates on the first derivative of the sliding surface, TOSMC acts on the second-order derivative, similar to the STA approach. The control input for TOSMC is defined as the sum of three components, as expressed in (III.44) [11], [74], [75]:

$$\begin{cases} u = u_1 + u_2 + u_3 \\ u_1 = \alpha_x \int sign\left(S\right) dt \\ u_2 = \beta_x \left|S\right|^{0.5} sign\left(S\right) \\ u_3 = \delta_x sign\left(S\right) \end{cases} \quad \text{(III.45)}$$

III.4.1.1 Application of HOSMC for a DSIG

Through the application of governing equations (III.13) and (III.45), the control laws for the regulator are derived in the following manner:

- For the speed regulator:

$$\begin{cases} i_{qs}^{*} = i_{qs\_1} + i_{qs\_2} + i_{qs\_3} \\ i_{qs\_1} = \alpha_1 \int sign\left(S\left(\Omega_{mec}\right)\right) dt \\ i_{qs\_2} = \beta_1 \left|S\left(\Omega_{mec}\right)\right|^{0.5} sign\left(S\left(\Omega_{mec}\right)\right) \\ i_{qs\_3} = \delta_1 sign\left(S\left(\Omega_{mec}\right)\right) \end{cases} \quad \text{(III.46)}$$

With

$$i^{*}_{qs} = i^{*}_{qs1} + i^{*}_{qs2} \quad \text{(III.47)}$$

$$i^{*}_{qs1} = i^{*}_{qs2} \quad \text{(III.48)}$$

- For the flux regulator:

$$\begin{cases} i_{ds}^{*} = i_{ds\_1} + i_{ds\_2} + i_{ds\_3} \\ i_{ds\_1} = \alpha_2 \int sign\left(S\left(\varphi_{rd}\right)\right) dt \\ i_{ds\_2} = \beta_2 \left|S\left(\varphi_{rd}\right)\right|^{0.5} sign\left(S\left(\varphi_{rd}\right)\right) \\ i_{ds\_3} = \delta_2 sign\left(S\left(\varphi_{rd}\right)\right) \end{cases} \quad \text{(III,49)}$$

With

$$i_{ds}^{*} = i_{ds1}^{*} + i_{ds2}^{*} \quad \text{(III.50)}$$

$$i_{ds1}^{*} = i_{ds2}^{*} \quad \text{(III.51)}$$

- For the stator currents regulators:

$$\begin{cases} v_{ds1}^{*} = v_{ds\_1} + v_{ds\_2} + v_{ds\_3} \\ v_{ds\_1} = \alpha_3 \int sign\left(S\left(i_{ds1}\right)\right) dt \\ v_{ds\_2} = \beta_3 \left|S\left(i_{ds1}\right)\right|^{0.5} sign\left(S\left(i_{ds1}\right)\right) \\ v_{ds\_3} = \delta_3 sign\left(S\left(i_{ds1}\right)\right) \end{cases} \quad \text{(III.52)}$$

$$\begin{cases} v_{qs1}^{*} = v_{qs\_1} + v_{qs\_2} + v_{qs\_3} \\ v_{qs\_1} = \alpha_4 \int sign\left(S\left(i_{qs1}\right)\right) dt \\ v_{qs\_2} = \beta_4 \left|S\left(i_{qs1}\right)\right|^{0.5} sign\left(S\left(i_{qs1}\right)\right) \\ v_{qs\_3} = \delta_4 sign\left(S\left(i_{qs1}\right)\right) \end{cases} \quad \text{(III.53)}$$

$$\begin{cases} v_{ds2}^{*} = v_{ds\_1} + v_{ds\_2} + v_{ds\_3} \\ v_{ds\_1} = \alpha_5 \int sign\left(S\left(i_{ds2}\right)\right) dt \\ v_{ds\_2} = \beta_5 \left|S\left(i_{ds2}\right)\right|^{0.5} sign\left(S\left(i_{ds2}\right)\right) \\ v_{ds\_3} = \delta_5 sign\left(S\left(i_{ds2}\right)\right) \end{cases} \quad \text{(III.54)}$$

$$\begin{cases} v_{qs2}^{*} = v_{qs\_1} + v_{qs\_2} + v_{qs\_3} \\ v_{qs\_1} = \alpha_6 \int sign\left(S\left(i_{qs2}\right)\right) dt \\ v_{qs\_2} = \beta_6 \left|S\left(i_{qs2}\right)\right|^{0.5} sign\left(S\left(i_{qs2}\right)\right) \\ v_{qs\_3} = \delta_6 sign\left(S\left(i_{qs2}\right)\right) \end{cases} \quad \text{(III.55)}$$

To enhance the performance of the HOSMC algorithms, a strategy involving the adjustment of coefficients $\alpha_{1\text{-}6}$, $\beta_{1\text{-}6}$, and $\delta_{1\text{-}6}$ was implemented, as illustrated in **Figure III.4**, which shows the FOC-based configuration of the DSIG's FOSMC, SOSMC, and HOSM controllers.

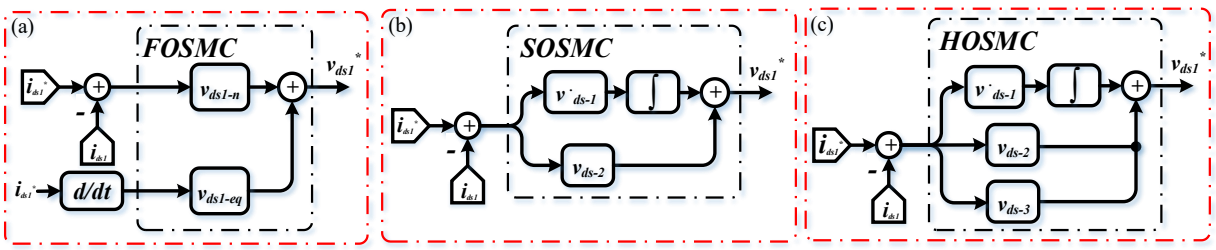

Figure III.4 The system architectures for: (a) FOSM, (b) SOSM, and (c) HOSM controller methods

The determination of optimal coefficient values presents a significant challenge due to the six controllers requiring tuning, each with multiple coefficient sets ($s_{1\text{-}6}$, $e_{1\text{-}6}$) for FOSMC, ($\rho_{1\text{-}6}$, $\sigma_{1\text{-}6}$) for SOSMC, and ($\alpha_{1\text{-}6}$, $\beta_{1\text{-}6}$, and $\delta_{1\text{-}6}$) for HOSMC. To address this, the ILA optimization method was employed as the most effective approach for determining the appropriate coefficients while ensuring precise control of speed, flux, and currents with minimal electromagnetic torque oscillations, making it the preferred choice for achieving optimal DSIG control performance in both FOSMC and SOSMC implementations.

III.5 ILA ALGORITHM

This section presents the fundamental principles and modeling of the proposed ILA approach.

III.5.1 Introduction to optimization

Many complex problems resist optimal solutions through traditional optimization methods due to inherent difficulties such as computational complexity, high dimensionality, expansive search spaces, and temporal limitations. Conventional approaches might require impractical timeframes to achieve exact solutions. Advances in soft computing have transformed optimization methodologies, yielding approaches that deliver enhanced computational efficiency with satisfactory precision. The widespread importance of optimization across disciplines has prompted extensive evaluation of algorithmic performance in locating optimal solutions.

Contemporary optimization increasingly favors innovative algorithmic approaches that efficiently discover near-optimal solutions, albeit not always perfect ones. These modern techniques fall into several classifications, primarily divided between nature-inspired methods (such as evolutionary-based genetic algorithms) and non-nature-inspired approaches (including harmony search). Additionally, swarm intelligence represents another significant category, where collective group behavior produces sophisticated problem-solving capabilities rather than individual performance evaluation. Notable examples include artificial bee colony and particle swarm optimization techniques.

Optimization continues its rapid evolution, constantly developing and refining new algorithms. Each methodology offers distinct advantages and constraints while contributing to solving complex, multidisciplinary challenges. This continuous advancement stems from the fundamental nature of optimization problems, prompting annual introductions of novel techniques applied across diverse domains - from structural engineering to mechanical systems.

Optimization is crucial in artificial intelligence, particularly in machine learning, where effective optimization strategies can significantly enhance model training efficiency and accuracy. This study introduces the ILA (IbI Logic Algorithm), an optimization approach grounded in IbI logic

theory. Following a detailed explanation of its structural framework and computational processes, we assess its performance through comparison with 73 benchmark problems (both constrained and unconstrained cases) against existing optimization methods [76].

III.5.1.1 The primary process of the ILA

This section presents a novel optimization approach based on IbI logic theory, formally termed the ILA. The algorithm's primary objective is to identify IbI logic configurations exhibiting high P_t values (hereafter referred simply as "logic").

ILA features a sophisticated three-phase architecture comprising:

i. **Exploration**: Initial solution space investigation
ii. **Integration**: Logical combination of discovered solutions
iii. **Exploitation**: Intensive local search refinement

The algorithm's unique sequential operation distinguishes it from conventional approaches - solutions progress unidirectionally through phases without regression to previous stages. As illustrated in **Figure III.4**, the complete workflow encompasses integration, IbI logic search, and collaborative group processing stages. The computational process distributes $N_T = n_{t1} + n_{t2} + n_{t3}$ iterations across the three phases (with n_{t1} to n_{t3} = representing phase-specific iteration counts). Subsequent sections provide a detailed examination of each operational stage and the complete algorithmic workflow.

III.5.1.2 The ILA parameters

The proposed optimization method requires configuring two critical parameters before execution: (i) the number of experts and (ii) the total iteration count. While **Table III.1** in the ILA framework provides additional adjustable parameters that can be fine-tuned for specific problem instances to enhance algorithmic performance, the method remains effective even when using default parameter settings. It is important to note that all ILA parameters in this study are adopted from the reference. [76] except for the expert count and iteration number, which represent our design choices. Properly selecting these configurable parameters can significantly improve the algorithm's problem-solving efficacy for particular optimization challenges.

a. Preparation phase: During the initialization phase, stage 1, the ILA parameters from **Table III.1** are first configured with their baseline values. Subsequently, the iteration count, $t_{m,}$ for each of the nm models is calculated according to the methodology presented in the reference [76], as expressed by the following relationship: [equation/expression from [76]].

Table III.1– ILA Parameters

Parameter	Description	Value
N_T	Number of iterations	5
n_{NL}	Number of experts	15
n_m	Models' number	5
$n_{g,max}$	Groups' maximum number in each model	$(n_{NL})/2$
B_{min}	IbI parameters minimum boundary	0.4
B_{max}	IbI parameters maximum boundary	0.5
p_{s1}	Iterations' maximum percentage in stage 1	33%
p_{s2}	Iterations' maximum percentage in stage 2	33%
n_{rep}	Number of replications for clustering	10
t_{clus}	Number of attempts to converge the classification in n_{rep} replications	100

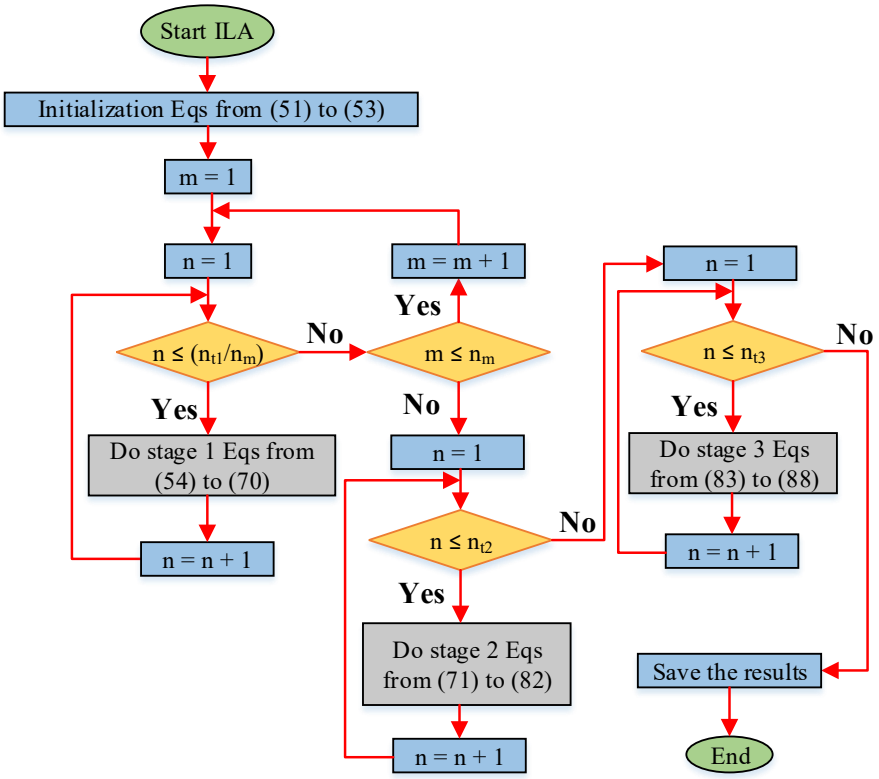

Figure III.5 The general format of the ILA

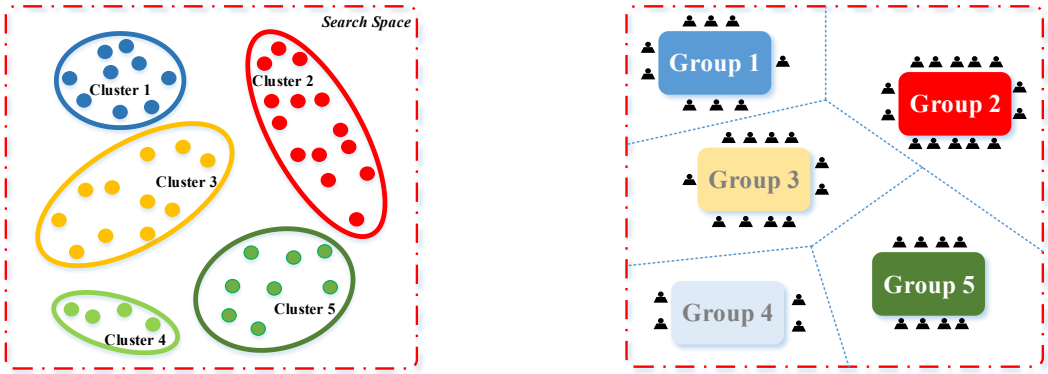

a. Clustering approach on the search space b. Assigning the experts to each group

Figure III.6 The grouping of the experts

$$t_m = \frac{n_{t1}}{n_m} \tag{III.56}$$

Here, n_{t1} represents the count of stage 1 iterations that can be attained by applying the method from [76]:

$$n_{t1} = p_{s1} N_T \tag{III.57}$$

Afterward, each of the n_m models undergoes individual optimization for t_m iterations. In other words, the final results from one model are passed to the next, further refined over another t_m iterations. This cycle continues until all n_m models have been optimized. Once this stage is complete, the iterations for Stage 1 conclude, and all outcomes proceed to Stage 2.

Before optimization begins in Stage 1, the experts (entire population) are clustered using the *k*-means approach **Figure III.6**. Each cluster represents a distinct aspect of the subject under study, for which experts aim to define future logic, referred to as IbI at this stage. Experts are grouped based on their knowledge (i.e., their current positions in the problem's search space). The number of groups (n_g) for each model is randomly determined using (III.58), where the *randi* function selects a random integer between 1 and its specified upper limit, $n_{g,max}$.

$$n_{g,m} = randi\left(n_{g,\max}\right), m = 1,...,n_m \tag{III.58}$$

However, if a model's required number of clusters is fewer than $n_{g,m}$, (III.58) is bypassed, and the clusters from the previous model are reused. Due to the *k*-means method, group sizes may vary. The algorithm employs the Squared Euclidean Distance (SED) as the clustering metric, though other distance measures could also be applied. Once clustering is complete, each expert is assigned to a group, and these defined clusters are then carried into Stage 1 for optimization.

b. Stage 1: Groupwork: In this stage, which represents the algorithm's global search or exploration phase, each group focuses on a specific region of the solution space to identify the optimal *NL* (New Logic) within their assigned domain. All experts (E) within a group work to improve their initial fitness *NL* through t_m iterations by utilizing the collective knowledge available in their group. Before each iteration begins, three key parameters are established: (i) the Logic (L), which is the expert (E_i) with the best *NL* value from the previous iteration across all groups; (ii) the group's best-performing expert ($E_{I,g}$); and (iii) the group's average performance (A_g) from the previous iteration. Subsequently, the three fundamental parameters of the IbI logic theory - comprehensibility (C_i), degree (D_i), and probability (P_i) - are calculated for each n_{NL} expert using (III.59) through (III.61), where $E_{i,p}$ denotes the value of expert E_i in the preceding iteration.

$$C_i = \sqrt{\sum_{i=1}^{n_{NL}} \left(E_i - L\right)^2} \tag{III.59}$$

$$D_i = \sqrt{\sum_{i=1}^{n_{NL}} \left(E_i - E_{i,p}\right)^2} \tag{III.60}$$

$$P_i = \sqrt{\sum_{i=1}^{n_{NL}} \left(E_i - E_{i,g}\right)^2} \quad , g = 1,...,n_{g,m} \tag{III.61}$$

To implement the values derived from (III.59) to (III.61), a normalization method is applied to constrain the values within the [0,1] range. The normalized outputs, calculated through (III.62) to (III.64), yield the relative ratios of comprehensibility ($R_{c,i}$), degree ($R_{D,i}$), and probability ($R_{P,i}$). These ratios undergo dynamic updates at the beginning of every stage 1 iteration, where the min and max indices in these equations correspond to the respective lower and upper bounds of each parameter.

Stage 1 follows a structured iterative process where each iteration begins by evaluating each expert's knowledge, incorporates the group's best NL for the current iteration, and concludes with a comparison. The first step involves calculating two knowledge components: $K_{0,S1}$ (determined using III.65- III.68) and $K_{1,S1}$ (derived from III.69- III.70), with parameters B_D, B_C, and B_P randomly selected between B_{min} and B_{max} each iteration. The calculation of $K_{0,S1}$ depends on $R_{C,i}$:

when $R_{C,i} < B_C$, the expert's current values (E_i) are used, while $R_{C,i} > B_C$ incorporates the group's best expert.

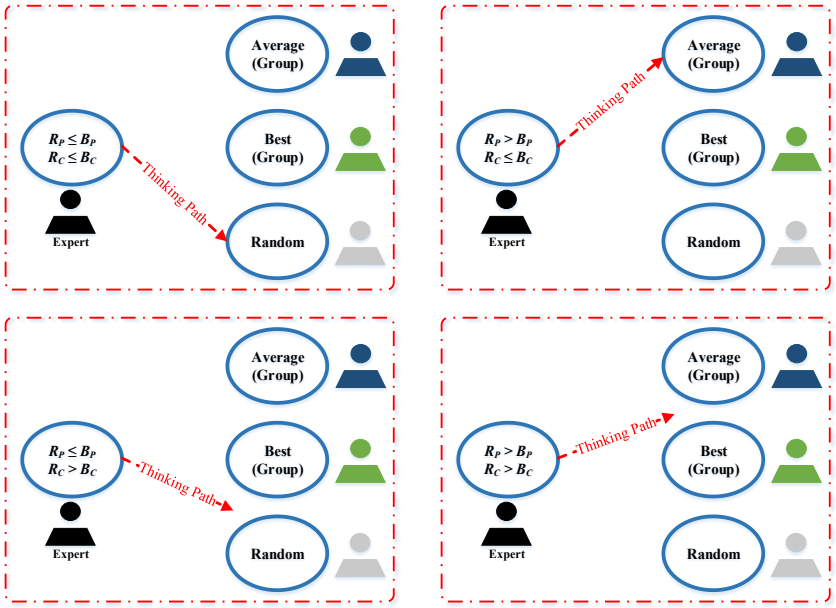

Figure III.7 Calculation process of K_0

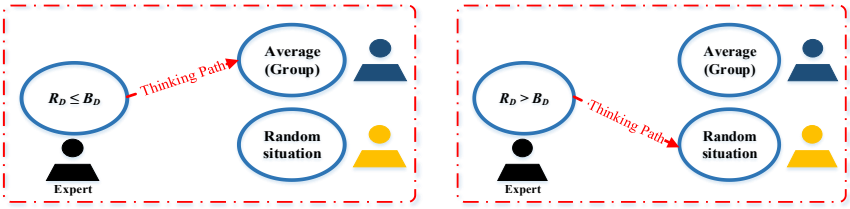

Figure III.8 Calculation process of K_1

This approach maintains experts closer to the current iteration's logic (previous best performer) while restricting those further away (higher $R_{C,i}$) from excessive exploration. The second term's calculation considers R_P: experts with $R_P > B_P$ (near the group's best) explore more solutions, while others use the group average for refinement. This process, illustrated in **Figure III.7**, ensures a balanced approach between maintaining promising solutions and exploring new possibilities.

$$R_{C,i} = \frac{C_i - C_{\min}}{C_{\max} - C_{\min}} \quad , i = 1,...,n_{NL} \tag{III.62}$$

$$R_{D,i} = \frac{D_i - D_{\min}}{D_{\max} - D_{\min}} \quad , i = 1,...,n_{NL} \tag{III.63}$$

$$R_{P,i} = \frac{P_i - P_{\min}}{P_{\max} - P_{\min}} \quad , i = 1,...,n_{NL} \tag{III.64}$$

$$K_{0,i,S1} = R_{P,i} \frac{E_i + E_r}{2} \qquad \text{for } R_{C,i} \le B_C \text{ and } R_{P,i} \le B_P \tag{III.65}$$

$$K_{0,i,S1} = R_{P,i} \frac{E_i + E_{a,g}}{2} \qquad \text{for } R_{C,i} \le B_C \text{ and } R_{P,i} > B_P \tag{III.66}$$

$$K_{0,i,S1} = R_{P,i}\frac{E_{I,g} + E_r}{2} \qquad \text{for } R_{C,i} > B_C \text{ and } R_{P,i} \le B_P \tag{III.67}$$

$$K_{0,i,S1} = R_{P,i}\frac{E_{I,g} + E_{a,g}}{2} \qquad \text{for } R_{C,i} > B_C \text{ and } R_{P,i} > B_P \tag{III.68}$$

The distance parameter $R_{D,i}$ determines how new knowledge is applied to the ith expert, as illustrated in **Figure III.8**. When an expert's current position differs significantly from their previous value ($R_{D,i} > B_D$), this indicates insufficient knowledge evolution. In such cases, Equation (III.74) incorporates the group's average to guide the expert toward improved solutions. Conversely, when $R_{D,i} \le B_D$, Equation (III.75) introduces new random knowledge to facilitate exploration of alternative solutions. This dual approach ensures balanced refinement of expert knowledge, leveraging collective wisdom when progress stalls while allowing controlled exploration when appropriate.

$$K_{1,i,S1} = c_1 \mathrm{E}_{a,g} \qquad \text{for } R_{D,i} \le B_D \tag{III.69}$$

$$K_{1,i,S1} = c_1 \mathrm{E}_{u} \qquad \text{for } R_{D,i} > B_D \tag{III.70}$$

Here, E_r denotes a randomly selected expert from the group, E_{ag} represents the average of all expert values within the group, and E_u corresponds to a randomly generated solution in the search space. The weighting coefficient c_1 is a uniformly distributed random number in the range [0, 1]. The consolidated knowledge update is computed through Equation (III.71), which integrates these components to determine the expert's new position.

$$K_{S1} = \frac{\left|K_{0,S1} + K_{1,S1}\right|}{2} \tag{III.71}$$

The knowledge acquired for the i^{th} expert directly influences the value of E_i through Equation (III.72), where the coefficient c_2 represents a randomly generated vector with components uniformly distributed in the interval [−1.5, 1.5]. This stochastic weighting ensures diversified solution space exploration while maintaining bounded perturbations to the expert's position.

$$E_{S1,new1} = E_i + c_2 K_{S1} \tag{III.72}$$

This step updates the expert knowledge and assigns a new value to the proposed *NL*. Given that the group's best expert is more likely to become the future logic, its knowledge is leveraged to enhance other members' positions through a secondary update via Equation (III.73). This equation performs a weighted combination of the target expert's knowledge and the best group member's knowledge.

Subsequently, the optimal *E* value (here, the minimum) is selected using Equation (III.74), where *f* denotes the fitness function. The update incorporates two stochastic coefficients:

- c_3: A random scalar uniformly distributed in [−1.5, 1.5]
- c_4: A random scalar uniformly sampled from [0, 1]

These coefficients introduce controlled randomness to balance exploitation (guided by the best expert) and exploration (via stochastic perturbations).

$$E_{S1,new2} = c_3 E_{S1,new1} + c_4 K_{I,g} \tag{III.73}$$

Algorithm 1. Preparation and Stage (Groupwork)

Pseudocode for the preparation phase and stage 1

Input: N_T, n_{NL}, n_m, B_{min}, B_{max}, p_{s1}, $n_{g,max}$, n_{rep}, n_{rep}, t_{clus}
Initialization:
  Randomly initialize current *NLs* for all experts E_i (i = 1, …,n_{NL})
  Randomly initialize previous *NLs* for all experts $E_{i,p}$ (i = 1, …,n_{NL})
  Compute fitness $f(E_i)$ for each E_i ; Identify best fitness as *IbI*
  Compute fitness $f(E_{i,p})$ for each $E_{i,p}$; Identify best fitness as *L*
  Randomly select several groups $n_{g,m}$ in [1, $n_{g,ma}$] for each class
For m = 1 : n_m >> (Preparation Phase)
  Perform *k*-means clustering using experts, $n_{g,m}$, n_{rep}, t_{clus}
  Assign experts to their respective clusters (groups)
  For n = 1: (p_{s1} N_T)/n_m. >> (Start of the Stage 1)
    For each group g = 1: $n_{g,m}$
      Identify the group's best expert (optimal fitness) of the g^{th} group as $E_{I,g}$
      Calculate group expert average $E_{a,g}$
    End
    For g = 1: $n_{g,m}$
      For i = 1 : n_{NL}
        If $E_i \in g^{th}$ group
          Compute R_C using (62) with B_{min}, B_{max}
          Compute R_D using (63) with B_{min}, B_{max}
          Compute R_P using (64) with B_{min}, B_{max}
        End
        For i = 1 : n_{NL}
          If $E_i \in g^{th}$ group
            Determine K_{S1} using Eq. (71)
            Update E_i as $E_{S1,i}$ using Eq. (75)
            Refresh E_I, *L,* and $E_{P,i}$
          End
        End
      End
    End
  End
End
Return $E_{S1,i}$ (i = 1, …, n_{NL}), $E_{P,i}$ (i = 1, …, n_{NL}), *L, EI*

$$E_{S1,new} = \min imum\left(E_{S1,new1}, E_{S1,new2}\right) \tag{III.74}$$

This step involves comparing the newly generated value with the expert's previous value, retaining the solution with the superior (minimum) fitness value according to Equation (III.75). Upon concluding Stage 1, the refined solutions progress to Stage 2 for integration, with no subsequent return to earlier stages permitted. The complete Stage 1 optimization procedure is detailed in Algorithm 1, where parameter EI represents the globally optimal E_i across all experts, as visualized in **Figure III.9**.

c. Stage 2: Integration: During this phase, all groups merge into a single unified team where experts collectively refine their *NL* values by leveraging the complete knowledge base available in each iteration. The process executes through n_{t2} iterations, with the entire population working together to optimize their *NL* outcomes. The computation begins by deriving R_C and R_D ratios using (III.57) and (III.58).

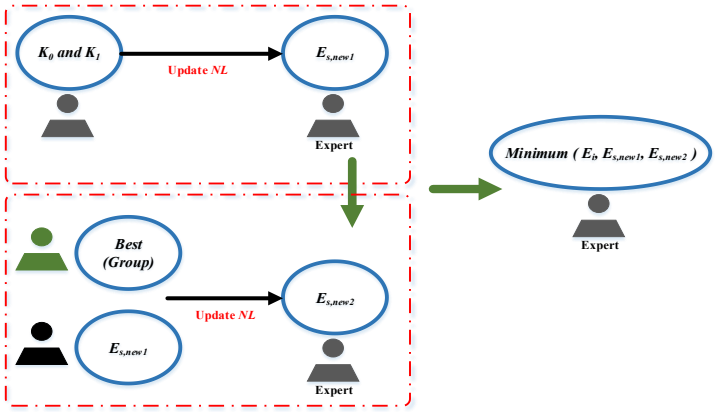

Figure III.9 Process for determining the final *NL* in Stage 1

$$E_{i,S1} = \min imum\left(E_i, E_{S1,new}\right) \tag{III.75}$$

As all experts now belong to a single group, R_P calculation utilizes the globally best solution (E_I) across the entire population. Consequently, (III.59) is substituted with (III.76) for R_P determination at the beginning of every stage 2 iteration.

$$P_i = \sqrt{\sum_{i=1}^{n_{NL}} \left(E_i - E_I\right)^2} \quad , g = 1, \ldots, n_{g,m} \tag{III.76}$$

During each iteration, after determining the R_P, R_C, and R_D ratios, new knowledge ($K_{S,2}$) is applied to every expert. This involves calculating $K_{0,S2}$ using Equations (III.77)-(III.80) and $K_{1,S2}$ through (III.81)-(III.82), which are then combined via (III.83) to determine the final $K_{S,2}$ value for each ith expert. The process systematically transforms the computed ratios into updated knowledge parameters that drive the optimization process forward while maintaining all critical mathematical relationships and references from the original framework.

$$K_{0,i,S2} = R_{P,i} \frac{E_i + E_R}{2} \qquad \text{for } R_{C,i} \le B_C \text{ and } R_{P,i} \le B_P \tag{III.77}$$

$$K_{0,i,S2} = R_{P,i} \frac{E_i + E_A}{2} \qquad \text{for } R_{C,i} \le B_C \text{ and } R_{P,i} > B_P \tag{III.78}$$

$$K_{0,i,S2} = R_{P,i} \frac{E_I + E_R}{2} \qquad \text{for } R_{C,i} > B_C \text{ and } R_{P,i} \le B_P \tag{III.79}$$

$$K_{0,i,S2} = R_{P,i} \frac{E_I + E_A}{2} \qquad \text{for } R_{C,i} > B_C \text{ and } R_{P,i} > B_P \tag{III.80}$$

Within this framework, E_R denotes a randomly selected expert from the complete population, while E_A represents the mean value across all experts. (III.81) incorporates the coefficient c_5, a uniformly distributed random variable within the range [0,1]. The ultimate knowledge update, derived from K_{S2}, is computed through (III.84). This equation features c_6 as a randomly generated vector whose components fall within the interval [-0.75, 0.75], introducing controlled stochastic variation into the optimization process while maintaining bounded perturbations to the expert knowledge.

$$K_{1,i,S2} = c_5 \mathrm{E}_A \qquad \text{for } R_{D,i} \le B_D \tag{III.81}$$

$$K_{1,i,S2} = c_5 \mathrm{E}_u \qquad \text{for } R_{D,i} > B_D \tag{III.82}$$

$$K_{S2} = \frac{\left| K_{0,S2} + K_{1,S2} \right|}{2} \tag{III.83}$$

$$E_{S2,new1} = E_i + c_6 K_{S6} \tag{III.84}$$

The initial knowledge update is implemented through Equation (III.85), which combines the output from (III.84) with the optimal knowledge from the best-performing expert (E_I). For minimization objectives, the final expert value (E_i) is determined through (III.86) and (III.87), enabling continuous evaluation and refinement of each expert's knowledge at every iteration cycle. The process incorporates a randomization element through coefficient c_7, which is sampled uniformly from the interval [-0.75, 0.75], ensuring controlled exploration around current best solutions while maintaining optimization stability.

The coefficient c_8 is randomly sampled from a uniform distribution over the interval [0,1].

The initial update is calculated through (III.85), which incorporates both the output from (III.84) and the current knowledge of the top-performing expert (E_I). Following each iteration's knowledge assessment, the expert's final position (E_i) is computed using (III.86) and (III.87) for fitness function minimization objectives. The process utilizes two randomized parameters: c_7, uniformly distributed between -0.75 and 0.75, and c_8, randomly selected from the [0,1] interval. The complete stage 2 procedure is formally outlined in Algorithm (2).

$$E_{S2,new2} = c_7 E_{S2,new1} + c_8 E_I \tag{III.85}$$

$$E_{S2,new} = \min imum\left(E_{S2,new1}, E_{S2,new2} \right) \tag{III.86}$$

$$E_{i,S2} = \min imum\left(E_i, E_{S2,new} \right) \tag{III.87}$$

Algorithm 2. The Stage 2 (Integration)

Pseudocode for stage 2

Input: $E_{S1,i}$ (i = 1, …, n_{NL}), $E_{P,i}$ (i = 1, …, n_{NL}), L, E_I, p_{s2}
  For n = 1: (p_{s2} N_T)
    For i = 1: n_{NL}
      Specify the best expert (an expert with the optimum fitness) E_I
      Specify the average between the experts as E_A
    End
      For i = 1: n_{NL}
        Calculate R_c based on B_{min} and B_{max} using Eq. (62)
        Calculate R_D based on B_{min} and B_{max} using Eq. (63)
        Calculate R_P based on B_{min} and B_{max} using Eq. (64)
      End
      For i = 1: n_{NL}
        Calculate K_{S2} using Eq. (83)
        Update E_i as $E_{S2,i}$ using Eq. (87)
        Update E_I, L, and $E_{p,i}$
      End
  End
Return $E_{S2,i}$ (i = 1, …, n_{NL}), E_I

d. Stage 3: The third stage of the algorithm focuses on precision optimization through fine-tuned adjustments, targeting the best possible solution. In this phase, each expert's knowledge is enhanced by incorporating the collective average knowledge of all experts, followed by a secondary update influenced by the best-performing expert (E_I). These two steps iterate n_{t3} times until the stopping criterion (iteration count) is met. At the start of each iteration, the algorithm computes the average of current expert knowledge. The refined knowledge (K_{S3}) is then derived using (III.88) and (III.89). Subsequently, the expert's updated position ($E_{S3,i}$) is determined via (III.90)–(III.93), optimized for fitness function minimization. Key parameters include:

- c_9: Random vector ∈ [−0.25, 0.25]
- c_{10}: Random scalar ∈ [−0.25, 0.25]
- c_{11}: Random scalar ∈ [0, 1]

The complete stage 3 procedure is formalized in Algorithm (3).

Algorithm 3. The Stage 3 (IbI Logic Search)

Pseudocode for the stage 3

Input: $E_{S2,i}$ (i = 1, …, n_{NL}), E_I, n_{t3}
  For n = 1: n_{t3}
    For i = 1: n_{NL}
      Specify the average between the experts as E_A
        Calculate K_{S3} using Eqs. (88) and (89)
        Update E_i as $E_{S3,i}$ using Eq. (93)
        Update E_I
    End
  End
Return E_I

$$K_{i,S3} = \left|E_A - E_I\right| \quad if \quad knowledge\ factor = 1 \tag{III.88}$$

$$K_{i,S3} = \left|E_A - E_I\right| \quad if \quad knowledge\ factor = 2 \tag{III.89}$$

$$E_{S3,new1} = E_i + c_9 K_{S3} \tag{III.90}$$

$$E_{S3,new2} = c_{10} E_{S3,new1} + c_{11} E_I \tag{III.91}$$

$$E_{S3,new} = \min imum\left(E_{S3,new1}, E_{S3,new2}\right) \tag{III.92}$$

$$E_{i,S3} = \min imum\left(E_i, E_{S3,new}\right) \tag{III.93}$$

III.5.2 Discussion of the proposed algorithm

Through a structured three-stage optimisation process, the ILA algorithm addresses two key limitations of conventional optimization methods—slow convergence and susceptibility to local optima. Unlike traditional approaches, it provides users with adjustable parameters and flexible iteration counts for each stage, enabling tailored optimization based on problem-specific requirements. This adaptability enhances solution quality and computational efficiency.

A unique feature of ILA is its modular implementation: users can execute Stage 1 independently, evaluate intermediate solutions, and only proceed to subsequent stages if results meet expectations.

This stepwise progression ensures validation at each phase, granting users greater control over the optimization trajectory while mitigating the risk of premature convergence. The algorithm combines methodological rigor with operational flexibility by decoupling stages and incorporating verification checkpoints, making it particularly advantageous for complex or high-stakes optimization scenarios.

III.5.3 Optimization algorithms for comparison study

The performance of the ILA algorithm was evaluated against nineteen state-of-the-art optimization techniques cited in [76]: Genetic Algorithm (GA), Particle Swarm Optimization (PSO), Differential Evolution (DE), Harmony Search (HS), Imperialist Competitive Algorithm (ICA), Artificial Bee Colony (ABC), Cuckoo Search (CS), Bat-inspired Algorithm (BA), Teaching-Learning-Based Optimization (TLBO), Grey Wolf Optimizer (GWO), Monarch Butterfly Optimization (MBO), Elephant Herding Optimization (EHO), Whale Optimization Algorithm (WOA), Salp Swarm Algorithm (SSA), Harris Hawks Optimization (HHO), Henry Gas Solubility Optimization (HGSO), Arithmetic Optimization Algorithm (AOA), Artificial Hummingbird Algorithm (AHA), and Transit Search (TS).

III.5.4 Implementation of ILA for FOSMC, SOSMC, and HOSMC parameter optimization

The ILA is employed to optimize the parameters of FOSMC, SOSMC, and HOSMC controllers. For all three control strategies, the objective function minimizes the sum of ITAEs between actual and reference values for speed, flux, and stator currents, expressed as:

$$\begin{aligned}\min(Obj) = &\int_0^t t.\left(\Omega_{mec}^* - \Omega_{mec}\right)\,dt + \int_0^t t.\left(\phi_{rd}^* - \phi_{rd}\right)\,dt + \frac{1}{w_1}\int_0^t t.\left(i_{ds1}^* - i_{ds1}\right)\,dt \\ &+ \frac{1}{w_2}\int_0^t t.\left(i_{qs1}^* - i_{qs1}\right)\,dt + \frac{1}{w_3}\int_0^t t.\left(i_{ds2}^* - i_{ds2}\right)\,dt + \frac{1}{w_4}\int_0^t t.\left(i_{qs2}^* - i_{qs2}\right)\,dt\end{aligned} \tag{III.94}$$

Variable optimization bounds are specified in **Table III.2**. The targeted parameters include:

- **FOSMC**: Gains $s_{1\text{-}6}$ and $e_{1\text{-}6}$ for speed, flux, and stator current control
- **SOSMC**: Gains $\rho_{1\text{-}6}$ and $\sigma_{1\text{-}6}$ for speed, flux, and stator current regulation
- **HOSMC**: Gains $\alpha_{1\text{-}6}$, $\beta_{1\text{-}6}$, and $\delta_{1\text{-}6}$ governing speed, flux, and stator current dynamics

Table III.2– ILA parameters optimized

CONTROLLER	PARAMETERS		
	Number of variables	Lower bound (V_{min})	Upper bound (V_{max})
FOSMC	12; [s_1 e_1 s_2 e_2 s_3 e_3 s_4 e_4 s_5 e_5 s_6 e_6]	[500 0.1 500 0.001 1000 10 1000 10 1000 10 1000 10]	[15000 1000 5000 1 20000 1000 20000 1000 20000 1000 20000 1000]
SOSMC	12; [ρ_1 σ_1 ρ_2 σ_2 ρ_3 σ_3 ρ_4 σ_4 ρ_5 σ_5 ρ_6 σ_6]	[5000 100 5000 1000 5000 10 5000 10 5000 10 5000 10]	[60000 2000 15000 10000 60000 2000 60000 2000 60000 2000 60000 2000]
HOSMC	18; [α_1 β_1 δ_1 α_2 β_2 δ_2 α_3 β_3 δ_3 α_4 β_4 δ_4 α_5 β_5 δ_5 α_6 β_6 δ_6]	[1000 4000 1 4000 100 1 1000 20000 500 1000 20000 500 1000 5000 1000 1000 5000 1000]	[2000 6000 10 6000 1000 10 2000 30000 1500 2000 30000 1500 2000 15000 2000 2000 15000 2000]

The ILA algorithm was implemented in MATLAB simulations to determine optimal parameter sets for offline FOSMC, SOSMC, and HOSMC controllers, accounting for their cross-controller interactions. **Table III.3** presents the optimized gains obtained through ILA alongside those

derived from conventional trial-and-error tuning methods, enabling direct performance comparison between the approaches.

Table III.3– FOSMC, SOSMC, and HOSMC controllers' gains and performance of the tuned controllers

Tuning method	Controller	Gains										ITAEs		
		Rotor speed control			Rotor flux control			Stators currents control				$\Delta e_{\Omega mec}$	Δe_{drd}	Δe_{ds1}
Trial and Error	FOSMC	$s_1 = 1e^4$	$e_1 = 10$		$s_2 = 1e^5$	$e_2 = 1$		$s_{3\text{-}6} = 2e^4$	$e_{3\text{-}6} = 1.5e^3$			0.2	0.2	1500
	SOSMC	$\rho_1 = 10000$	$\sigma_1 = 500$		$\rho_2 = 10000$	$\sigma_2 = 1500$		$\rho_{3\text{-}6} = 10000$	$\sigma_{3\text{-}6} = 100$			0.06	0.03	1500
	HOSMC	$\alpha_1 = 5e^4$	$\beta_1 = 1.5e^3$	$\delta_1 = 10$	$\alpha_2 = 1e^3$	$\beta_2 = 5e^3$	$\delta_2 = 10$	$\alpha_{3\text{-}6} = 5e^4$	$\beta_{3\text{-}4} = 1e^3$	$\beta_{5\text{-}6} = 1e^3$	$\delta_{3\text{-}6} = 10$	0.02	0.006	1700
ILA	FOSMC	$s_1 = 1.128e^4$	$e_1 = 0.927$		$s_2 = 2.543e^3$	$e_2 = 0.017$		$s_{3\text{-}6} = 1.57e^4$	$e_{3\text{-}6} = 50.43$			0.12	0.04	1400
	SOSMC	$\rho_1 = 5.054\ e^4$	$\sigma_1 = 1.455e^3$		$\rho_2 = 1.0768e^3$	$\sigma_2 = 5.021e^3$		$\rho_{3\text{-}6} = 5.167e^4$	$\sigma_{3\text{-}6} = 1.185e^3$			0.02	0.005	1400
	HOSMC	$\alpha_1 = 1.139e^3$	$\beta_1 = 5.222\ e^3$	$\delta_1 = 1.49035$	$\alpha_2 = 5.109e^3$	$\beta_2 = 6.539e^2$	$\delta_2 = 1.790977$	$\alpha_{3\text{-}6} = 1.32e^3$	$\beta_{3\text{-}4} = 2.2e^4$	$\beta_{5\text{-}6} = 9.9e^3$	$\delta_{3\text{-}6} = 10e^2$	0.01	0.001	1300

III.6 Simulation results and Discussion

The developed control approach is tested on a 1.5 MW (DSIG) integrated within a wind turbine system through MATLAB/Simulink simulations **Figure III.1**. The study compares the effectiveness of the optimized controllers with conventional counterparts under variable wind speed conditions. The DSIG's technical specifications are provided in **Appendix D**, while optimal controller parameters for a sampling time of $T_s = 1\times10^{-5}$ seconds are presented in **Table III.3**. All analyses consider fluctuating wind speed profiles.

The obtained results are presented in **Figs. III.10-III.30**, showcasing the performance of the implemented controllers under variable wind speed conditions. **Figs. III.10-III.27** display:

- Rotor speed
- Electromagnetic torque
- Direct rotor flux
- Direct and quadrature components of stator #1 current
- Phase currents of stators #1 and #2
- Corresponding reference values

The figures include magnified views of both transient and steady-state operation and the applied wind profile. Furthermore, **Table III.4** presents the time-integral performance metrics (IAE and ISE) and THD values for each controller configuration under the variable wind speed conditions.

Based on the analysis of these graphical results and tabulated data in **Table III.4**, several key findings emerge:

- All designed controllers ensure the DSIG's measured speed, electromagnetic torque, and stator currents follow the wind profile while preserving constant rotor flux.
- The enhanced FOSM controller shows better dynamic and steady-state behavior, with lower IAE and ISE values than standard FOSMC, as evidenced in **Figs III.10-15** and **Table III.4**. In particular, the improved controllers allow actual speed, torque, flux, and stator #1 current *dq* components to accurately track their reference averages **(see Figs III.13(b)-(f) and III.15(b)-(f))** with negligible steady-state oscillations. Standard controllers produce significant ripples and steady-state errors in actual speed, torque, and flux, as visible in **Figs III.12(b)-(d)** and **III.14(b)-(d)**.
- The refined FOSMC achieves quicker speed and flux transient responses, reaching a 0.17-second

settling time versus 0.19 seconds for conventional FOSMC, shown in **Figs III.12(b)-(d)** and **III.13(b)-(d)**.

- As displayed in **Figs III.16-21** and **Table III.4**, the upgraded SOSM controller outperforms traditional versions in transient and steady-state operation, yielding smaller IAE and ISE values. Detailed examination reveals substantially reduced oscillations **(see Figs III.19(b)-(f), III.21(b)-(f), III.18(b)-(f), and III.20(b)-(f))** with the optimized design.
- The tuned HOSM controller demonstrates better performance through faster dynamics, reduced steady-state ripples, and lower IAE/ISE errors compared to standard HOSMC. These enhancements are apparent in **Figs III.22** and **III.27**, showing precise tracking of speed, torque, flux, and stator #1 current *dq* components to their references with 0.16-second settling.
- Compared to optimized FOSM and SOSM versions, the improved HOSMC provides superior transient speed, fewer steady-state oscillations, and smaller static errors. While standard HOSMC has better transient response than optimized FOSMC, the latter shows improved steady-state behavior.
- Response time measurements confirm: optimized HOSMC (0.16s), SOSMC (0.17s), and FOSMC (0.19s), establishing the HOSMC's speed advantage **(refer to Figs 13(e)-(g), 19(e)-(g), and 25(e)-(g))**.
- The optimized controllers generate cleaner stator current waveforms with substantially decreased THD levels: HOSMC (25.12%), SOSMC (28.2%), and FOSMC (30.7%), compared to conventional versions showing higher THD values of 33.85% (HOSMC), 37.04% (SOSMC), and 40.9% (FOSMC).

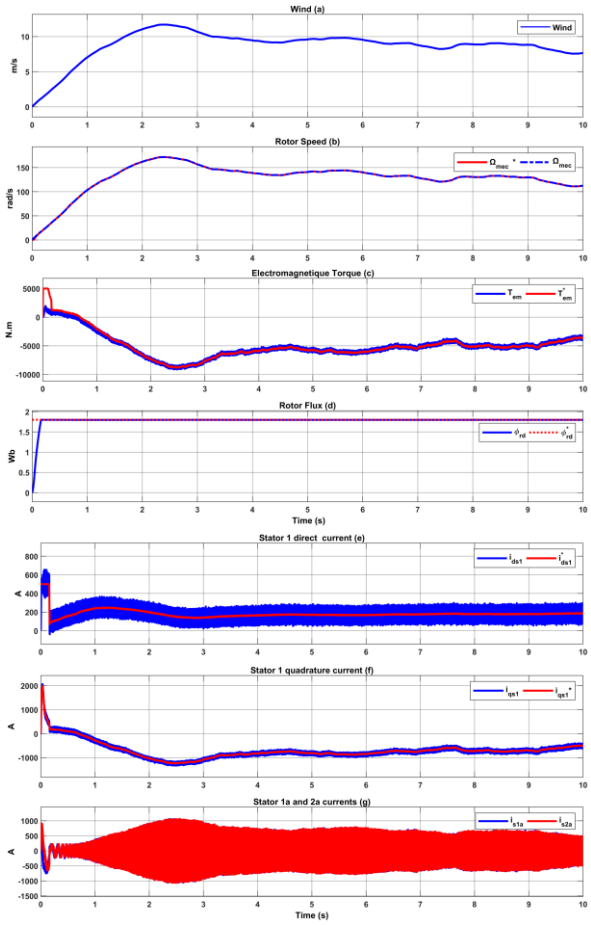

Figure III.10- Matlab results for variable wind with the conventional SM_1 regulator

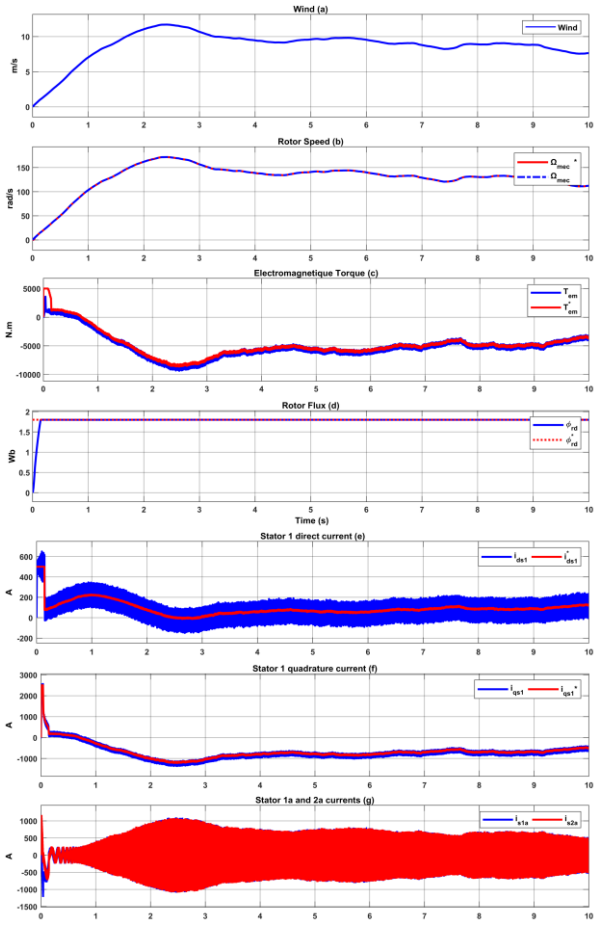

Figure III.11- Matlab results for variable wind with the optimized SM_1 regulator

Table III.4–Time-integral performance criteria and THD for different controllers

Tuning method		FOSMC						SOSMC						HOSMC						THD_{FO} %	THD_{SO} %	THD_{HO} %
		Ω_{mec}	ϕ_{rd}	i_{ds1}	i_{qs1}	i_{ds2}	i_{qs2}	Ω_{mec}	ϕ_{rd}	i_{ds1}	i_{qs1}	i_{ds2}	i_{qs2}	Ω_{mec}	ϕ_{rd}	i_{ds1}	i_{qs1}	i_{ds2}	i_{qs2}	i_{as1}	i_{as1}	i_{as1}
Trial-error	ISE	0.3	0.17	$1.5e^4$	$9e^3$	$1.5e^4$	$9e^3$	2.5	0.25	$15e^3$	$8e^3$	$15e^3$	$8e^3$	0.2	0.15	$2e^4$	$15e^3$	$2e^4$	$15e^3$	40.9%	37.04%	33.85%
	IAE	0.27	0.16	300	250	300	250	0.5	0.25	300	250	300	250	0.1	0.15	400	300	400	300			
ILA	ISE	0.09	0.15	$2e^4$	$5e^4$	$2e^4$	$5e^4$	0.2	0.15	$2e^4$	$1.2e^4$	$2e^4$	$1.2e^4$	0.01	0.02	$1e^4$	$12e^3$	$1e^5$	$12e^3$	30.7 %	28.2%	25.12%
	IAE	0.09	0.12	$4e^2$	$4e^2$	$4e^2$	$4e^2$	0.1	0.15	350	250	350	250	0.03	0.12	350	270	350	270			

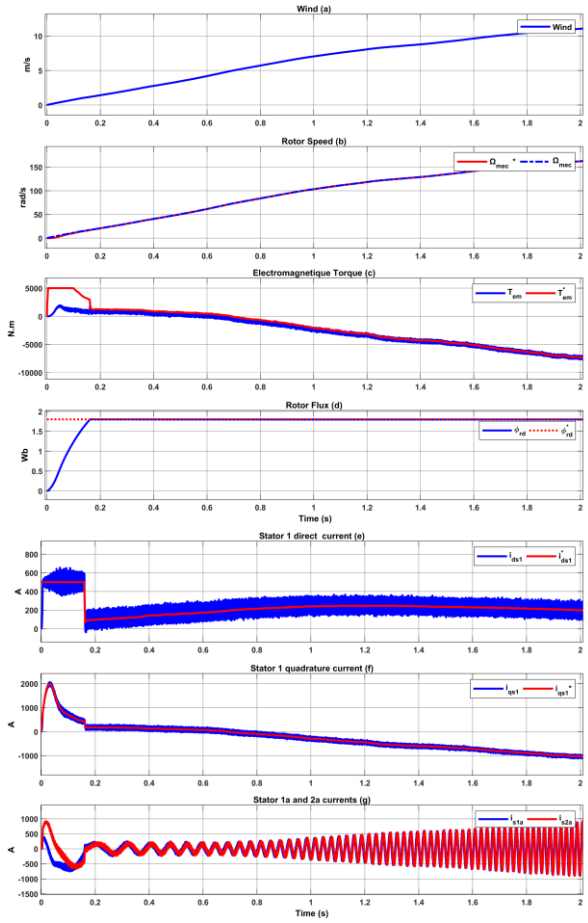

Figure III.12- Zoom in transient response matlab results with the conventional SM_1 regulator

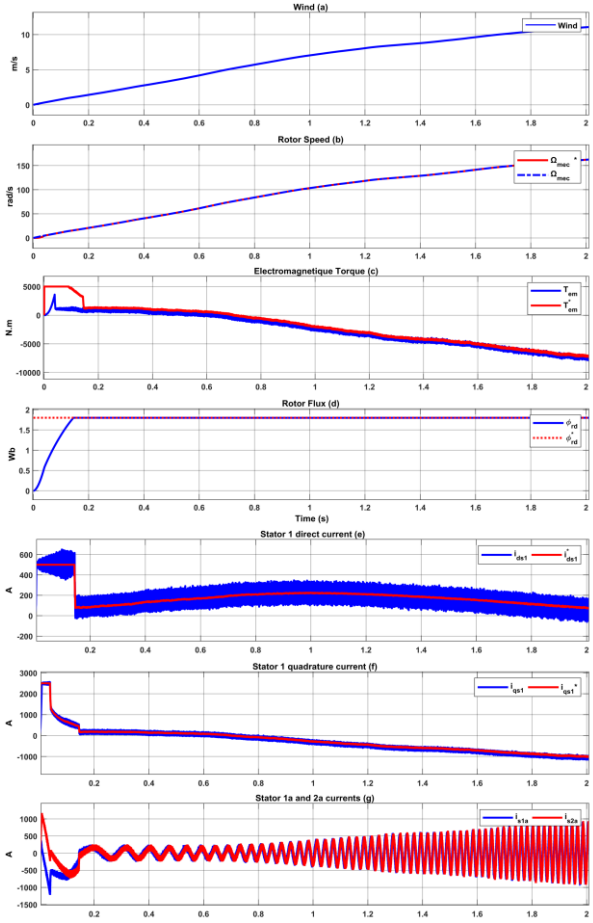

Figure III.13- Zoom in transient response matlab results with the optimized SM_1 regulator

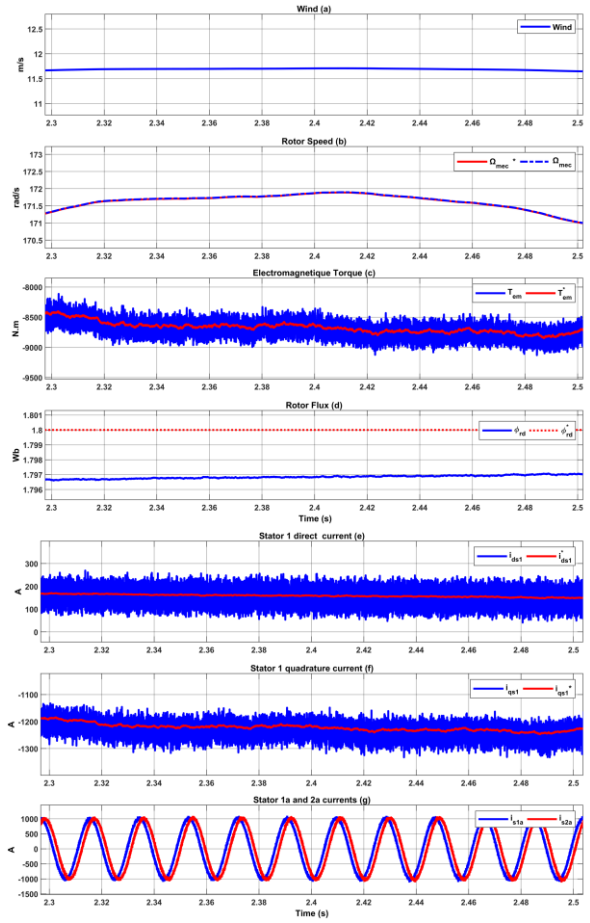

Figure III.14- Steady-state performance conventional SM_1: Matlab results Zoom in

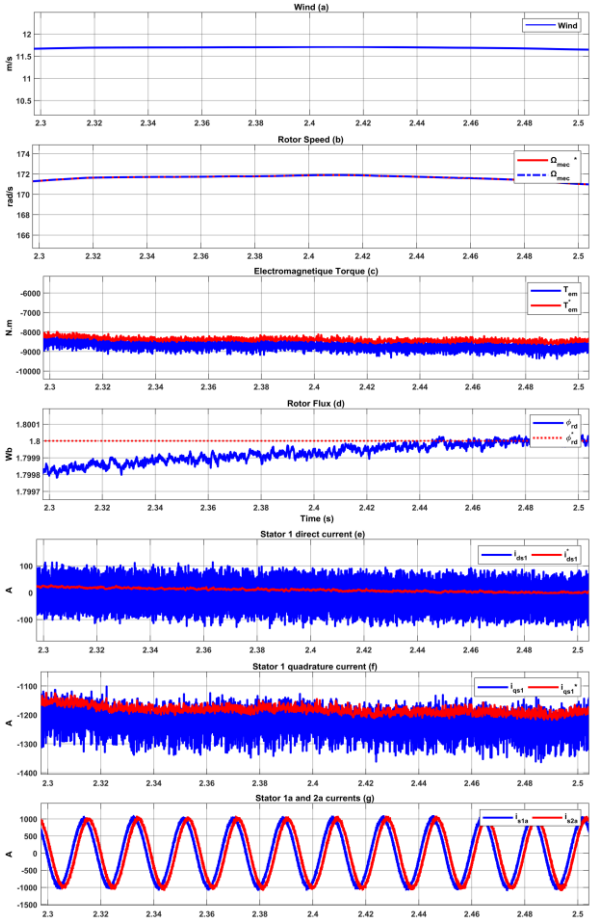

Figure III.15- Steady-state performance optimized SM_1: Matlab results Zoom in

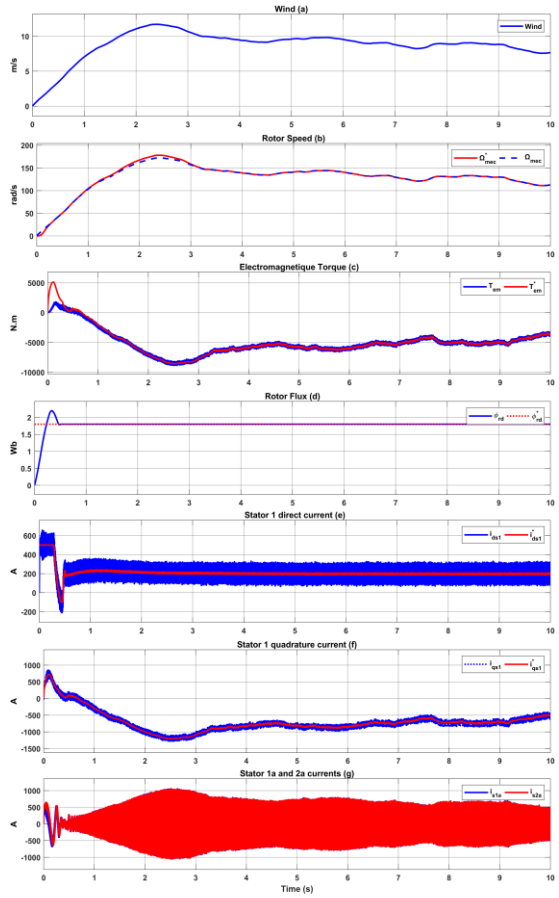

Figure III.16- Matlab results for variable wind with the conventional SM_2 regulator

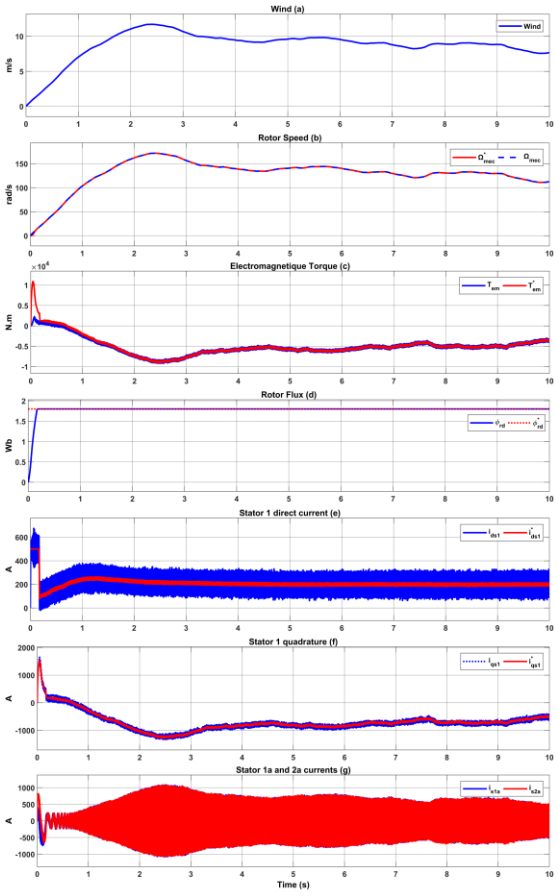

Figure III.17- Matlab results for variable wind with the optimized SM_2 regulator

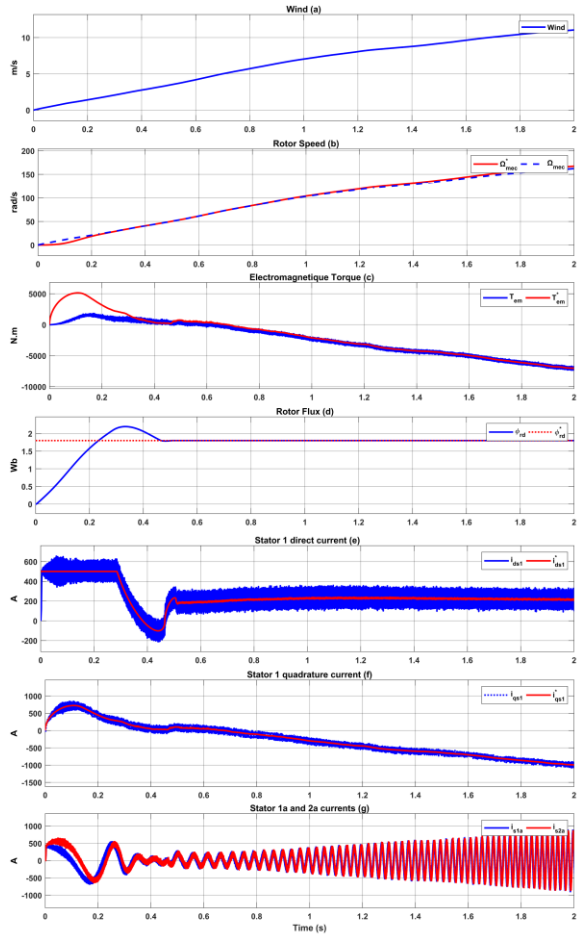

Figure III.18- Zoom in transient response matlab results with the conventional SM_2 regulator

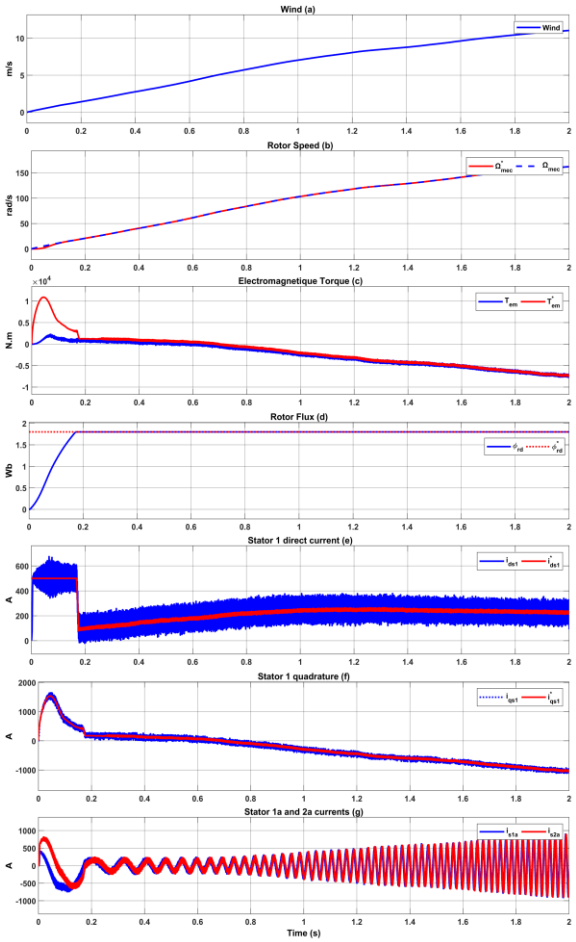

Figure III.19- Zoom in transient response matlab results with the optimized SM_2 regulator

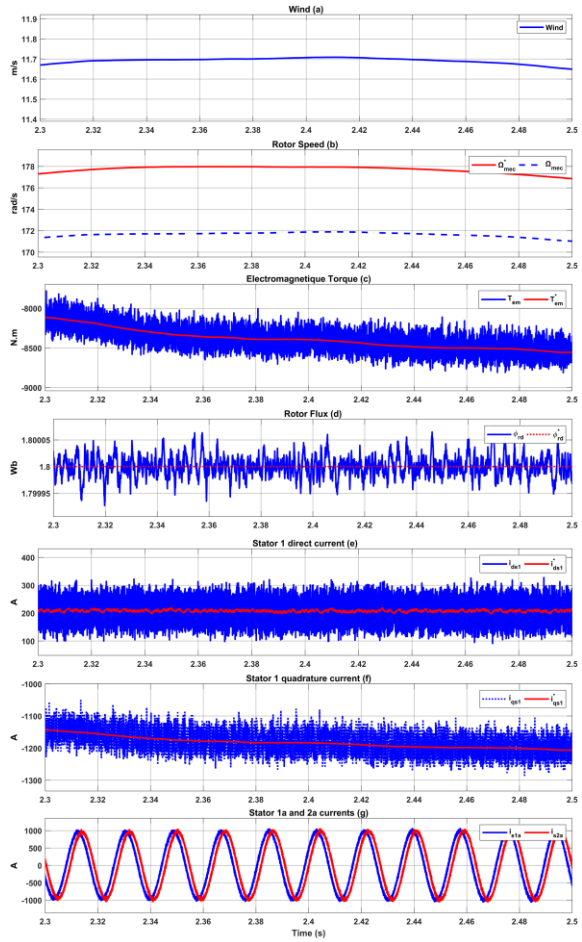

Figure III.20- Steady-state performance conventional SM_2: Matlab results Zoom in

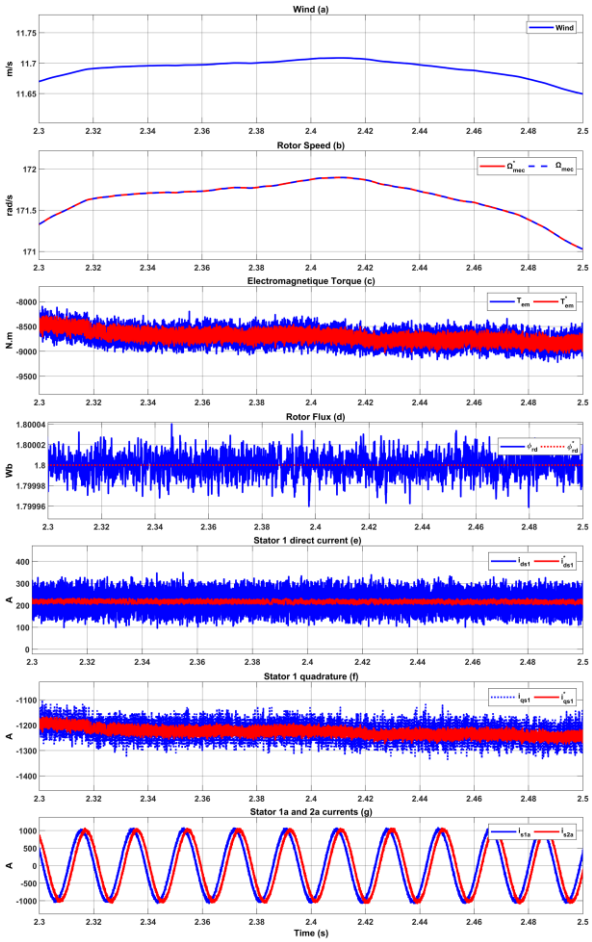

Figure III.21- Steady-state performance optimized SM_2: Matlab results Zoom in

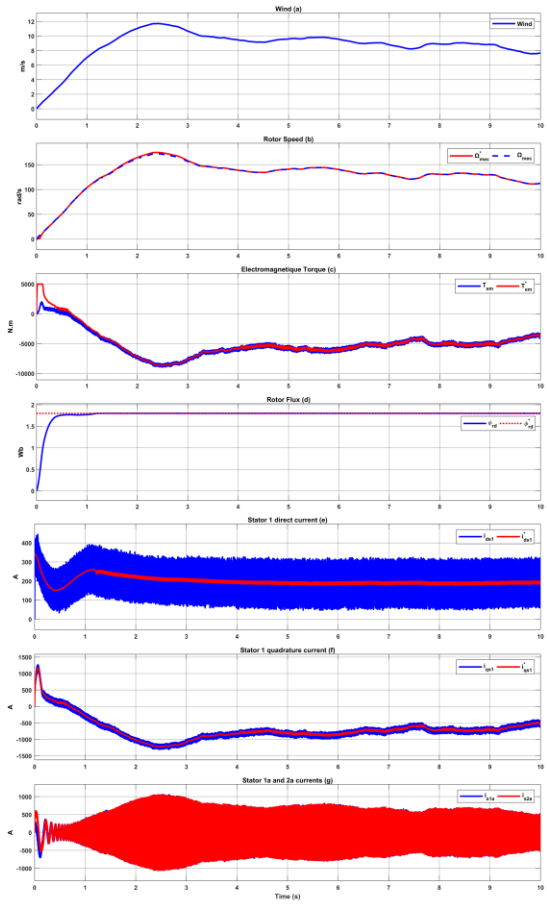

Figure III.22- Matlab results for variable wind with the conventional SM_3 regulator

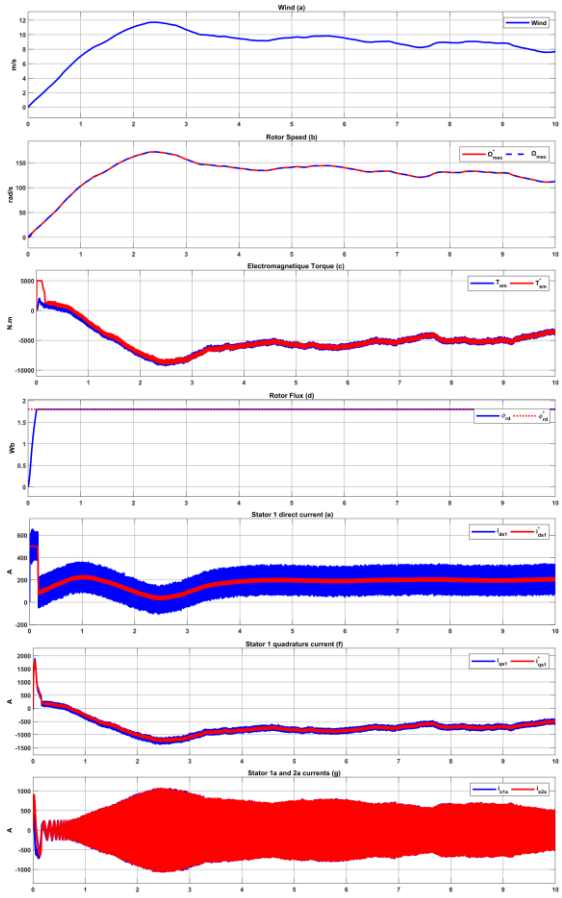

Figure III.23- Matlab results for variable wind with the optimized SM_3 regulator

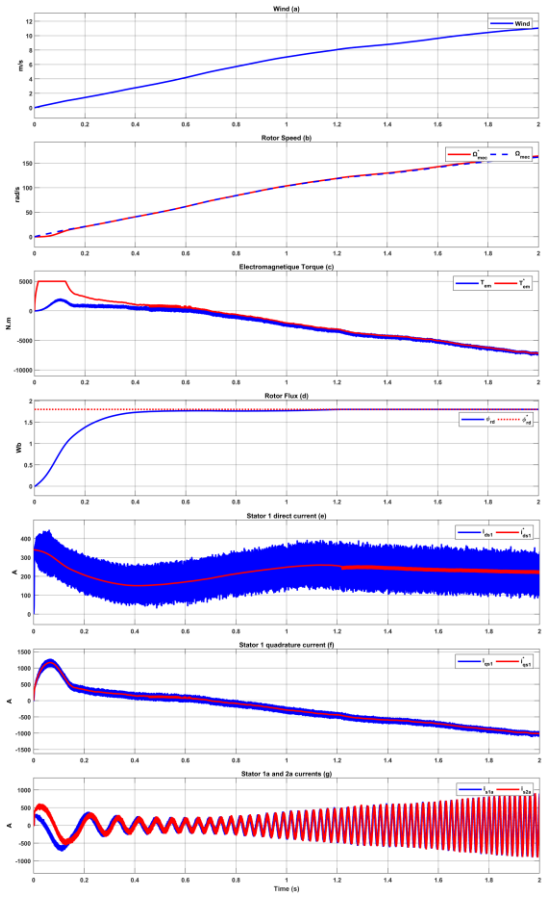

Figure III.24- Zoom in transient response matlab results with the conventional SM_3 regulator

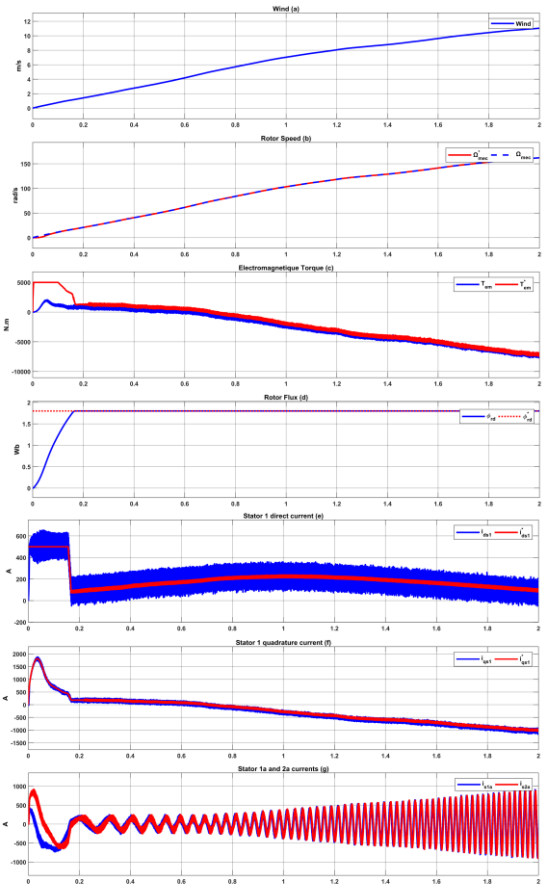

Figure III.25- Zoom in transient response matlab results with the optimized SM_3 regulator

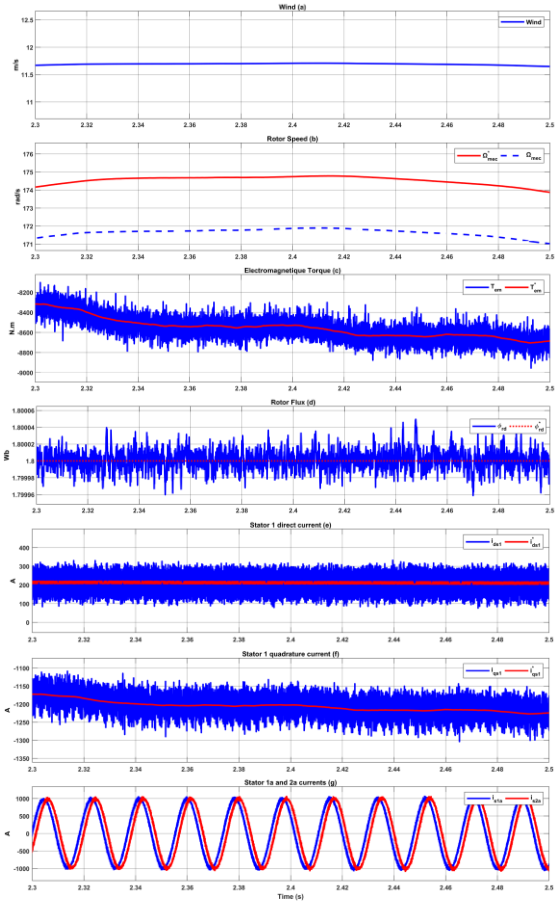

Figure III.26- Steady-state performance conventional SM_3: Matlab results Zoom in

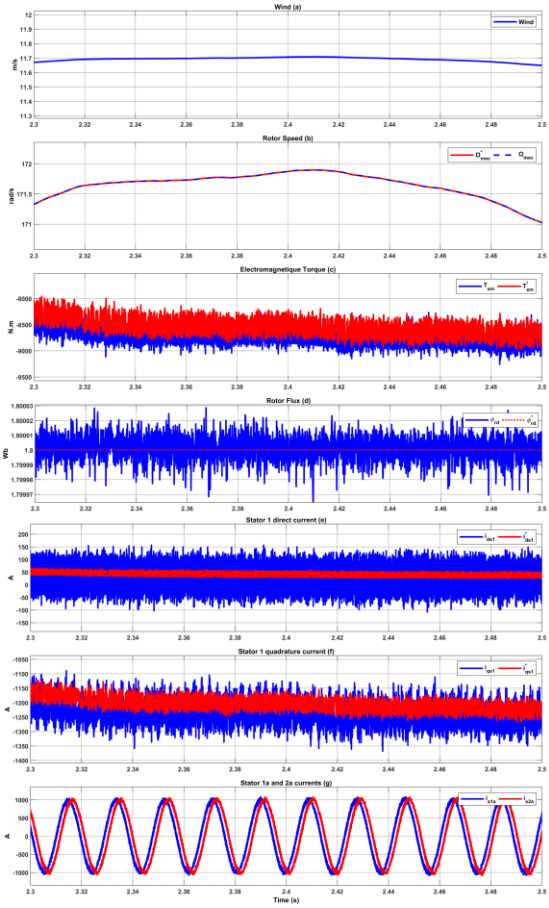

Figure III.27- Steady-state performance optimized SM_3: Matlab results Zoom in

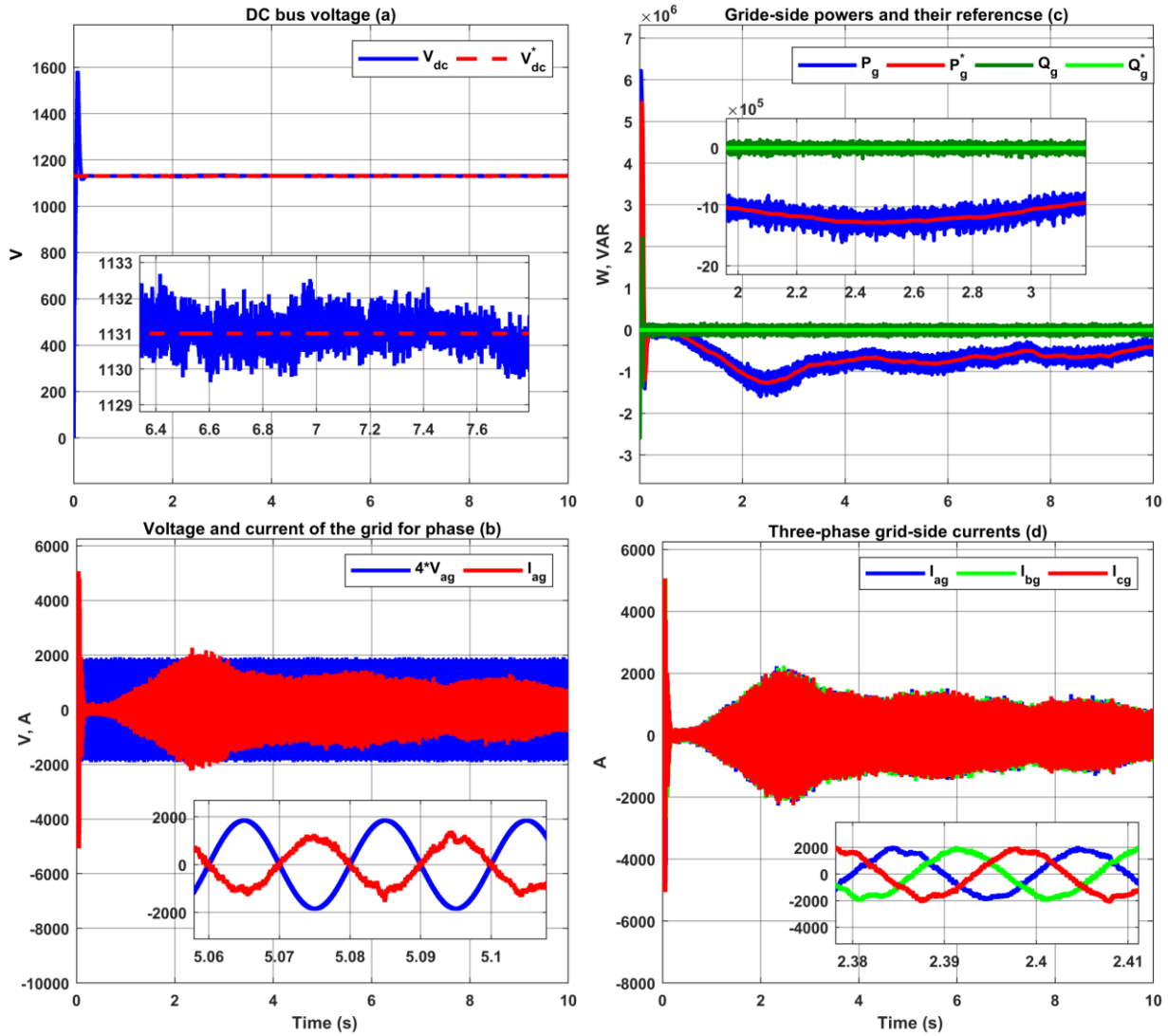

Figure III.28- Grid-side SM_1 results

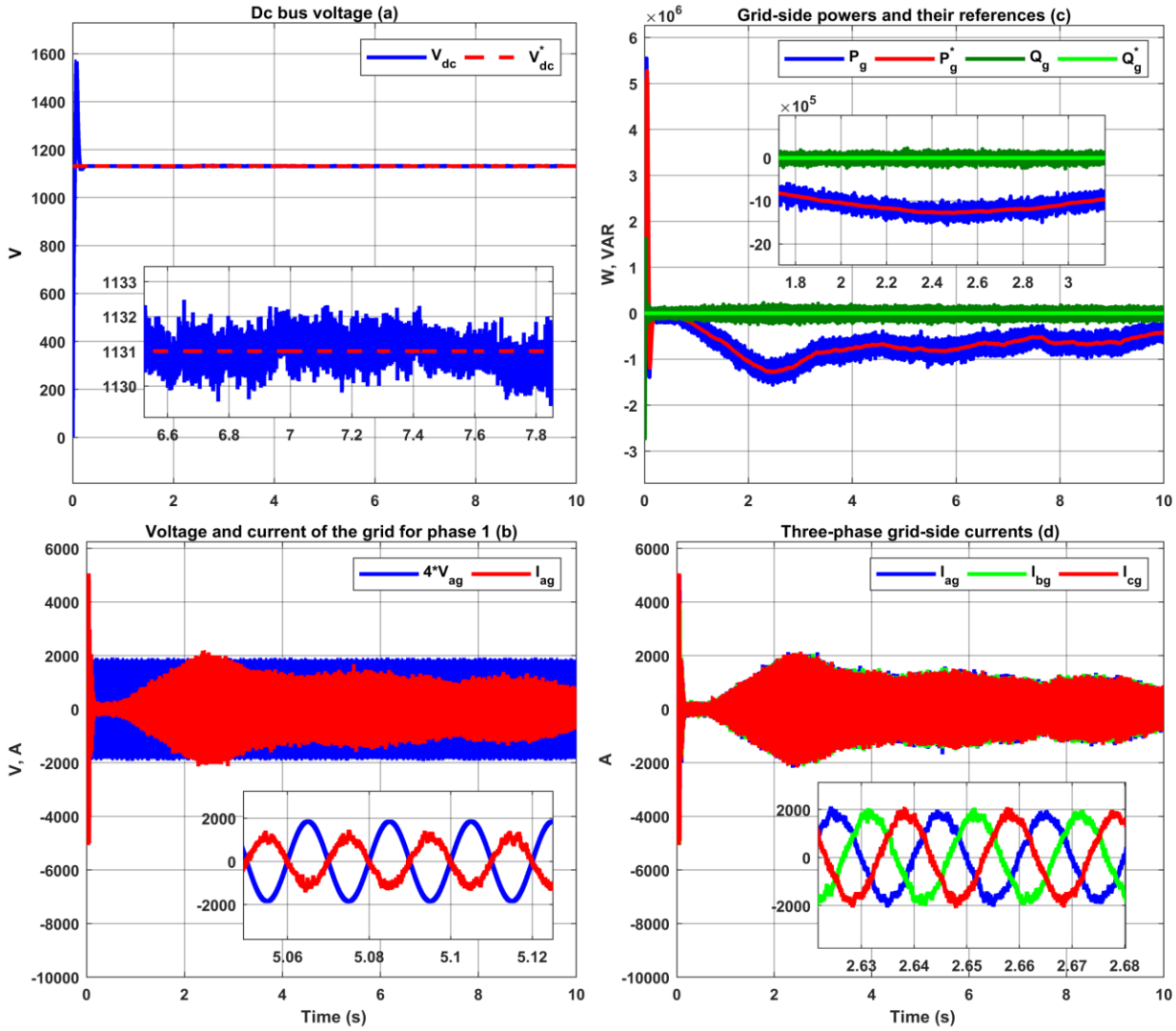

Figure III.29- Grid-side SM_2 results

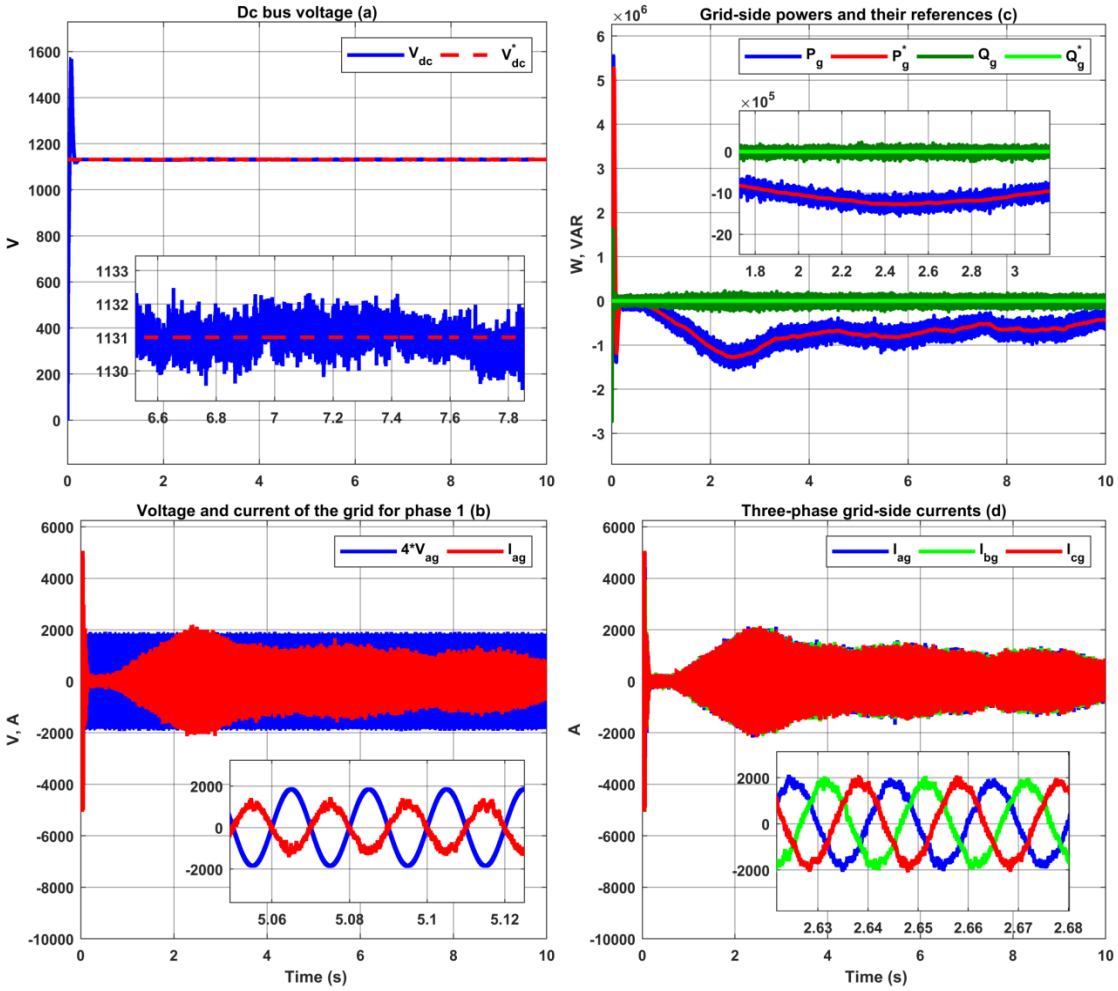

Figure III.30- Grid-side SM_3 results

III.7 Conclusion

This chapter explores advanced SMC techniques for optimizing the performance of a (DSIG) in wind turbine systems. The study introduces first-order (FOSMC), second-order (SOSMC), and high-order sliding mode control (HOSMC), each addressing key challenges such as chattering, steady-state ripple, and dynamic response. The proposed Intelligent-in-Time Logic Algorithm (ILA) plays a pivotal role in tuning controller parameters by minimizing the Integral Time Absolute Error (ITAE), demonstrating superior efficiency compared to conventional trial-and-error methods and outperforming 19 benchmark optimization algorithms, including GA and PSO. Simulation results validate the effectiveness of these optimized controllers, with HOSMC achieving the fastest transient response (0.16s settling time), the lowest steady-state ripple, and significantly reduced total harmonic distortion (25.12% vs. 33.85% in conventional HOSMC. The improved tracking of speed, flux, and current references, along with enhanced stability and power quality, underscores the practical benefits of this approach in real-world wind energy systems. By combining metaheuristic optimization with higher-order sliding mode control, this research presents a robust and adaptive control framework that enhances the reliability and efficiency of DSIG-based wind turbines, contributing to the advancement of renewable energy technologies.

Chapter IV. Hardware-in-the-loop (HIL) testing using RT-BOX1

Chapter IV. Hardware-in-the-loop (HIL) testing using RT-BOX1

IV.1 Introduction

Developing and validating advanced control strategies for renewable energy systems, such as wind turbines, requires a robust framework to bridge the gap between theoretical simulations and real-world implementation. HIL testing has emerged as a critical tool, enabling engineers to evaluate control algorithms in a real-time environment without the risks and costs associated with physical prototypes. This chapter focuses on applying RT-BOX1, a high-performance real-time simulation platform developed by Plexim for HIL testing of a WT-DSIG system. The study examines the optimization and comparative performance of advanced control strategies under variable wind conditions, including PI, BS, and HOSMC. A key aspect of this work is the detailed workflow for transitioning control models from Simulink MATLAB to PLECS and finally deploying them on the RT-BOX1 platform, with emphasis on ensuring real-time compatibility. Through experimental validation, the chapter highlights the effectiveness of a novel tuning technique in improving key performance metrics such as settling time, tracking accuracy (measured by IAE and ISE), and power quality (assessed via THD). The results demonstrate the superior performance of optimized HOSMC in terms of dynamic response and stability, while also showcasing the broader practical implications for enhancing the resilience and efficiency of WT-DSIG systems under fluctuating wind conditions. By integrating theoretical control design with real-time HIL validation, this chapter provides a comprehensive and scalable approach for developing reliable and high-performance wind energy systems, underscoring the critical role of optimization and advanced simulation platforms like RT-BOX1 in modern control engineering.

IV.2 Hardware-in-the-loop (HIL) testing

Figure IV.1 illustrates the block diagram of the Hardware-in-the-Loop concept, a powerful real-time simulation technique used in the development and testing of power electronic systems. The HIL includes a Host PC to develop models and control design, a Real-Time Simulator enabling the system model execution in real time on CPU and FPGA, and a device under test that represents the actual physical system being tested and communicates with the simulator through input/output devices.

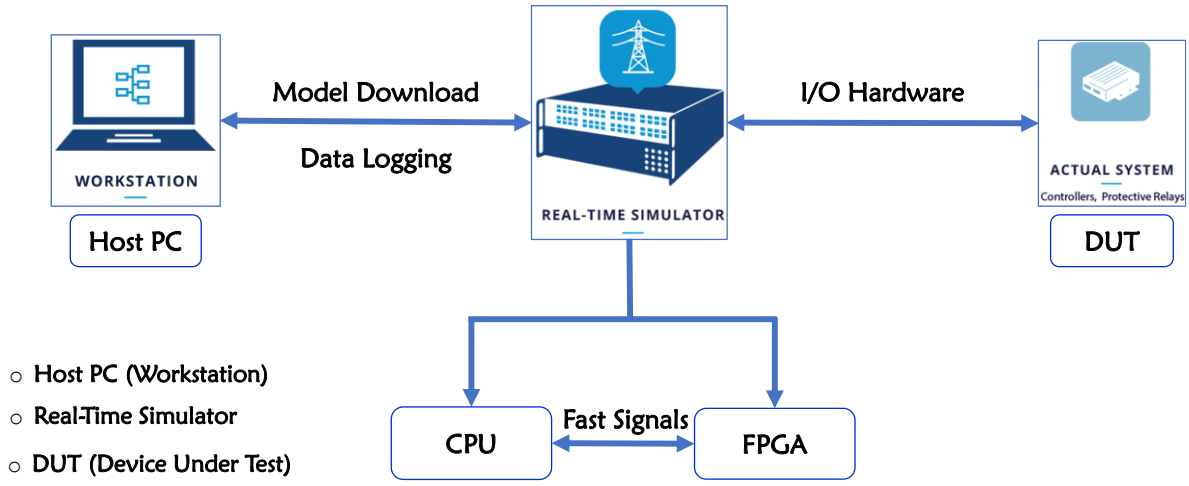

Figure IV.1. Hardware-in-the-loop implementation.

IV.3 RT-BOX1 Overview

The RT-BOX1, with a real photo shown in **Figure IV.2**, enables high-performance HIL simulations of power electronic systems, where the real controller interacts with a virtual power circuit. It offers fast real-time simulation with 1 µs resolution for high-speed computation using an FPGA and a multicore processor. Additionally, it integrates sensors/actuators through analogue/digital I/O.

Figure IV.2. RT-BOX1.

IV.4 The process of transitioning from Simulink (MATLAB) to Plecs and then implementing the model on RT Box1 for real-time simulation

As **Figure IV.3** shows, we first built the simulation model in MATLAB, then converted it to the Plexim software, which enables HIL implementation in RT-BOX1. In the following section, we will describe step-by-step the HIL implementation in RT-BOX1.

Figure IV.3. HIL implementation in RT-BOX1.

IV.2.1 Step 1: Convert the Simulink model to PLECS

Simulink and PLECS have different modeling environments, so no direct conversion tool exists. You need to manually rebuild the model in PLECS while ensuring equivalent functionality.

IV.2.1.1 Analyze the Simulink model

- Open your existing Simulink model and identify all key components, such as:
  - **Power electronics** (MOSFETs, IGBTs, diodes, inductors, capacitors)
  - **Control algorithms** (PI controllers, filters, lookup tables)
  - **Sources** (voltage/current sources, grid connections)
  - **Sensors** (voltage and current measurements)
  - **Load elements** (resistive, inductive, or complex loads)
- Check the **solver settings** in Simulink (usually variable-step for offline simulation) and note the sample time of discrete controllers.

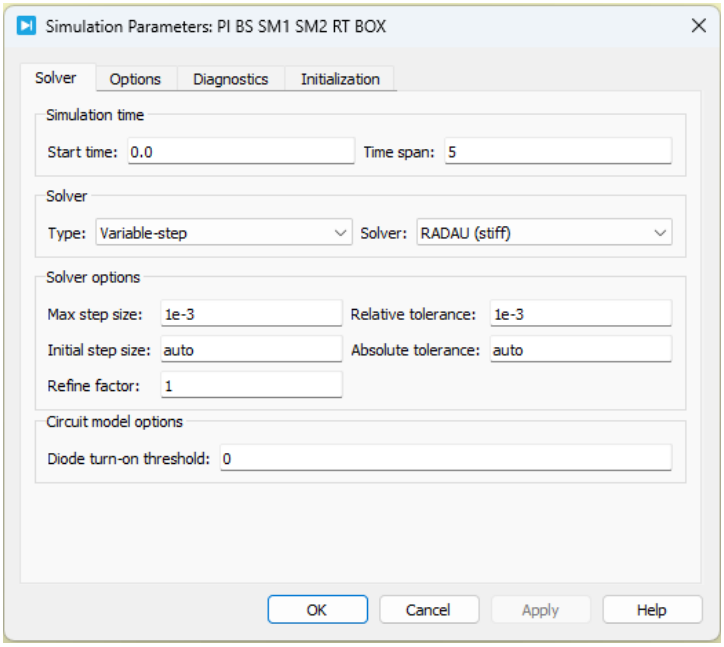

Figure IV.4. Simulation parameters on the PLECS software.

IV.2.1.2 Rebuild the Model in PLECS

- Open PLECS and start a **new schematic**.
- For power electronics:

  - Use **PLECS circuit components** such as IGBTs, diodes, capacitors, and inductors.
  - If using Simscape in Simulink, replace those elements with **PLECS circuit equivalents**.
- For control algorithms:
  - If your Simulink model uses discrete control blocks, replicate them using **PLECS Discrete Blocks** (Gain, Sum, Integrator, Transfer Function).
  - If using MATLAB scripting, implement equivalent functionality in PLECS using **C-Script** blocks or PLECS functions.

IV.2.1.3 Verify Model Equivalence

- Run **simulation tests in PLECS** to ensure the new model behaves like the original Simulink model.
- Compare **both simulations' output waveforms (voltage, current, power)**.
- Adjust parameters such as controller gains, PWM switching frequency, or solver settings if discrepancies exist.

IV.2.2 Step 2: Prepare PLECS Model for Real-Time Execution on RT Box

Since RT Box is a **real-time simulator**, the model must be optimized to ensure real-time execution without computational delays.

IV.2.2.1 Configure Fixed-Step Simulation

- Open **Simulation → Simulation Parameters** in PLECS.
- Set the solver to **Fixed Step** and specify a step size (e.g., 1-10 µs) based on RT Box processing speed.

IV.2.2.2 Optimize Model for Real-Time Execution

- Check computational load using the **PLECS Profiler** to ensure execution time per step is below the RT Box cycle time.
- Replace blocks that are not real-time compatible:
  - **Avoid variable-step solvers** and use fixed-step discretization.
  - **Remove algebraic loops** (use delay elements if necessary).
  - **Replace complex mathematical functions** (such as heavy trigonometric functions) with lookup tables.

IV.2.2.3 Add Required I/O Blocks for Hardware Implementation

- If the model requires external connections (e.g., PWM signals, ADC inputs), insert **RT Box I/O blocks**:
  - **Analog/Digital Inputs** for sensor readings.
  - **PWM Outputs** for controlling power converters.

- **Communication Interfaces** (SPI, UART, CAN) if interacting with external controllers.

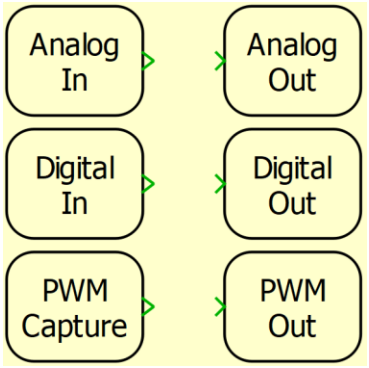

Figure IV.5. Required I/O Blocks.

IV.2.3 Step 3: Deploy the model on RT Box

Once the model is compatible with real-time, you can generate and deploy the code to RT Box.

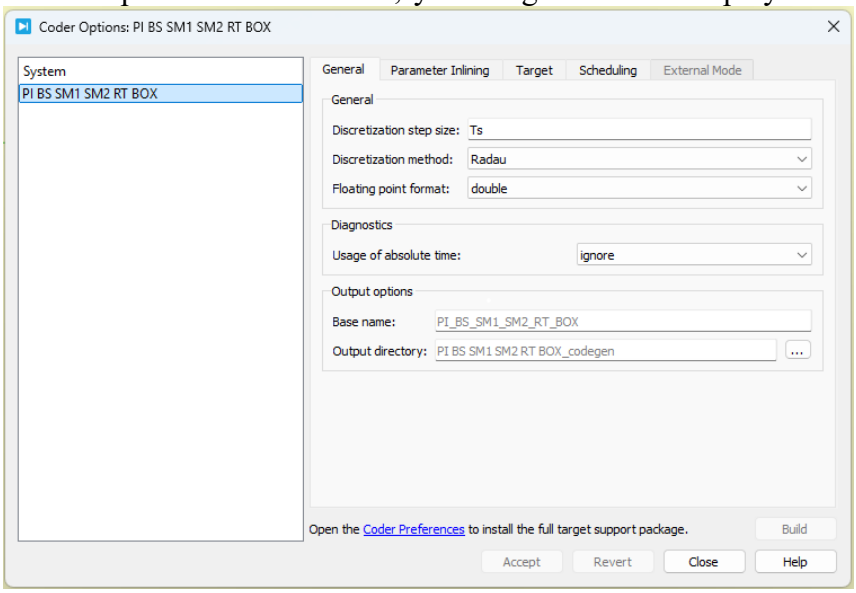

Figure IV.6. Coder options.

IV.2.3.1 Configure RT Box as the Target Hardware

- In PLECS, go to **System → Target for RT Box**.
- Select the appropriate RT Box version (RT Box 1, 2, or 3).
- Set the processor frequency and sample time.

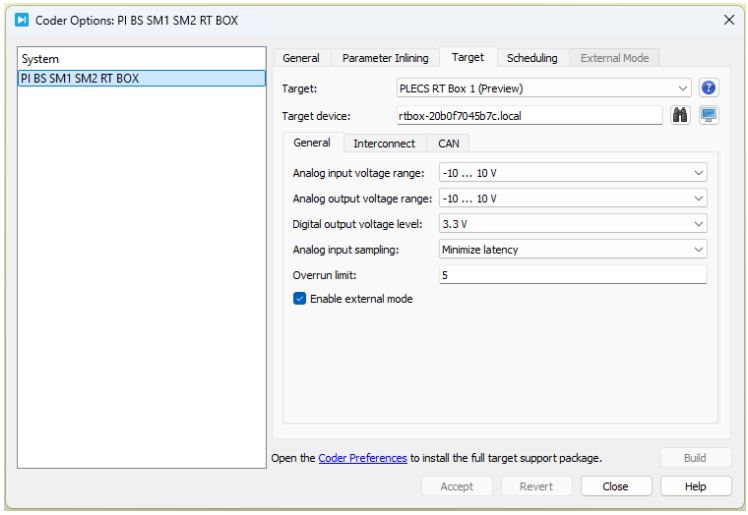

Figure IV.7. Target for RT Box.

IV.2.3.2 Generate Code and Deploy

- Enable **Code Generation** in PLECS.
- Compile and generate the real-time executable.
- Transfer the compiled model to **RT Box** using the PLECS RT Box software.

IV.2.3.3 Connect RT Box to External Hardware (if required)

- Use **digital I/Os** to send PWM signals to power converters.
- Connect **analog inputs** for real-time voltage and current sensing.
- If required, interface with an **external microcontroller or FPGA** using SPI/CAN/UART.

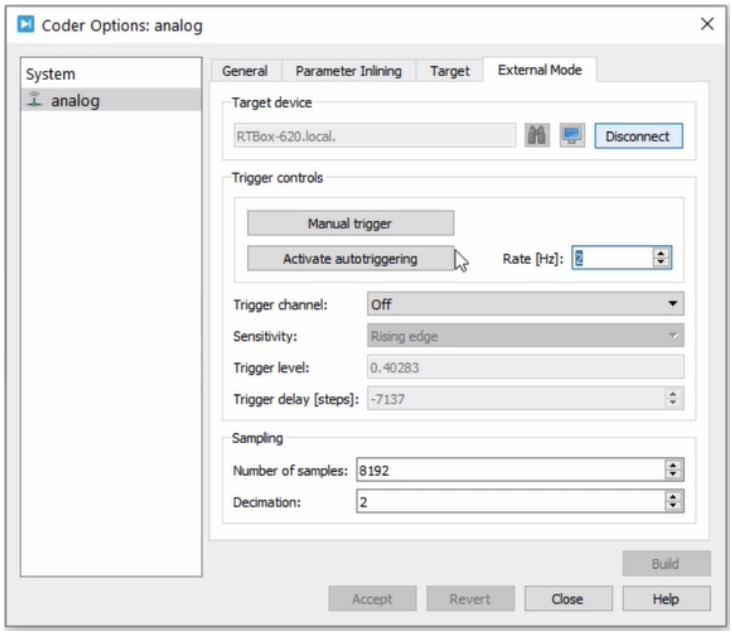

Figure IV.8. External Hardware.

IV.2.3.4 Run and Monitor the Real-Time Simulation

- Start the real-time execution from the **PLECS RT Box GUI**.
- Use the **PLECS Scope** or an oscilloscope to monitor real-time signals.
- Tune parameters and test system response.

IV.3 Hardware-In-The-Loop Results

IV.3.1 PI and Backstepping Controller Results

The hardware-in-the-loop (HIL) methodology employing the RT-BOX platform combines real-time simulation with physical hardware components to enable safe and efficient control system validation. The RT-BOX real-time simulator serves as a critical interface between virtual simulation environments and actual hardware devices. In this configuration, the system under test (e.g., a controller) interacts with a real-time simulated environment running on the RT-BOX, which accurately emulates the dynamic behavior of the target plant. Through continuous bidirectional data exchange, the RT-BOX provides realistic feedback to the physical controller, mimicking actual operating conditions. This approach enables comprehensive testing of control algorithms and hardware systems while avoiding the costs and risks associated with full-scale physical prototypes. The RT-BOX platform finds particular utility in automotive, aerospace, and renewable energy applications where field testing may be hazardous, prohibitively expensive, or logistically challenging. By facilitating early design validation and problem identification, HIL testing with RT-BOX significantly reduces development cycles while enhancing final system reliability.

The proposed control strategy for a 1.5 MW DSIG integrated within a wind turbine system is experimentally validated using the Plecs/RT-Box platform **Figure IV.9**. The study compares the performance of optimized controllers against conventional designs under variable wind speed conditions, with the DSIG specifications detailed in **Appendix D** and optimal controller parameters provided in **Table IV.1** (sampling time $T_s = 2\times10^{-5}$ s). The system configuration in **Figure IV.9** utilizes analog outputs to transmit system measurements to the control stage, while switch commands are communicated via PWM outputs to PWM capture interfaces.

The experimental results are presented in **Figures IV.10-IV.21**, demonstrating controller performance under dynamic wind conditions. These figures illustrate:

- Rotor speed tracking
- Electromagnetic torque response
- Direct rotor flux regulation
- *dq*-axis components of stator #1 current
- Phase currents for both stators (#1 and #2)
- Corresponding reference values

The plots include detailed transient and steady-state operation zooms along with the applied wind profile. **Table IV.2** comprehensively documents each controller configuration's quantitative performance metrics (IAE, ISE, and THD values).

The experimental data presented in these figures and **Table IV.2** demonstrate:

- All implemented controllers successfully maintain the DSIG's measured speed, electromagnetic torque, and stator currents following the wind profile while preserving constant

rotor flux.

- The enhanced PI controller demonstrates superior transient and steady-state performance with significantly reduced IAE and ISE errors compared to conventional PI regulators, as evidenced in **Figs IV.12-15** and **Table IV.2**. Specifically, the optimized controllers enable precise tracking of actual speed, electromagnetic torque, flux, and stator #1 current *dq* components to their reference values **(see Figs IV.13(a)-(e))** with minimal steady-state ripple. In contrast, conventional controllers exhibit substantial ripple and steady-state deviations in these parameters **(Figs IV.12(a)-(c))**.
- The improved PI controller achieves faster transient response with a settling time (t_s) of approximately 0.3s versus 0.4s for traditional PI controllers, as shown in **Figs IV.14** and **IV.15**.
- Similarly, the optimized BS controller shows excellent performance characteristics, including rapid dynamic response, negligible steady-state ripple, and low IAE/ISE errors compared to conventional BS implementations. These improvements are visible in **Figs IV.18** and **IV.19**, where speed, torque, flux, and current components accurately track their references with a settling time of about 0.1s.
- The refined BS controller provides superior transient response and lower steady-state error than the optimized PI controller. While traditional BS outperforms optimized PI in transient response, the optimized PI maintains better steady-state performance.
- Implementation of optimized regulators produces high-quality sinusoidal stator current waveforms with substantially reduced THD values: 0.8103% for PI and 0.5047% for BS controllers, compared to conventional versions showing higher THD levels of 3.3456% (PI) and 2.8665% (BS).

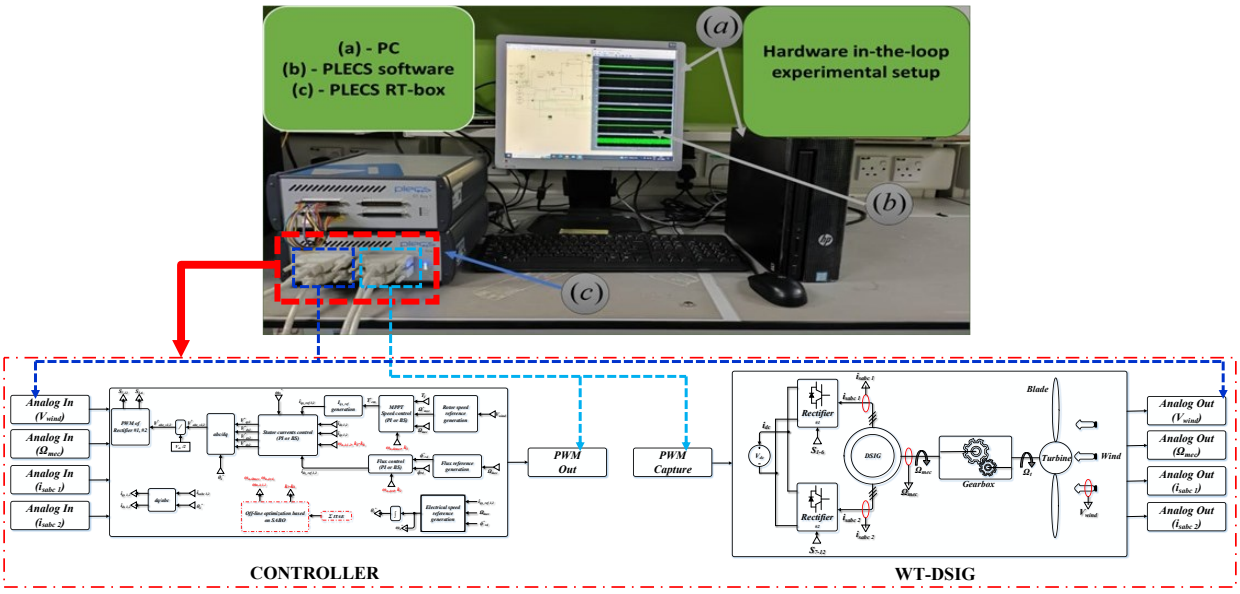

Figure IV.9. Hardware-in-the-loop experimental setup with PI and BS controllers.

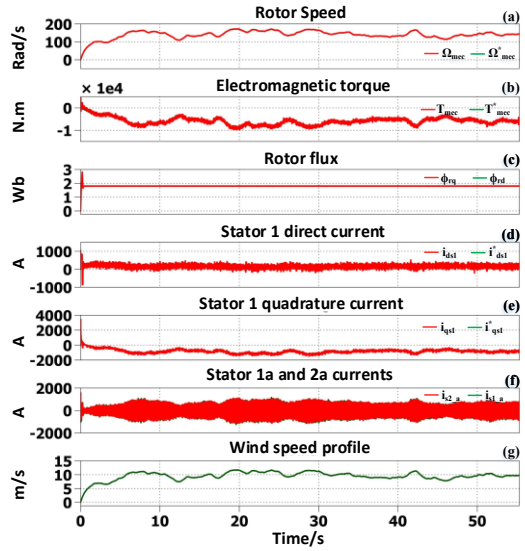

Figure IV.10. HiL results for variable wind with the conventional PI regulator.

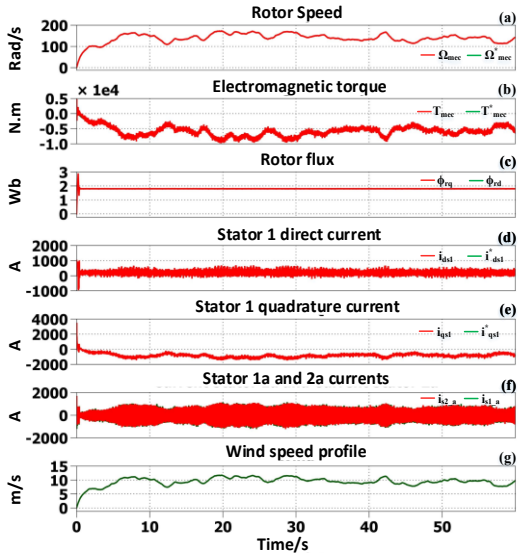

Figure IV.11. HiL results for variable wind with the optimized PI regulator.

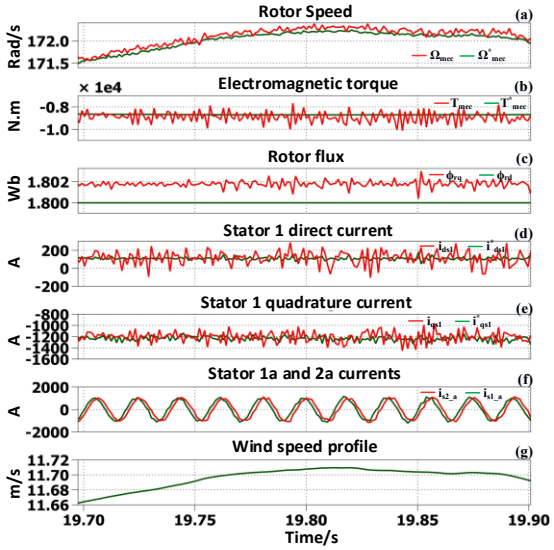

Figure IV.12. Steady-state performance: HiL results, Zoom in with the conventional PI regulator.

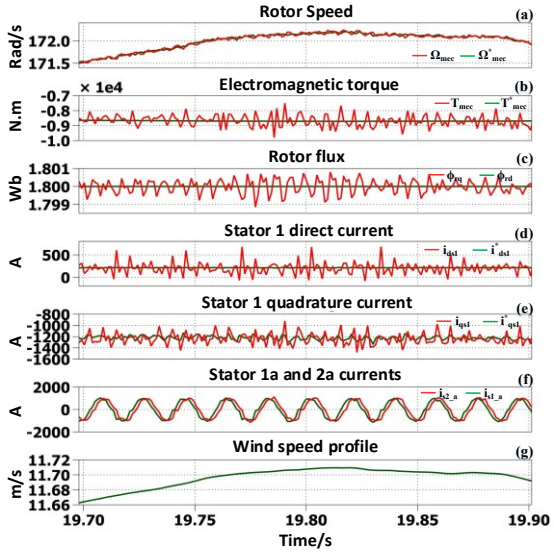

Figure IV.13. Steady-state performance: HiL results, Zoom in with the optimized PI regulator

Table IV.1– PI and BS controllers' gains and performance of the tuned controllers

Tuning method	Controller	Gains			ITAEs		
		Rotor speed control	Rotor flux control	Stators currents control	$\Delta e_{\Omega mec}$	$\Delta e_{\phi rd}$	Δe_{ids1}
Trial and Error	PI	$\omega_{n\text{-}\Omega mec} = 600$	$\omega_{n\text{-}\phi rd} = 65$	$\omega_{n\text{-}is1,2} = 2000$	0.3802	0.0278	23.3987
SABO	BS	$k_1 = 2000$	$k_2 = 5000$	$k_{3\text{-}6} = 30000$	0.1058	0.1464	8.4616
	PI	$\omega_{n\text{-}\Omega mec} = 402.123$	$\omega_{n\text{-}\phi rd} = 48.10$	$\omega_{n\text{-}is1,2} = 2227.17$	0.0248	0.6747	7.2567
	BS	$k_1 = 2.3424e^{+3}$	$k_2 = 8.8016e^{+3}$	$k_{3\text{-}6} = 1.8747e^{+4}$	0.0626	0.0247	0.0569

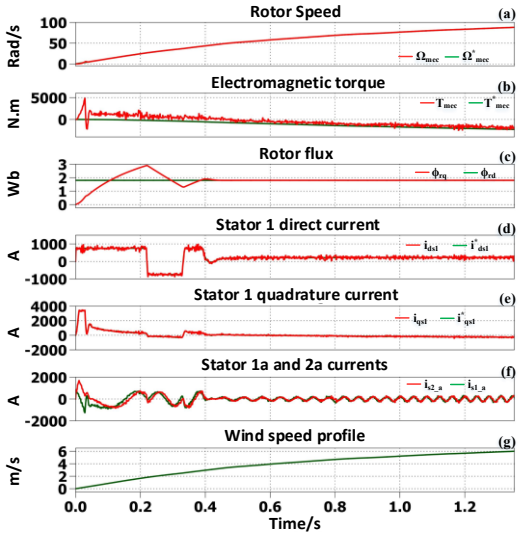

Figure IV.14. Zoom in transient response HiL results with the conventional PI regulator.

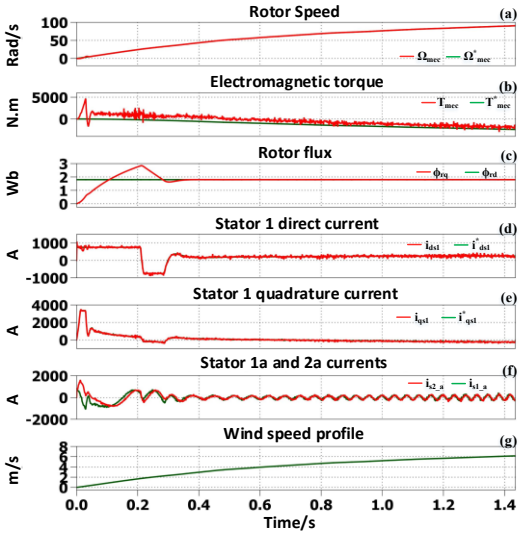

Figure IV.15. Zoom in transient response HiL results with the optimized PI regulator.

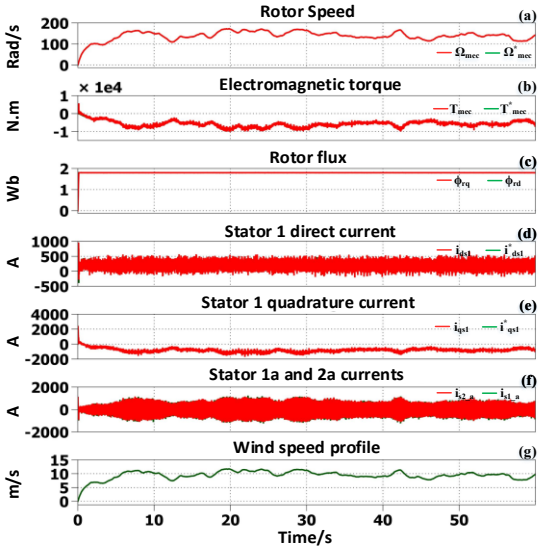

Figure IV.16. HiL results for variable wind with the conventional BS regulator.

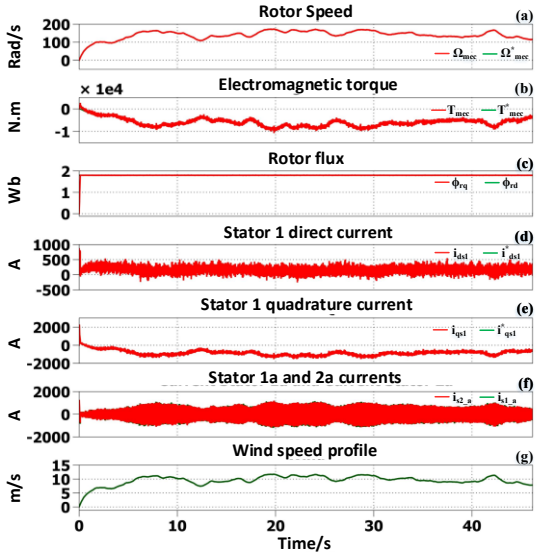

Figure IV.17. HiL results for variable wind with the optimized BS regulator.

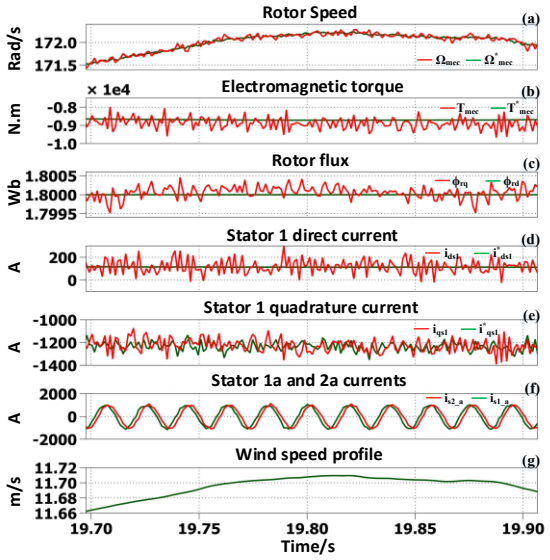

Figure IV.18. Steady-state performance: HiL results. Zoom in with the conventional BS regulator.

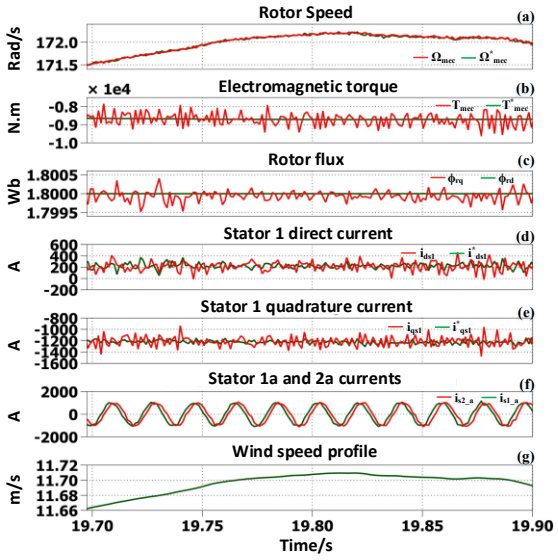

Figure IV.19. Steady-state performance: HiL results. Zoom in with the optimized BS regulator.

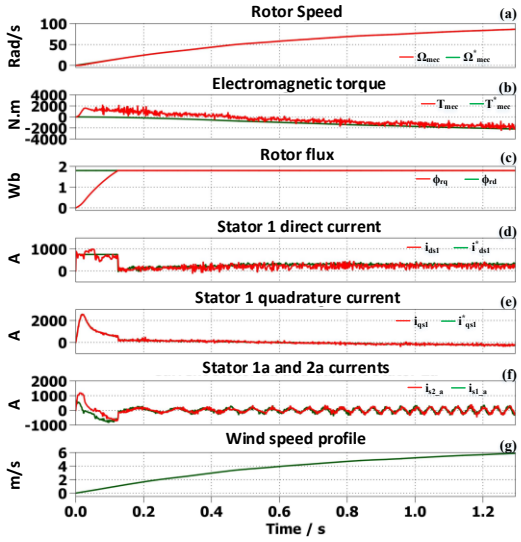

Figure IV.20. Zoom in transient response HiL results with the conventional BS regulator

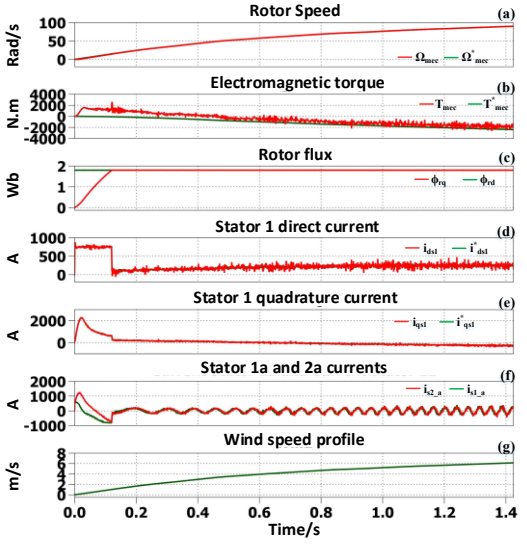

Figure IV.21. Zoom in transient response HiL results with the optimized BS regulator

Table IV.2– Time-integral performance criteria and THD for different controllers (PI and BS)

Tuning method		PI						BS						THD_{PI}%	THD_{BS}%
		Ω_{mec}	ϕ_{rd}	i_{ds1}	i_{qs1}	i_{ds2}	i_{qs2}	Ω_{mec}	ϕ_{rd}	i_{ds1}	i_{qs1}	i_{ds2}	i_{qs2}	i_{as1}	i_{as1}
Trial-error	ISE	0.19	0.18	$3e^5$	$8e^5$	$3e^5$	$8e^5$	0.18	0.12	$2e^5$	$7e^5$	$2e^5$	$7e^5$	3.3456%	2.8665%
	IAE	2.1	0.2	$3e^3$	$5e^3$	$3e^3$	$5e^3$	2	0.15	$3e^3$	$4e^3$	$3e^3$	$4e^3$		
SABO	ISE	0.16	0.17	$3e^5$	$4e^5$	$3e^5$	$4e^5$	0.14	0.12	$2e^5$	$3e^5$	$2e^5$	$3e^5$	0.8103%	0.5047%
	IAE	2	0.2	$3e^3$	$4e^3$	$3e^3$	$4e^3$	1	0.1	$3e^3$	$4e^3$	$3e^3$	$4e^3$		

IV.3.2 First, second, and high-order sliding mode controllers results

The simulation results are presented in **Figs. IV.23-IV.44** demonstrate the controllers' performance under both variable and step-change wind speed conditions. For the variable wind speed profile **(Figs. IV.23-IV.40)**, the figures show each controller's response in terms of rotor speed, electromagnetic torque, direct rotor flux, *dq*-axis components of stator #1 current, and phase

currents of stators #1 and #2, along with their reference values, including zoomed views of transient and steady-state operation and the applied wind profile. The HOSMC-specific responses to wind speed step changes are depicted in **Figs. IV.41-IV.44**, displaying the same measured signals. Furthermore, **Table IV.4** summarizes the time-integral performance criteria (IAE and ISE) and THD values for each controller under variable wind speed conditions.

Analysis of the presented data in these figures and **Table IV.4** reveals:

- All implemented controllers successfully maintain the DSIG's measured speed, electromagnetic torque, and stator currents following the wind profile while keeping rotor flux constant.
- The enhanced FOSM controller demonstrates superior transient and steady-state performance with reduced IAE and ISE errors compared to conventional FOSMC, as evidenced in **Figs IV.23-28** and **Table IV.4**. Specifically, the optimized controllers enable precise tracking of actual speed, electromagnetic torque, flux, and stator #1 current dq components to their reference values **(see Figs IV.26(a)-(e) and IV.28(a)-(e))** with minimal steady-state ripple. In contrast, conventional controllers exhibit substantial ripple and steady-state deviations, **Figs IV.25(a)-(c) and IV.27(a)-(c)**.
- The improved FOSMC achieves faster transient response with a settling time (t_s) of approximately 0.19s versus 0.4s for traditional FOSMC, as shown in **Figs IV.27(a)-(c)** and **IV.28(a)-(c)**.
- Similarly, the optimized SOSM controller shows enhanced performance including faster dynamics, reduced steady-state ripple, and lower IAE/ISE errors compared to conventional SOSM implementations **Figs IV.29-34, Table IV.4**. Detailed examination reveals significantly reduced oscillations compare **Figs IV.32(a)-(e), IV.34(a)-(e)** with **IV.31(a)-(e), IV.33(a)-(e)).**
- The refined HOSM controller with optimized parameters demonstrates excellent performance characteristics, including rapid dynamic response (0.1s settling), minimal steady-state ripple, and low IAE/ISE errors compared to traditional HOSMC **Figs IV.35, IV.40**.
- The optimized HOSM provides superior transient response and lower steady-state error than optimized FOSM and SOSM controllers. While traditional HOSMC outperforms optimized FOSM in transient response, the optimized FOSM maintains better steady-state performance.
- Response time measurements confirm: optimized HOSMC (0.1s), SOSMC (0.17s), and FOSMC (0.2s), establishing the HOSMC's speed advantage **(see Figs 27(d)-(f), 33(d)-(f), and 39(d)-(f))**.
- Implementation of optimized regulators produces high-quality sinusoidal stator current waveforms with substantially reduced THD values: 0.1281% (HOSMC), 0.4820% (SOSMC), and 0.6950% (FOSMC), compared to conventional versions showing higher THD levels of 0.8665% (HOSMC), 1.4604% (SOSMC), and 1.7590% (FOSMC).
- For wind speed step changes, the optimized HOSMC achieves fast, overshoot-free dynamic response **Fig IV.44**, while the conventional version suffers significant overshoots **Fig IV.43**.

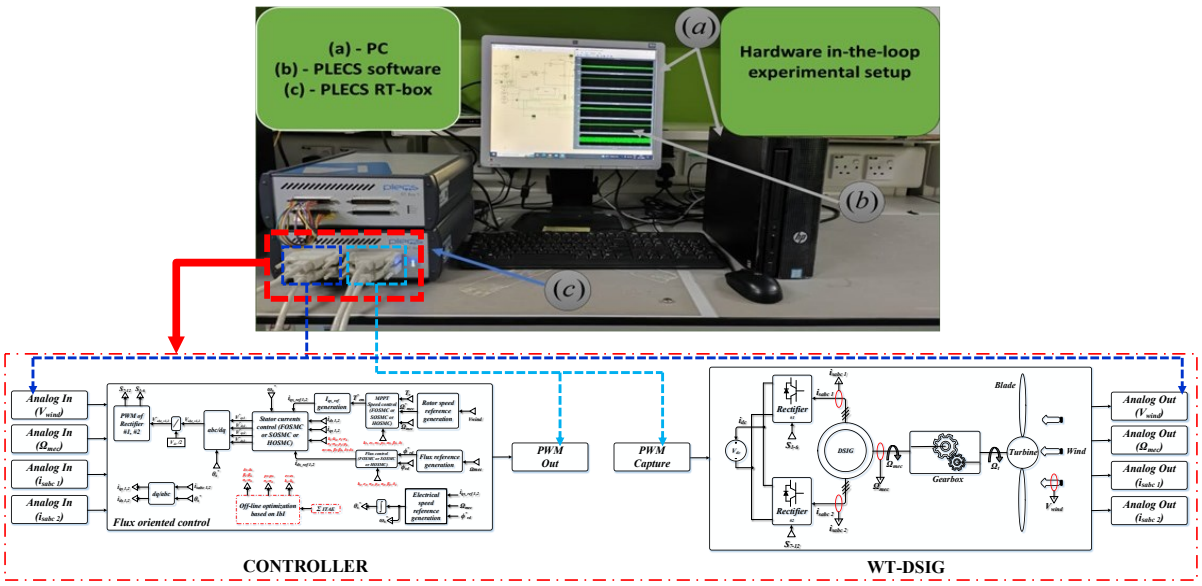

Figure IV.22. Hardware-in-the-loop experimental setup with SM_1, SM_2, and SM_3 controllers

Table IV.3– FOSMC, SOSMC, and HOSMC controllers' gains and performance of the tuned controllers

Tuning method	Controller	Gains									ITAEs		
		Rotor speed control			Rotor flux control			Stators currents control			$\Delta e_{\Omega mec}$	$\Delta e_{\phi rd}$	Δe_{ids1}
Trial and Error	FOSMC	$k_1 = 4000$	$e_1 = 30$		$k_2 = 2500$	$e_2 = 1$		$k_{3\text{-}6} = 100$	$e_{3\text{-}6} = 1$		0.5802	0.3278	9.3987
	SOSMC	$\rho_1 = 4200$	$\sigma_1 = 20$		$\rho_2 = 200$	$\sigma_2 = 450$		$\rho_{3\text{-}6} = 20000$	$\sigma_{3\text{-}6} = 2$		0.2058	0.2464	8.4616
	HOSMC	$\alpha_1 = 10$	$\beta_1 = 4500$	$\delta_1 = 50$	$\alpha_2 = 200$	$\beta_2 = 1000$	$\delta_2 = 1500$	$\alpha_{3\text{-}6} = 40$	$\beta_{3\text{-}6} = 700$	$\delta_{3\text{-}6} = 15$	0.1258	0.1464	6.0616
ILA	FOSMC	$k_1 = 5.128e^3$	$e_1 = 10.327$		$k_2 = 1.543e^3$	$e_2 = 0.013$		$k_{3\text{-}6} = 50,76$	$e_{3\text{-}6} = 0.5$		0.0626	0.0247	0.0569
	SOSMC	$\rho_1 = 2.054 e^3$	$\sigma_1 = 50,455$		$\rho_2 = 533,676$	$\sigma_2 = 349,021$		$\rho_{3\text{-}6} = 5,156 e^4$	$\sigma_{3\text{-}6} = 9,685$		0.0026	0.0047	0.0369
	HOSMC	$\alpha_1 = 53,87$	$\beta_1 = 2043$	$\delta_1 = 11,432$	$\alpha_2 = 355,76$	$\beta_2 = 499.892$	$\delta_2 = 987.799$	$\alpha_{3\text{-}6} = 9,78$	$\beta_{3\text{-}6} = 498,54$	$\delta_{3\text{-}6} = 6,709$	0.0006	0.0007	0.0189

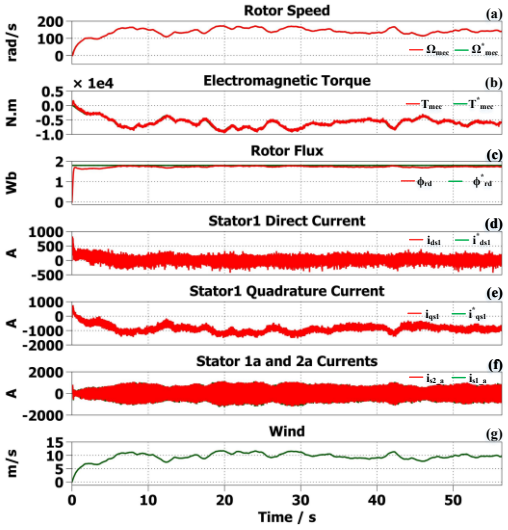

Figure IV.23. HiL results for variable wind with the conventional FOSMC regulator.

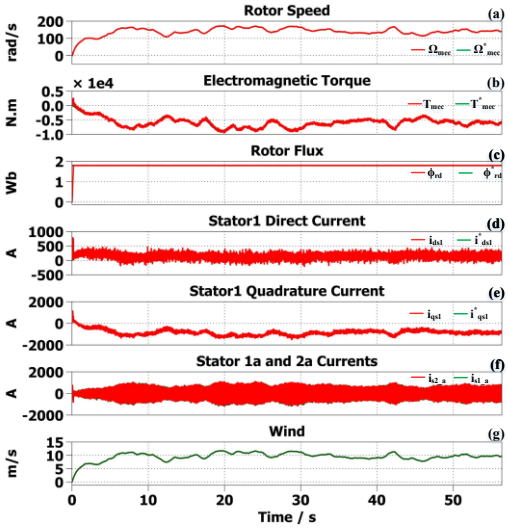

Figure IV.24. HiL results for variable wind with the optimized FOSMC regulator.

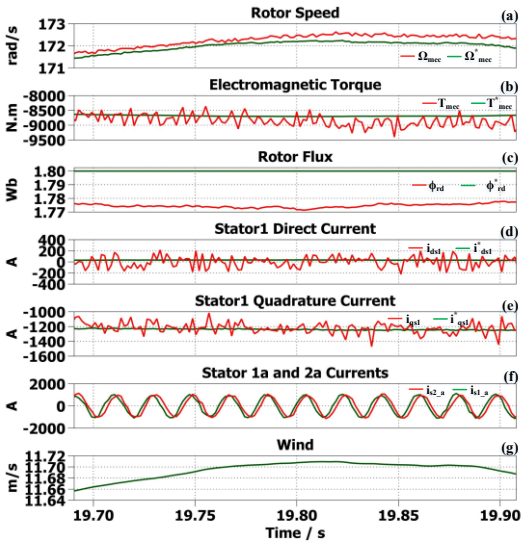

Figure IV.25. Steady-state performance: HiL results Zoom in with the conventional FOSMC regulator

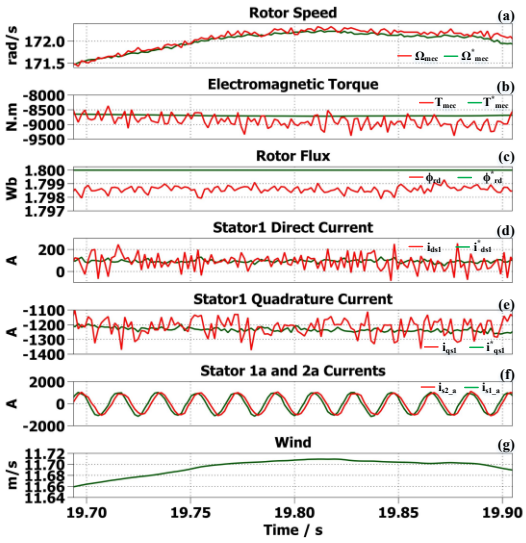

Figure IV.26. Steady-state performance: HiL results Zoom in with the optimized FOSMC regulator

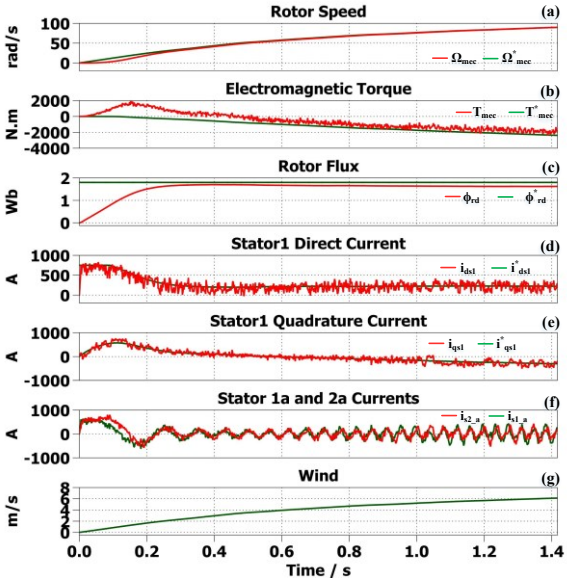

Figure IV.27. Zoom in transient response HiL results with the conventional FOSMC regulator

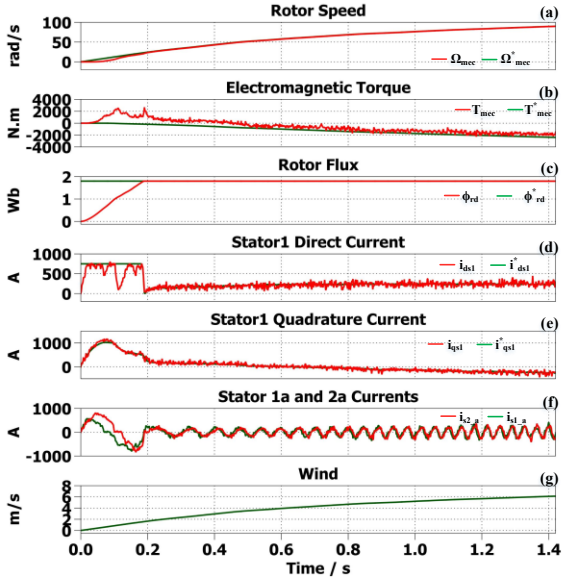

Figure IV.28. Zoom in transient response HiL results with the optimized FOSMC regulator

Table IV.4– Time-integral performance criteria and THD for different controllers of SMC

Tuning method		FOSMC						SOSMC						HOSMC						THD_{FO}%	THD_{SO}%	THD_{HO}%
		Ω_{mec}	ϕ_{rd}	i_{ds1}	i_{qs1}	i_{ds2}	i_{qs2}	Ω_{mec}	ϕ_{rd}	i_{ds1}	i_{qs1}	i_{ds2}	i_{qs2}	Ω_{mec}	ϕ_{rd}	i_{ds1}	i_{qs1}	i_{ds2}	i_{qs2}	i_{as1}	i_{as1}	i_{as1}
Trial-error	ISE	25	0.6	$8e^5$	$7e^5$	$8e^5$	$7e^5$	1	0.17	$7e^5$	$8e^5$	$7e^5$	$1e^6$	0.5	1	$2e^5$	$1e^6$	$2e^5$	$1e^6$	1.7590%	1.4604%	0.8665%
	IAE	30	4	$5e^3$	$5e^3$	$5e^3$	$5e^3$	4	0.7	$5e^3$	$5e^3$	$5e^3$	$6e^3$	4	0.3	$3e^3$	$6e^3$	$3e^3$	$6e^3$			
ILA	ISE	5	0.22	$4e^5$	$4e^5$	$4e^5$	$4e^5$	0.15	0.1	$4e^5$	$5e^5$	$4e^5$	$5e^5$	0.15	0.1	$2e^5$	$3e^5$	$2e^5$	$3e^5$	0.6950%	0.4820%	0.1281%
	IAE	6	0.3	$3e^3$	$4e^3$	$3e^3$	$4e^3$	2	0.2	$4e^3$	$4e^3$	$4e^3$	$4e^3$	2	0.15	$1e^3$	$1e^3$	$1e^3$	$1e^3$			

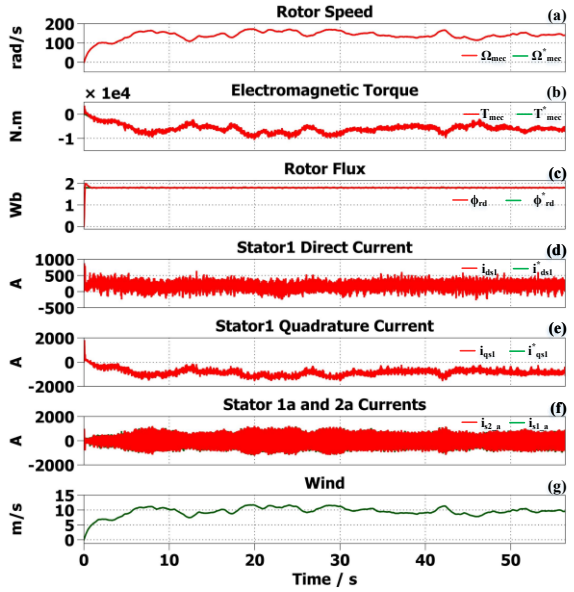

Figure IV.29. HiL results for variable wind with the conventional SOSMC regulator.

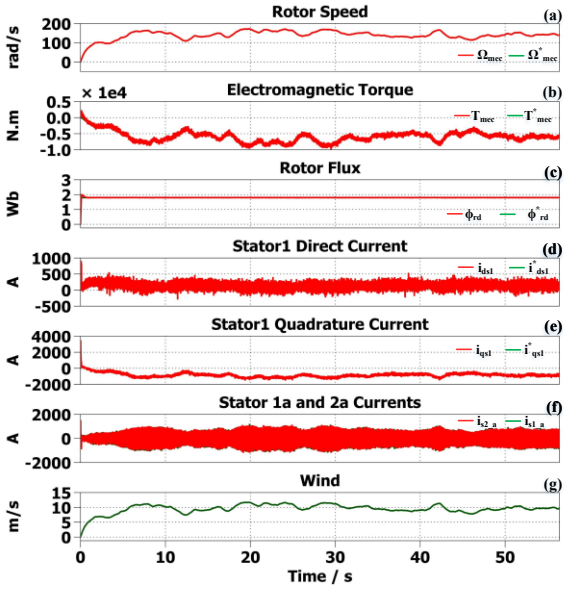

Figure IV.30. HiL results for variable wind with the optimized SOSMC regulator.

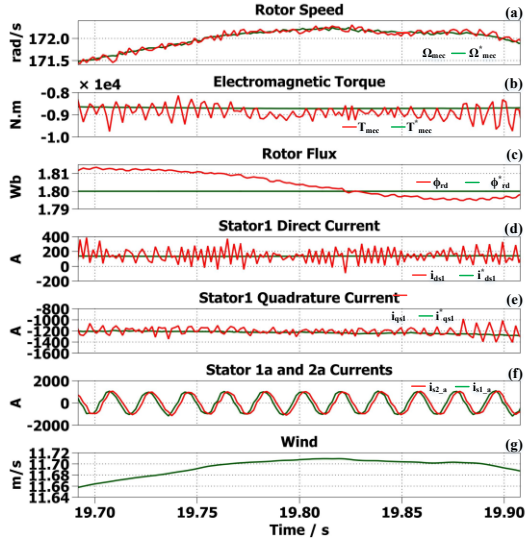

Figure IV.31. Steady-state performance: HiL results. Zoom in with the conventional SOSMC regulator

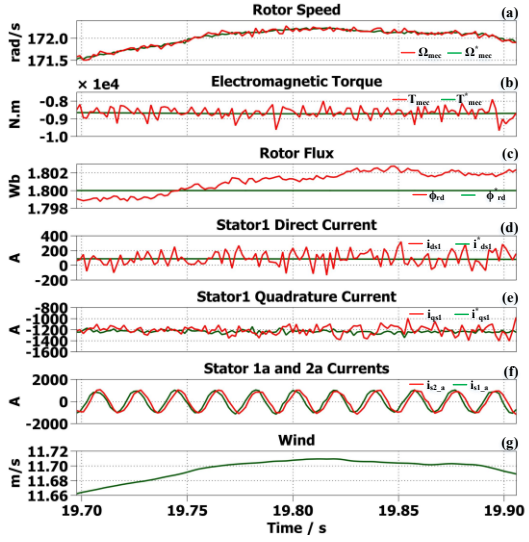

Figure IV.32. Steady-state performance: HiL results. Zoom in with the optimized SOSMC regulator

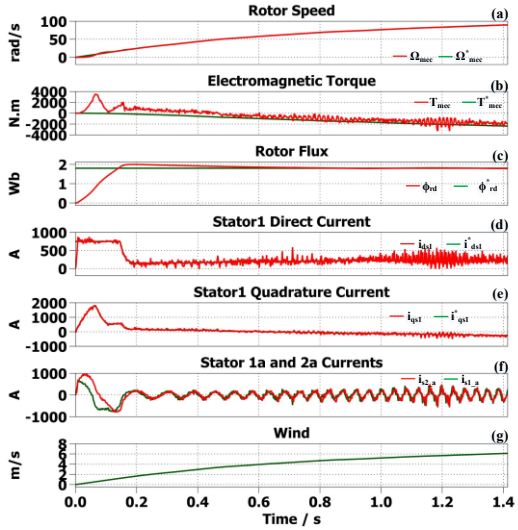

Figure IV.33. Zoom in transient response HiL results with the conventional SOSMC regulator

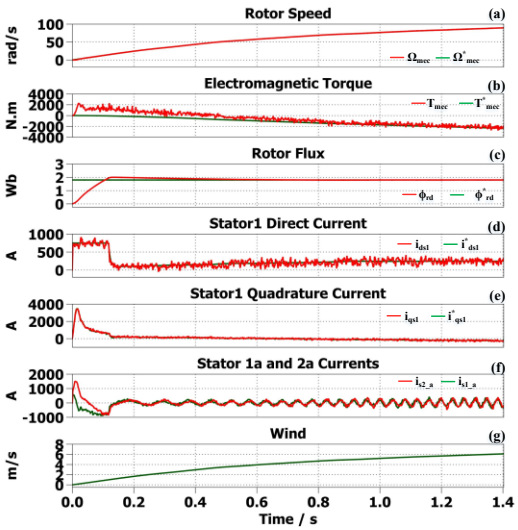

Figure IV.34. Zoom in transient response HiL results with the optimized SOSMC regulator

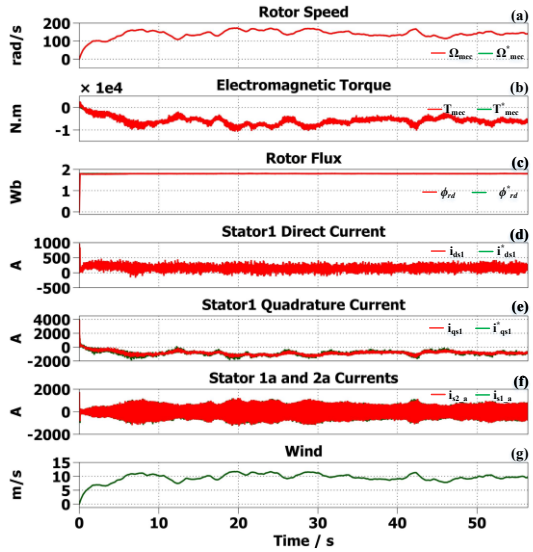

Figure IV.35. HiL results for variable wind with the conventional HOSMC regulator.

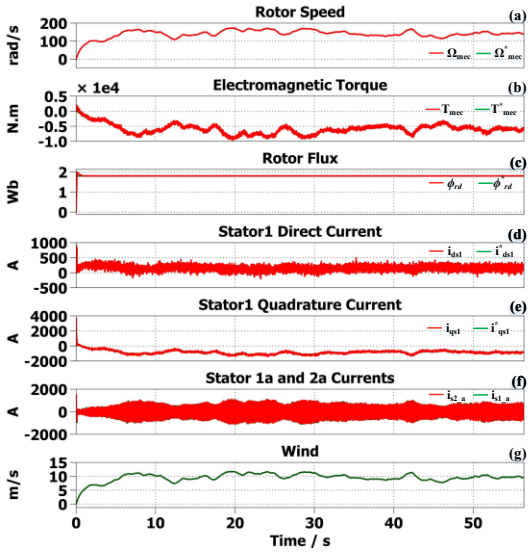

Figure IV.36. HiL results for variable wind with the optimized HOSMC regulator.

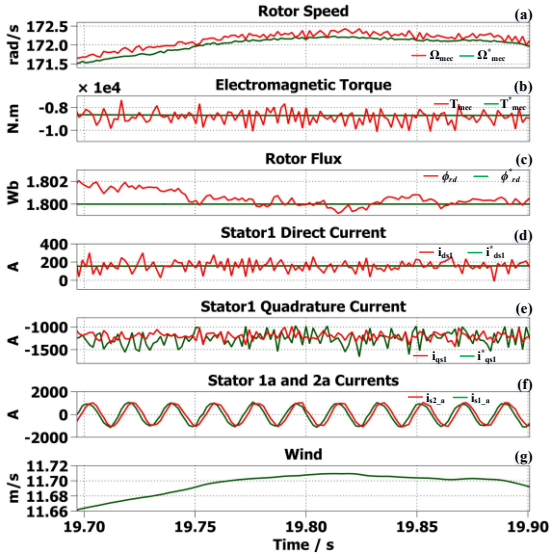

Figure IV.37. Steady-state performance: HiL results. Zoom in with the conventional HOSMC regulator

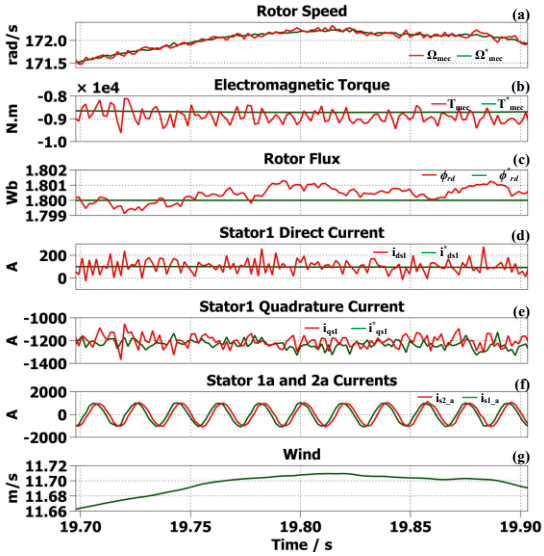

Figure IV.38. Steady-state performance: HiL results Zoom in with the optimized HOSMC regulator

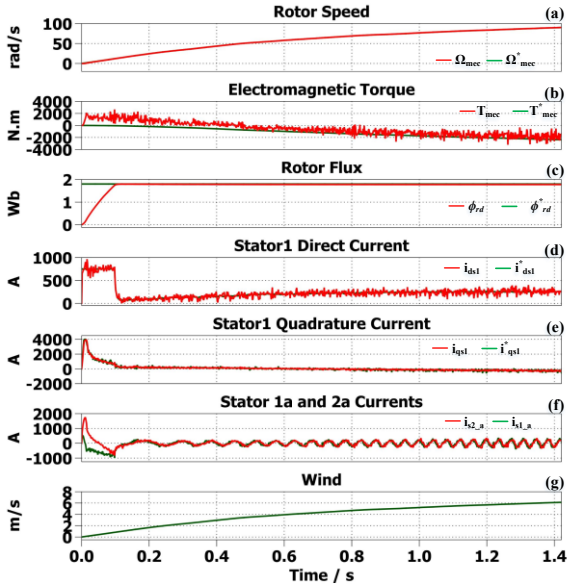

Figure IV.39. Zoom in transient response HiL results with the conventional HOSMC regulator

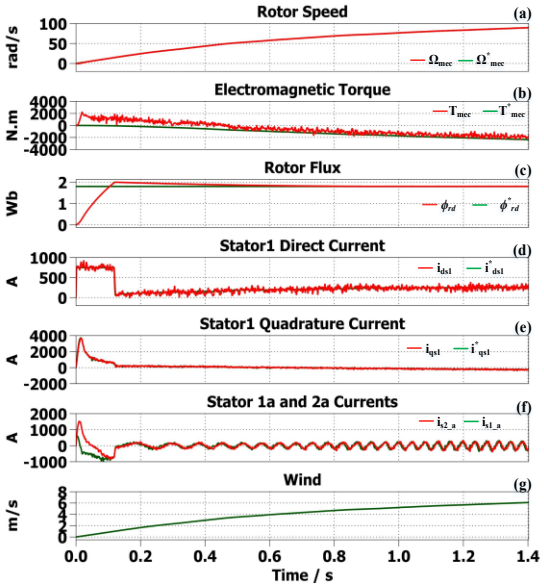

Figure IV.40. Zoom in transient response HiL results with the optimized HOSMC regulator

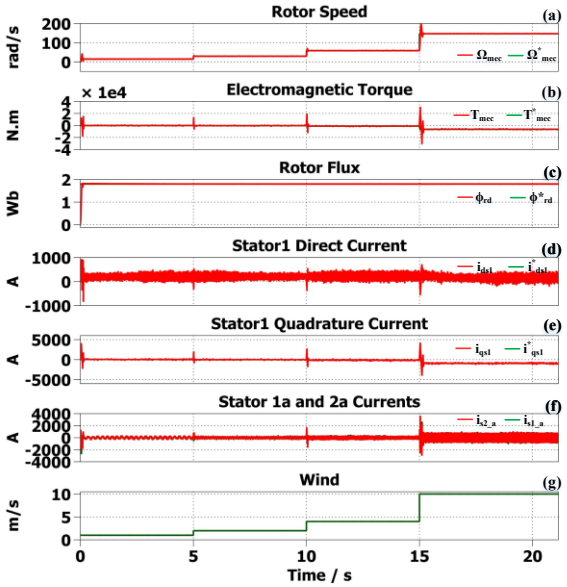

Figure IV.41. HiL results for speed step change with the conventional HOSMC regulator.

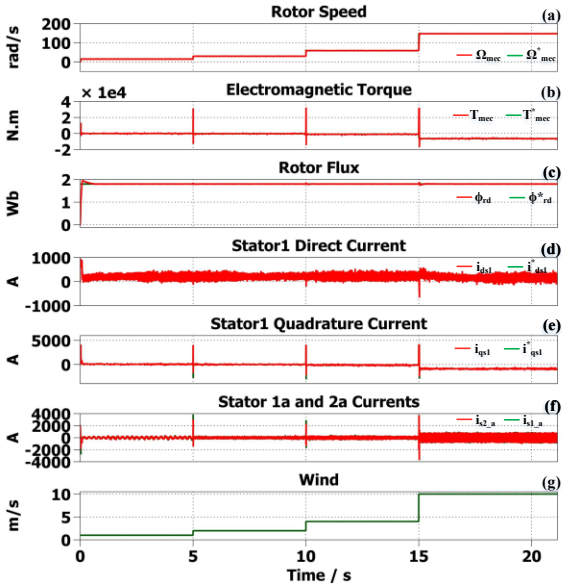

Figure IV.42. HiL results for speed step change with the optimized HOSMC regulator.

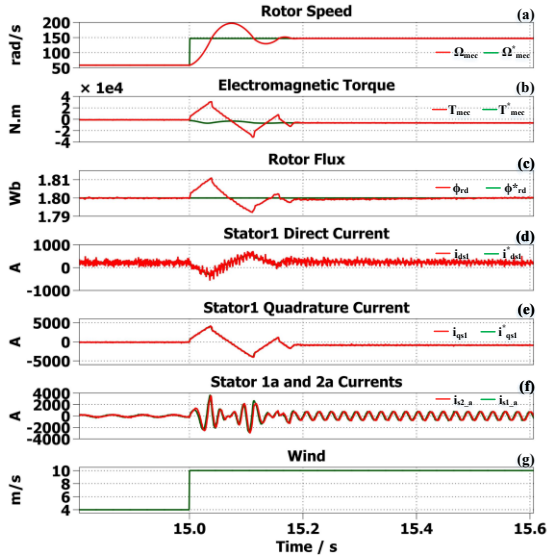

Figure IV.43. Steady-state performance: HiL results. Zoom in with the conventional HOSMC regulator

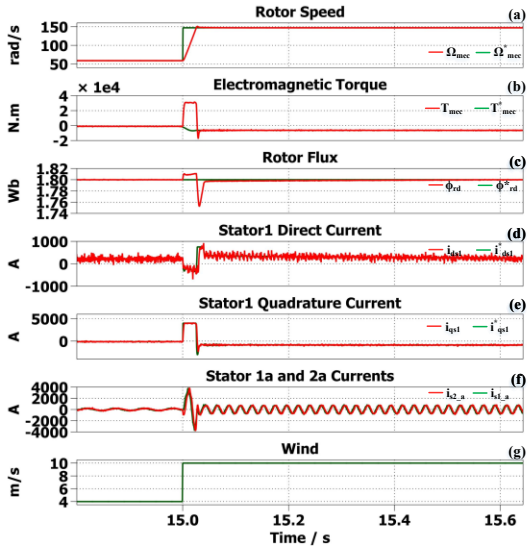

Figure IV.44. Steady-state performance: HiL results. Zoom in with the optimized HOSMC regulator

IV.4 Conclusion

This chapter proposes a new and effective optimization technique to optimally tune the parameters of advanced controllers, including PI (Proportional-Integral), BS (Backstepping), and HOSMC (Higher-Order Sliding Mode Control), incorporating FOC (Field-Oriented Control) for a WT-DSIG (Wind Turbine-Doubly Fed Induction Generator) system. The performance of the designed controllers is investigated against conventional controllers through HIL (Hardware-in-the-Loop) tests using the RT-Box platform. The results demonstrate that the proposed control approach with optimal tuning ensures high tracking performance of the desired references, with enhanced transient and steady-state responses, as well as comparatively

low IAE (Integral Absolute Error) and ISE (Integral Squared Error) under a variable wind speed profile.

In addition, the optimally designed controllers significantly improve the THD (Total Harmonic Distortion) of the stator currents. For the PI and BS controllers, the THD is reduced to 0.8103% for PI and 0.5047% for BS, compared to traditional controllers with 3.3456% for PI and 2.8665% for BS. Similarly, for the HOSMC, SOSMC, and FOSMC controllers, the THD is improved to 0.1281% for HOSMC, 0.4820% for SOSMC, and 0.6950% for FOSMC, compared to traditional ones with 0.8665% for HOSMC, 1.4604% for SOSMC, and 1.7590% for FOSMC. These results highlight the superior performance of the optimized controllers in terms of power quality and efficiency.

Furthermore, the findings emphasize the superiority of the optimally tuned HOSMC over all other controllers, including PI, BS, SOSMC, and FOSMC, in terms of fast transient response, reduced error, and low ripples during steady-state operation. The optimized PI and BS controllers also show significant improvements over their traditional counterparts, but the HOSMC stands out as the most effective solution for enhancing control performance and stability in the WT-DSIG system.

It is concluded that the use of optimization algorithms for tuning controller parameters, particularly for HOSMC, is an effective solution to improve the control performance and stability of the DSIG system. Moreover, this approach is highly versatile and suitable for application to various control types, making it a scalable solution for practical applications in diverse systems.

General Conclusion

General Conclusion

The growing demand for renewable energy and the urgent need to reduce dependence on fossil fuels have spurred significant advancements in wind energy systems. This sets the stage for the research presented in this doctoral thesis, centered on enhancing control strategies for a wind energy conversion system based on a Dual-Stator Induction Generator (DSIG).

This work addresses critical challenges related to system efficiency, operational stability, and robustness against disturbances. It focuses on developing and implementing advanced nonlinear control methodologies to optimize energy extraction, improve system performance, and ensure reliable grid integration. Through a comprehensive understanding of wind energy systems, incorporating both mechanical modeling integrating aerodynamic principles, Betz's law, and Maximum Power Point Tracking (MPPT) techniques and electrical modeling employing vector control strategies such as Field-Oriented Control (FOC) with Proportional-Integral (PI) regulators, this research establishes a robust foundation for precise control of speed, flux, and currents, vital for maintaining stability and maximizing power conversion.

The DSIG's dual-stator configuration is strategically utilized to enhance power output and system reliability, positioning it as a competitive solution for large-scale wind energy applications. Advancing beyond traditional control methods, robust nonlinear control techniques were explored and refined, including backstepping control optimized with the Subtraction Average Based Optimizer (SABO), which showed notable improvements in tracking accuracy, stability, and Total Harmonic Distortion (THD) reduction, outperforming conventional methods, particularly under variable wind conditions.

The investigation of Sliding Mode Control (SMC) in its various forms first-order (FOSMC), second-order (SOSMC) using the super twisting algorithm, and high-order (HOSMC) further underscored the importance of robustness and the mitigation of chattering phenomena, with higher-order techniques achieving superior transient and steady-state behavior. The Intelligent-in-Time Logic Algorithm (ILA) was also introduced to optimize HOSMC parameters, yielding controllers with exceptional transient response, minimized steady-state errors, and robustness against system uncertainties.

The developed control strategies were validated through Hardware-in-the-Loop (HIL) simulations using the RT-BOX1 platform to bridge the gap between theoretical constructs and practical applications. This validation confirmed that the optimized controllers significantly enhanced system response regarding stability, efficiency, and power quality; the BS-SABO controller notably reduced THD and improved tracking accuracy, while the HOSMC-ILA controller achieved an optimal balance between robustness and chattering suppression. Successful validation under dynamic wind conditions provided compelling evidence for the feasibility of deploying the proposed control solutions in real-world settings.

The outcomes of this research have led to substantial advancements in wind energy system control, improving energy conversion efficiency, ensuring greater stability and robustness, and

addressing the long-standing challenge of chattering in sliding mode controllers. Furthermore, experimental validation through HIL testing has reinforced these advanced control strategies' practical relevance and implementation potential, moving closer to bridging the gap between simulation-based studies and real-world wind energy applications.

Future Research Directions

While this research has made significant advancements, there are still opportunities for further exploration and improvement:

- **Integration of Machine Learning and Artificial Intelligence:** Future studies could incorporate AI-based techniques for real-time optimization and adaptive control to further enhance the performance of wind energy systems.
- **Hybrid Control Strategies:** Combining different control approaches, such as model predictive control (MPC) with sliding mode or backstepping control, could provide additional benefits in terms of adaptability and robustness.
- **Grid Integration and Smart Energy Management:** Investigating the interaction between wind energy systems and smart grids, including demand-side management and energy storage integration, could enhance the reliability of renewable energy sources.
- **Experimental Implementation on Full-Scale Wind Turbines:** Extending the research to full-scale wind farms and conducting long-term field tests would provide further validation and insights into real-world applications.

Appendices

Appendix A: Description of the Studied Wind Turbine

A 1.5 MW wind turbine has variable blade pitch and variable rotational speed.

A.1 Rotor

The rotor consists of three blades fixed to the central hub with a flange. An electric motor adjusts the blade angle individually for each blade. The rotor is positioned facing the wind. The total rotor diameter is 72 meters.

At partial load (power below 1.5 MW), the wind turbine operates at variable rotational speed, with a fixed blade angle. When the wind speed exceeds the nominal wind speed (power reaches 1.5 MW), power regulation is achieved by adjusting the blade angle. Wind gusts are not absorbed solely by changing the blade position; short-term variations in rotational speed are also acceptable.

A.2 Gearbox

The gearbox is a high-performance planetary epicyclic type. The gear ratio is 90. It is installed on an elastic support fixed to the nacelle. Special attention has been given during its development to reducing noise pollution.

A.3 Braking Systems

Since the blade position control system is autonomous and independent for each blade, it can also be used as both a primary and secondary braking system. To safely stop the wind turbine, setting just one blade to feathering position is sufficient. Each pitch motor is equipped with a backup battery inside the hub, ensuring blade feathering in case of grid failure. Additionally, a disc brake is installed on the high-speed shaft between the gearbox and the generator. This brake is only activated during emergency stops, manual stops, or in case of grid failure.

A.4 Generator

The generator is a double-star asynchronous machine with a squirrel-cage rotor. The mechanical energy captured by the three-bladed turbine is converted into electrical energy by the generator. Since there are two stator windings (two stars), this energy is rectified by two AC-DC converters and then injected, via a DC bus, into a frequency converter for adaptation to the grid.

The generator has an IP54 protection class, ensuring complete protection against contact with all conductive or moving parts inside the generator. The generator is grounded. The windings are cooled by an internal air-to-air heat exchanger cooling system, so the rotor and stator are not exposed to the external air, which is often highly aggressive. For temperature control, the machine is equipped with temperature sensors on both bearings and the windings. The generator is mounted on elastic supports on the nacelle.

A.5 Yaw System

The nacelle is mounted on the tower using a four-point contact bearing. The nacelle rotates through three electric gear motors, which are equipped with disc brakes on the high-speed shaft. A permanent friction torque keeps the nacelle at a constant yaw angle for standard rotation moments without strong turbulence. In the case of stronger moments due to gusts or turbulence, three braking motors actively stabilize the orientation.

The fail-safe brakes are engaged when the machine is stopped. The startup duration and rotation direction of the motor are controlled by a wind vane. The yaw system operates even at wind speeds below the startup wind speed, meaning it functions before the generator is able to produce energy.

A.6 Nacelle

The nacelle is protected by a fiberglass-reinforced composite cover and has thick acoustic insulation on the inner walls. Access from the tower is through a hatch in the generator nacelle. Both the nacelle and the base of the tower are equipped with a control unit, allowing operators to monitor and control the wind turbine. It is possible to start the turbine, adjust its orientation to face the wind, or apply braking from the nacelle.

When inside the nacelle, operators can prevent remote control from the tower base, including blade positioning and hydraulic systems. Activating the emergency stop button prevents unintentional startup of the wind turbine.

The full acoustic insulation of the nacelle cover, along with noise reduction systems for the gearbox and generator, ensures maximum noise reduction.

A.7 Tower

The tower is a conical steel tube consisting of three or four sections (with a hub height of 92 meters) and is coated with a three-layer protective finish. The welds undergo 100% quality control following DIN 18-800 standards.

In compliance with safety regulations, the tower includes rest platforms, and each section is equipped with lighting. The interior ladders allow climbing, with certified access protection devices. For a generator with a hub height of 92 meters, an optional elevator is available. The electrical cabinets of the wind turbine are installed inside the tower, ensuring that the control and power electronics are doubly protected from weather conditions, humidity, dust, etc.

A.8 Corrosion Protection

A multi-layer special coating protects the various parts of the wind turbine against corrosion. Components that are particularly exposed to harsh weather conditions, such as the rotor hub, are galvanized.

A.9 Lightning Protection

The rotor blades are equipped with a proven lightning protection system, tested in real-world conditions. Additionally, the wind turbine is protected against lightning by being directly grounded through underground metal rods.

Appendix B: Technical Data of the Studied Wind Turbine

B.1 Operational Data

- Cut-in wind speed: 3 m/s
- Nominal wind speed: ~11.8 m/s
- Cut-out wind speed: 25 m/s
- Rotational speed: 11.0 – 20.0 rpm
- Conical steel tower height: 92 m

B.2 Rotor

- Number of blades: 3
- Rotor shaft tilt angle: 4°
- Rotor cone angle: 0°
- Rotor diameter: 72 m
- Orientation: Upwind
- Maximum blade tip speed: 73.8 m/s

Hub

- Material: Cast steel
- Corrosion protection: Sandblasting + multi-layer coating

B.3 Blade Pitch Control

- Principle: Individual blade position adjustment via electric motor
- Pitch bearings: Double-row ball bearings, four-point contact
- Drive mechanism: Internal gear ring with 3-stage planetary gearbox

B.4 Gearbox

- Type: 3-stage gearbox
    - 1^{st} stage: Planetary (epicyclic)
    - 2^{nd} and 3^{rd} stages: Straight-toothed gears

- Nominal power: 1650 kW
- Gear ratio: 89.9
- Nominal efficiency: 96.8%

B.5 Generator/Converter

- Nominal power: 1,500 kW
- Type: Dual-stator induction generator
- Phase-to-phase voltage: 693 V, 50 Hz
- Full-load current: 1,255 A
- Protection class: IP 54
- Insulation class: F
- Synchronous speed: 1,500 r/m
- Nominal rotational speed: 1,800 r/m
- Speed range: 1,000 to 2,000 r/m
- Nominal efficiency: 96.1%
- Power factor ($\cos\phi$): Adjustable from -0.95 to +0.95

B.6 Masses

- Blades: ~5,230 kg
- Hub (with blades): ~14,000 kg
- Complete nacelle without rotor: ~49,000 kg

B.7 Braking Systems

- Primary braking system: Individual blade adjustment (with backup battery)
- Secondary braking system: Individual blade adjustment (with backup battery)
- Mechanical stop brake: Spring-actuated disc brake on the high-speed side with intrinsic safety

B.8 Yaw System

- Rotation speed: ~0.5°/second
- Electric motor + 4-stage planetary gearbox

Appendix C: Approximation of the Performance Coefficient Using Analytical Functions

The curves $C_p(\lambda,\beta)$ obtained through measurement or calculation can also be approximated using nonlinear functions. According to reference [77], a model for a large-scale wind turbine can be expressed as:

$$C_p(\lambda,\beta) = c_1.\left(c_2\lambda^i - c_3.\beta - c_4\right).e^{\left(-c_5\lambda^i\right)} + c_6.\lambda$$

can be used for the three-bladed horizontal turbine, where v_{wind} represents the wind speed and Ω_{turb} is the angular velocity of the turbine. However, the procedures in reference [78] Provide:

$c_1 = 0.5109 \quad c_2 = 116 \quad c_3 = 0.4$

$c_4 = 5 \quad c_5 = 21 \quad c_6 = 0.0068$

With:

$$\lambda^i = \frac{1}{\lambda + 0.08\beta} - \frac{0.035}{1+\beta^3}$$

Appendix D: Simulation Parameters of the Studied Wind Turbine

(WT-DSIG) SYSTEM PARAMETERS

Parameters	Values	Unit
Wind parameters		
Attenuation factor on the rotor	$\gamma = 0.25375$	
Average wind speed	$V_{moy} = 8.12$	$m.s^{-1}$
Turbine parameters		
Turbine's radius	$R = 32$	M
Gain of the gearbox	$G = 58$	
Coefficient of maximum power	$C_{pmax} = 0.47$	
Optimal relative wind velocity	$\lambda_{opt} = 8.1$	
DSIG parameters		
Nominal power of DSIG	$P_n = P_{max} = 1.5$	MW
Voltage (RMS)	$E = 400$	V
Pole pairs number	$P = 2$	
Resistance of the stator	$R_{s1} = R_{s2} = 0.008$	Ω
Inductance of the stator	$L_{s1} = L_{s2} = 0.134$	mH
Magnetizing inductance	$L_m = 0.0045$	H
Resistance of the rotor	$R_r = 0.007$	Ω
Inductance of the rotor	$L_r = 0.067$	mH
Moment of inertia	$J = 10$	$kg.m^2$
Coefficient of viscous	$k_f = 0.0015$	Nm s/rd
DC bus parameters		
DC bus capacitor	$C_{dc} = 0.089$	F
DC bus voltage	$v_{dc} = 1131$	V
LCL-filter parameters		
Grid line-to-line RMS voltage	$V_{LL} = 693$	V
Grid frequency	$f_{s,g} = 50$	Hz
Filter capacitance	$C_f = 50$	µF
Filter inductor grid side	$L_g = 0.1$	mH
Filter inductor converter side	$L_c = 0.1$	mH
The damping resistor	$R_D = 0.9$	Ω
Resistance of the filter	$L_f = 0.2$	mH
Inductance of the filter	$R_f = 0.1$	mH
Grid parameters		
Phase to phase voltage (V_{rms})	$400*\sqrt{2}$	V
Grid frequency	50	Hz

Appendix E: PLL in MATLAB function

```
function [Theta,Wf]=PLL(Vqref,V_max,Ksi_pll,Wn_pll,Ts,f_pll,Vsa,Vsb,Vsc)
% alpha beta transformation
Valpha=sqrt(2/3)*(Vsa-Vsb/2-Vsc/2);
Vbeta=sqrt(2/3)*(sqrt(3)/2*Vsb-sqrt(3)/2*Vsc);
persistent vq
if isempty(vq)
vq=0;
end
persistent tetaP
if isempty(tetaP)
tetaP=0;
end
Vd=cos(tetaP)*Valpha+sin(tetaP)*Vbeta;
Vq=-sin(tetaP)*Valpha+cos(tetaP)*Vbeta;
Wff=2*pi*f_pll;
Kp=(2*Ksi_pll*Wn_pll)/(sqrt(3/2)*V_max);
Ki=Wn_pll^2/(sqrt(3/2)*V_max);
% q axis voltage error
evq=Vqref-Vq;
% Integral of evq
persistent int_evq
if isempty(int_evq)
int_evq=0;
end
int_evq=int_evq+evq*Ts;
% Output of PI controller
Wf=Kp*evq+Ki*int_evq+Wff;
persistent int_W
if isempty(int_W)
int_W=0;
end
% Theta calculation
int_W=int_W+Wf*Ts;
Theta_=int_W;
tetaP=mod(Theta_,2*pi);
Theta=tetaP;
end
```

Bibliographic references

Bibliographic references

[1] T. Azzouz, "Modélisation et commande d'un système de conversion d'énergie éolienne à base d'une MADA," PhD Thesis, Université Mohamed Khider-Biskra, 2015. Accessed: Dec. 17, 2024. [Online]. Available: http://thesis.univ-biskra.dz/id/eprint/1996

[2] L. Mourad, "Synthèse de lois de commande non-linéaires pour le contrôle d'une machine asynchrone à double alimentation dédiée à un système aérogénérateur," PhD Thesis, Ph. D. thesis, Université Aboubakr Belkaid–Tlemcen–Faculté de Technologie, 2016. Accessed: Dec. 17, 2024. [Online]. Available: https://www.researchgate.net

[3] A. A. Firoozi, A. A. Firoozi, and F. Hejazi, "Innovations in Wind Turbine Blade Engineering: Exploring Materials, Sustainability, and Market Dynamics," *Sustainability*, vol. 16, no. 19, Art. no. 19, Jan. 2024, doi: 10.3390/su16198564.

[4] B. Alt, "WWEA Annual Report 2024: A Challenging Year for Windpower - Sonnenseite - Ökologische Kommunikation mit Franz Alt," Sonnenseite. Accessed: Jul. 06, 2025. [Online]. Available: https://www.sonnenseite.com/en/energy/wwea-annual-report-2024-a-challenging-year-for-windpower/

[5] K. El Mezdi *et al.*, "Performance improvement through nonlinear control design and power management of a grid-connected wind-battery hybrid energy storage system," *Results in Engineering*, vol. 20, p. 101491, Dec. 2023, doi: 10.1016/j.rineng.2023.101491.

[6] H. Amimeur, R. Abdessemed, and E. Merabet, "Modeling and analysis of dual-stator windings self-excited induction generator," *Journal of Electrical Engineering*, vol. 8, no. 3, pp. 6–6, 2008.

[7] F. Ameur and K. Kouzi, "Optimized PI and fuzzy speed vector control of dual stator induction generator used in a variable speed wind," *International Journal of Electrical Energy*, vol. 2, no. 1, pp. 74–81, 2014.

[8] P. Trojovský and M. Dehghani, "Subtraction-Average-Based Optimizer: A New Swarm-Inspired Metaheuristic Algorithm for Solving Optimization Problems," *Biomimetics*, vol. 8, no. 2, Art. no. 2, Jun. 2023, doi: 10.3390/biomimetics8020149.

[9] H. Rahali, S. Zeghlache, L. Benyettou, and L. Benalia, "Backstepping Sliding Mode Controller Improved with Interval Type-2 Fuzzy Logic Applied to the Dual Star Induction Motor," *Int. J. Comp. Intel. Appl.*, vol. 18, no. 02, p. 1950012, Jun. 2019, doi: 10.1142/S1469026819500123.

[10] K. Benzaoui *et al.*, "SABO optimization algorithm-based backstepping controller for DSIG within a wind turbine system," *Electr Eng*, Nov. 2024, doi: 10.1007/s00202-024-02839-1.

[11] K. Walid, M. Sofiane, H. Benbouhenni, G. Hamza, and T. Es-saadi, "Application of third-order sliding mode controller to improve the maximum power point for the photovoltaic system," *Energy Reports*, vol. 9, pp. 5372–5383, 2023.

[12] E. Terfia, S. Mendaci, S. E. Rezgui, H. Gasmi, and W. Kantas, "Optimal third-order sliding mode controller for dual star induction motor based on grey wolf optimization algorithm," *Heliyon*, 2024, Accessed: Jul. 29, 2024. [Online]. Available: https://www.cell.com/heliyon/fulltext/S2405-8440(24)08700-0

[13] A. Guettab, E. Bounadja, Z. Boudjema, and R. Taleb, "Third-order super-twisting control of a double stator asynchronous generator integrated in a wind turbine system under single-phase open fault," *Circuit Theory & Apps*, vol. 51, no. 4, pp. 1858–1878, Apr. 2023, doi: 10.1002/cta.3511.

[14] K. Benzaoui *et al.*, "IbI logics optimization algorithm-based high-order sliding mode control for DSIG within a wind turbine system," *Results in Engineering*, vol. 25, p. 103916, Mar. 2025, doi: 10.1016/j.rineng.2025.103916.

[15] P. A. Hosseinabadi, H. Pota, S. Mekhilef, and H. Schwartz, "Fixed-time observer-based control of DFIG-based wind energy conversion systems for maximum power extraction," *International Journal of Electrical Power & Energy Systems*, vol. 146, p. 108741, 2023.

[16] S. Zhao, N. Felderer, and J. Allmeling, "Real-time simulation of three-phase current source inverter using sub-cycle averaging method," in *2020 IEEE 21st workshop on control and modeling for power electronics (COMPEL)*, IEEE, 2020, pp. 1–6. Accessed: Dec. 28, 2023. [Online]. Available: https://ieeexplore.ieee.org/abstract/document/9265719/

[17] M. Aguilar, S. Riffo, A. Veliz, C. González-Castaño, and C. Restrepo, "RT Box card for studying the control communication impacts on microgrid performance and stability," *HardwareX*, vol. 12, p. e00322, 2022.

[18] J. S. Lee and G. Choi, "Modeling and hardware-in-the-loop system realization of electric machine drives—A review," *CES Transactions on Electrical Machines and Systems*, vol. 5, no. 3, pp. 194–201, 2021.

[19] A. Gaillard, "Système éolien basé sur une MADA: contribution à l'étude de la qualité de l'énergie électrique et de la continuité de service," PhD Thesis, Université Henri Poincaré-Nancy 1, 2010. Accessed: Dec. 12, 2024. [Online]. Available: https://hal.univ-lorraine.fr/tel-01748204

[20] H. J. Asl and J. Yoon, "Power capture optimization of variable-speed wind turbines using an output feedback controller," *Renewable Energy*, vol. 86, pp. 517–525, 2016.

[21] O. CHARROUF, "Optimisation d'un système de dessalement renouvelable," PhD Thesis, Université Mohamed Khider-Biskra, 2012. Accessed: Dec. 15, 2024. [Online]. Available: http://thesis.univ-biskra.dz/2337/

[22] J. G. Slootweg, H. Polinder, and W. L. Kling, "Representing wind turbine electrical generating systems in fundamental frequency simulations," *IEEE Transactions on energy conversion*, vol. 18, no. 4, pp. 516–524, 2003.

[23] J. Morren, J. Pierik, and S. W. De Haan, "Inertial response of variable speed wind turbines," *Electric power systems research*, vol. 76, no. 11, pp. 980–987, 2006.

[24] S. Ghoudelbourk, D. Dib, A. Omeiri, and A. T. Azar, "MPPT control in wind energy conversion systems and the application of fractional control (PI^α) in pitch wind turbine," *IJMIC*, vol. 26, no. 2, p. 140, 2016, doi: 10.1504/IJMIC.2016.078329.

[25] R. Aubrée, F. Auger, M. Macé, and L. Loron, "Design of an efficient small wind-energy conversion system with an adaptive sensorless MPPT strategy," *Renewable Energy*, vol. 86, pp. 280–291, 2016.

[26] F. Z. Tria, K. Srairi, M. T. Benchouia, and M. E. H. Benbouzid, "An integral sliding mode controller with super-twisting algorithm for direct power control of wind generator based on a doubly fed induction generator," *Int J Syst Assur Eng Manag*, Mar. 2017, doi: 10.1007/s13198-017-0597-5.

[27] Z. TIR, "Contribution à l'Étude d'une Machine Asynchrone à Double Alimentation sans Balais en vue de son Application dans le Domaine de l'Energie Eolienne," PhD Thesis, Université de Batna 2, 2014. Accessed: Dec. 17, 2024. [Online]. Available: http://eprints.univ-batna2.dz/1243/

[28] T. ZOHEIR, "Contribution à l'Étude d'une Machine Asynchrone à Double Alimentation sans Balais en vue de son Application dans le Domaine de l'Energie Eolienne. Doctorat thesis (2014), Université de Batna 2.," 2017, Accessed: Dec. 17, 2024. [Online]. Available: https://dspace.univ-batna2.dz/handle/123456789/1367

[29] S. El Aimani, "Modélisation des différentes technologies d'éoliennes intégrées dans un réseau de moyenne tension," These de doctorat, Ecole Centrale de Lille, 2004. Accessed: Jun. 25, 2024. [Online]. Available: https://theses.fr/2004ECLI0004

[30] B. Multon, G. Robin, O. Gergaud, and H. B. Ahmed, "Le Génie Electrique dans le vent: état de l'art et recherches dans le domaine de la génération éolienne," *JCGE*, vol. 3, no. 5, pp. 141–145, 2003.

[31] Y. Errami, M. Ouassaid, and M. Maaroufi, "Optimal power control strategy of maximizing wind energy tracking and different operating conditions for permanent magnet synchronous generator wind farm," *Energy Procedia*, vol. 74, pp. 477–490, 2015.

[32] D. Hadiouche, L. Baghli, and A. Rezzoug, "Space-vector PWM techniques for dual three-phase AC machine: analysis, performance evaluation, and DSP implementation," *IEEE Transactions on Industry Applications*, vol. 42, no. 4, pp. 1112–1122, 2006.

[33] E. Levi, "Multiphase electric machines for variable-speed applications," *IEEE Transactions on industrial electronics*, vol. 55, no. 5, pp. 1893–1909, 2008.

[34] J. BONAL, "La machine asynchrone double étoile régimes transitoires alimentation à fréquence variable," 1993, Accessed: Dec. 20, 2024. [Online]. Available: https://pepite-depot.univ-lille.fr/LIBRE/Th_Num/1993/50376-1993-49.pdf

[35] D. Traore, "Commande non linéaire sans capteur de la machine asynchrone," PhD Thesis, Ecole Centrale de Nantes (ECN), 2008. Accessed: Dec. 21, 2024. [Online]. Available: https://theses.hal.science/tel-00582690/

[36] L. Abdelhamid, "Contribution à l'Amélioration des Performances des Générateurs Eoliens-Evaluation de l'Impact des Energies Renouvelables sur l'Environnement," PhD Thesis, Université de Batna 2, 2008. Accessed: Dec. 22, 2024. [Online]. Available: http://eprints.univ-batna2.dz/1354/1/inj%20ABDELHAMID%20LILIA.pdf

[37] R. Abdessemed, *Modélisation et simulation des machines électriques: électrotechnique*. ellipses, 2011.

[38] G. K. Singh, K. Nam, and S. K. Lim, "A simple indirect field-oriented control scheme for multiphase induction machine," *IEEE transactions on industrial electronics*, vol. 52, no. 4, pp. 1177–1184, 2005.

[39] D. Pan and F. Wang, "Modeling and simulation of fuzzy control system for dual stator winding induction generator," in *2007 International Conference on Electrical Machines and Systems (ICEMS)*, IEEE, 2007, pp. 1227–1230. Accessed: Dec. 23, 2024. [Online]. Available: https://ieeexplore.ieee.org/abstract/document/4411984/

[40] A. Abdelkarim, "Amélioration des performances de la commande directe de couple (DTC) de la machine asynchrone par des techniques non-linéaires," PhD Thesis, Université Mohamed Khider-Biskra, 2017. Accessed: Dec. 24, 2024. [Online]. Available: http://thesis.univ-biskra.dz/3016/

[41] Z. Tir, O. P. Malik, and A. M. Eltamaly, "Fuzzy logic based speed control of indirect field oriented controlled Double Star Induction Motors connected in parallel to a single six-phase inverter supply," *Electric Power Systems Research*, vol. 134, pp. 126–133, 2016.

[42] E. Merabet, "Commande Floue Adaptative d0une Machine Asynchrone Double Etoile," PhD Thesis, Université de Batna 2, 2008. Accessed: Dec. 25, 2024. [Online]. Available: http://eprints.univ-batna2.dz/1364/1/inj%20MERABET%20ELKHIR.pdf

[43] J.-W. Jung and P. H. DStudent, "PROJECT# 2 Space vector PWM inverter," *Mechatronic Systems Laboratory, Dept. of Electrical and Computer Eng. The Ohio State University*, 2005, Accessed: Dec. 25, 2024. [Online]. Available: https://www.academia.edu/download/56854077/SpaceVector_PWM_Inverter.pdf

[44] R. Teodorescu, M. Liserre, and P. Rodriguez, *Grid converters for photovoltaic and wind power systems*. John Wiley & Sons, 2011. Accessed: Dec. 27, 2024. [Online]. Available: https://books.google.com/books?hl=fr&lr=&id=5k4tmcVIaM0C&oi=fnd&pg=PP8&dq=Grid+converters+for+photovoltaic+and+wind+power+systems&ots=veO_czaiyk&sig=MMrtnTlYM3iOQny9dYdbY7NeOHk

[45] C. Bao, X. Ruan, X. Wang, W. Li, D. Pan, and K. Weng, "Step-by-step controller design for LCL-type grid-connected inverter with capacitor–current-feedback active-damping," *IEEE Transactions on Power Electronics*, vol. 29, no. 3, pp. 1239–1253, 2013.

[46] R. W. Erickson, "Optimal single resistors damping of input filters," in *APEC'99. Fourteenth Annual Applied Power Electronics Conference and Exposition. 1999 Conference Proceedings (Cat. No. 99CH36285)*, IEEE, 1999, pp. 1073–1079. Accessed: Jan. 04, 2025. [Online]. Available: https://ieeexplore.ieee.org/abstract/document/750502/

[47] C. SAMIRA, "Evaluation des performances de l'aérogénérateur à base de la machine asynchrone double etoile connecté au réseau electrique.," PhD Thesis, Université de Béjaia-Abderrahmane Mira, 2011. Accessed: Jan. 07, 2025. [Online]. Available: https://www.pnst.cerist.dz/detail.php?id=60511

[48] A. Boyette, "Contrôle-commande d'un générateur asynchrone à double alimentation avec système de stockage pour la production éolienne," PhD Thesis, Université Henri Poincaré-Nancy I, 2006. Accessed: Jan. 08, 2025. [Online]. Available: https://theses.hal.science/tel-00133836/

[49] H. Amimeur, "Contribution au contrôle de la machine asynchrone double étoile," PhD Thesis, Batna, 2012. Accessed: Jan. 09, 2025. [Online]. Available: https://www.ccdz.cerist.dz/admin/notice.php?id=000000000000000314082000000

[50] J. Tow, "A step-by-step active-filter design," *IEEE Spectrum*, vol. 6, no. 12, pp. 64–68, Dec. 1969, doi: 10.1109/MSPEC.1969.5214222.

[51] "A DC bus capacitor design method for various inverter applications | IEEE Conference Publication | IEEE Xplore." Accessed: Feb. 02, 2025. [Online]. Available: https://ieeexplore-ieee-org.sndl1.arn.dz/abstract/document/6342196

[52] "PLL (3ph)." Accessed: Jan. 25, 2025. [Online]. Available: https://ch.mathworks.com/help/sps/powersys/ref/pll3ph.html

[53] I. Kanellakopoulos, P. V. Kokotovic, and A. S. Morse, "Systematic design of adaptive controllers for feedback linearizable systems," in *1991 American control conference*, IEEE, 1991, pp. 649–654. Accessed: Jan. 12, 2025. [Online]. Available: https://ieeexplore.ieee.org/abstract/document/4791451/

[54] A. Herizi, R. Balla, and S. A. Ahmani, "''Backstepping control of induction motors'',"" *El Wahat pour les Recherches et les Etudes*, vol. 8, no. 1, pp. 132–145, 2015.

[55] B. Bossoufi, M. Karim, A. Lagrioui, M. Taoussi, and A. Derouich, "Observer backstepping control of DFIG-Generators for wind turbines variable-speed: FPGA-based implementation," *Renewable Energy*, vol. 81, pp. 903–917, 2015.

[56] S. V. Emelyanov, "Variable structure control systems." Nauka, Moscow, 1967.

[57] A. Šabanovic, "Variable structure systems with sliding modes in motion control—A survey," *IEEE Transactions on Industrial informatics*, vol. 7, no. 2, pp. 212–223, 2011.

[58] V. Utkin, "Variable structure systems with sliding modes," *IEEE Transactions on Automatic control*, vol. 22, no. 2, pp. 212–222, 1977.
[59] D. V. Anosov, "On stability of equilibrium points of relay systems," *Automatica i telemechanica (Automation and Remote Control)*, vol. 2, pp. 135–149, 1959.
[60] A. G. Bondarev, S. A. Bondarev, N. Y. Kostyleva, and V. I. Utkin, "On stability of equilibrium points of relay systems," *Automatica i telemechanika (Automation and Remote Control)*, vol. 46, pp. 679–684, 1985.
[61] B. l aw Jakubczyk and W. Respondek, "On linearization of control systems," *Bull. Acad. Polon. Sci. Ser. Sci. Math*, vol. 28, no. 9–10, pp. 517–522, 1980.
[62] H. Hashimoto, H. Yamamoto, S. Yanagisawa, and F. Harashima, "Brushless servo motor control using variable structure approach," *IEEE Transactions on industry applications*, vol. 24, no. 1, pp. 160–170, 1988.
[63] B. Bandyopadhyay, F. Deepak, and K.-S. Kim, *Sliding mode control using novel sliding surfaces*, vol. 392. Springer Science & Business Media, 2009. Accessed: Jan. 14, 2025. [Online]. Available: https://books.google.com/books?hl=fr&lr=&id=6V3yJcqGIewC&oi=fnd&pg=PP2&dq=sliding+mode+control+G+2009&ots=XdZRPVnTNn&sig=nThKSYdeif6iudaghIPO49YKMH8
[64] J.-J. E. Slotine and W. Li, *Applied nonlinear control*, vol. 199. Prentice hall Englewood Cliffs, NJ, 1991. Accessed: Jul. 26, 2024. [Online]. Available: https://www.academia.edu/download/33582713/Applied_Nonlinear_Control_Slotine.pdf
[65] M. F. Benkhoris and A. Gayed, "Discrete sliding control technique of DC motor drive," in *1996 Sixth International Conference on Power Electronics and Variable Speed Drives (Conf. Publ. No. 429)*, IET, 1996, pp. 81–86. Accessed: Jul. 26, 2024. [Online]. Available: https://ieeexplore.ieee.org/abstract/document/708307/
[66] S. V. Emelyanov, S. K. Korovin, and L. V. Levantovskiy, "A drift algorithm in control of uncertain processes.," *PROB. CONTROL INFO. THEORY.*, vol. 15, no. 6, pp. 425–438, 1986.
[67] S. EMELJANOV, S. K. Korovin, and L. V. Levantovskii, "2ND-ORDER SLIDING MODES IN CONTROLLING UNCERTAIN SYSTEMS," *Soviet journal of computer and systems sciences*, vol. 24, no. 4, pp. 63–68, 1986.
[68] A. Bouyekni, R. Taleb, Z. Boudjema, and H. Kahal, "A second-order continuous sliding mode based on DPC for wind-turbine-driven DFIG," *Elektrotehniski Vestnik*, vol. 85, no. 1/2, pp. 29–36, 2018.
[69] Z. Boudjema, R. Taleb, Y. Djeriri, and A. Yahdou, "A novel direct torque control using second order continuous sliding mode o f a doubly fed induction generator for a wind energy conversion system," *Turkish Journal of Electrical Engineering and Computer Sciences*, vol. 25, no. 2, pp. 965–975, 2017.
[70] A. P. Shah and A. J. Mehta, "Direct power control of DFIG using super-twisting algorithm based on second-order sliding mode control," in *2016 14th International Workshop on Variable Structure Systems (VSS)*, IEEE, 2016, pp. 136–141. Accessed: Jul. 28, 2024. [Online]. Available: https://ieeexplore.ieee.org/abstract/document/7506905/
[71] M. Hafiane, J. Sabor, M. Taleb, H. Gualous, and H. Chaoui, "Adaptive second order sliding mode speed control of doubly fed in duction generator wind turbines," in *2015 3rd International Renewable and Sustainable Energy Conference (IRSEC)*, IEEE, 2015, pp. 1–6. Accessed: Jul. 28, 2024. [Online]. Available: https://ieeexplore.ieee.org/abstract/document/7454956/
[72] B. Belabbas, T. Allaoui, M. Tadjine, M. Denai, and U. K. Hatfield, "Higher performance of the super-twisting sliding mode controller for indirect power control of wind generator based on a doubly fed induction generator," in *2017 5th International Conference on Electrical Engineering-Boumerdes (ICEE-B)*, IEEE, 2017, pp. 1–6. Accessed: Jul. 28, 2024. [Online]. Available: https://ieeexplore.ieee.org/abstract/document/8192006/
[73] H. Gasmi, S. Mendaci, S. Laifa, W. Kantas, and H. Benbouhenni, "Fractional-order proportional-integral super twisting sliding mode controller for wind energy conversion system equipped with doubly fed induction generator," *J. Power Electron.*, vol. 22, no. 8, pp. 1357–1373, Aug. 2022, doi: 10.1007/s43236-022-00430-0.
[74] H. Benbouhenni and N. Bizon, "Third-order sliding mode applied to the direct field-oriented control of the asynchronous generator for variable-speed contra-rotating wind turbine generation systems," *Energies*, vol. 14, no. 18, p. 5877, 2021.
[75] H. Benbouhenni, "Amelioration effectiveness of torque and rotor flux control applied to the asynchronous generator for dual-rotor wind turbine using neural third-order sliding mode approaches," *International Journal of Engineering*, vol. 35, no. 3, pp. 517–530, 2022.
[76] M. Mirrashid and H. Naderpour, "Incomprehensible but Intelligible-in-time logics: Theory and optimization algorithm," *Knowledge-Based Systems*, vol. 264, p. 110305, 2023.
[77] O. Wasynczuk, D. T. Man, and J. P. Sullivan, "Dynamic behavior of a class of wind turbine generators during randon wind fluct uations," *IEEE Transactions on power apparatus and systems*, no. 6, pp. 2837–2845, 1981.
[78] M. Annoukoubi, A. Essadki, H. Laghridat, and T. Nasser, "Comparative study between the performances of a three-level and two-level converter for a Wind Energy Conversion System," in *2019 International Conference on Wireless Technologies, Embedded and Intelligent Systems (WITS)*, IEEE, 2019, pp. 1–6. Accessed: Feb. 10, 2025. [Online]. Available: https://ieeexplore.ieee.org/abstract/document/8723739/